# Microchemical Systems for Kinetic Studies of Catalytic Processes

By

Sameer K. Ajmera

B.S. Chemical Engineering
The University of Texas at Austin, 1997

Submitted to the Department of Chemical Engineering in Partial Fulfillment of the Requirements for the Degree of

Doctor of Philosophy in Chemical Engineering

at the

MASSACHUSETTS INSTITUTE OF TECHNOLOGY

June 2002



Author……
Sameer K. Ajmera
Department of Chemical Engineering
May 16, 2002

Certified by……
Klavs F. Jensen
Lammot duPont Professor of Chemical Engineering
Professor of Materials Science and Engineering
Thesis Supervisor

Certified by……
Martin A. Schmidt
Professor of Electrical Engineering and Computer Science
Thesis Supervisor

Accepted by……
Daniel Blankschtein
Professor of Chemical Engineering
Chairman, Departmental Committee on Graduate Students

# Microchemical Systems for Kinetic Studies of Catalytic Processes

By

Sameer K. Ajmera

# Abstract

Silicon microfabrication techniques and scale-up by replication have for decades fueled spectacular advances in the electronics industry. More recently, with the rise of microfluidics, microfabrication has enabled the development of microchemical systems for a variety of chemical and biological applications. This work focuses on the development of these systems for improved gas phase heterogeneous catalysis research. The catalyst development process often requires fundamental information such as reaction rate constants, activation energies, and reaction mechanisms to gauge and understand catalyst performance. To this end, we have examined the ability of microreactors with a variety of geometries to efficiently obtain accurate kinetic information. This work primarily focuses on microfabricated packed-bed reactors that utilize standard catalyst particles and briefly explores the use of membrane based reactors to obtain kinetic information. Initial studies with microfabricated packed-beds led to the development of a microfabricated silicon reactor that incorporates a novel cross-flow design with a short pass multiple flow-channel geometry to reduce the gradients that often confound kinetics in macroscale reactors. The cross-flow geometry minimizes pressure drop though the particle bed and incorporates a passive flow distribution system composed of an array of shallow flow channels. Combined experiments and modeling confirm the even distribution of flow across the wide catalyst bed with a pressure drop ~1600 times smaller than typical microfabricated packed-bed configurations. Coupled with the inherent heat and mass transfer advantages at the sub-millimeter length scale achievable through microfabrication, the cross-flow microreactor has been shown to operate in near-gradientless conditions and is an advantageous design for catalyst testing. The ability of microfabricated packed-beds to obtain accurate catalytic information has been demonstrated through experiments with phosgene generation over activated carbon, and CO oxidation and acetylene hydrogenation over a variety of noble metals on alumina. The advantages of using microreactors for catalyst testing is quantitatively highlighted throughout this work.

Thesis Supervisors: Professor Klavs F. Jensen and Professor Martin A. Schmidt

# Acknowledgments

I have had a most enjoyable time being a graduate student in Boston. Once I adjusted to the winters, this city, and particularly the people at MIT, have really embraced me. I have had the fortunate privilege of working directly with many impressive people. First and foremost, I would like to thank my advisors, Dr. Klavs F. Jensen and Dr. Martin A. Schmidt for their guidance. I appreciate the freedom they have given to explore ideas without outside pressure. I particularly thank Klavs for not letting me settle early on a less fulfilling project. His mentorship and insight have been the glue that holds this thesis together, and his ability to understand and constructively utilize the fundamentals from such a diversity of fields will always inspire me in my professional career. I thank Marty for adding a needed dose of practicality to the design and development of the devices presented in this work. Under his advisement, I was saved from countless hours (days? months?) of design iteration and process development.

I also thank the members of my thesis committee, Dr. William H. Green and Dr. Sylvia T. Ceyer. Their time commitment and input are greatly appreciated. In addition, I would like to specially thank Dr. Charles N. Satterfield for helping shape the early stages of my project.

The expertise and time commitment of the personnel of the Microsystems Technology Laboratories (MTL) is gratefully acknowledged. Their hard work and patience in training this graduate student made the fabrication of all the devices in this thesis possible. The artful eye and lens of Felice Frankel is also gratefully acknowledged for the nicer photographs of our microreactors that appear throughout these pages.

I also gratefully acknowledge the NSF Graduate Fellowship Program for financial support.

It has been my privilege to work in the KFJ group alongside such fine researchers and colleagues. Their scientific insight, curiosity, and wonderful conversations have kept me always pointed in the right direction, even when my laboratory progress would have suggested otherwise. I especially thank Dr. Kathy Vaeth and Dr. Samara Firebaugh for introducing me to the laboratory and the clean room when I first entered the group.

Most of the work on phosgene production presented in Chapter 2 and packaging in Appendix B was done in collaboration with Dr. Mathew Losey. His ability to get straight to the heart of the problem and fearlessness in trying new ideas helped give our “side-projects” their legs to stand on. I also thank the patience and hard work of Margaret Shyr who took on the difficult task of developing a robust packaging scheme as part of her undergraduate research. Her contributions to the work presented in Appendix B are gratefully acknowledged.

The work in Chapters 5 and 6 on running different reactions in the cross-flow reactor was greatly benefited by a productive collaboration with Dr. Cyril Delattre. In particular, Sections 5.4 and 5.6 have grown directly from his work. It was a pleasure to work with Cyril. His laboratory skill is quite impressive, and I'll always remember his ability to turn a plastic tube, a stainless-steel rod, duct tape, sodium disks, and a box of tissue paper into a functioning IR flow cell. If it wasn't for Cyril's expertise, I would still be struggling to get reproducible data in the laboratory. I also acknowledge the help of Dr. Justin McCue who helped characterize the surface area of our noble metal on alumina catalysts.

The work in Chapter 7 on the membrane reactor was done in collaboration with Dr. Aleks J. Franz. Although significantly misled in the ways of college football, his excellent engineering expertise helped the project progress. Although the chapter is presented last in this work, it was actually the first project I began, and Aleks provided significant guidance, insight, and advisement that were essential for helping me realize what research was all about.

Finally, I must thank all the people that made this thesis possible. The friends I have made here at MIT have provided support, humor, fun, and fulfillment as a graduate student and I will always treasure and reflect fondly upon these years.

I would also like to gratefully thank my parents, Pratul and Meena Ajmera. Their dedication to education and learning has been the inspiration for my academic career, and their countless sacrifices and unwavering support will always be cherished. It is to them that I respectfully and humbly dedicate this thesis. I would also like to thank my little sister, Sujata, for her love, support, and most importantly, her humor.

Finally, I would like to thank my dear wife, Geeta, for her unending love and support which cannot be expressed in words. I am forever indebted to her for her sacrifices and for making life with her, my ultimate treasure.

# Table of Contents

# List of Figures

# List of Tables

# Chapter 1

# Introduction

## 1.1 Microreaction Technology

Silicon microfabrication techniques and scale-up by replication have for decades fueled spectacular advances in the microelectronics industry. More recently, with the rise of MEMS (MicroElectroMechanical Systems) and microfluidics [1, 2], microfabrication has enabled the development of microchemical systems for a variety of chemical and biological applications [3, 4]. Microreaction technology, in specific, has grown in recent years utilizing a variety of fabrication techniques ranging from silicon (as detailed in this thesis) to LIGA and more conventional machining of metals [5, 6]. Silicon microfabrication offers the advantages of direct integration of sensors, actuators, and electronics, as well as reproducible and economical large scale manufacturing that may ultimately limit the commercialization and adoption of other techniques.

The microreaction field has quickly extended beyond chemical reactors to include a variety of unit operations such as mixers [7], separations [8], and chemical detection [9, 10]. In broad strokes, microreaction technology can be split into two large areas: enhanced chemical production through process intensification, and improved research and development or diagnostics through superior tools. The primary focus of this work lies on the latter. However, process intensification still holds significant promise as the inherent heat and mass transport benefits (discussed later in this chapter) of the micro scale can allow reactions to be performed under more aggressive conditions with higher yields than achievable with conventional reactors [11, 12]. Process intensification can be achieved in a variety of ways. For example, reactions can be operated under extreme conditions, ordinarily dangerous in macroscopic systems [13]. Fluid contacting can be enhanced by increasing the interfacial

area in a mass transfer limited reaction to enhance throughput [14]. Microreaction technology can also enable reaction pathways that are too difficult or dangerous to run in macroscale systems such as the direct fluorination of aromatic compounds [15]. Also, the ability to produce toxic or corrosive chemicals in a safe manner could potentially shift synthesis from large chemical plants with global shipping to distributed on-site/point-of-use chemical units. As examples, DuPont has synthesized a number of potentially hazardous chemicals in a silicon wafer bonded chemical reactor [5] and in Chapter 2, the production of phosgene in a micro packed-bed reactor will be discussed [16]. The scale-up of microchemical systems (commonly referred to as "scale-out") is significantly different from macroscale systems. Instead of increasing reactor size to increase throughput, a microchemical plant would have multiple identical reactors running in parallel. Once a reactor design is optimized, minimal effort is needed to fabricate more reactors. However, general systems issues such as process control, fluid distribution, and chemical monitoring scale with the number of reactors creating significant (but surmountable) hurdles in the successful implementation of such a system for chemical production [17].

More promising, perhaps, is the potential of microchemical systems to improve the investigation of chemical processes. The integration of sensors and actuators holds significant promise in the development of chemical sensors, diagnostic components such as calorimeters, and biological screening. The "lab on a chip" and "pharmacy on a chip" concepts are rooted deeply in microfluidics and have seen recent success with the commercialization of a variety of technologies. Microreactors provide the opportunity to control reaction temperature and reactor thermal characteristics to open up new performance regimes. These new operating regimes can provide better understanding and insight into

chemical properties such as reaction kinetics, thermodynamics, and rate mechanisms, or make data gathering and analysis simpler and more accurate. In Chapter 7, a membrane microreactor is discussed that achieves milder oxidation conditions (lower temperatures) than previous systems [18]. Chapter 5 details a reactor geometry that allows the extraction of differential kinetics (see Section 1.3.1) at traditionally large reactor conversions without the aid of external mixing, simplifying data analysis and experimentation. With respect to classical chemical engineering, microreaction technology looks to fundamentally change the way researchers discover and optimize catalysts. The parallel nature of microreactors naturally lends itself to high-throughput or combinatorial catalysis applications. Further, the reduction of heat and mass transfer limitations in microfabricated reactors facilitate the quantitative extraction of kinetic parameters, the primary goal of this work.

## 1.2 The Catalyst Development Bottleneck

The scale-up of chemical processes from discovery to industrial production often requires ~10+ years with catalyst development being a contributing factor to the long process. Heterogeneous catalysts (catalyst-solid phase, reactants/products- gas and/or liquid) are essential to realize productive chemical processes and their discovery and optimization require extensive experimentation. Catalysts are complex mixtures of materials for which subtle differences in preparation procedure, surface oxidation state, crystal structure, and electronic interactions strongly influence performance [19], making the extraction of useful information inherently time consuming and slow [20]. Obtaining accurate and timely information during catalyst development in the laboratory is essential for successful scale-up.

Erroneous data and inefficient methods of collecting information in the laboratory during the evaluation of process kinetics, thermodynamics, and catalyst properties lead to expensive developmental delays and non-optimized performance costing companies time and profit [21].

### 1.2.1 High-throughput Catalyst Development

Catalyst development has traditionally been a combination of experience, fundamental chemistry, and trial and error. However, the onset of high-throughput materials development such as high-throughput catalyst screening and combinatorial catalysis has enabled a variety of new methodologies to complement traditional catalyst development. These new technologies, typically qualitative in nature, involve the rapid testing and analysis of a large library of potential samples for promising catalysts. High-throughput screening would normally be applied during catalyst optimization procedures, where parameters such as calcination temperature or additive concentration can be rapidly screened for improved catalytic performance. Combinatorial catalysis is considered during new catalyst discovery where catalyst samples are created using a combination of materials in a statistical fashion to create a large array of potential candidates. This library is then screened to determine promising composition spaces for further study. To speed up development, increasing efforts are being devoted to miniaturizing and automating catalyst screening and optimization [22-26], including efforts towards microfabricated chip-based screening tools [27].

The second slow step in development is the *quantitative* characterization of the chemical kinetics (i.e., rate of reaction, activation energy) of the catalytic process [28, 29].

Once promising leads have been discovered by a rapid screening procedure, information such as kinetic rate constants, thermal stability, poisoning, deactivation, activity, and selectivity must be known in great detail for accurate and useful scale-up. This phase of catalyst testing is significantly more quantitative than the high-throughput methods mentioned earlier and therefore requires strict control over gradients in the reactor. Obtaining kinetic data is also crucial for chemical plant design as kinetic parameters are incorporated into plant simulations to size reactors and related process equipment such as pumps, heat exchangers, and separation columns. Detailed laboratory catalyst testing is also important for research and development and knowledge generation as understanding reaction mechanisms and rates gives insight into very fundamental aspects of chemistry and catalysis. However, the tools available for such experiments are quite lacking.

### 1.2.2 Catalyst Screening versus Catalyst Testing

In order to differentiate between the various aspects of catalyst development, a semantic distinction will be made in this thesis between "catalyst screening" and "catalyst testing." The former will be used to refer to the broad category of high-throughput and combinatorial procedures for catalyst discovery and optimization involving scanning through large libraries of catalysts for promising candidates. "Catalyst testing," the main focus of this thesis, will be used to describe the quantitative characterization of catalyst performance such as obtaining rate constants, activations energies, and reaction orders.

## 1.3 Bench-scale Laboratory Catalyst Testing Today

Testing of heterogeneous gas phase catalysts is commonly performed in bench-scale mini-tubular reactors (~5 mm diameter) in which catalyst particles are packed against a frit to form a 10-20 mm long reaction zone [30]. Temperature control is achieved with an external heat source/sink such as a tube furnace, sand bath, or cooling jacket. The reactors are placed in parallel and take up significant space in a research laboratory, limiting the number of reactors that can be run simultaneously. The loading and replacement of samples, typically performed manually, is time consuming. Although laboratory tube reactors use smaller catalyst volumes than industrial reactors, reactions with dangerous compounds still require additional investment in infrastructure such as protective enclosures that add complexity and expense to the testing setup.

Obtaining accurate kinetics at known reaction conditions is often a difficult challenge. Even small tube reactors can be susceptible to heat and mass transfer limitations for which measurable bulk values differ significantly from the true values in the small catalyst pores, reducing the accuracy of kinetics measurements. Surface catalytic reactions can present many problems due to their speed, complexity, and high exo- or endothermicity. Hotspots can form inside the reactor for exothermic reactions, yielding a non-isothermal catalyst bed. Isothermal operation is difficult to achieve, even though this is the preferred method of operation [31]. Bypassing, channeling, and local variations in activity also lead to temperature gradients in common macroscale laboratory reactors. Temperature acquisition instruments such as thermocouples are often located far away from areas of high activity. Data taken from a reactor operating in this way can lead to misinterpretations of the true nature of the surface reaction, and oftentimes, research is limited to general or statistical

information about the reaction. Pressure gradients along the packed-bed can further convolute true reaction kinetics. Nevertheless, these mini-tube reactors have been used for decades in laboratories and researchers have sizable working experience to draw from in interpreting data from such systems. In general, a gradientless reactor (i.e., a reactor without thermal, mass, and pressure gradients) is desired for measuring the intrinsic kinetics of catalytic reactions. Obtaining a gradientless reactor has proven to be a challenge. Researchers have developed a variety of reactors to reduce gradients such as micropulse reactors, single pellet diffusion reactors, recycle reactors, and rotating basket reactors [21, 31-33]. These reactors are typically difficult to run in a robust manner consistent with the broad range of chemistries and reaction conditions seen in heterogeneous catalysis. For example, some of these reactors can be costly and complicated to operate, and some perform well in one process attribute such as isothermal operation, but are lacking in other process characteristics such as flow uniformity.

### 1.3.1 Differential Kinetics

Aside from thermal and mass transfer limitations, reactors can develop significant variations in reactant concentration as the reaction progresses to high conversions. Known as "integral" operation, the large variation in concentrations (although not necessarily mass transfer limited) complicates data analysis because the rate of reaction is a function of concentration and varies throughout the reactor. Useful data is only extracted with the use of reactor models to deconvolute the transport and reaction processes. Kinetic data extracted is therefore limited by the accuracy of the global reactor model employed. Alternatively,

operating the reactor with low conversions, known as "differential" reactor operation, allows the direct determination of reaction rates [34, 35]. If conversion is kept low enough, the concentration of reactants can be considered constant throughout the reactor. The entire catalyst bed can then be assumed to operate with the same reaction rate, simplifying kinetic analysis by eliminating the need for complicated reactor models. For differential reactors, the average rate of reaction is used throughout the reactor, resulting in a simple mole balance for kinetic analysis,

$$F_{io}\xi_i = -\bar{r}_i \tag{1-1}$$

where $F_{io}$ is the molar flow rate of reactant feed in mol/s, $\xi_i$ is the reactant conversion, and $-\bar{r}_i$ is the average reaction rate in mol/s. Compared to the complicated plug flow reactor analysis, an example of which is given in Chapter 2, the differential reactor assumption when correctly applied, significantly facilitates catalyst testing. This thesis mainly focuses on the development of a microchemical reactor that both eliminates gradients *and* operates differentially for improved catalysis research.

## 1.4 Microfabricated Reactors for Catalysis Research: Motivation

The capabilities of microchemical reaction systems with sub-millimeter length scales have the potential to exceed those of conventional macroscopic systems. The primary attribute of shrinking reactor volume is the corresponding increase in the surface area-to-

volume ratio. This translates directly into an increased ability to add and remove heat from the reactor. Coupled with the reduced characteristic length across the reactor, thermal gradients from the center to the reactor walls are reduced. For exothermic processes, this increased heat transfer can suppress the formation of hot spots that otherwise would confound kinetic data or lead to thermal runaway. For example, in Chapter 7, a membrane reactor is discussed that is capable of removing heat fast enough to achieve low temperature partial oxidation. Furthermore, silicon's thermal conductivity of 150 W/m/K is larger than that of stainless-steel. Therefore, the reactor bulk can quickly come into thermal equilibrium with the reaction zone, reducing gradients.

The characteristic time of diffusion scales with the square of length. Unlike larger systems where diffusion can often be neglected, the sub-millisecond diffusion time seen across sub-millimeter microchannels shows that diffusion in microchemical systems is a significant form of mass transport, serving to reduce concentration gradients across the microreactor. The reduction of heat and mass gradients inherent in microsystems makes microfabricated reactors an interesting choice for the development of gradientless packed-beds. These advantages are discussed throughout the thesis both qualitatively and quantitatively and are demonstrated via both experimental and modeling results. The benefits of diffusive mixing are most clearly seen in Chapter 5 where diffusion is so large that the window of operation for differential kinetics is expanded, providing additional functionality to the reactor. Microsystem technology offers a host of additional features that makes it an attractive choice for reactor development. As highlighted in this thesis, microfabrication technology allows for greater control over reactor geometry and flow manifolds due to the nature of silicon fabrication. The ability to tailor highly specific and

complicated features during reactor design would be moot if the appropriate fabrication procedures are not available. Silicon microfabrication provides an excellent platform for the production of highly reproducible, highly controllable devices that can be manufactured in a parallelized fashion. This reduces costs and enables a wide variety of device designs. The choice of silicon based microreactors is important for the eventual adoption of microsystems in industrial and research laboratories.

## 1.5 Miniaturized Catalyst Testing: Choice of Catalyst

In order that kinetic results from a miniaturized catalyst testing platform be applicable to an industrial process, it is critical to use catalysts that are similar to those used in the scaled-up process. In this way, results in the microsystem will be relevant to macroscale catalyst via standard synthesis procedures and catalytic parameters. A variety of work has been done with microchemical systems using thin film catalysts or metal catalysts supported on thin film supports [22, 23, 25, 26, 36-38]. However, important aspects of heterogeneous catalysis such as surface oxidation state, metal-support interactions, and secondary adsorptions are lost with these simple thin film catalysts, making it difficult to translate specific information obtained in such systems to macroscale catalytic systems.

A common heterogeneous catalyst is a noble metal such as platinum or palladium dispersed onto a mesoporous support such as alumina or silica in powdered or pellet form. These catalyst particles are prepared using a variety of well developed techniques such as precipitation, sol-gels, and impregnation [39]. There is a significant investment over the past decades in knowledge and techniques for catalyst preparation, and it is important to leverage

this advantage when employing microchemical systems for catalyst testing. Therefore, the reactor designs discussed in this thesis (with the exception of Chapter 7) are limited to micro packed-beds that use catalysts in particle form. These particles are prepared using standard techniques and characterized using common methods such as BET and CO adsorption. Particles of larger size that are conventionally prepared can be crushed and sieved to obtain the desirable range of diameter for use with the microreactor.

## 1.6 Thesis Objectives and Overview

The primary objective of this study is to determine in what capacity microreaction technology can contribute to the improvement of heterogeneous catalyst testing. By determining the issues related to the development of these microfabricated reactors, the benefits and limitations are elucidated. A second objective is to demonstrate the power of silicon microfabrication technology to control reactor geometry by tailoring reactor features for very specific purposes. Throughout this work, an effort is made to quantify, when possible, these advantages and limitations, and use the relevant concepts of macroscale reactor engineering to characterize the performance of microreactors. Finally, another goal of this work is to explore areas where employing microreactors opens new opportunities for gaining information that would not have been achievable, or less easily achievable, on the macroscale. These areas of new opportunity will be highlighted as points where the technology can make clear impact on catalysis research. This study aims to delineate the important parameters and issues of concern when designing microreactors for catalyst

development and give a point of reference for the future development of microfabricated gradientless reactors.

The next chapter begins with an examination of a microfabricated packed-bed reactor that utilizes a geometry commonly used in chemical reactors of all length scales. In this chapter, the advantages and limitations of employing micro packed-beds are presented leading directly to the novel reactor design presented in Chapters 3, 4, and 5. These three chapters constitute the bulk of this thesis and detail the design, characterization, and performance of a reactor with a novel flow geometry for catalyst testing. Although briefly described in Chapter 3, a detailed fabrication procedure of this microreactor is found in Appendix A. Chapter 6 examines the application of macroscale correlations for mass transfer in packed-bed reactors to the microreactor length scale. Based upon experimental and modeling results, it has been found that caution must be exercised in translating common correlations to the microreactor. Chapter 7 is a stand-alone chapter that examines the use of membrane microreactors for catalyst testing. Although deviating from the desire to employ catalyst particles, the membrane reactor yields useful thermal advantages. Chapter 8 closes with a summary, discussions, and final thoughts, as well as prospects for the future of silicon microfabricated reactors. Finally, Appendix B details current progress on the development on a new packaging technique to obtain high temperature/pressure fluidic connections.

Literature cited and notation that are not specifically defined in the text are given at the end of each respective chapter.

## Literature Cited


[1] G. Kovacs, in: "Micromachined Transducers Sourcebook," McGraw-Hill, Boston, 1998.

[2] M.J. Madou, in: "Fundamentals of Microfabrication," CRC Press, Boca Raton, Florida, 1997.

[3] A. Van Den Berg, W. Olthuis, P. Bergveld, in: "Micro Total Analysis Systems 2000," Kluwer Academic Publishers, Enschede, The Netherlands, 2000.

[4] "IMRET 4: 4th International Conference on Microreaction Technology," in: AIChE Spring National Meeting, 2000, Atlanta, USA, 2000.

[5] J.J. Lerou, M.P. Harold, J. Ryley, J. Ashmead, T.C. O'Brien, "Microfabricated Minichemical Systems: Technical Feasibility," in: Microsystem Technology for Chemical and Biological Microreactors, Mainz, Germany, 1995, pp. 51-67.

[6] R.S. Wegeng, C.J. Call, M.K. Dronst, "Chemical System Miniaturization," in: AIChE 1996 Spring National Meeting, New Orleans, Louisiana, 1996. Also available at: http://www.pnl.gov/edo/license/programs/fliers/microfly.stm.

[7] H. Lowe, W. Ehrfeld, V. Hessel, T. Richter, J. Schiewe, "Micromixing Technology," in: IMRET 4: 4th International Conference on Microreaction Technology, Atlanta, GA, 2000, pp. 31.

[8] A.J. Franz, K.F. Jensen, M.A. Schmidt, "Palladium Membrane Microreactors," in: IMRET 3: Proceedings of the Third International Conference on Microreaction Technology, Frankfurt, Germany, 1999, pp. 267.

[9] T.M. Floyd, K.F. Jensen, M.A. Schmidt, "Towards Integration of Chemical Detection for Liquid Phase Microchannel Reactors," in: IMRET 4: 4th International Conference on

Microreaction Technology, AIChE 2000 Spring National Meeting, Atlanta, USA, 2000, pp. 461.

[10] S.L. Firebaugh, K.F. Jensen, M.A. Schmidt, "Miniaturization and Integration of Photoacoustic Detection with a Microfabricated Chemical Reactor System," *J. Microelectromechanical Sys.* **10** (2001) 232-238.

[11] R.S. Wegeng, M.K. Drost, D.L. Brenchley, "Process Intensification Through Miniaturization of Micro Thermal and Chemical Systems in the 21st Century," in: IMRET 3: 3rd International Conference on Microreaction Technology, Frankfurt, Germany, 1999.

[12] K.F. Jensen, "Microchemical Systems: Status, Challenges, and Opportunities," *AICHE Journal.* **45** (1999) 2051.

[13] A.J. Franz, D. Quiram, R. Srinivasan, I.-M. Hsing, S.L. Firebaugh, K.F. Jensen, M.A. Schmidt, "New Operating Regimes and Applications Feasible with Microreactors," in: Process Miniaturization: 2nd International Conference on Microreaction Technology-Topical Conference Preprints, New Orleans, LA, 1998, pp. 33.

[14] M.W. Losey, "Novel Multiphase Chemical Reaction Systems Enabled by Microfabrication Technology," Thesis, M.I.T., Cambridge, MA, 2001.

[15] N. de Mas, R.J. Jackman, M.A. Schmidt, K.F. Jensen, "Microchemical Systems for Direct Fluorination of Aromatics," in: IMRET 5: Proceedings of the Fifth International Conference on Microreaction Technology, Strasbourg, France, 2001, pp. 60.

[16] S.K. Ajmera, M.W. Losey, K.F. Jensen, M.A. Schmidt, "Microfabricated Packed-bed Reactor for Phosgene Synthesis," *AIChE J.* **47** (2001) 1639-1647.

[17] D.J. Quiram, I.M. Hsing, A.J. Franz, K.F. Jensen, M.A. Schmidt, "Design Issues for Membrane-based, Gas Phase Microchemical Systems," *Chemical Engineering Science.* **55** (2000) 3065-3075.

[18] A.J. Franz, S.K. Ajmera, S.L. Firebaugh, K.F. Jensen, M.A. Schmidt, "Expansion of Microreactor Capabilities through Improved Thermal Management and Catalyst Deposition," in: IMRET 3: Microreaction Technology: Industrial Prospects, Frankfurt, Germany, 1999, pp. 197-206.

[19] C.N. Satterfield, in: "Heterogeneous Catalysis in Industrial Practice," Krieger Publishing Company, Malabar, Florida, 1996.

[20] W.H. Weinberg, B. Jandeleit, K. Self, H. Turner, "Combinatorial methods in homogeneous and heterogeneous catalysis," *Current Opinion in Solid State & Materials Science.* **3** (1998) 104-110.

[21] V.W. Weekman, Jr., "Laboratory Reactors and Their Limitations," *AICHE JOURNAL.* **20** (1974) 833.

[22] P. Cong, R.D. Doolen, Q. Fan, D.M. Giaquinta, S. Guan, E.W. McFarland, D.M. Poojary, K. Self, H.W. Turner, W.H. Weinberg, "High-Throughput Synthesis and Screening of Combinatorial Heterogeneous Catalyst Libraries," *Angew. Chem. Int. Ed.* **38** (1999) 483-488.

[23] F.C. Moates, M. Somani, J. Annamalai, J.T. Richardson, D. Luss, R.C. Willson, "Infrared Thermographic Screening of Combinatorial Libraries of Heterogeneous Catalysts," *Ind. Eng. Chem. Res.* **35** (1996) 4801-4803.

[24] M. Orschel, J. Klein, H.W. Schmidt, W.F. Maier, "Detection of Reaction Selectivity on Catalyst Libraries by Spatially Resolved Mass Spectrometry," *Angew. Chem. Int. Ed.* **38** (1999) 2791-2794.

[25] S. Senkan, "Combinatorial Heterogeneous Catalysis- A New Path in an Old Field," *Angew. Chem. Int. Ed.* **40** (2001) 312-329.

[26] B. Jandeleit, D.J. Schaefer, T.S. Powers, H.W. Turner, W.H. Weinberg, "Combinatorial Materials Science and Catalysis," *Angew. Chem. Int. Ed.* **38** (1999) 2494-2532.

[27] P. Claus, D. Hönicke, T. Zech, "Miniaturization of screening devices for combinatorial development of heterogeneous catalysts," *Catal. Today.* **67** (2001) 319-339.

[28] S. Senkan, K. Krantz, S. Ozturk, V. Zengin, I. Onal, "High-Throughput Testing of Heterogeneous Catalyst Libraries Using Array Microreactors and Mass Spectrometry," *Angew. Chem. Int. Ed.* **38** (1999) 2794-2799.

[29] J. Pérez-Ramírez, R.J. Berger, G. Mul, F. Kapteijn, J.A. Moulijn, "The six-flow reactor technology- A review on fast catalyst screening and kinetic studies," *Catal. Today.* **60** (2000) 93-109.

[30] C.N. Satterfield, in: "Heterogeneous Catalysis in Industrial Practice," Krieger Publishing Company, Malabar, Florida, 1996, pp. Ch. 11.

[31] P. Sunderland, "An Assessment of Laboratory reactors for Heterogeneously Catalysed Vapour Phase Reactions," *Transactions of the Institution of Chemical Engineers.* **54** (1976) 135.

[32] C.O. Bennett, M.B. Cutlip, C.C. Yang, "Gradientless reactors and transient methods in heterogeneous catalysis," *CHEMICAL ENGINEERING SCIENCE.* **27** (1972) 2255.

[33] E.G. Christoffel, "Laboratory Reactors and Heterogeneous Catalytic Processes," *Catalysis Reviews- Science and Engineering.* **24** (1982) 159-232.

[34] H.S. Fogler, in: "Elements of Chemical Reaction Engineering," Prentice-Hall Inc., Upper Saddle River, NJ, 1999, pp. 243.

[35] O. Levenspiel, in: "The Chemical Reactor Omnibook," Oregon State University Press, Corvallis, Oregon, 1989, pp. Chapter 21.

[36] E. Reddington, A. Sapienza, B. Guraou, R. Viswanathan, S. Sarangapani, E.S. Smotkin, T.E. Mallouk, "Combinatorial Electrochemistry: A Highly Parallel, Optical Screening Method for Discovery of Better Electrocatalysts," *Science.* **280** (1998) 1735-1737.

[37] R. Srinivasan, I.-M. Hsing, P.E. Berger, K.F. Jensen, S.L. Firebaugh, M.A. Schmidt, M.P. Harold, J.J. Lerou, J.F. Ryley, "Micromachined Reactors for Catalytic Partial Oxidation Reactions," *AICHE JOURNAL.* **43** (1997) 3059.

[38] M.T. Janicke, H. Kestenbaum, U. Hagendorf, F. Schuth, M. Fichtner, K. Schubert, "The Controlled Oxidation of Hydrogen from an Explosive Mixture of Gases Using a Microstructured Reactor/Heat Exchanger and Pt/Al2O3 Catalyst," *Journal of Catalysis.* **191** (2000) 292-293.

[39] C.N. Satterfield, in: "Heterogeneous Catalysis in Industrial Practice, Second Edition," Krieger Publishing Company, Malabar, Florida, 1996, pp. Chapter 4.

# Chapter 2
# Microfabricated Tube-Flow Reactor: Phosgene Synthesis

---

In order to explore the potential for using microfabricated reactors for catalyst testing, a silicon micro packed-bed reactor for phosgene synthesis was initially examined. This chapter details the results of these studies, including a quantitative characterization of chemical productivity and the extraction of chemical kinetics. The issue of chemical compatibility, which underlies every chemical process, is addressed for the harsh chlorine chemistry through the use of a protective coating. The increased heat and mass transfer inherent at the sub-millimeter reactor length scale provides a larger degree of safety, control, and suppression of gradients than is available in macroscale systems. These advantages are explored in the extraction of chemical kinetics from microreactor experiments and reactor performance is compared qualitatively to bench scale experiments. The chapter closes with an analysis of the advantages and disadvantages of microfabricated packed-bed reactors with traditional flow geometries and lays the groundwork for the cross-flow microreactor discussed in Chapters 3, 4, and 5.

## 2.1 Motivation for Phosgene Synthesis in Microchemical Systems

Due to economies of scale, chemical production is usually performed in large facilities from where products are shipped. However, increasing safety and environmental concerns could shift this current model towards one of distributed chemical synthesis, with smaller plants located near the intended point of application. This is particularly the case for hazardous and toxic chemical intermediates that have serious storage and shipping constraints. One such intermediate used throughout the chemical and pharmaceutical industry is phosgene ($COCl_2$, carbonyl dichloride), manufactured from gaseous chlorine and carbon monoxide over activated carbon catalyst. The reaction is moderately fast and exothermic [1, 2].

$$Cl_2 + CO \rightarrow COCl_2 \qquad -\Delta H = 26 \text{ kcal/mol} \qquad (2\text{-}1)$$

Phosgene is widely used as a chemical intermediate for the production of isocyanates used in polyurethane foams and in the synthesis of pharmaceuticals and pesticides. Processes using phosgene require specialized cylinder storage, environmental enclosures, pipelines and fixtures under negative pressure, and significant preventative maintenance. To demonstrate the ability to produce hazardous compounds from microfabricated devices, The DuPont Company has synthesized a number of hazardous chemicals such as isocyanates in a microreactor formed by bonded silicon layers [3].

Phosgene synthesis provides an interesting case study for kinetic experimentation in microreactors. The increased safety and small chemical quantities are clear advantages for catalytic studies and provide motivation for using microchemical systems for chemistry that

is difficult and dangerous on the macroscale. Further, the exothermic reaction makes temperature control of the catalyst bed difficult on the macroscale making accurate kinetic studies very challenging. Microchemical reactors stand to alleviate such concerns as will be discussed later in this chapter and in greater detail in Chapter 5. Finally, the harsh chemistry involved in the production of phosgene, particularly the use of chlorine which is highly corrosive and reactive, provides an interesting challenge in implementing chemically stable microchemical systems for both chemical production and kinetic studies.

## 2.2 Microfabricated Tube-Flow Reactor Design

A micro tube-flow reactor was initially chosen to assess the performance of microfabricated packed-bed reactors for the extraction of kinetic information. This reactor was originally designed and fabricated at MIT for multiphase chemistry (gas and liquid reactants over a solid catalyst). The reactor is a microfabricated version of a classical macroscale packed-bed reactor, which is essentially a tube packed with catalyst particles with flow down the long axis of the tube. This flow geometry is referred to as "axial" or "tube-flow" (Figure 2-1) and is the standard configuration for flow in pipes and tubes. This reactor geometry provides an excellent starting point for understanding the benefits and limitations of microfabricated packed-bed reactors as relevant comparisons can be made to classical packed-bed reactors.

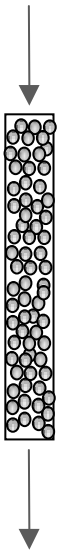


**Figure 2-1.** Typical axial or tube-flow where flow is down the long axis of the bed.

The reactor chip, shown in Figure 2-2, consists of a 20 mm long, 625 μm wide, 300 μm deep reaction channel (3.75 μL volume) capped by Pyrex. Figure 2-2b shows a scanning electron micrograph (SEM) of the inlet where flow is split among several interleaved channels (25 μm wide) that meet at the entrance of the reaction channel. Perpendicular to the inlet channels are 400 μm wide loading channels used to deliver catalyst particles to the reactor.

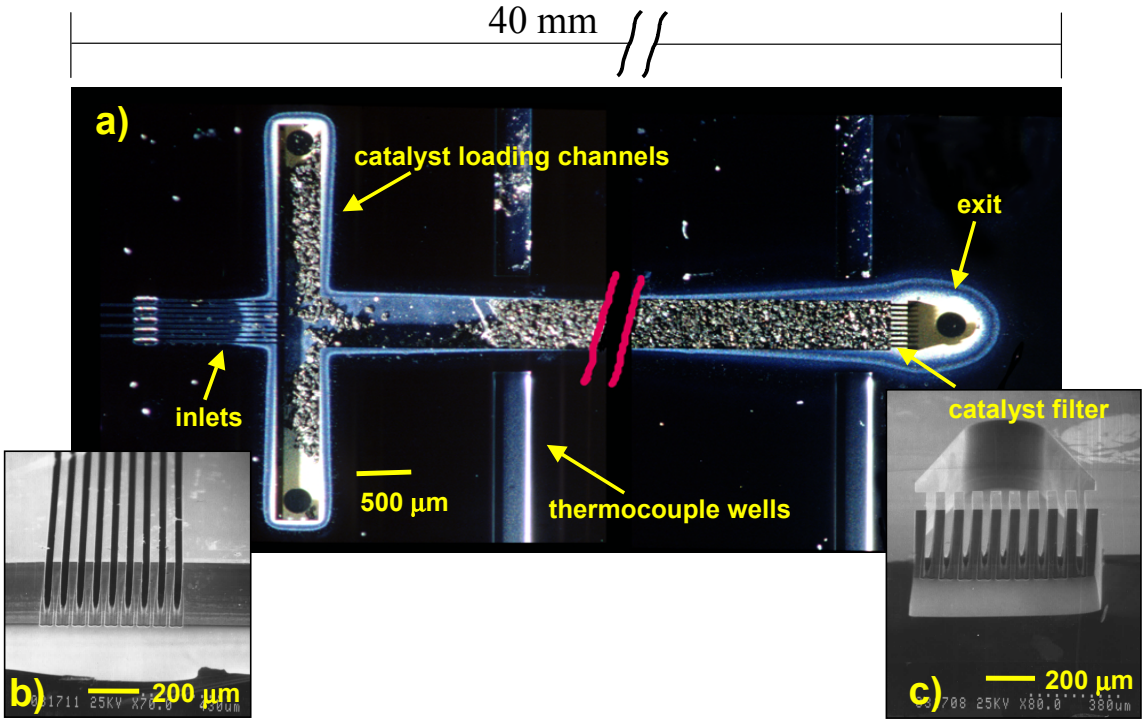


**Figure 2-2.** Microfabricated silicon packed-bed reactor (Losey [4]). a) Top-view of reactor partially loaded with 60 µm activated carbon particles. The reactor channel is 20 mm long. The image is spliced to fit the 20 mm reaction channel by omitting the long channel mid-section (Photograph by Felice Frankel, MIT); b) SEM of the 25 µm wide interleaved inlets. c) SEM of the catalyst filter structure.

Catalyst is loaded by placing a vacuum at the exit of the reactor and drawing in particles through the loading channels. An inert gas is used to load catalyst if contamination or deactivation are an issue. At the outlet of the reaction chamber, a series of posts with 25 µm gaps acts as a filter to retain the catalyst bed (Figure 2-2c). There are also four 325 µm wide channels perpendicular to the reaction channel along its length for holding thermocouples. Access ports for flow come from underneath at the inlets (not shown in Figure 2-2), the reactor exit, and at the ends of the catalyst loading channels.

### 2.2.1 Reactor Fabrication

The microreactor, shown in Figure 2-2, is fabricated out of single crystal silicon with standard microfabrication processes developed for integrated circuits and MEMS. The geometry is defined using photolithography and created with silicon etching. The thermocouple wells, inlets, the reactor and catalyst loading channels, and the catalyst filter are etched first in a silicon substrate (100 mm diameter wafer, 500 μm thick) using a time-multiplexed inductively coupled plasma etch [5]. The wafer is then turned over, patterned, and etched on its back-side to create the access ports. Since chlorine etches silicon, a conformal silicon dioxide film about 5000 Å thick is grown around the entire wafer in a wet oxidation furnace to protect the reactor before wafer bonding. The use of this oxide coating is discussed further in Section 2.4. Finally, the oxide coated channels are capped by a Pyrex wafer (Corning 7740), which has a similar thermal coefficient of expansion as silicon, using an anodic bond [6]. The anodic bond is usually done between silicon and Pyrex with 800 Volts applied across the wafers at 500$^{o}$C for approximately 5 minutes. For the anodic bonding of the silicon wafer with oxide, the bond time was increased to 10 minutes to allow for stabilization of the bond current. The bonded wafer stack is cut with a die saw to obtain individual devices. A 100 mm diameter wafer yields twelve single channel reactors (10 mm × 40 mm × 1.0 mm) after bonding and dicing. A detailed description of the motivation, design issues, characterization, and fabrication of this micro packed-bed reactor is given by Losey et al. [7, 8].

## 2.3 Experimental Setup

The reactor is compressed with a metal cover plate against a thin elastomer gasket (0.8 mm thick Kalrez™) with punched through-holes to form fluidic connections to a stainless-steel base. External fluidic connections are made directly to the metal base (Figure 2-3). This packaging technique is the same as that described by Losey [8] and is similar to the packaging scheme described in detail in Section 4.1.

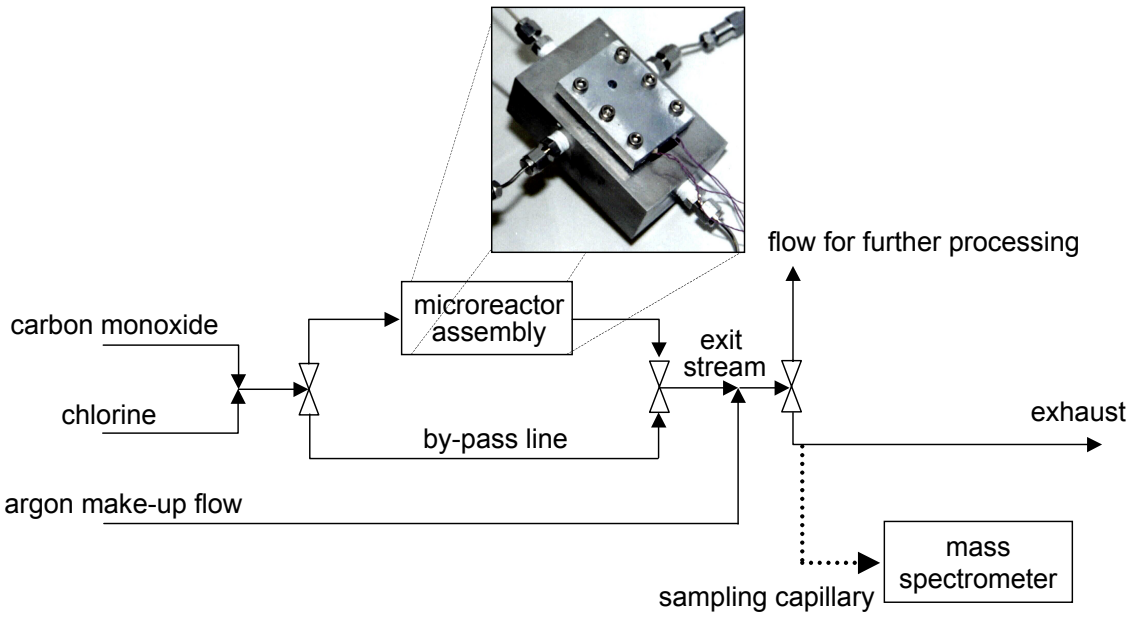


**Figure 2-3.** Schematic of the experimental setup. Flow controllers, purge lines and other equipment have been eliminated for simplicity.

The metal compression plate contains cartridge heaters (*Omega Engineering*, Model No. CSS-01125/120V) which are fit into machined 1/8 inch diameter bores. Thermocouples (*Omega Engineering*, Model No. 5TC-TT-K-36-36) are threaded into the side wells of the reactor. The 0.005 inch (127 μm) diameter type K thermocouples fit snugly into the thermocouple wells in the reactor and do not require any glue or fixing agent. Once the reactor is loaded with catalyst, the catalyst inlets are closed off by substituting a sealing gasket without catalyst loading through-holes. This creates a small dead volume in the reactor chamber.

The reactor/base assembly is connected to the rest of the system via standard *Swagelok* fittings, valves, and 1.6 mm (1/16 inch) O.D. stainless-steel tubing. All materials in contact with chlorine, with exception of the reactor, are stainless-steel, TEFLON™, or Kalrez™. The chlorine (*BOC Gases,* >99.96% purity) and carbon monoxide (*BOC Gases*, >99.3% purity) gas feeds are controlled by mass flow controllers (*UNIT Instruments*). The carbon monoxide flow controller was specially refit with stainless-steel internal components (*Laminar Technologies).* This was done because most standard gas mass flow controllers have a variety of nickel internal components which are known to degrade under exposure to carbon monoxide. This would cause the nickel in the flow controller to form nickel carbonyl which would decompose and redeposit further downstream inside the micro packed-bed, poisoning the activated carbon catalyst. The chlorine flow controller was refitted with Kalrez™ internal fluidic seals (*Laminar Technologies*) to minimize degradation of the internal components. The gas feeds are mixed in a tee junction, and enter either the reactor or a by-pass line. The exit stream is diluted with ultra pure argon (*BOC Gases*, 99.9999% purity) further purified with an oxygen and moisture scrubber (*Matheson*, Model No. I0T-2-

SS-HP) and interfaced to a mass spectrometer via a sampling capillary as described in detail in the next section. Any flow not drawn into the sampling capillary is directed to the exhaust, which is bubbled through a NaOH solution to remove any phosgene/chlorine. A switching valve is placed before the sampling capillary which either directs flow to the mass spectrometer or to other laboratory equipment for further processing. The high pressure dry argon also serves as a purge gas at the beginning and end of each experiment. Before beginning an experiment, the entire system is heated to approximately 150 $^{o}$C for 2 hours under a constant flow of dry argon. This removes moisture adsorbed on the sidewalls of the tubing, fittings, and the mass flow controllers. Even the slightest amount of adsorbed moisture reacts with chlorine to form HCl which subsequently corrodes the metal in the setup and deposits $FeCl_3$ throughout the system (predominantly in the packed-bed). It was found that the heating/drying procedure was essential to the success of the phosgene experiments. The entire system is placed inside a ventilated enclosure similar to a standard chemical fume hood, highlighting an inherent benefit of working with microreactors as additional safety structures and cooling mechanisms, which add expense and complexity to even typical laboratory work, are not needed.

The experiments were carried out with approximately 1.3 mg of activated carbon particles sieved between 53-73 μm with a surface area of 850 $m^2/g$ (*American Norit Company (Alpha Aesar)*, DARCO G-60). The catalyst was loaded in air through a vacuum. A mixture of 2/3 CO and 1/3 $Cl_2$ was mixed at a total flow rate of 4.5 sccm and fed into the reactor. Some experiments were also done with a 50/50 stoichiometric feed at a total flow rate of 8.0 sccm. The reactor was incrementally heated without external cooling from room

temperature to approximately 220 $^{o}$C. The absolute pressure at the inlet of the reactor was approximately 1.35-1.40 atm (132 KPa) and was nominally atmospheric pressure at the exit.

### 2.3.1 Gas Sampling System- Interface to Mass Spectrometer

Gas analysis was done using a quadrapole mass spectrometer pumped through a two-stage vacuum system for continuous real-time spectrometry as shown in Figure 2-4 below. The first stage is pumped via a standard roughing pump and is maintained at approximately 1 torr. The second stage, pumped by a turbo pump, is maintained at $10^{-7}$ torr.

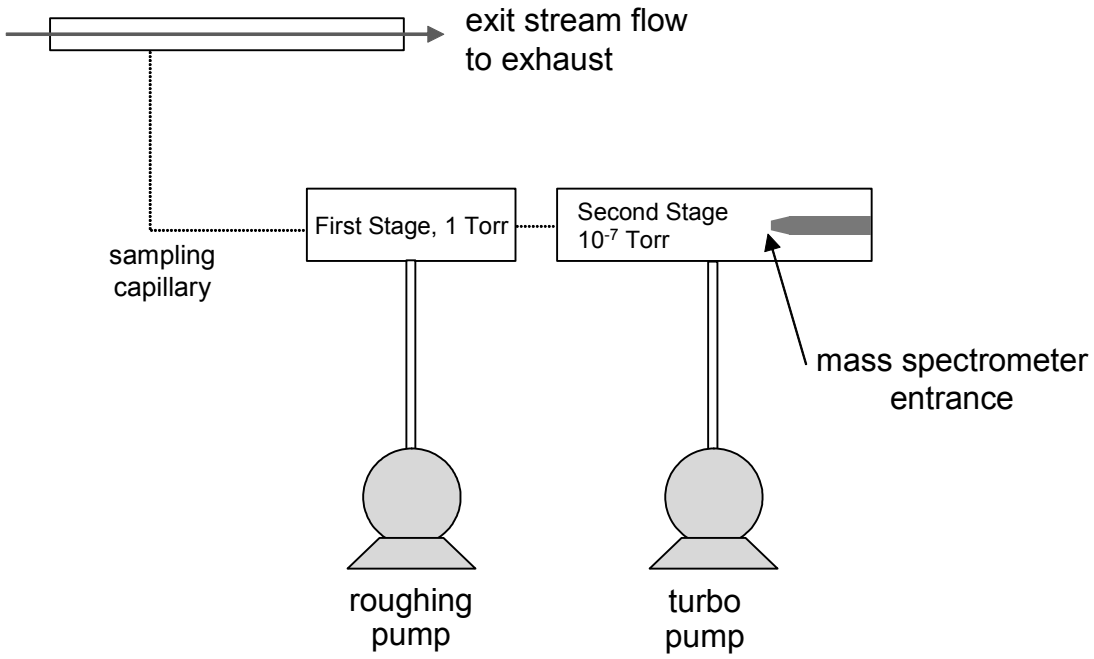


**Figure 2-4.** Diagram of gas analysis system. A small gas sample is continuously fed via a sampling capillary to a mass spectrometer.

The exit stream from the microreactor is interfaced to the vacuum system via a 26 inch long glass capillary (*Polymicro Technologies, Inc.*, 350 µm O.D., 160 µm I.D.). The capillary, with its small diameter, provides the pressure drop from atmospheric pressure at the exit stream side to ~1 torr in the first stage of the vacuum system. The pressure drop provided by the capillary limits the sampling draw rate into the first stage allowing low flow rates to be sampled. The sampling connection to the capillary is made via a T-junction (*Swagelok*, 1/8 inch). To provide mechanical support for the capillary, the capillary is placed inside a 1/8 inch O.D. stainless steel tube and the ends are sealed with a silicone based vacuum sealant (*Varian Vacuum Products*, Torr Seal) as shown below.

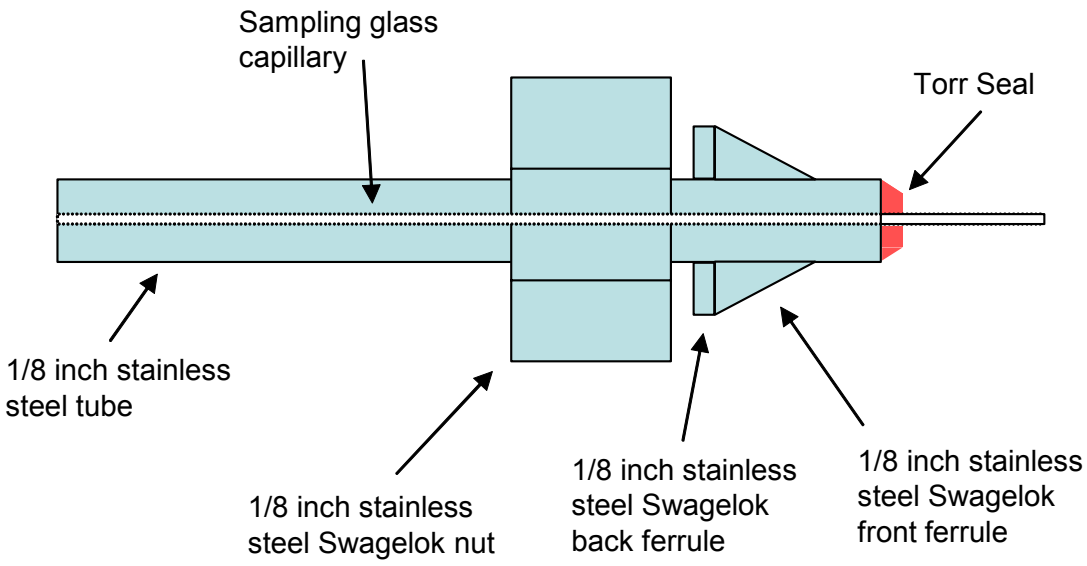


**Figure 2-5.** Sampling capillary connections to standard Swagelok components

Even with the large pressure drop through the sampling capillary, the vacuum typically draws in a larger flow into the sampling system than the total flow rate (up to 8 sccm) used in the phosgene experiments. In order to prevent the difference from being drawn from the exhaust, argon purified in an oxygen and moisture scrubber is mixed with the exit stream just before the sampling capillary. The dry argon flow rate is adjusted with a mass flow controller to make the total flow rate at the capillary inlet larger than the capillary draw rate. This prevents exhaust gas from being drawn into the sampling system, but dilutes the quantity of reaction gases sampled. Therefore, the quantity of argon used was kept at a minimum in order to maintain the accuracy of the measurements. The effect of the argon make-up gas on the measurements was taken into account during data analysis and is described in detail in Section 2.5.

## 2.4 Chemical Compatibility

As previously mentioned, the harsh reactants and products pose a chemical compatibility problem. Specifically, chlorine is known to react with silicon at elevated temperatures and form silanes such as $SiCl_4$. Consequently, microreactors made from silicon would be etched away, releasing chlorine and phosgene as well as losing the utility of defined features such as the inlets and catalyst retainers. Figure 2-6a shows the deleterious effects of exposing a silicon reactor to chlorine at 250 $^{o}$C for approximately 6 hours. The reactor inlet and channel are severely etched. In contrast, a reactor shown in Figure 2-6b with a 0.5 μm silicon oxide coating shows no visible change after 6 hours of continuous chlorine exposure.

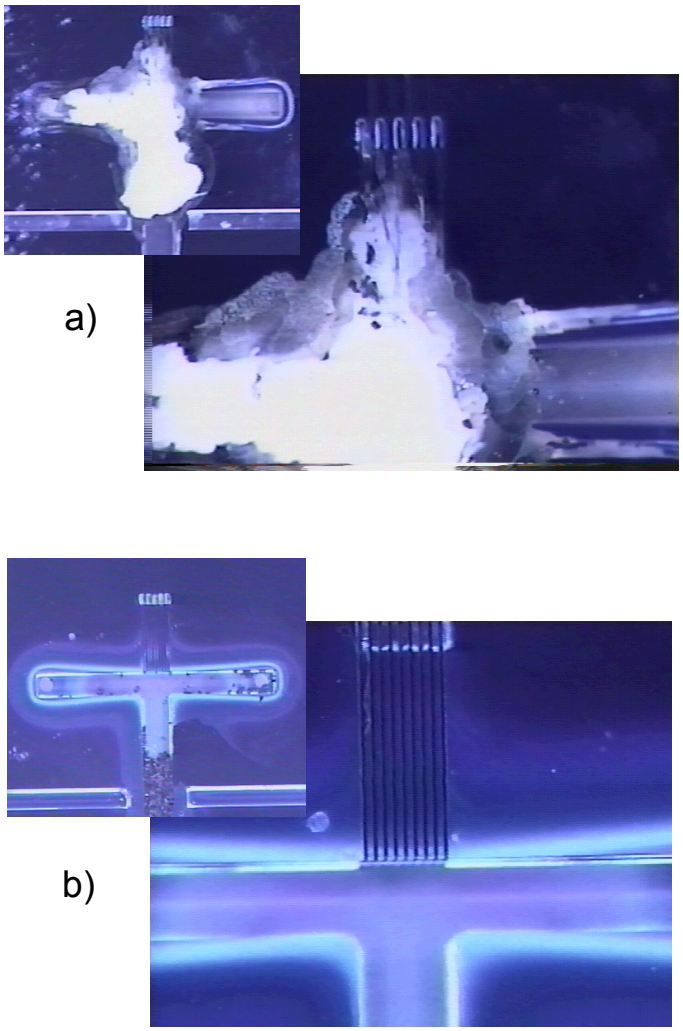


**Figure 2-6.** A protective coating of silicon dioxide prevents etching of the silicon reactor by chlorine. a) A microreactor etched catastrophically at the inlets under a constant 50/50 $Cl_2$/CO flow at elevated temperatures. b) A reactor protected with a conformal 5000 Å oxide layer grown in a wet oxidation furnace. After high temperature flow for over 6 hours, the reactor shows no noticeable degradation.

This example illustrates first, the importance of microfabricating chemically compatible systems, and second, that even for systems where silicon is not suitable, thin chemically resistant coatings can be used to render a stable device. In addition to silicon oxide, microfabrication technology gives a robust set of materials that can be fabricated

directly into the reactor in the clean room such as silicon nitride and a variety of evaporated metals such as nickel and gold. In addition, coatings can be applied after reactor fabrication such as a variety of ceramics like alumina, and polymers such as chlorofluorocarbons. Through the proper use of materials, microfabricated chemical systems can be a robust platform for kinetic studies and can simplify obtaining kinetic information for harsh chemistries.

## 2.5 Data Analysis

Data from the mass spectrometer were recorded on a PC with LABVIEW software (*National Instruments*). Each mass fraction of interest was sampled approximately once a second and was recorded as an intensity value normalized between zero and 10. Using a mass spectrometer for phosgene production introduces some complicated data analysis because the main mass fractions for the product, phosgene (M/E= 70, 63, 35, 28), overlap with those of the reactants, chlorine (M/E= 70, 35) and carbon monoxide (M/E= 28). Further complicating the data is the fact that the gas sample is diluted by argon. The data analysis procedure involves two steps: Firstly, the argon is accounted for by appropriately scaling-up the other mass fraction intensities to compensate for the diluatory effect. Secondly, the overlapping scaled-up mass fraction intensities are deconvoluted yielding the partial pressures of CO, chlorine, and phosgene for each data point. From the partial pressures, reactant conversions can be calculated.

### 2.5.1 Accounting for the Argon Diluent

Since the exit stream is diluted with argon, post-run analysis is necessary to back out relevant partial pressures using calibrations performed at the beginning of each experiment. The calibration procedure involves flowing pure argon, chlorine, and carbon monoxide separately and in combination to the mass spectrometer and calibrating the intensities of the relevant mass fractions to the partial pressures of the respective species. Using the calibrations, the partial pressure of argon is calculated at each data point during the experiment and is then used to scale the other mass fraction intensities [9].

Mass fraction intensity is assumed to be linear with partial pressure as suggested by Millard [9]:

$$I_X = P_i \cdot S_{X \cdot i} \tag{2-2}$$

where $I_x$ is the intensity of M/E= X (e.g., 28) recorded in the data log, $P_i$ = the partial pressure of the species *i* (e.g, CO), and $S_{Xi}$= the sensitivity ratio for species *i* at mass fraction X. For example, if only pure CO is introduced through the system, and M/E=28 is monitored, $S_{28 \cdot CO}$ can be measured since the partial pressure of CO is approximately equal to 1 atm (the pressure at the exit of the reactor is approximately atmospheric). This gives the response at M/E=28 to CO at every partial pressure. This calibration procedure is repeated for $Cl_2$ and argon (M/E=40) to obtain their sensitivity ratios. Using the sensitivity ratio for argon, the dilution of the remaining species can be accounted for. Since the total pressure at the capillary entrance is 1 atmosphere and the partial pressure of argon can be calculated from the mass fraction intensities, the following equations apply:

$$P_{Ar} + P_{CO} + P_{Cl_2} + P_{COCl_2} = 1 \tag{2-3}$$

$$P_{Ar} = \frac{I_{40}}{S_{40 \cdot Ar}} \tag{2-4}$$

The other intensities can thus be scaled-up to yield the intensities that would have been recorded had there been no argon diluent as follows:

$$M_X = I_X \left( \frac{1}{1 - P_{Ar}} \right) \tag{2-5}$$

where $M_X$ = the intensity of M/E = X that would be seen had there been no argon diluent and,

$$P_{CO} + P_{Cl_2} + P_{COCl_2} = 1 \tag{2-6}$$

as is seen at the exit of the microreactor (the primary point of interest for study). Figure 2-7 shows raw data ($I_X$) taken from a particular experimental run along with the appropriate mass intensities calculated after accounting for the diluting effect of argon ($M_X$).

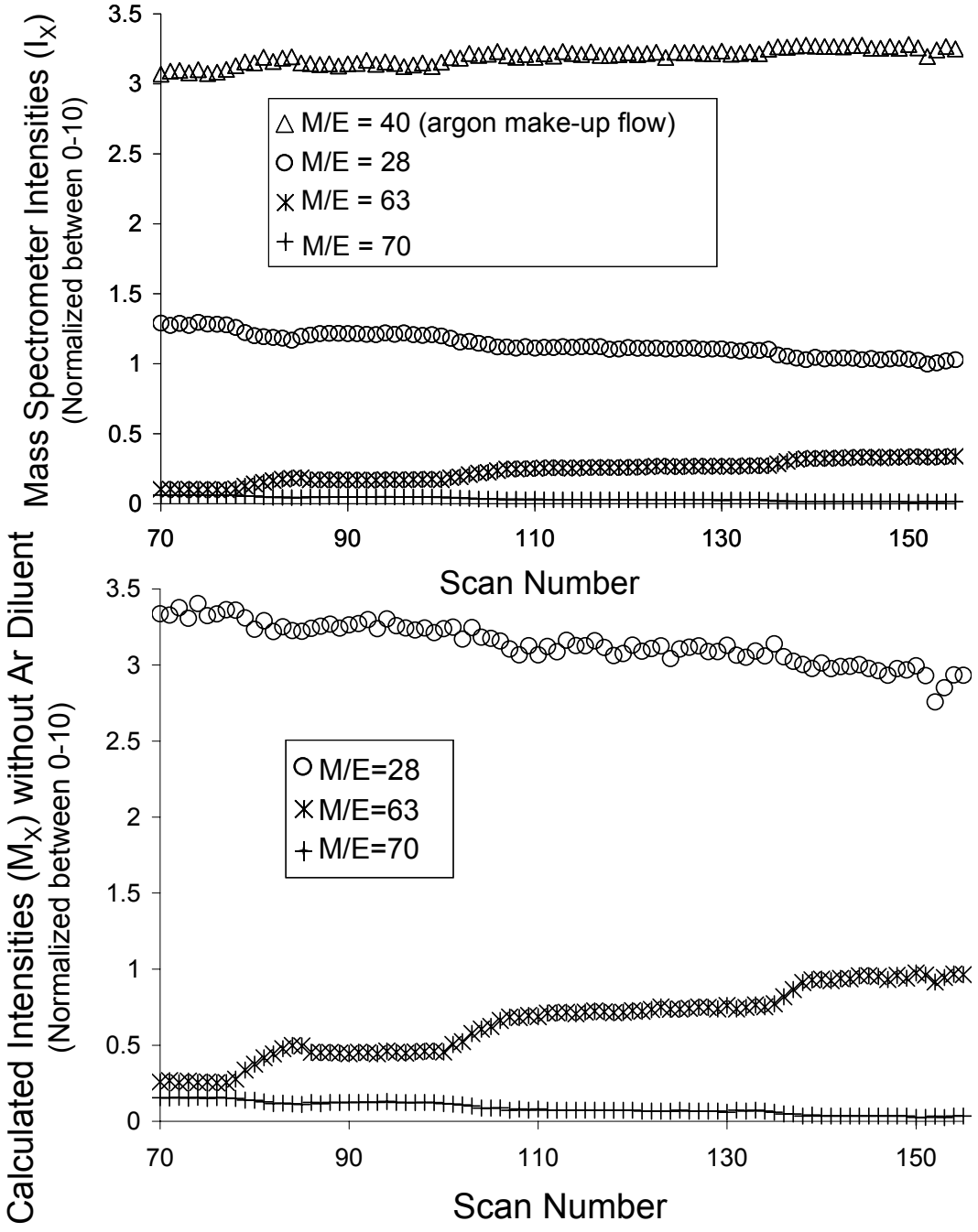


**Figure 2-7.** Mass Intensities in raw form before data analysis ($I_X$) and after accounting for the effect of argon ($M_X$). The mass intensities $M_X$ represent the intensities that would have been recorded had there been no argon diluent.

### 2.5.2 Deconvolution of overlapping mass fractions

Once the diluting factor of argon is removed from the data, the overlapping mass fractions must be deconvoluted to yield the correct partial pressures. This is done by setting up a system of equations for which the unknowns are the partial pressures of all species of interest; in this case, CO, phosgene, and chlorine. The sensitivity ratios have been previously determined during the calibration procedure. Since the mass fraction intensity output by the mass spectrometer is a linear combination of the fractions produced by each species [9], a system of equations can be set up as follows.

$$M_{28} = S_{28 \cdot CO} \cdot P_{CO} + S_{28 \cdot COCl_2} \cdot P_{COCl_2}$$
$$M_{63} = S_{63 \cdot COCl_2} \cdot P_{COCl_2} \qquad \text{(2-7, 2-8, 2-9)}$$
$$M_{70} = S_{70 \cdot Cl_2} \cdot P_{Cl_2} + S_{70 \cdot COCl_2} \cdot P_{COCl_2}$$

However, we decided not to calibrate the mass spectrometer using pure phosgene from an external gas cylinder during the calibration procedure due of the potential dangers and increased complexity of maintaining a pressured phosgene source. Instead, the calibration was done using phosgene produced in the microreactor at complete conversion of chlorine. The overlapping mass fractions with chlorine (M/E=70, M/E=35) and carbon monoxide (M/E=28) were deconvoluted by noting where the M/E=70 chlorine mass fraction (minimal contribution from phosgene) stopped decreasing with increasing temperature. At this point, complete conversion of chlorine was assumed, the sensitivity ratios for phosgene at M/E=63, 70, and 35 were determined, and the self-consistency of the calculations based on the complete conversion assumption was examined. Stoichiometry and the mass fraction

intensities of the excess CO can be used to calibrate the remaining phosgene mass fraction overlapping with CO. Using the complete set of calibration ratios, the partial pressures of all three species were calculated for the entire data set. If the sensitivity ratios for phosgene were determined correctly, the mass balance for all three species should hold at every data point. A correctly deconvoluted system should give the same value for conversion regardless of which of the three species the calculations were based. The conversion of chlorine ($\xi_{Cl_2}$) to phosgene was computed from the carbon monoxide, chlorine, and phosgene mole fractions (calculated from the partial pressures at 1 atm total pressure) using stoichiometric balances:

$$\xi_{Cl_2} = \frac{x_{f\,Cl_2}(1+Y)-1}{(x_{f\,Cl_2}-1)} = \frac{(x_{f\,CO}Y)+x_{f\,CO}-Y}{(x_{f\,CO}-1)} = \frac{x_{f\,COCl_2}(1+Y)}{(x_{f\,COCl_2}+1)} \qquad (2\text{-}10)$$

where $x_{fi}$ is the mole fraction of species $i$ at the exit of the reactor, and $Y$ is the ratio of $CO/Cl_2$ in the feed. Figure 2-8 shows conversion computed independently from the three species over the entire temperature ramp from an experimental run using the data analysis procedure described above. The consistency between the independently calculated values validates the original assumption of complete conversion made at the beginning of the data analysis and gives confidence to the data analysis procedure. Further, a pressurized phosgene source is not needed for accurate data analysis.

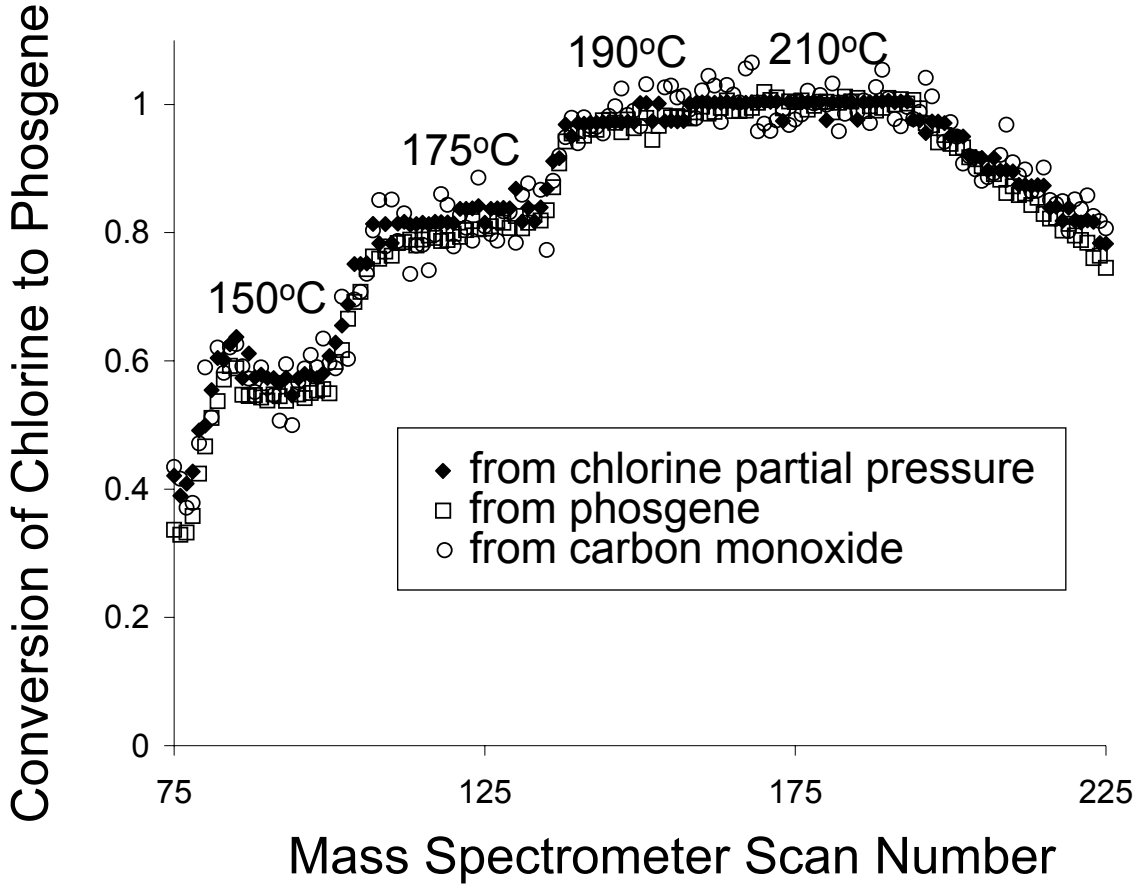


**Figure 2-8.** Conversion of chlorine to phosgene independently calculated from chlorine, phosgene, and carbon monoxide mass fractions. The temperature was increased until complete conversion and then ramped down.

### 2.5.3 Equilibrium Conversion of CO to Phosgene

The equilibrium constant, $K_a$, for the reaction given in Equation 2-1 confirms that the complete conversion assumption made during data analysis is reasonable where $K_a$ for a vapor mixture is defined as [10],

$$K_a = \exp\left(\frac{-\Delta G^o}{RT}\right) = K_\phi K_y P^\nu \tag{2-11}$$

and $K_y$ for the phosgene reaction is given by,

$$K_y = \frac{x_{COCl_2}}{x_{Cl_2} x_{CO}} \tag{2-12}$$

Assuming an ideal vapor mixture, $K_\phi = 1$. Since the reaction stoichiometry indicates that the forward reaction leads to a net reduction in moles, $\nu = -1$. Assuming an ideal vapor mixture at 450K and 1.35 atmospheres (pressure at the reactor inlet), and using the heats of formation reported by Chase et al. [11] to calculate $\Delta G^o$, $K_y$ indicates that a 2:1 mixture of carbon monoxide and chlorine would equilibrate at 99.99% conversion of chlorine. Complete conversion to the limit of detection was also reported by Shapatina et al. [12].

## 2.6 Phosgene Production

During phosgene experimentation, no temperature increase could be measured upon switching flow from the bypass line to the reactor. This is expected because single crystal silicon has a large thermal conductivity (150 W/m/K) and readily dissipates heat from the packed-bed. The thermal mass of the stainless-steel packaging is many orders of magnitude larger than the reactor and provides a significant heat-sink. Likewise, the energy provided by the cartridge heaters to maintain the temperature of the reactor/packaging is orders of magnitude larger than the energy generated from the reaction. This gives fine temperature control over the exothermic reaction. No deactivation as reported by Shapatina et al. [12] was observed during the experimental time-scales (6-10 hours) possibly due to the high level of purity in the gas feeds. No side-products were observed in a full mass spectrum scan, presumably a result of suppressing hot-spots common in larger reactors and using high purity feeds. Products such as silicon tetrachloride, which would form if chlorine were reacting with silicon, were also not detected.

Figure 2-9 shows the conversion of chlorine to phosgene as a function of temperature for a 1:2 $Cl_2$:CO feed at 4.5 sccm. The conversion of chlorine peaks at about 200 $^oC$ where it stops increasing with increasing temperature. Using the rationale described in the data analysis section, it was confirmed that the tailing off was not a result of mass transfer limitations but from complete conversion.

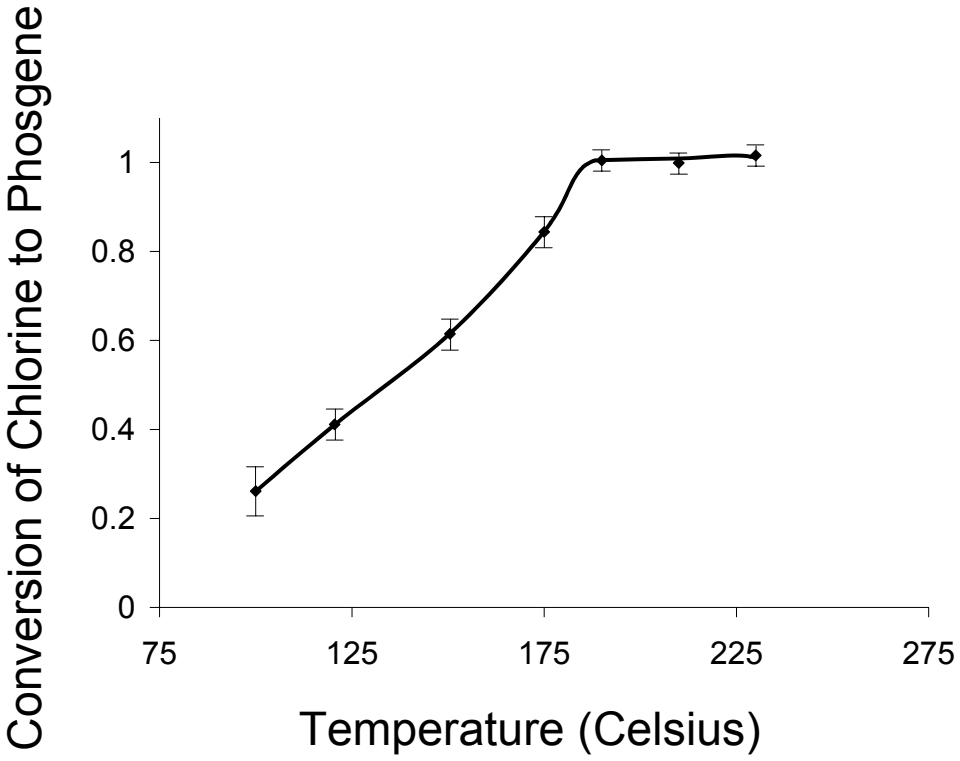


**Figure 2-9.** Conversion of chlorine with a 1:2 chlorine/carbon monoxide feed at 4.5 sccm total flow rate. Complete conversion is seen at approximately 200°C giving a projected productivity of 3.5 kg/year (0.40 g/h) of phosgene from the single channel reactor.

At 4.5 sccm total feed rate with 33.3% chlorine, a phosgene productivity of 3.5 kg/year (0.40 g/h) is projected for a continuously operating single channel device. Experiments were also done with an 8 sccm stoichiometric feed. Complete conversion to phosgene was observed with a corresponding phosgene productivity of 9.3 kg/year (1.1 g/h). The flow rates were not increased due to limitations of the mass flow controllers, but the ability to control thermal runaway in these microsystems would safely allow an aggressive increase in temperature and flow rate into ordinarily dangerous regimes, further increasing the range of temperature where kinetic data can be gathered.

## 2.7 Comparison to Bench Scale Experiments: Heat Transfer

Bench scale phosgene experiments were performed to better understand the advantages of employing microreaction technology for catalytic studies. In order to assess the difficulties in macroscale catalyst testing, a standard tube-in-furnace reactor system was built similar to that used in common practice today for heterogeneous catalytic studies. A 1/4 inch O.D. quartz tube was custom made with a glass frit in the center of the tube. Approximately, 1 cm of the same activated carbon particles used in the microreactor experiments was packed against the frit. The tube was fitted with standard *Cajon* O-ring fittings. At the top of the reactor, a T-junction was placed from which a type K thermocouple was threaded down to the center of the packed-bed. The thermocouple was sealed against the T-junction with Torr Seal vacuum sealant to eliminate leaks. With approximately 20-50 sccm of flow of 50/50 CO and $Cl_2$ and *no* external heat source applied, the packed-bed autothermally heated to over 200 $^{o}$C. At this point, the flow of reactants was cut off for safety reasons, but the rate of temperature increase indicated that if left alone, the reactor would have reached considerably higher temperatures. This simple experiment indicates the difficulty in accurately obtaining kinetic information. With autothermal heating to at least 200$^{o}$C, there is little question that significant thermal gradients existed across the packed-bed which would have convoluted kinetic information. The fine temperature control seen in the microreactor, even for a reaction as exothermic as phosgene generation, is a clear advantage for catalyst testing.

## 2.8 Extraction of Kinetics from the Microreactor System

### 2.8.1 Representative Criteria for Transport Limitations

In order to examine the potential for gradients in the micro packed-bed, characteristic dimensionless numbers can be considered on the basis of experimental data. Anderson [13] proposed a criterion for assuring that the observed reaction rate does not differ from the actual reaction rate within a catalyst particle by more than 5% due to intraparticle temperature gradients:

$$\frac{|\Delta H| R_{rxn} r_p^2 E_{act}}{k_p T_s (RT)} < 0.75 \qquad (2\text{-}13)$$

The carbon catalyst in the phosgene experiments may be considered isothermal as the left hand side of the inequality ranges between ~0.0006-0.006 using experimental data and a thermal conductivity of ~0.27 W/m/K for porous activated carbon [14].

The Weisz modulus, $M_w$, which gives the ratio of the reaction rate to the diffusion rate in a porous catalyst particle is:

$$M_W = \frac{R_{rxn} r_p^2 \rho_p}{C_s D_E} \qquad (2\text{-}14)$$

BET nitrogen adsorption and specifications from the catalyst manufacturer indicate Knudsen diffusion effects are important. With a calculated effective diffusivity ~$10^{-7}$ $m^2/s$, the Weisz modulus was determined to be between 0.1-0.5 indicating minimal intraparticle mass transfer limitations, even with the low diffusivity.

In traditional packed-beds, low particle Reynolds numbers typically result in poor mass transfer to the catalyst particle surface. Relationships have been developed for the Sherwood number in packed-beds governing mass transfer from the fluid film around a particle to the particle surface [15-17]. Their applicability to microfabricated reactors where diffusive mixing is fast is unclear. However, an order of magnitude analysis can be made by examining the concentration gradient needed to maintain a flux corresponding to reactant consumption at the largest reaction rate observed in the experiments. Detailed discussions of this procedure and the issues surrounding the applicability of various mass and heat transfer correlations to micro packed-beds are found in Section 5.5 and Chapter 6.

In the limiting case of mass transfer, where Reynolds number approaches zero, diffusion is the only form of transport to the catalyst surface. For a 63 micron particle at the fastest rate of phosgene formation observed in the experiments, the concentration difference is calculated to be approximately 0.01 $mol/m^3$ over a characteristic length of one particle diameter using a Fick's Law analysis. This is negligible compared to the bulk concentration of ~15 $mol/m^3$. Therefore, mass transfer to the catalyst surface is not limiting and the reactant concentrations at the catalyst surface may be taken as the same as the bulk concentrations. Furthermore, the interstitial diffusion time from one particle to another (taken as 1 particle diameter) is on the same order as the single particle residence time based on the superficial velocity of the gases, i.e. $Pe_{particle} \sim 1$. The preceding analyses demonstrate

how the small microreactor length scale reduces heat and mass transfer gradients in packed-beds. Since characteristic thermal and mass transport times decrease as a square of the characteristic length, the micro packed-bed reactor operates in a regime where diffusive mixing and heat transfer across the small catalyst pellets are fast enough to suppress gradients, clearly in contrast to the bench scale experiment performed in the previous section.

### 2.8.2 Reactor-Kinetic Model

The small dimensions reduce gradients that otherwise would complicate the determination of reaction kinetics from packed-bed reactor data. In order to demonstrate the microreactor as a tool for measuring reaction kinetics, rate constants for phosgene formation were extracted assuming plug flow (PFR). The PFR assumption is reasonable based on the reactor Peclet number. Calculated values range between 180 and 360. The number of catalyst particles across the reactor diameter is ~6.4, whereas a value of 10 or more is typically desired for plug flow analysis.

The PFR equation material balance,

$$F_{i_o} d\xi_i = -r_i dW \tag{2-15}$$

is integrated, where $F_{io}$ is the flow rate of species $i$ in mol/time at the reactor inlet, $\xi_i$ is the conversion of species $i$, $r_i$ is the rate of formation/consumption of species $i$, and $W$ is the mass of catalyst. The rate of reaction (mol/s/g catalyst) is taken from a rate expression reported by Shapatina et al. [12],

$$R_{rxn} = kP_{CO}\left(\frac{P_{Cl_2}}{AP_{CO} + P_{COCl_2}}\right)^{1/4} \tag{2-16}$$

where $k$ is the Arrhenius rate constant (mol/s/atm/g catalyst), $P_i$ is the partial pressure (atm) of species $i$, and the constant $A$ is a temperature dependent equilibrium constant. This expression was obtained from experiments performed between 70°- 130°C. The temperatures in this analysis extend to 180°C, and Equation 2-16 is extrapolated outside the range reported by Shapatina et al. for both data analysis and comparison. Eq. 2-16 only applies to regions of intermediate CO surface coverage occurring at chlorine mole fractions above 3% [18]. As chlorine partial pressure decreases, the reaction passes from a region of intermediate surface coverage to a region of high coverage where the catalyst is almost completely covered by adsorbed CO. The expression in Eq. 2-16 does not capture this change in surface characteristic. Low chlorine concentrations occur in the micro packed-bed reactor towards the exit of the reactor at high conversions. Therefore, Eq. 2-16 was only used to obtain kinetics below 80% chlorine conversion to ensure that the chlorine mole fraction was always above 3%.

The Ergun equation (Eq. 2-17) is often used to describe the pressure drop in traditional packed-beds [19].

$$\frac{dP}{dL} = -\frac{G}{\rho D_p}\left(\frac{1-\phi}{\phi^3}\right)\left[\frac{150(1-\phi)\mu}{D_p} + 1.75G\right] \tag{2-17}$$

Experiments measuring the pressure drop through the micro packed-bed were performed using nitrogen (0-20 sccm). Eq. 2-17 was integrated assuming a compressible gas, and the void fraction ($\phi$) was determined to be approximately 0.4 by fitting the data using $\phi$ as the only variable parameter. Using the determined $\phi$, the Ergun equation gives a good prediction of the pressure drop for the range of gas flow studied in the phosgene experiments, justifying its use in further analysis.

The reduction in the total number of moles in Reaction 2-1 causes the density of the gas stream to increase with conversion. This causes a non-linear decrease in total pressure along the reactor channel. Substituting Eq. 2-10 and an expression for density as a function of conversion into Eq. 2-17, the pressure drop along the reactor channel with respect to catalyst weight can be written as:

$$\frac{dP}{dW} = -\frac{G}{\sigma_C \rho_0 D_p}\left(\frac{1-\phi}{\phi^3}\right)\left[\frac{150(1-\phi)\mu}{D_p} + 1.75G\right]\frac{P_0}{P}\left(1+\varepsilon\xi_{Cl_2}\right) \qquad (2\text{-}18)$$

where P is the total pressure at any point along the reactor, $W$ is the weight of catalyst along the reactor, $\sigma_C$ is the catalyst packing density in terms of the weight per unit length along the reactor channel (kg catalyst/m channel), $\varepsilon$ is the % change in the number of moles at complete conversion as defined by Fogler [20], and $\xi_{Cl2}$ is the conversion of limiting reagent (chlorine) along the reactor. $\varepsilon$ = -1/3 for the case of a 2:1 $CO/Cl_2$ feed. The viscosity of the gas mixture is assumed to be constant for this analysis. Plugging Eqs. 2-10 and 2-16 into Eq. 2-15, the conversion of chlorine along the reactor with respect to catalyst weight is:

$$\frac{d\xi_{Cl_2}}{dW} = k\left(\frac{Y-\xi_{Cl_2}}{Y+1-\xi_{Cl_2}}\right)\left(\frac{1-\xi_{Cl_2}}{A\left(Y-\xi_{Cl_2}\right)+\xi_{Cl_2}}\right)^{1/4}\frac{P}{F_{Cl_2\,o}} \tag{2-19}$$

Eqs. 2-18 and 2-19 together give a system of coupled differential equations in both $P$ and $\xi$ for which all the parameters are known except the rate constant, $k$. Values for $k$ were extracted by iteratively solving the coupled system at different temperatures using a fourth order Runge-Kutta algorithm [21] with the constraint that conversion at the exit of the reactor matches the data shown in Figure 2-9.

### 2.8.3 Determination of Rate Constants and Activation Energies

Using BET measurements on the catalytic surface area, the rate constants with respect to surface area are calculated and compared to values from Shapatina et al. [12] in Figure 2-10. The experimental error bars are calculated using statistical analysis on the repeatability of the data at 95% confidence. Shapatina et al. reported catalyst surface area before and after each experiment. The post reaction surface area is used in Figure 2-10.

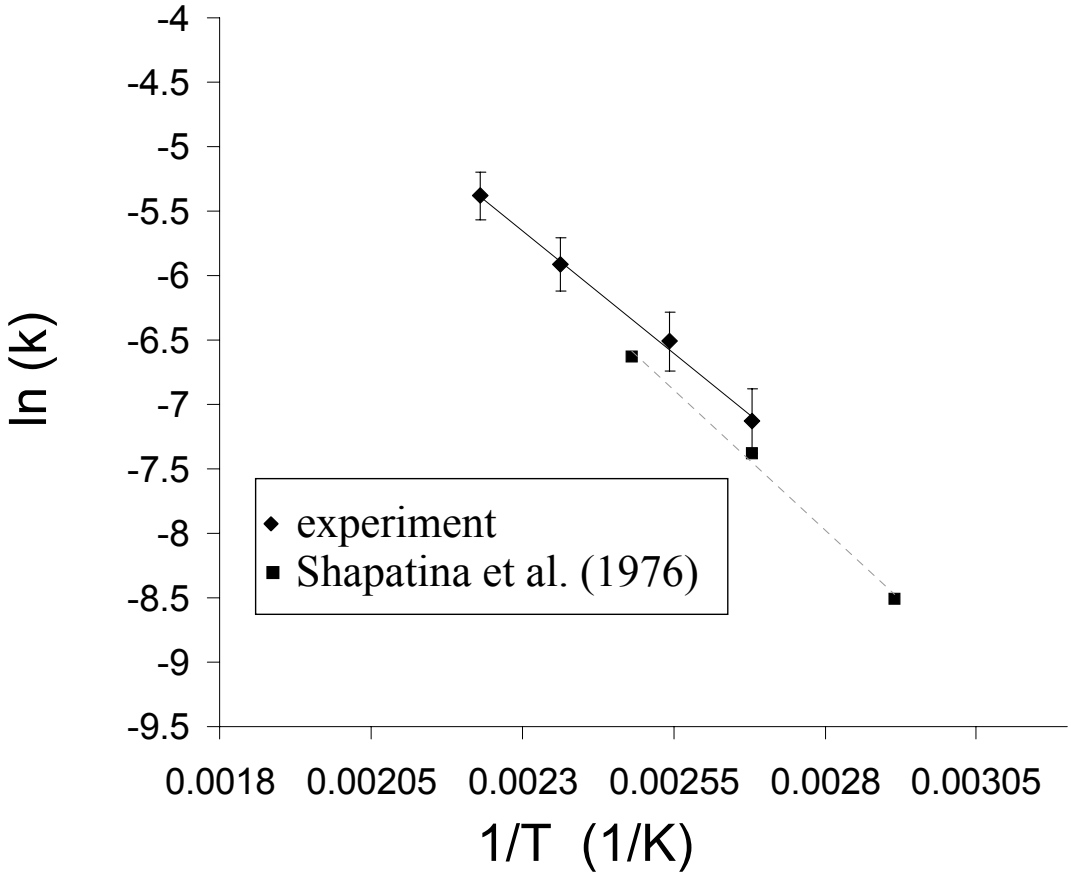


**Figure 2-10.** ln (k) vs. 1/T for the phosgene experiments and Shapatina et al. (1976) [12]. The experimental activation energy of 7.6 kcal/mol compares favorably to 8.6 kcal/mol from Shapatina et al.

A reasonable agreement is seen between the experimental values and the values reported by Shapatina et al. given that they did not report error analysis, they only reported three data points, and that this analysis extrapolated their expressions outside of their reported temperature range. Furthermore, Shapatina et al. is the only set of data we could obtain with phosgene kinetics, and gives us only one point of comparison. The apparent activation energy from the experiments of 7.6 kcal/mol compares with the 8.6 kcal/mol

reported by Shapatina et al. The rate constants extrapolated from the microreactor also favorably compare to the previously published values. The data falls on a straight line, even at the higher temperatures, giving further evidence for the lack of mass transfer limitations. Compared to the tube-in-furnace experiments where temperature control was not achievable, the ease at which the same reaction can be controllably run in the microreactor clearly provides an advantage for kinetics extraction.

## 2.9 Advantages and Disadvantages of Micro Packed-Beds

The phosgenation experiments detailed in this chapter provide a good understanding of the various advantages and disadvantages of using microfabricated packed-bed reactors for both chemical production, and more relevant to this work, catalyst testing.

### 2.9.1 Advantages

The smaller reactor geometry allows for lower flow rates to be employed during experimentation. With toxic and corrosive compounds such as chlorine and phosgene, this is of particular advantage. Further, the small system size, even when including tubing and chemical analysis, eases safety concerns as the entire system can easily fit into a standard chemical fume hood. Again, with chemistry involving compounds such as chlorine and phosgene, this can lead to a significant reduction in expense.

From a performance standpoint, the small particle size (50-70 μm) and high surface area-to-volume ratio naturally lend themselves to reducing thermal and mass transport

gradients across the reactor. The fine thermal control achievable in the microreactor greatly contrasts the autothermal heating observed in traditional bench scale experiments. By reducing these unwanted gradients, microreactors enable the extraction of chemical kinetics without extra investment in cooling devices or diluted catalyst beds. The advantages in reducing gradients can be quantitatively seen by examining Equation 2-14, which gave a criterion for internal mass transport limitations.

$$M_W = \frac{R_{rxn} r_p^2 \rho_p}{C_s D_E} \tag{2-14}$$

As the catalyst particle radius, $r_p$, appears squared in the numerator, reducing particle size significantly reduces internal mass transport gradients. Thermal transport effects scale analogously.

### 2.9.2 Disadvantages

The primary disadvantage of using microfabricated packed-beds can be seen by reexamining the Ergun Equation given in Equation 2-17.

$$\frac{dP}{dL} = -\frac{G}{\rho D_p}\left(\frac{1-\phi}{\phi^3}\right)\left[\frac{150(1-\phi)\mu}{D_p} + 1.75G\right] \tag{2-17}$$

As the particle diameter, $D_p$, appears twice in the denominator, the pressure drop across the packed-bed increases significantly as particle diameter decreases. For the phosgenation experiments performed in the microreactor, a gas flow rate as low as 4.5 sccm (small by macroscale standards) yielded a pressure drop as high as 0.4 atm. This pressure drop along the reactor was accounted for by coupling the kinetic model with a reactor model for pressure along the reactor. However, for larger flow rates, the pressure drop would get too severe to accurately represent catalyst surface characteristics through only one kinetic model making kinetic analysis extremely difficult. Therefore, the primary advantages of smaller particle size yielded through the use of microfabricated packed-beds in the tube-flow geometry are compromised by the increased pressure drop due to the smaller particles creating a balance that must be considered when such systems are used for catalyst testing.

## 2.10 Summary

A silicon micro packed-bed tube-flow reactor has been studied for the heterogeneous gas phase production of phosgene. The microreactor utilizes high surface area catalyst particles synthesized by standard procedures. By using catalyst particles instead of thin-films or coatings, current industrial catalysts can be utilized for a wide range of applications. An example of the robustness of microfabrication technology for chemical processing was demonstrated through the use of a silicon dioxide layer to protect the reactor from chemical attack. The microreactor with the oxide coating proved stable to chlorine at elevated temperatures.

Phosgene production was used as an example of the potential for the safe production of a hazardous compound for catalyst testing. The production of phosgene, normally requiring significant investment in infrastructure, was easily performed in a standard ventilated enclosure. Even with test-tube scale reactors, catalyst temperature control and thermal gradients proved difficult to control. With toxic compounds such as phosgene, a bank of these "macroscale" reactors for catalyst testing would require special enclosures and expensive safety precautions. In contrast, a bank of microreactors would offer minimal structural investment beyond a small ventilated enclosure or fume hood while providing fine temperature control and reduction of both thermal and concentration gradients. Preliminary productivity values for a single reaction channel device yielded 9.3 kg/year (1.1 g/hour) of phosgene for an 8 sccm stoichiometric feed of carbon monoxide and chlorine. Although the flow rates were not increased due to limitations in the mass flow controllers, opportunity exists for increasing productivity as temperature and flow rates can be aggressively increased without compromising safety, extending the range of temperatures for which kinetic data can be gathered.

The suppression of hot spots and increased mass transfer capabilities were explored as advantages for the extraction of chemical kinetics. Quantitative analysis indicates that the catalyst particles are small enough to be isothermal and that mass transfer resistances are not severe indicating the intrinsic advantage of employing microfabricated packed-beds. Rate constants for phosgene formation were extracted from the packed-bed data and compared favorably with literature, demonstrating the potential for micro packed-bed reactors as practical laboratory research tools. However, the advantages of reduced thermal and mass transport gradients that are created by smaller particle size and reactor geometry are

compromised by increased pressure gradients. In conclusion, micro packed-bed reactors have great potential for efficient and robust catalyst testing platforms; however, traditional axial or tube-flow is perhaps not the best microreactor geometry for suppressing heat, mass, and pressure gradients simultaneously. The next chapter discusses a different microreactor geometry for catalyst testing that addresses this issue.

## Notation

$\rho_p$ = catalyst density, kg/m$^3$

$\rho_f$ = fluid or gas density, kg/m$^3$

$\mu_i$ = viscosity of species i, Pa·s

$\nu$ = net change in moles from stoichiometry of the forward reaction

$C_s$ = concentration of limiting reactant at the catalyst surface, g mol/m$^3$

$D_p$ = diameter of catalyst particle, m

$E_{act}/RT$ = Arrhenius group (activation energy, universal gas constant, temperature)

$G$ = superficial mass velocity, kg/(m$^2$ s)

$\Delta G^o$ = change in standard Gibbs free energy of the forward reaction, J/mol

$\Delta H$ = change in enthalpy of forward reaction, J/g mol

$k_p$ = catalyst thermal conductivity, W/(m·K)

$K_\phi$ = equilibrium constant with respect to fugacity, equals unity for ideal gas

$M/E$ = mass-to-charge ratio indicating a mass spectrometer mass fraction

$P_o$ = measured pressure at the inlet of the reactor, atm

$r_p$ = catalyst particle radius, m

$T_s$ = catalyst surface temperature taken as the bulk fluid temperature, K

## Literature Cited


[1] A. Lord and H.O. Pritchard, "Thermodynamics of Phosgene Formation from Carbon Monoxide and Chlorine," *Journal of Chemical Thermodynamics.* **2** (1970) 187-191.

[2] J.H. Saunders, E.E. Hardy, R.J. Slocombe, in: "Phosgene," Interscience Encyclopedia, Inc., New York, 1953, pp. 391.

[3] J.J. Lerou, M.P. Harold, J. Ryley, J. Ashmead, T.C. O'Brien, "Microfabricated Minichemical Systems: Technical Feasibility," in: Microsystem Technology for Chemical and Biological Microreactors, Mainz, Germany, 1995, pp. 51-67.

[4] M.W. Losey, M.A. Schmidt, K.F. Jensen, "Microfabricated Multiphase Packed-Bed Reactors: Characterization of Mass Transfer and Reactions," *Ind. Eng. Chem. Res.* **40** (2001) 2555-2562.

[5] A.A. Ayon, R. Braff, C.C. Lin, H.H. Sawin, M.A. Schmidt, "Characterization of a Time Multiplexed Inductively Coupled Plasma Etcher," *J. Electrochem. Soc.* **146** (1999) 339-349.

[6] M.A. Schmidt, "Wafer-to-Wafer Bonding for Microstructure Formation," *PROCEEDINGS OF THE IEEE.* **86** (1998) 1575-1585.

[7] M.W. Losey, S. Isogai, M.A. Schmidt, K.F. Jensen, "Microfabricated Devices for Multiphase Catalytic Processes," in: IMRET 4: 4th International Conference on Microreaction Technology, Atlanta, GA USA, 2000, pp. 416.

[8] M.W. Losey, "Novel Multiphase Chemical Reaction Systems Enabled by Microfabrication Technology," Thesis, M.I.T., Cambridge, MA, 2001.

[9] B.J. Millard, in: "Quantitative Mass Spectrometry," Heyden, London, 1978, pp. 91-115.

[10] J.W. Tester and M. Modell, in: "Thermodynamics and Its Applications (Third Edition)," Prentice-Hall, Inc., Upper Saddle River, NJ, 1997, pp. 749.

[11] Chase et al., *Journal of Physical Chemistry Reference Data.* **14** (1985).

[12] E.N. Shapatina, V.L. Kuchaev, B.E. Pen'kovoi, M.I. Temkin, "The Kinetics of Catalytic Synthesis of Phosgene," *Kinetics and Catalysis.* **17** (1976) 559-566.

[13] J.B. Anderson, "A criterion for isothermal behaviour of a catalyst pellet," *Chem. Eng. Sci.* **18** (1963) 147.

[14] C.N. Satterfield, in: "Heterogeneous Catalysis in Industrial Practice- Second Edition," Krieger Publishing Company, Malabar, Florida, 1996, pp. 516-518.

[15] N. Wakao and S. Tanisho, "Chromatographic measurements of particle-gas mass transfer coefficients at low Reynolds numbers in packed beds," *Chemical Engineering Science.* **29** (1974) 1991.

[16] D. Kunii and M. Suzuki, "Particle-to-Fluid Heat and Mass Transfer in Packed Beds of Fine Particles," *Int. J. Heat Mass Transfer.* **10** (1967) 845.

[17] C.N. Satterfield, in: "Mass Transfer in Heterogeneous Catalysis," R.E. Krieger, Huntington, NY, 1970.

[18] E.N. Shapatina and V.L. Kuchaev, "Kinetics of the Synthesis of Phosgene Using Low Chlorine Concentrations," *Kinetics and Catalysis.* **20** (1980) 972.

[19] R.B. Bird, W.E. Stewart, E.N. Lightfoot, in: "Transport Phenomena," Wiley, New York, 1960, pp. 200.

[20] H.S. Fogler, in: "Elements of Chemical Reaction Engineering," Prentice-Hall Inc., Upper Saddle River, NJ, 1992, pp. Chapter 14.

[21] J.D. Hoffman, in: "Numerical Methods for Engineers and Scientists," McGraw-Hill, New York, 1992, pp. 294.

# Chapter 3
# The Cross-Flow Microreactor

This chapter introduces a microreactor design for catalyst testing that addresses the increased pressure drop typical of micro packed-beds. This microreactor design utilizes a novel cross-flow geometry and a flow distribution scheme directly fabricated into the reactor to achieve an even distribution of flow across the packed-bed while minimizing pressure drop. Along with an introduction to the reactor geometry, basic design considerations are discussed such as the reduction of dead volume in the reactor. The chapter closes with a discussion of the fabrication of this microreactor. The cross-flow microreactor introduced in this chapter leverages the heat and mass transfer advantages of microscale packed-beds seen in the previous chapter while reducing pressure drop, enabling differential operation for catalyst testing.

## 3.1 Cross-Flow Packed-bed Geometry

### 3.1.1 Motivation for Cross-Flow- ΔP and Differential Kinetics

Standard packed-bed reactors have axial or tube-flow (i.e., flow along the longitudinal axis of the tube) as was shown in Figure 2-1. As presented in Chapter 2, the microfabricated packed-bed reactor based on an axial flow design demonstrated the potential of using microfabricated reactors for obtaining chemical kinetics [1, 2]. Although the reduced reactor length scale helped suppress thermal and concentration gradients, the pressure drop along the micro packed-bed increased significantly due to the small catalyst particle size and was prohibitive for operating as a robust catalyst testing reactor at larger flow rates. Gas flow rates as low as 4.5 sccm through the 20 mm long bed yielded a pressure drop as large as 0.4 atm. Since pressure drop in a packed-bed is roughly inversely proportional to the square of the particle diameter, a micro packed-bed of a given bed length with 60 micron catalyst particles has ~275× larger pressure drop than a bed with 1 mm particles, and ~27500× larger pressure drop than a bed with 10 mm particles (as calculated from the Ergun equation, Eq. 2-17).

The microreactor for phosgene production in Chapter 2 was run between 20% and 80% conversion. The long and narrow tube flow geometry yielded Peclet numbers between 180-300 and naturally lent itself to integral operation due to minimal axial dispersion effects. It is often desirable in catalyst testing, particularly with unknown kinetic mechanisms, to run a catalyst testing reactor differentially (low reactant conversions) which can be achieved by

using larger reactant flow rates. However, larger flow rates serve to further increase the already large pressure drop in microfabricated packed-bed reactors. Using less catalyst by reducing the bed length would lower conversions and decrease the pressure drop. However, it is desirable to have as much catalyst as possible in microfabricated reactors to allow measurable reactant conversions while still maintaining practical flow rates, particularly for slow reactions. A larger quantity of catalyst also affords an increased flow rate that reduces lag time in testing systems and helps average out variances in catalytic properties between particles. In general, for microfabricated chemical systems, it is desirable to have as much catalyst as possible, but it is necessary to shorten the length of the catalyst bed to reduce pressure drop. In order for micro packed-beds to be useful for catalyst testing, an alternate reactor geometry is necessary.

### 3.1.2 The Cross-Flow Packed-Bed Concept

Multiple, short packed-beds operating in parallel can increase the effective catalyst area, and thereby throughput, and reduce the pressure drop by decreasing bed length and reducing gas velocity. Harris et al. have recently demonstrated the use of a cross-flow micro heat exchanger to reduce pressure drop while enhancing heat transfer [3]. Our cross-flow design integrates short parallel beds into a continuous wide packed-bed (Fig. 3-1).

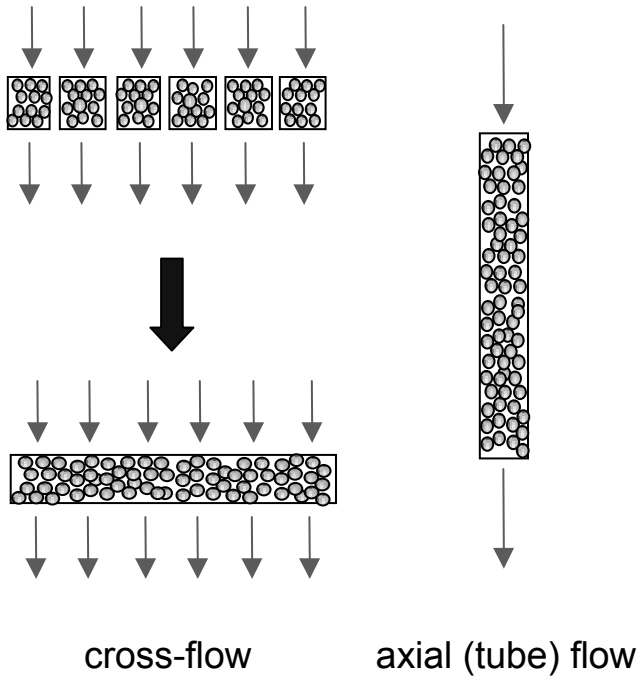


**Figure 3-1.** The cross-flow design: Parallel short packed-beds are integrated into one continuous wide bed with flow across the short length of the bed. This contrasts typical axial or tube-flow for which flow is down the long axis of the bed.

The cross-flow geometry effectively turns a classical tube reactor 90 degrees on its side. The flow distribution in this geometry strongly contrasts that in a tube reactor. In tube-flow, a significant number of particle layers lie along the flow direction. The tube-flow microreactor in Chapter 2, for example, has approximately 333 particles (60 microns diameter) down the length of the reactor. In this situation, a few particle voids would have a negligible effect on the total pressure drop through the reactor. In contrast, in cross-flow, only a few layers of particles lie between the beginning and end of the packed-bed. Here, a few particle voids would greatly impact the total pressure drop in that section of the reactor. The variations in

packing density (voids) would result in bypassing of catalyst as fluid would preferentially take paths of lower pressure drop and unevenly distribute across the wide bed. Such uneven flow would confound kinetic experiments and ultimately produce erroneous results. On the macroscale, tailoring a cross-flow reactor geometry to ensure even distribution of reactants would be difficult. Microfabrication technology, on the other hand, enables the design of a cross-flow reactor without these disadvantages as is discussed in the next section.

## 3.2 The Cross-Flow Microreactor

Figs. 3-2 to 3-4 detail the silicon microfabricated cross-flow reactor designed for catalyst testing. The reactor has one inlet and one outlet for gas flow. The inlet channels bifurcate into 64 parallel channels that feed a wide catalyst bed. The curved inlet/exit channels are 350 μm wide. The catalyst bed is 25.55 mm wide, 500 μm deep, 400 μm long (flow direction), and is approximately 5.1 μℓ in total volume. With 60 μm diameter catalyst, the packed-bed holds only 6-8 layers of particles in the direction of flow. An array of catalyst retainer posts (50 μm wide) acts as a filter to hold the bed in place (Fig. 3-3). The heads of the retainer posts expand out to leave a 35-40 μm gap between posts, setting the lower limit for particle size. Along the perimeter of the microreactor are four side-wells 350 μm wide and 370 μm deep to insert thermocouples. Each reactor chip is 15 mm × 40 mm and is 1.5 mm thick.

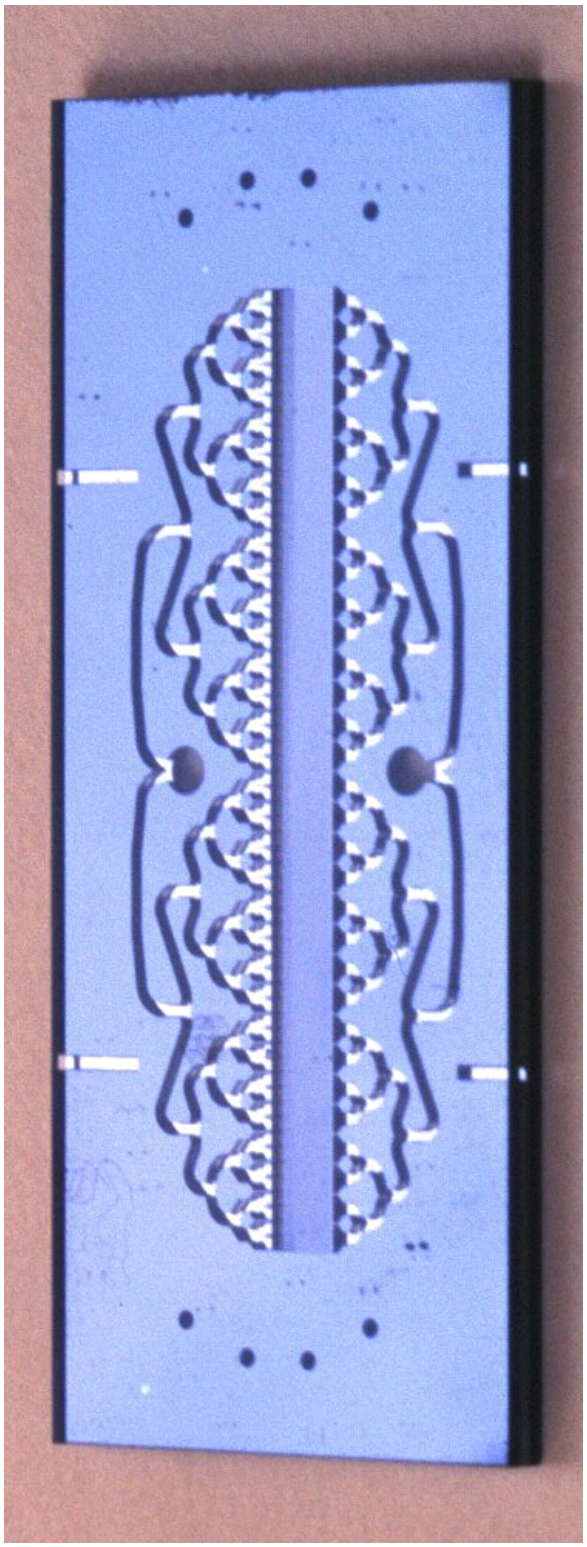

**Figure 3-2.** Photomicrograph of a single cross-flow microreactor chip. The chip dimensions are 15 mm x 40 mm and the chip is 1.5 mm thick. (Picture courtesy of Felice Frankel, MIT)

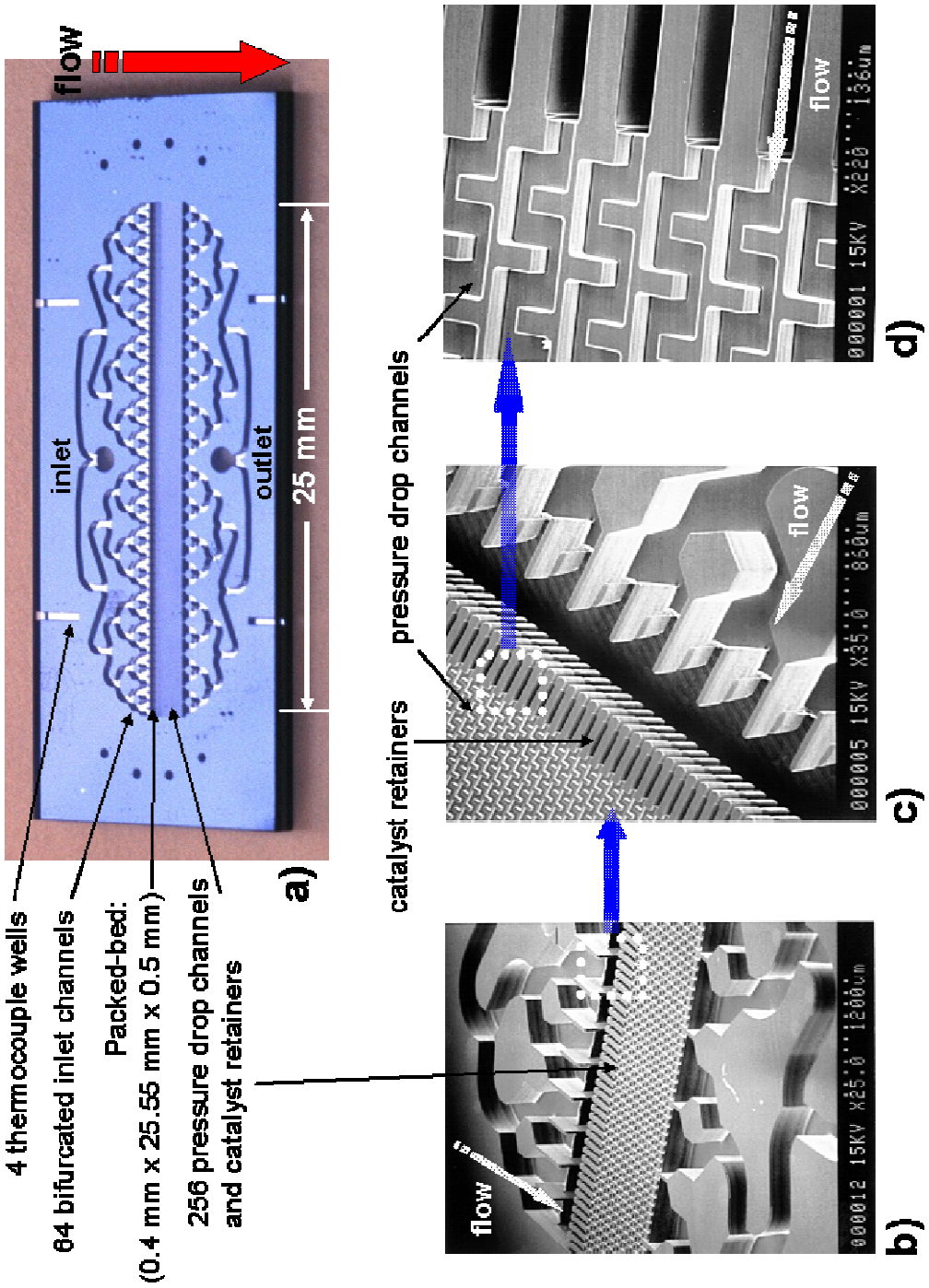


**Figure 3-3.** The microfabricated silicon cross-flow reactor. a) Photograph of the silicon microreactor chip. b-d) Scanning electron micrographs of the microreactor at different magnifications. The reactants are bifurcated into 64 inlets that feed a shallow catalyst bed. Catalyst retainers keep the bed in place while shallow pressure drop channels maintain even flow distribution across the bed.

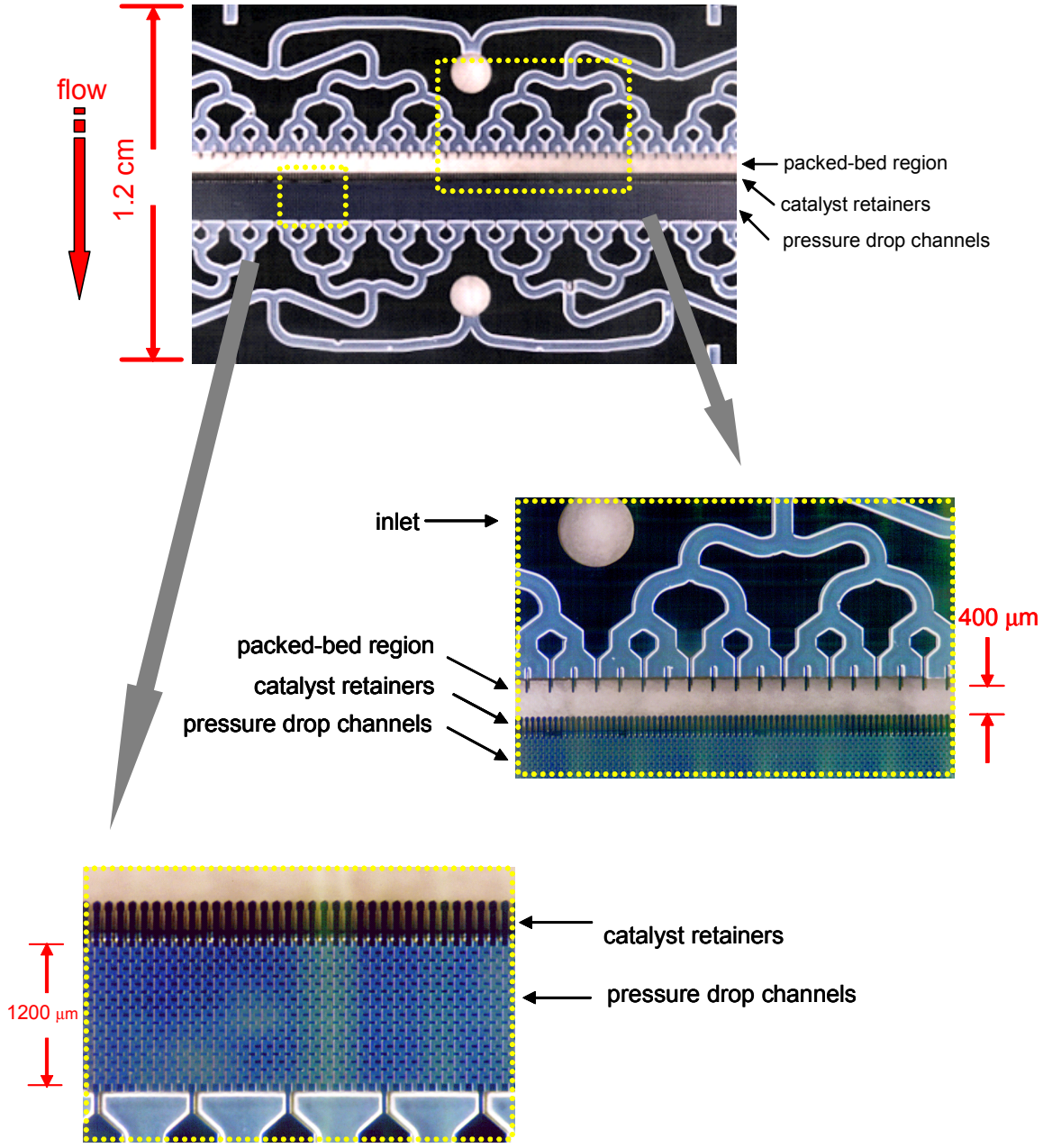


**Figure 3-4.** Photographs of the top-view of the microreactor taken through a microscope.

Because there are only 6 layers of particles in the flow direction, the pressure drop is quite variable depending on the local catalyst packing density. To ensure even flow across the reactor, a designed pressure drop created by 256 shallow channels is fabricated into the reactor structure right after the packed-bed region. These channels are 40 μm wide, only 20-25 μm deep, and meander for 1.265 mm in length (net center-line length = 2.165 mm) with 36 right-angle turns. The pressure drop through these channels is intentionally designed to be significantly greater than the pressure drop through the rest of the reactor, including the catalyst bed. In this way, the pressure drop created by the catalyst particles is dwarfed by the global flow resistance created by the pressure drop channels. Consequently, variances in local catalyst packing density minimally influence the pressure drop through the reactor and negligibly impact the overall flow distribution. This design is analogous to a circuit with a large resistor in series with a very small variable resistor. The small variations provided by the variable resistor negligibly impact the total resistance of the circuit, and thus the current through the circuit is nearly constant. Likewise, the pressure drop channels keep the flow through the reactor approximately constant regardless of variations in catalyst packing. The key enabler of this design is the ability to microfabricate the pressure drop channels with uniformity and repeatability as these channels govern the flow through the reactor. In Chapter 4, the functionality of the microreactor, particularly the pressure drop channels, is characterized through a combination of modeling and experimental studies.

The reactor contains three different channel depths as is discussed in the next section. The pressure drop channels are ~20 μm deep, while the inlet and exit flow manifold is etched 370 μm deep. The packed-bed region is 500 μm deep (a single silicon wafer thickness). Fig. 3-5 shows a cross-section schematic detailing the relative depths of these microchannels.

The impact of these various channel depths on the flow through the packed-bed is addressed in Chapter 4.

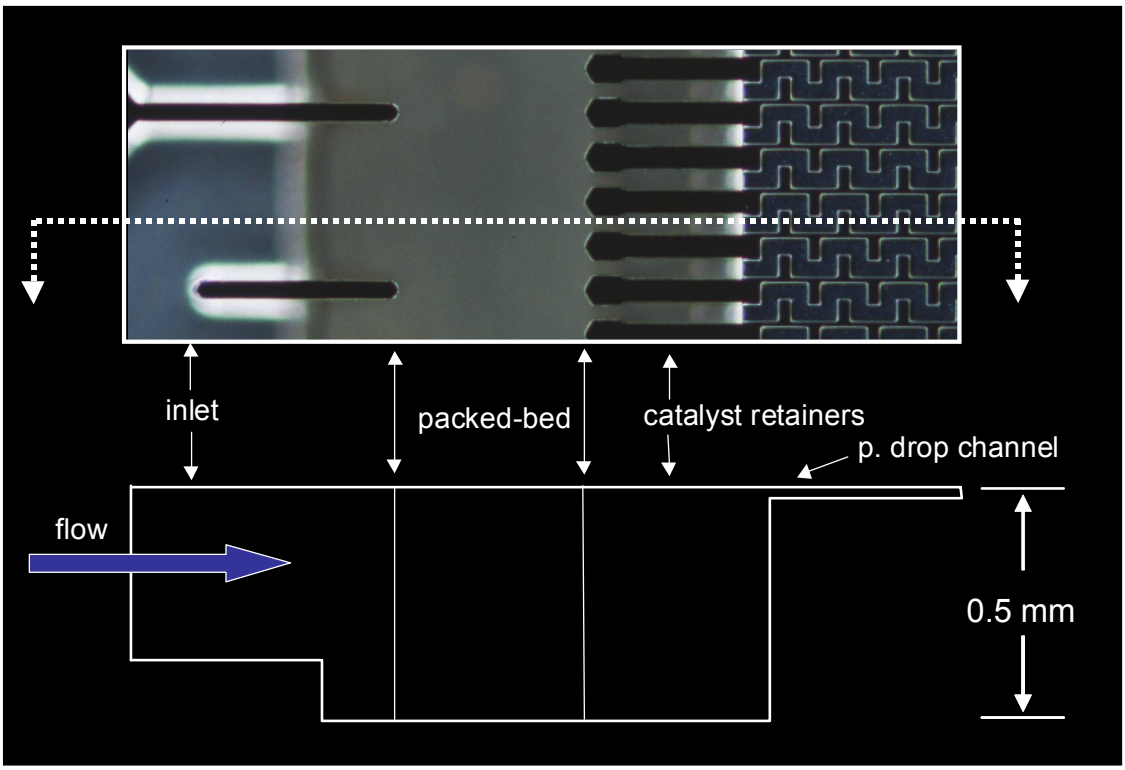


**Figure 3-5.** A photomicrograph of the packed-bed region of the microreactor and an accompanying cross-section detailing the relative depths of the microchannels. Photo courtesy of Felice Frankel, MIT.

## 3.3 Design Considerations

### 3.3.1 Packed-bed Geometry- reducing stagnation volumes

The final geometry of the cross-flow reactor was greatly influenced by various design considerations stemming from both physical geometric concerns and microfabrication issues. Primarily, the final geometry was guided by the desire to reduce reactor dead and stagnation volumes while assuring even gas flow through the packed-bed region. As is seen easily in Figure 3-4b, bifurcated structures naturally create islands that separate each channel. If the channels are etched all the way through the wafer, these islands would fall out of the wafer destroying the bifurcation geometry. Therefore, a timed etch is necessary to stop before etching through the wafer. However, the anisotropic deep reactive ion etch (DRIE) used to fabricate the cross-flow microreactor etches wider regions faster than narrow and confined ones, particularly for high aspect ratio structures. This is presumably due to transport limitations impeding the flux of reactive ions to the bottom surface as the aspect ratio of the etch increases. This effect can be seen in Figure 3-6 which shows the inlets and catalyst retainers which are ~50 μm apart and the main reactor channel which is approximately 625 μm wide for the micro packed-bed tube-flow reactor presented in Chapter 2.

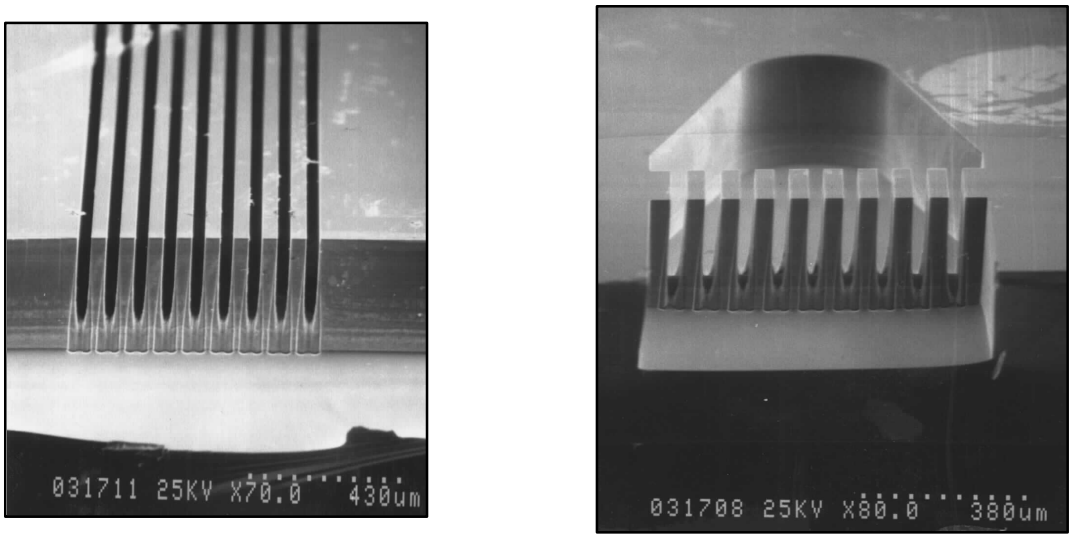


**Figure 3-6.** Uneven etching due to transport limitations in high aspect ratio structures in the micro tube-flow reactor presented in Chapter 2. The spaces between the inlet channels and catalyst retainers are etched about 75 µm less than the 350 µm deep channel.

The spaces between the inlet channels and catalyst retainers are etched ~75 µm less than the 350 µm deep reactor channel. This creates the potential for a stagnation volume in the catalyst bed as is illustrated below in Figure 3-7 if a timed etch similar to that shown in Figure 3-6 is used.

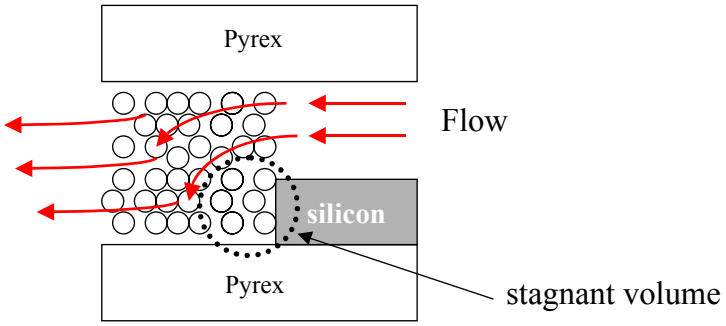


**Figure 3-7.** Potential stagnation volume at the step between the flow manifold or catalyst retainers and the packed-bed due to uneven etching of the silicon channels.

For the 2 cm long packed-bed in the micro tube reactor in Chapter 2, the effects of a stagnation volume covering only a few particle layers would be negligible. However, with only 6 particle layers in the cross-flow design, such a stagnation layer could significantly impact the performance of the reactor.

In the cross-flow reactor design, the regions between the catalyst retainer posts are only 50 μm wide whereas the packed-bed region is over 25 mm across. To avoid the possibility of non-uniform reactor depth and hence, stagnation volumes, the packed-bed region is etched all the way through the wafer. The region before the packed-bed and the channels between the catalyst retainer posts are also etched through to provide even flow of gases at the entrance and exit of the catalyst bed. This creates the three different channel depths shown in Figure 3-5. The through etch of the packed-bed region rigidly defines the packed-bed depth as the wafer thickness instead of relying on a timed etch. The flow manifold channels are only etched 370 microns in order to prevent the etched features from falling out. This creates a step at the interface between the flow inlets and the packed-bed. To avoid any stagnant volume within the catalyst bed at this interface, the step is designed to occur 275 microns before the packed-bed. By only filling catalyst particles up to the edge of the catalyst inlet guides as is shown in Figure 3-8, gas flow has plenty of time to stabilize before hitting the packed-bed. This is validated through flow modeling studies detailed in the next chapter.

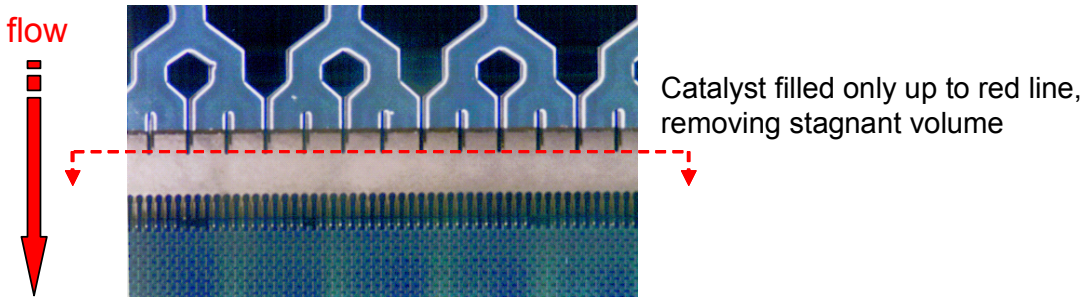


**Figure 3-8.** Spacer region above packed-bed to avoid stagnation volume.

To further avoid any stagnation or bypassing of catalyst particles butted up against the posts, both the inlet guides and the catalyst retainers were designed with rounded ends as shown below. The catalyst retainers are 50 microns wide and spaced 100 microns apart. The heads of the retainers expand out to leave a 35 micron gap between posts in order to retain particles of smaller diameters. Only the heads of the retainers were flared out to keep the 50 µm spacing as open as possible. This way, transport of reactive ions to the silicon substrate between the retainer posts is less hindered during the DRIE.

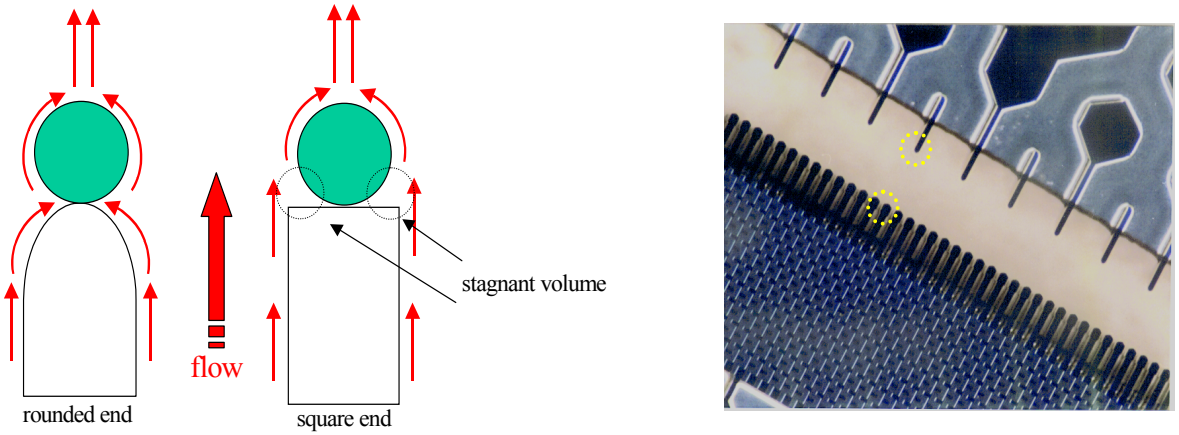


**Figure 3-9.** Rounded ends versus square ends, photograph of rounded posts

It will be shown in Chapter 5 that this small stagnant volume would in fact minimally impact reactor performance as diffusion effects are significantly large. However, the ability to easily tailor the reactor geometry with such detail through simple modifications of photolithography masks is one of the most powerful advantages of microfabrication technology.

The loading and unloading of catalyst particles was one of the most important considerations during reactor design. The micro tube-flow reactor in Chapter 2 utilized separate catalyst loading channels placed immediately before the packed-bed, adding dead volume to the reactor. In order to avoid this dead volume, it was chosen to use the inlet channels and inlet port to introduce catalyst into the wide particle bed. It is known that particles typically less than 100 μm fluidize relatively easily in a flow stream. Therefore, using the inlet port and bifurcating channels to distribute the catalyst bed is feasible in a moderate gas stream. The pressure drop channels serve to evenly distribute the flow, and hence the catalyst particles, over the wide bed. The shallow 20 μm deep pressure drop channels were placed after the catalyst bed to allow the ~60 μm particles to be loaded through the inlet. Likewise, the particles can be unloaded through the inlet channel, eliminating any potential dead volume.

### 3.3.2 Pressure Drop Channels

To design the dimensions of the reactor, pressure drop calculations were performed. However, correlations for pressure drop in laminar flow through non-circular channels are not well established. Therefore, design estimates were made using approximations found in literature. The most common dimensional approximation for non-circular channels is the

hydraulic diameter, $D_H$, defined as four times the channel cross-sectional area divided by the wetted perimeter [4]. However, this approximation has been found to work poorly for laminar flow because the channel geometry affects the flow resistance in a way that cannot be expressed as a function of only the ratio of cross-sectional area to wetted perimeter. For a few common shapes, the Navier-Stokes equations have been integrated to yield relations between flow rate and pressure drop that are expressed in relation to an equivalent diameter, $D_E$ [4]. $D_E$ can be used directly with the Hagen-Poiseuille equation [5] as given below.

$$Q = \frac{\pi \Delta P D_E^4}{128 \mu L} \tag{3-1}$$

where $\Delta P$ is the pressure drop, $Q$ is the volumetric flow rate (volume/time), $\mu$ is the viscosity, and $L$ is the length of the channel. Owen [6] has provided an estimation for $D_E$ in units of length for rectangular channels as given below in Eq. 3-2.

$$D_E = \left( \frac{128 a b^3}{\pi K} \right)^{1/4} \tag{3-2}$$

where $a$ is the channel width, $b$ is the channel height, and $K$ is a fitted parameter that is a function of the ratio of $a$ to $b$. An estimate for the pressure drop through the particle bed was made using the Ergun equation (Equation 2-17) with a void fraction of 0.4. Using the equations given above, a design estimate was made with a target that the pressure drop created by the pressure drop channels would be 95% of the total pressure drop through the reactor, including the inlet/exit channels, pressure drop channels, and the particle bed. The

net center-line length was used as the equivalent length of each channel as suggested by Crane Co. [7] for strongly laminar flow in rectangular channels (very low Re), as is seen in the microreactor. A comparison of the experimental pressure drop through the microreactor to the pressure drop predicted by the above design equations is given in Chapter 4.

The criteria that the pressure drop through the pressure drop channels is 95% of the total pressure drop through the reactor was chosen as a practical limit for the maximum deviation of flow rate tolerable to still measure accurate kinetics. In standard chemical engineering practice, a deviation of reaction rate due to gradients of less than 5% is considered acceptable for quantitative catalyst testing. Similarly, by designing the pressure drop through the catalyst bed to be only ~5% of the total pressure drop, the maximum error of the reaction rate measured at differential conversions due to poor catalyst packing is 5% in the worst case scenario described in the example below. In a typical packing situation where the catalyst is reasonably evenly distributed, the induced error on kinetic measurements due to uneven packing or voids is significantly less than 5%.

The illustrations below give examples of a normal reactor filled completely and evenly with catalyst particles and two extreme cases of uneven packing, one with only half the reactor filled with particles, and the other, with only 10% of the reactor filled with particles. In the two later cases, flow is not perfectly even across the reactor width as the empty section of the reactor has a lower pressure drop than the section with catalyst particles.

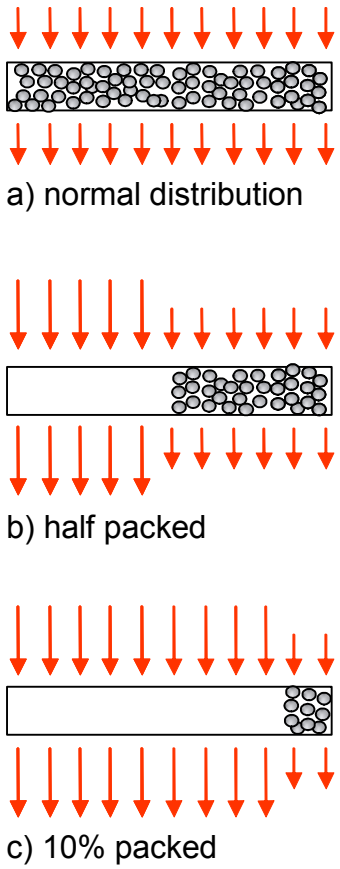


**Figure 3-10**. Illustrations of three catalyst packing scenarios.

The reaction rate that would be measured in differential experiments using each of these packing scenarios can be calculated assuming a constant reaction rate per unit catalyst volume due to the differential approximation, no lateral diffusion, and a catalyst bed which contributes 5% to the pressure drop through the reactor. The different packing densities cause the residence time through the reactor to vary between the two regions. As will be shown in Chapter 5, diffusion effects are significant in the cross-flow microreactor and

would actually serve to reduce any measurement errors induced by uneven packing. The well packed reactor (Fig. 3-10a) with even flow distribution, differential conversions, and no transport limitations can be assumed to yield the true catalytic reaction rate. Calculations show that experiments with the reactor half filled with particles (Figure 3-10b) would produce a measured rate that deviates from the true rate by ~2.5%, and the reactor only 10% filled (Fig. 3-10c) would give results that deviate by ~4.6%. The theoretical limit for deviation in these calculations is 5% which would occur as the percent of the reactor filled with particles approaches zero. It can be seen from these calculations that a reactor packed reasonably well will generate an error in kinetic measurements caused by variations in catalyst packing that is significantly less than 5%. In contrast, repeating the calculations with the pressure drop channels contributing only 50% of the total pressure drop in the reactor gives an error of 50% for the second case and 90% for the third case. Therefore, the design criteria that the pressure drop channels create 95% of the total pressure drop in the reactor is reasonable for accurate kinetics.

Although the pressure drop channels are placed after the packed-bed in order to facilitate loading of the catalyst particles, there are other advantages to their placement in terms of flow distribution. If the pressure drop channels were placed before the catalyst bed, the flow would be evenly distributed at the entrance of the bed. However, the flow would be free to channeling effects through the bed as the pressure drop through the bed would be strictly governed by the local flow paths through the particles. In this way, random channeling effects could be possible. By placing the pressure drop channels at the exit of the catalyst bed, flow is evenly distributed at the exit of the particle bed. Because the bed is so short, this forces a more even flow through the entire particle bed countering local

channeling effects. There is not enough time or space for flow to unevenly channel through the packed-bed and then redistribute evenly before the pressure drop channels.

## 3.4 Microreactor Fabrication

The microreactor is fabricated from single crystal silicon (100 mm diameter wafer, 500 μm thick) with standard microfabrication processes. The fabrication process (Fig. 3-10) involves three photolithography masks for reactor features, and one more for alignment marks. The reactor features are etched using anisotropic deep reactive ion etching (DRIE) with a time-multiplexed inductively coupled plasma etcher (*Surface Technology Systems*) [8]. This etch will be henceforth referred to as "STS" throughout this work. The final reactor contains three different channel depths. The pressure drop channels are ~20 μm deep, whereas the inlet and exit bifurcated flow channels are etched 370 μm deep. The packed-bed region is 500 μm deep (a single silicon wafer thickness). Both front-side and back-side etches are used to fabricate the three different channel depths as described in the next paragraph. Appendix A contains a detailed fabrication section complete with a process flow and photolithography masks.

In summary, in the first fabrication step, 0.5-1.5 μm of oxide is thermally grown (or PECVD deposited and thermally annealed) on both sides of the starting wafer (Fig. 3-11a). The oxide protects the bonding surfaces during processing from physical damage such as scratches or unwanted deposits from the STS. On the front-side, the oxide also serves as a nested mask for etching the pressure drop channels. In order to prevent wafer bow, it is

important if using deposited oxide to maintain the same thickness on both sides of the wafer. Both thermal and deposited oxide work equally well in this procedure. Next, the entire reactor geometry is patterned into the oxide on the front-side of the wafer. This mask includes the inlet/outlet ports, flow channels, packed-bed region, pressure drop channels, and thermocouple wells. On the back-side, the features to be etched through the wafer (packed-bed region and inlet/outlet ports) are patterned (Fig. 3-11b). The back-side features are then etched with DRIE ~150 μm deep (Fig. 3-11c). Using a photoresist (AZ P4620, *Clariant*) spin-coated 10 μm thick, the entire reactor geometry except the pressure drop channels is aligned to the oxide and patterned on the wafer front-side (Fig. 3-11d). A second DRIE is performed approximately 350 μm deep (Fig. 3-11e). This step opens up the features etched on the back-side and creates the flow channels. Removal of the photoresist reveals the previously patterned oxide layer. A timed etch is performed to etch all the features ~20-25 μm, creating the pressure drop channels (Fig. 3-11f). During this final etch process, the wafer is rotated approximately 5 times, to ensure that the overall etch depth across the wafer is as uniform as possible. Typically, a variation of 1 μm is seen across an entire wafer, with sub-micron variation seen across any individual reactor. The oxide layer is thick enough to serve as a resist against the shallow etch as the silicon to oxide etch rate in the STS is at least 50:1. The flow channels and thermocouple wells end up ~370 μm deep. In the final step, the oxide is stripped and the channels are capped on the top and bottom with Pyrex wafers (*Corning* 7740) by anodic bonding [9] (Fig. 3-11g). The optically transparent Pyrex enables visualization of the reactor and sets the maximum operating temperature of the device at ~775 K, which is sufficient for a broad range of catalytic processes. Mechanically drilled holes (2 mm) in the bottom Pyrex wafer are aligned to the inlet/outlet ports during the

bonding process. The final bonded wafer stack is diced to obtain eight individual reactor chips (15 mm × 40 mm × 1.5 mm). If higher temperatures are desired, silicon capping wafers can be used, extending the operating limit to ~1275 K. For initial microreactor characterization, Pyrex offers the advantage of being optically transparent. Other technologies such as ceramic molding or the lamination of thin layers of ceramics or intermetallics are under development to achieve microstructures for high temperature operation [10-12]. However, silicon offers better dimensional control and the advantages of highly parallel and reproducible manufacturing. The Pyrex wafer can be metalized with patterned heaters and temperature sensors before bonding integrating direct functionality to the reactor design.

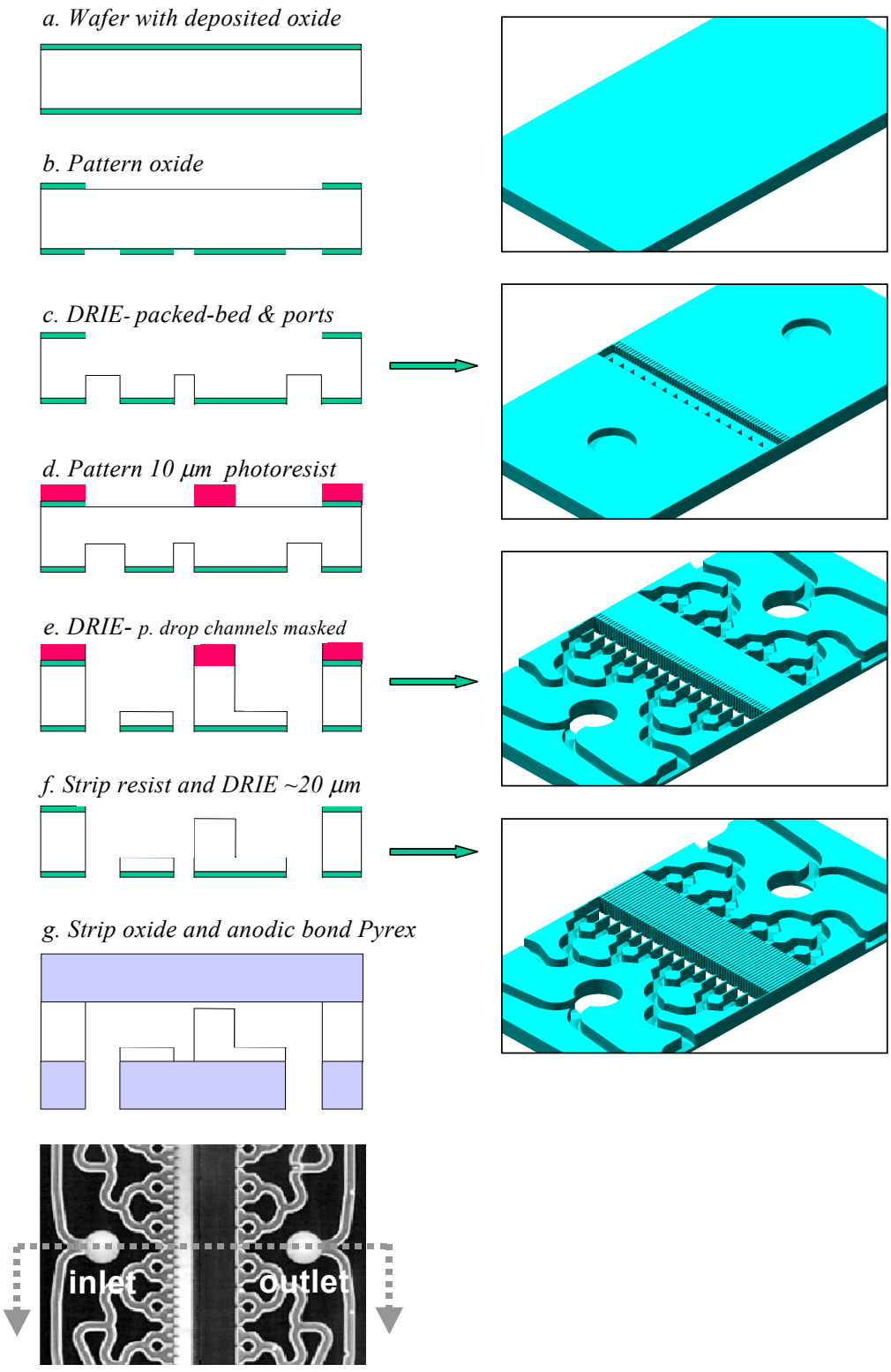


**Figure 3-11.** The cross-flow microreactor fabrication sequence. The photograph at the bottom is a top view of the cross section represented by the illustrations.

## 3.5 Summary

In this chapter, a silicon microfabricated cross-flow reactor has been presented for testing catalyst particles relevant to chemical process applications. In contrast to microfabricated tube-flow reactors that are prone to large pressure drops and integral operation, the cross-flow reactor incorporates a short pass multiple flow-channel geometry that naturally lends itself to low pressure drop and differential operation that is desirable for catalyst testing. Flow distribution is achieved through an array of 256 shallow pressure drop channels that minimize the influence of the catalyst packing on the flow in the reactor. In this design, the uniformity of the pressure drop channels is critical to ensuring even flow through the reactor. Microfabrication technology enables the fabrication of this device with high accuracy and reproducibility. In the next chapter, the cross-flow microreactor is characterized through both modeling and experimentation to assess the performance of the cross-flow geometry for even flow distribution.

## Literature Cited


[1] M.W. Losey, M.A. Schmidt, K.F. Jensen, "Microfabricated Multiphase Packed-Bed Reactors: Characterization of Mass Transfer and Reactions," *Ind. Eng. Chem. Res.* **40** (2001) 2555-2562.

[2] S.K. Ajmera, M.W. Losey, K.F. Jensen, M.A. Schmidt, "Microfabricated Packed-bed Reactor for Phosgene Synthesis," *AIChE J.* **47** (2001) 1639-1647.

[3] C. Harris, M. Despa, K. Kelly, "Design and Fabrication of a Cross Flow Micro Heat Exchanger," *Journal of Microelectromechanical Systems.* **9** (December, 2000) 502-508.

[4] R.H. Perry, D.W. Green, J.O. Maloney, in: "Perry's Chemical Engineers' Handbook, Seventh Ed.," McGraw-Hill, New York, 1997, pp. 6-10 - 6-12.

[5] W.L. McCabe, J.C. Smith, P. Harriott, in: "Unit Operations of Chemical Engineering, Fifth Edition," McGraw-Hill, New York, 1993, pp. 88.

[6] Owen, *Trans. Am. Soc. Civ. Eng.* **119** (1954) 1157-1175.

[7] Crane, in: "Flow of Fluids through Valves, Fittings, and Pipe, Technical Paper No. 410," GAU, New York, 1969, pp. 2-11.

[8] A.A. Ayon, R. Braff, C.C. Lin, H.H. Sawin, M.A. Schmidt, "Characterization of a Time Multiplexed Inductively Coupled Plasma Etcher," *J. Electrochem. Soc.* **146** (1999) 339-349.

[9] M.A. Schmidt, "Wafer-to-Wafer Bonding for Microstructure Formation," *PROCEEDINGS OF THE IEEE.* **86** (1998) 1575-1585.

[10] P.M. Martin, D.W. Matson, W.D. Bennett, D.C. Stewart, C.C. Bonham, "Laminated Ceramic Microfluidic Components for Microreactor Applications," in: IMRET 4: 4th

International Conference on Microreactor Technology, AIChE Spring National Meeting, Atlanta, USA, 2000, pp. 410-415.

[11] R. Knitter, D. Gohring, M. Bram, P. Mechnich, R. Broucek, "Ceramic Microreactor for High-Temperature Reactions," in: IMRET 4: 4th International Conference on Microreactor Technology, AIChE Spring National Meeting, Atlanta, USA, 2000, pp. 455-460.

[12] B.K. Paul, T. Dewey, D. Alman, R. Wilson, "Intermetallic Microlamination for High-Temperature Microreactors," in: IMRET 4: 4th International Conference on Microreactor Technology, AIChE Spring National Meeting, Atlanta, USA, 2000, pp. 236-243.

# Chapter 4
# Characterizing the Cross-Flow Reactor

---

By understanding the flow properties of the microreactor, kinetic data can be analyzed with increased confidence. This chapter details the characterization of the flow properties in the cross-flow microreactor introduced in Chapter 3. The reactor's performance is analyzed with respect to providing even distribution of flow to the catalyst bed and suppressing the effects of stagnant volumes. Practical issues such as reactor packaging and the loading of catalyst particles are discussed as are a variety of details on their advantages and limitations.

## 4.1 Microreactor Packaging- Initial Design for Testing

After fabrication, the microreactor must be packaged for integration with macroscopic devices such as syringe pumps, pressurized gas lines, and chemical detection equipment. The packaging scheme employed (Fig. 4-1) involves compressing the reactor with a metal cover plate against a thin elastomer gasket (0.8 mm Kalrez™ or Viton™) in a fashion similar to Losey et al. [1]. The gasket material has punched through-holes that form fluidic connections to a stainless-steel base. External fluidic connections are made directly to the metal base via standard fittings, valves, and 1.6 mm O.D. stainless-steel tubing (Fig. 4-2).

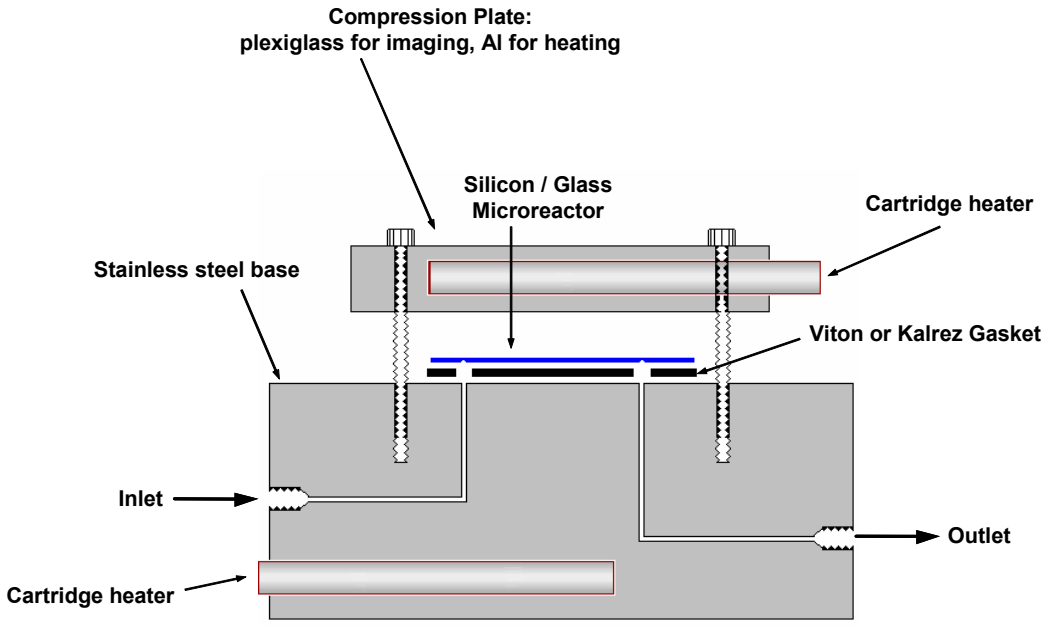


**Figure 4-1.** The microreactor packaging scheme. The reactor is compressed against a gasket with a metal top plate to form fluidic connections to a stainless steel base. Cartridge heaters are used to heat the assembly, if necessary.

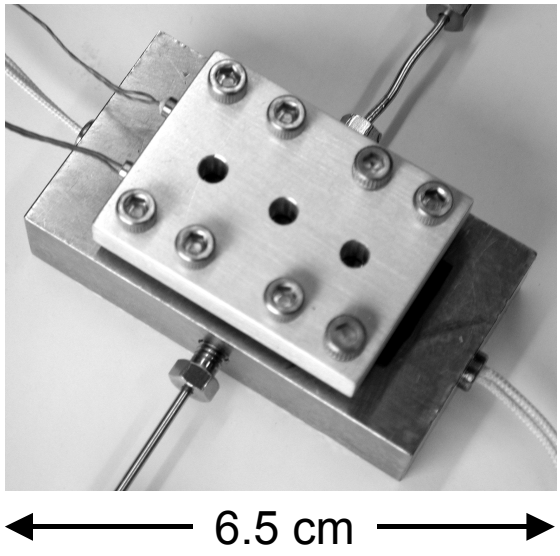


**Figure 4-2.** A photograph of the microreactor assembly with 1/16" HPLC fluidic connections and cartridge heaters inserted in both the top plate and the base.

The metal compression plate and the base contain cartridge heaters (*Omega Engineering,* CSS-01125/120V and CSH-101100/120V respectively) and thermocouples (*Omega Engineering,* 5TC-TT-K-36-36) that are inserted into the side-wells of the reactor. Temperature control is achieved using a standard temperature controller. Mass flow controllers are used to control gas flow. The entire system is placed inside a small ventilated enclosure similar to a standard chemical fume hood. Similar to the microreactor system for phosgene generation, an inherent benefit of working with microreactors is structures such as tube furnaces and sand baths that add size and complexity to laboratory work are not needed. Multiple reactors can be run side-by-side with minimal increase in system size. This is very important when considering running many microreactors in parallel to create a high-

throughput testing or combinatorial catalysis platform. Microreactor sizes naturally lend themselves to these types of applications.

### 4.1.1 Advantages and Disadvantages of the Packaging Scheme

The packaging scheme described above has a variety of advantages for research and development. The assembly is relatively quick to set up and the fluidic seals are reproducible from reactor to reactor. This prevents any influence from packaging on data taken from multiple reactors. Since the stainless-steel base and top plate contain cartridge heaters, reactor designs that do not have heaters can still be tested at high temperatures. This eliminates extra fabrication effort and reactor design and allows new reactor geometries or concepts to be tested quickly. A variety of materials can be used for both the metal base and the gasket material to accommodate a variety of chemistries. For example, Teflon, aluminum, or Plexi-glass can be used for the base while a variety of fluoropolymers can be used interchangeably for the gasket. This flexibility eliminates chemical compatibility issues with the packaging materials and allows the researcher to isolate the reactor for study. The packaging is also mechanically robust once assembled. Impacts and vibrations have negligible effect on the quality of the seal or the integrity of the reactor. This gives significant flexibility in assembling/disassembling apparatus and running experiments. The packaging also provides a significant heat sink for the microreactor. This helps keep the microreactor isothermal during high temperature operation and reduces the thermal effects of the packaging on microreactor performance. With exothermic reactions, the large thermal

mass of the packaging helps remove heat quickly from the reactor, keeping the catalyst bed isothermal and improving control over the bed temperature.

However, a few limitations with this packaging scheme must be noted. Firstly, if metals such as stainless steel are used as the base and compression plate material, the upper temperature limit for operation directly depends on the thermal stability of the gasket material. For typical fluoropolymers such as Viton or Kalrez, this upper limit lies between $250^{o}$ and $300^{o}$ C. Secondly, for this compression seal, it has been found that reproducible sealing becomes difficult above 10 atm of pressure, limiting the operating range for the microreactor. Finally, disassembly with this packaging scheme can be difficult if the reactor has been heated above $250^{o}$C. The gasket softens and forms a temporary bond with both the metal base and the microreactor. This sometimes makes it difficult to remove the microreactor from the assembly without breaking it. However, for testing a new reactor geometry such as the cross-flow microreactor, the advantages of the compression seal packaging technique outweigh the disadvantages and this scheme was chosen to conduct the experiments detailed in this chapter and in Chapters 5 and 6.

### 4.1.2 Alternate Packaging Scheme: Direct Brazing of Tubing

One difficulty that arises when employing the packaging scheme given in the previous section is that the metal compression plate and base provide a significant heat sink preventing the use of on-chip integrated heaters such as those designed by Losey [2] for packed-bed microreactors. The power required for microheaters to heat the entire reactor and the packaging limits the use of these heaters in practical experimentation. The inability to

use integrated microfabricated heaters coupled with the limitations of temperature, pressure, and disassembly discussed in the previous section led to the examination of an alternate packaging scheme.

In order to eliminate the direct contact of the large heat sink, the concept of using tubing directly brazed to the microreactor to form fluidic connections was explored. This idea has been previously demonstrated for the direct connection of Kovar tubing to silicon fluidic ports by Harrison [3] for the packaging of the MIT microengine. Harrison brazed preformed glass frits that were thermally matched to the Kovar tubing and silicon to create a hermetic seal directly at the surface of the silicon wafer. This concept was extended to microreactors with the development of a similar technique to braze tubing directly to the Pyrex capping wafers in the cross-flow microreactor. Unfortunately, the same materials used by Harrison cannot be used for the microreactor as the temperatures employed during the braze to silicon is hundreds of degrees higher that the upper operating limit of Pyrex. Therefore, new materials and recipes had to be employed for this process. Appendix B details the work on direct brazing to the cross-flow microreactor, including the entire brazing procedure and methodology for making fluidic connections to the brazed tubing.

Shown below are photographs of microreactor test pieces with Pyrex and Kovar tubes brazed to the Pyrex capping wafer. It has been found that Pyrex 7740 tubes give better reproducibility and higher yields than Kovar, but Kovar tubing is rated to higher pressures than the Pyrex tubing.

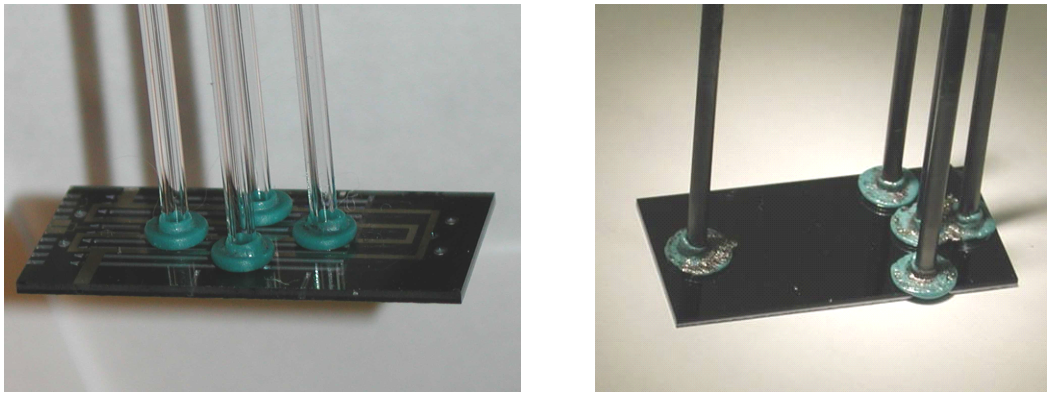

**Figure 4-3.** Photograph of test pieces with Pyrex (left) and Kovar (right) tubes brazed to the Pyrex capping wafer

With Pyrex tubing, bonds have been tested at pressures up to 25 atm at 450-500$^{o}$C. The upper pressure limit is controlled by manufacturer ratings on the Pyrex tubing and not by the bond quality. Room temperature tests with the Kovar tubing have been performed successfully at pressures up to 50 atm. The tubes are stabilized with a plate epoxied to every tube, preventing moments at the tube ends from being transferred to the bond. The stabilizer plate also spreads out any torque on the reactor to all the tubes, strengthening the entire reactor package. Once the stabilizer plate is epoxied, the package is quite robust to impacts and moments. Fluidic connections to the package are made using o-ring seals to a machined metal base as shown in the photograph below. These seals are reversible, allowing multiple packaged reactors to be tested on the same platform while maintaining the integrity of both the metal base/o-rings and the reactor/tube package.

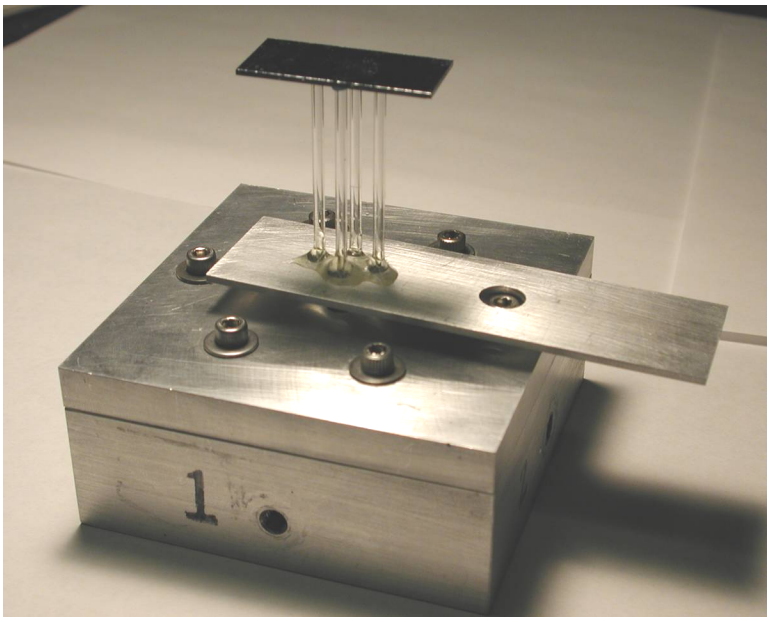


**Figure 4-4.** Photograph of the fully packaged microreactor. Fluidic connections are made to direct brazed tubing via an o-ring seal to a stainless-steel base.

Losey [2] calculated the Biot number for a typical microreactor suspended in air to be approximately 0.0001. This small number indicates that the microreactor chip is isothermal and the largest resistance to heat transfer is external to the chip. However, this can create a problem for temperature control with exothermic reactions. Unlike the compression seal packaging where the heat generated by reaction is dwarfed by the heat needed to maintain the packaging temperature, the suspended tube packaging can lead to unwanted heating of the reactor. To maintain a suspended tube reactor at 200$^{o}$C, roughly 8 Watts of power is needed. The phosgene reaction performed in Chapter 2 produces approximately 0.4 Watts of heat at 200$^{o}$C, adding about 5% more heat to the reactor. Thus, the heat of reaction can influence the reactor temperature in contrast to the compression packaging in Chapter 2 where no temperature increase was noted. Therefore, it may necessary to reincorporate a heat sink into

a tube packaged cross-flow reactor via integrated heat exchangers, external cooling fins, or a heat-sink/fan package similar to that used with microprocessors in order to maintain the high resolution of temperature control desired for catalyst testing.

The brazed tube packaging scheme is described in its entirety in Appendix B. The ability to reproducibly create high quality high temperature/high pressure hermetic seals will open the door to a wider range of chemistry and operating conditions for catalyst testing. However, further development is still required on this packaging technique as described in the Appendix. Therefore, for the experiments performed in this chapter and Chapters 2, 4, 5, and 6, the compression seal scheme shown in Figures 4-1 and 4-2 has been used exclusively.

## 4.2 Catalyst (Particle) Loading

Catalyst particles between 53-71 μm diameter are loaded into the reactor through the inlet port using a vacuum placed on the outlet. The particles are small enough that the flow of gas generated by the vacuum fluidizes the catalyst and draws it into the reactor. Figure 4-5 shows a photomicrograph of a microreactor filled with 60 micron glass beads (*MO-Science Inc.*). The beads are packed tightly against the catalyst retainers. Clogging or plugging in the curved inlet channels does not occur, due to the easy fluidization of the particles.

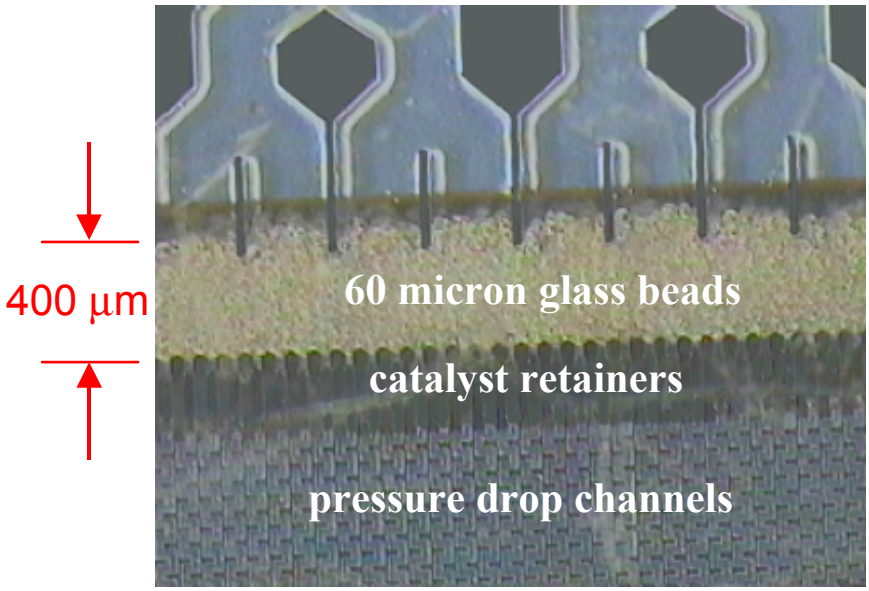


**Figure 4-5.** Photomicrograph of a microreactor packed with glass beads.

With a high pressure applied to the outlet, the catalyst particles can be blown out of the inlet port. In this way, the reactor can be reused for multiple chemistries or different catalysts. If post reaction analysis is desired, the particles can be captured on a filter fitted to the metal base as they are blown out of the reactor. The particle size range of 53-71 µm was chosen for the cross-flow microreactor because it is large enough to be retained by the catalyst retainer posts while being small enough to yield as many particles as possible in the catalyst bed. Smaller diameter particles also serve to reduce internal mass transfer limitations, improving the reactor performance for catalyst testing [4].

The curved inlet channels, however, do have an effect on the particle loading. Even though the particles fluidize easily, they still have momentum effects as they negotiate the

curves. This causes the particles to load unevenly against the catalyst retainers as shown in Figure 4-6.

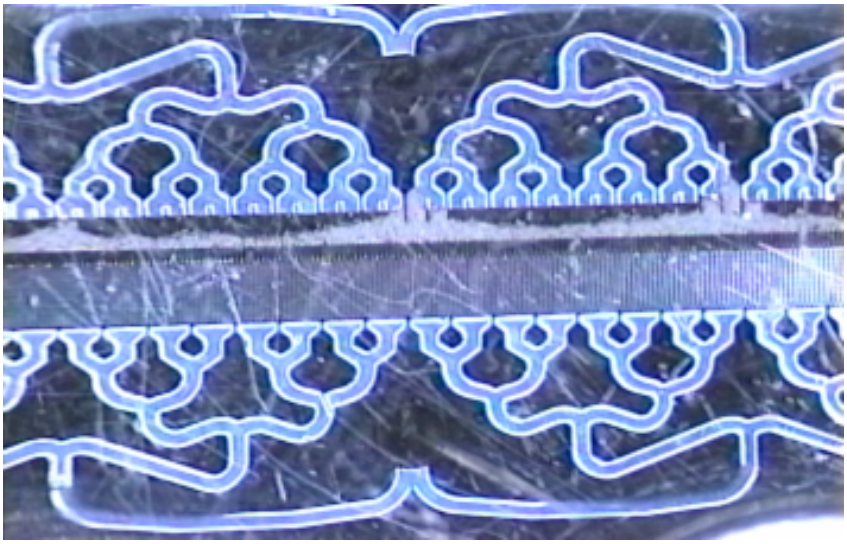

**Figure 4-6.** Photomicrograph of a reactor loaded with glass beads. Due to momentum effects, the beads load unevenly. However, tapping or shaking leads to the even distribution seen in Figure 4-5.

The particles pack in a periodic fashion across the reactor width, with areas of increased particle count repeating with areas with decreased number of particles. However, simple tapping or shaking by hand is enough to even out the particles resulting in the even distribution seen in Figure 4-5. The pressure drop channels, as will be shown in this chapter, serve to prevent uneven reactant distribution even if there are slight variations in catalyst packing. Furthermore, if the reactor is run at low conversions such that all parts of the reactor are operating differentially, the distribution of the catalyst particles has no effect on the overall operation of the reactor. For example, assume one half of a reactor has twice as

much catalyst as the other half, and the reactor is run at 3% total conversion. Because all parts of the reactor have the same residence time, one half of the reactor would be operating at ~4% total conversion, and the other half at ~2%. The differential approximation assumes that the total conversion is sufficiently low that the kinetic rate is the same at all points in the reactor because the concentration of species is approximately the same. In this case, the same kinetic parameters would be extracted (to within the error limits inherent in the differential approximation) as from a reactor packed evenly and operating uniformly at 3% conversion. Therefore, as long as the reactor is run at sufficiently low conversions, even a poorly packed reactor will yield results accurate to the level of certainty assumed in the differential approximation. A well packed reactor after tapping or shaking gives a high level of confidence to the utility of the reactor for differential operation.

## 4.3 Pressure Drop Studies in the Microreactor

To study the effect of the pressure drop channels on the overall pressure drop in the reactor, experiments with gas flow were performed. The pressure drop across the reactor was measured using Grade A (ASME) pressure gauges and 60 μm glass beads as packing (*MO-Science Inc.*) as shown in the previous section. Nitrogen gas was used and the flow rate was controlled by standard mass flow controllers (*UNIT Instruments, Inc.*). The pressure was measured at the inlet of the reactor using a T-junction. The exit of the reactor was left open to the atmosphere and the exit pressure was considered to be atmospheric.

The pressure drop across the reactor was measured for both an empty reactor and one packed with glass beads (Fig. 4-7). The pressure drop across the empty reactor was

approximately 0.075 atmospheres for a flow of 100 sccm nitrogen at room temperature. The addition of beads minimally increased the pressure drop, contributing only ~7% to the total pressure drop in the packed-bed. In the worst case, if there were a large void in the catalyst packing (unlikely in normal operation), it would only experience a ~7% increase on the average in flow compared to the rest of the reactor. In normal operation with evenly distributed packing, the flow can be considered independent of packing voids.

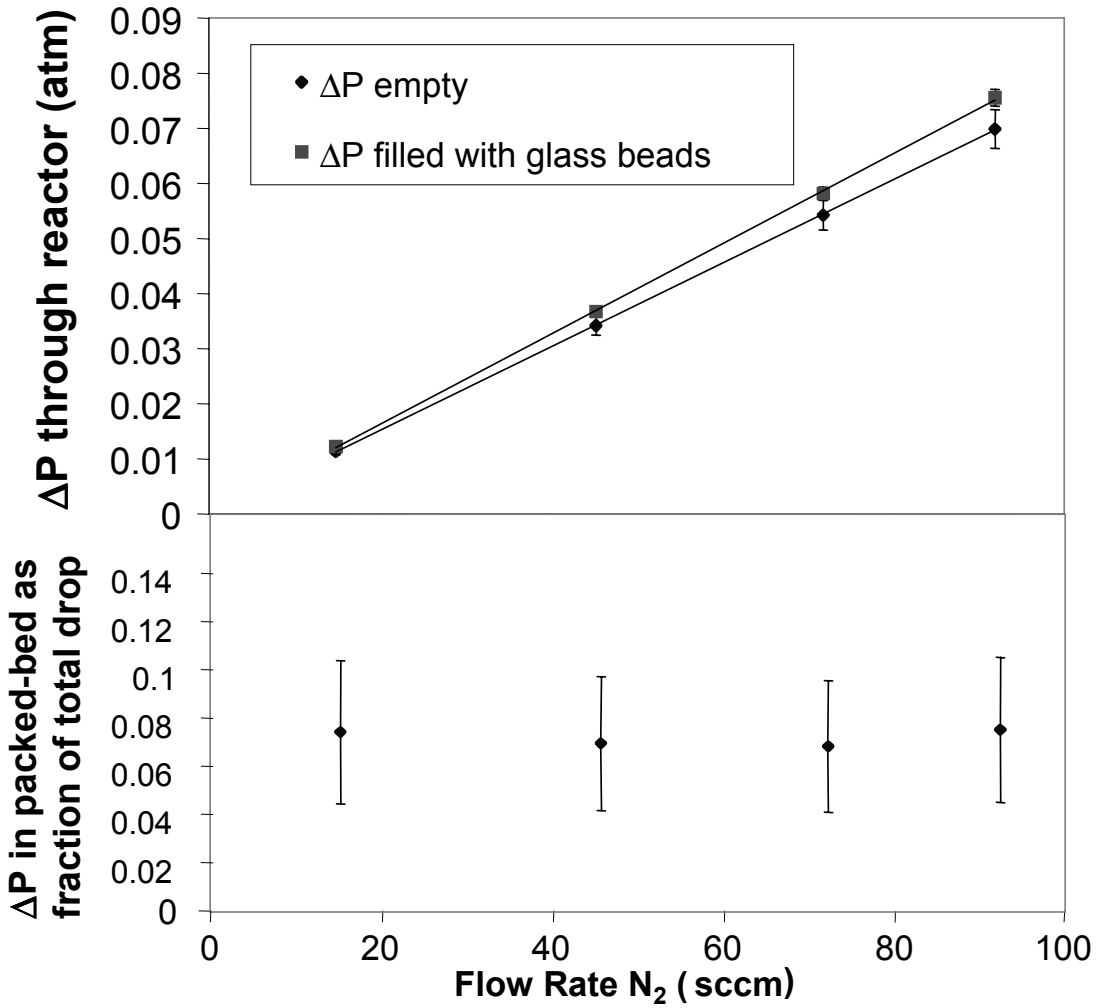


**Figure 4-7.** *(top portion) P*ressure drop across an empty reactor (lower curve) and a reactor packed with 60 μm glass beads (upper curve). The addition of packing has a small effect on the total pressure drop. *(bottom portion)* The pressure drop is primarily over the shallow pressure drop channels- the packing contributes only ~7% to the total pressure drop in the reactor. Error bars indicate standard instrument error for Grade A pressure gauges.

Further, the pressure drop across the catalyst bed is negligible as the drop across the bed is only 0.006 atm for 100 sccm nitrogen flow. The benefit of the cross-flow design is seen when compared to the pressure drop with axial flow. The micro tube-flow reactor in Chapter 2 had a 0.4 atm pressure drop for only a 4.5 sccm flow rate. In general, the pressure drop in an axial flow reactor of the same dimensions packed with the same quantity of glass spheres as the cross-flow reactor would be ~1600 times larger for 100 sccm gas flow as predicted by the Ergun equation [5] given in Equation 2-17. The small pressure drop with even flow distribution obtained in the cross-flow design is clearly advantageous for reaction kinetics studies.

Even though the pressure drop channels are designed to intentionally add a pressure drop to the reactor, the total pressure drop through the cross-flow reactor is still small. The total pressure drop of the cross-flow reactor is only ~0.7% of an equivalent axial flow reactor. This means the cross-flow geometry is viable option for chemical production where the increased operating cost from a large pressure drop might be of particular concern. Section 5.6 discusses in detail how the cross-flow geometry enables the design of a microfabricated well mixed reactor that may be useful for chemical production. For catalyst testing, the pressure drop across the catalyst bed, not the total pressure drop, is of greatest importance. In this case, the cross-flow design yields isobaric conditions for catalyst testing.

### 4.3.1 Comparison to Design Equations

As described in Section 3.3.2, the dimensions of the pressure drop channels were designed using various correlations for laminar flow in square channels at very low Reynolds

numbers. These correlations are not well established as they have generally been of less interest than correlations for macroscale flows at higher Reynolds numbers. As the field of microfluidics develops, these correlations will be of greater interest, and it is important to understand their relevance to accurate microfluidic design. Figure 4-8 shows a comparison of the actual pressure drop though the reactor to that predicted by the design equations used in Chapter 3.

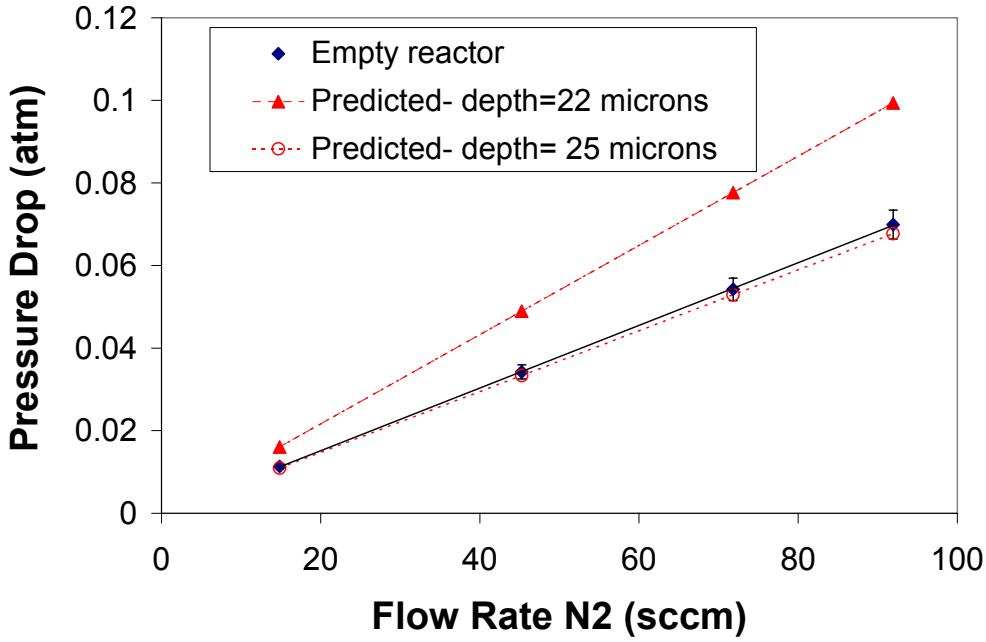


**Figure 4-8.** Predicted pressure drop calculated from design equations compared to experimental results in an empty microreactor.

The original design estimate detailed in Section 3.3.2 using equivalent diameters, $D_E$, was found to be within 40% of the measured values for the true pressure drop channel depth of 22 microns. However, the calculations are quite sensitive to channel dimensions. Even though the calculations at a channel depth of 22 µm ($D_E$=31.2 µm) overestimate the true

pressure drop, calculations performed for a slightly larger $D_E$ of 33.7 μm (channel depth = 25 μm) give an excellent prediction of the pressure drop in the pressure drop channels. Therefore, the design equations give a reasonable order of magnitude basis for micro flow-channel design, and are a good first approximation for estimating low Reynolds number gas flows in microfabricated channels.

## 4.4 Flow Distribution Across Reactor Width- Visualization

Although the pressure drop experiments presented in the previous section characterize the global functionality of the pressure drop channels, flow visualization experiments were performed to confirm the ability of the reactor to evenly distribute fluid across the entire width of the packed-bed. These flow visualization experiments were performed at room temperature using liquid flow through a microreactor. 1 μL plugs of 20 mM phenol red were injected into an ethanol stream and sent through the reactor using a 4-port internal volume sample injector (*VICI)* and a syringe pump (*Cole Parmer Instrument Co.*). The Reynolds number based on the inlet channel width was approximately 2.6, i.e., very laminar flow. To minimize dead volume, 500 μm inner diameter PEEK tubing (*Upchurch Scientific)* was glued directly to the reactor with epoxy (*DEVCON,* 5 minute epoxy) using a 1/16 inch stainless steel ferrule (*Swagelok*) as a guide. The ferrule was first glued to the reactor with the epoxy, and the tube was then inserted into the ferrule and epoxy was applied around the outside of the ferrule. This bond gives a seal that has been tested successfully at 50 atm of gas pressure, and is limited by the upper temperature limit of epoxy of around 100$^{o}$C for high

temperature operation. Flow images were captured using a stereomicroscope (*Leica MZ12)* connected to a charged coupled device (CCD) camera (*Cohu Electronics)* positioned directly above the reactor connected directly to a S-VHS video recorder.

Fig. 4-9a shows a sequence of images spanning ~500 ms as a plug of phenol red in ethanol flows through an empty microreactor where the pressure drop channels are the normal 20-25 μm deep and are uniformly etched throughout the reactor. The flow is well distributed across the width of the reactor demonstrating the ability of the device to deliver uniform flow and confirming the utility of the pressure drop channels.

In contrast, Fig. 4-9b shows a close-up view of a phenol red sample through a different microreactor with non-uniform pressure drop channels. Due to operator error during the fabrication of this particular wafer, a section of pressure drop channels was under-etched during the oxide removal detailed in Figure 3-10c leaving patches of thin oxide throughout the pressure drop channels. As a consequence, these patches were etched only ~5 μm deep (dark spots in Figure 4-9b) instead of the normal 20-25 μm during the STS etch, leaving the pressure drop in this region significantly larger than in the rest of the reactor. The images show flow curving sharply towards regions of the reactor with lower pressure drop giving non-uniform flow across the reactor. The flow visualization experiments clearly illustrate the importance of the pressure drop channels for realizing even flow distribution in the microreactor and enabling the cross-flow geometry for catalyst testing. Further, the necessity for control of reactor dimensions in the fabrication process is paramount. With proper microfabrication procedures, such dimensional control is achievable on a reactor-to-reactor as well as a wafer-to-wafer basis.

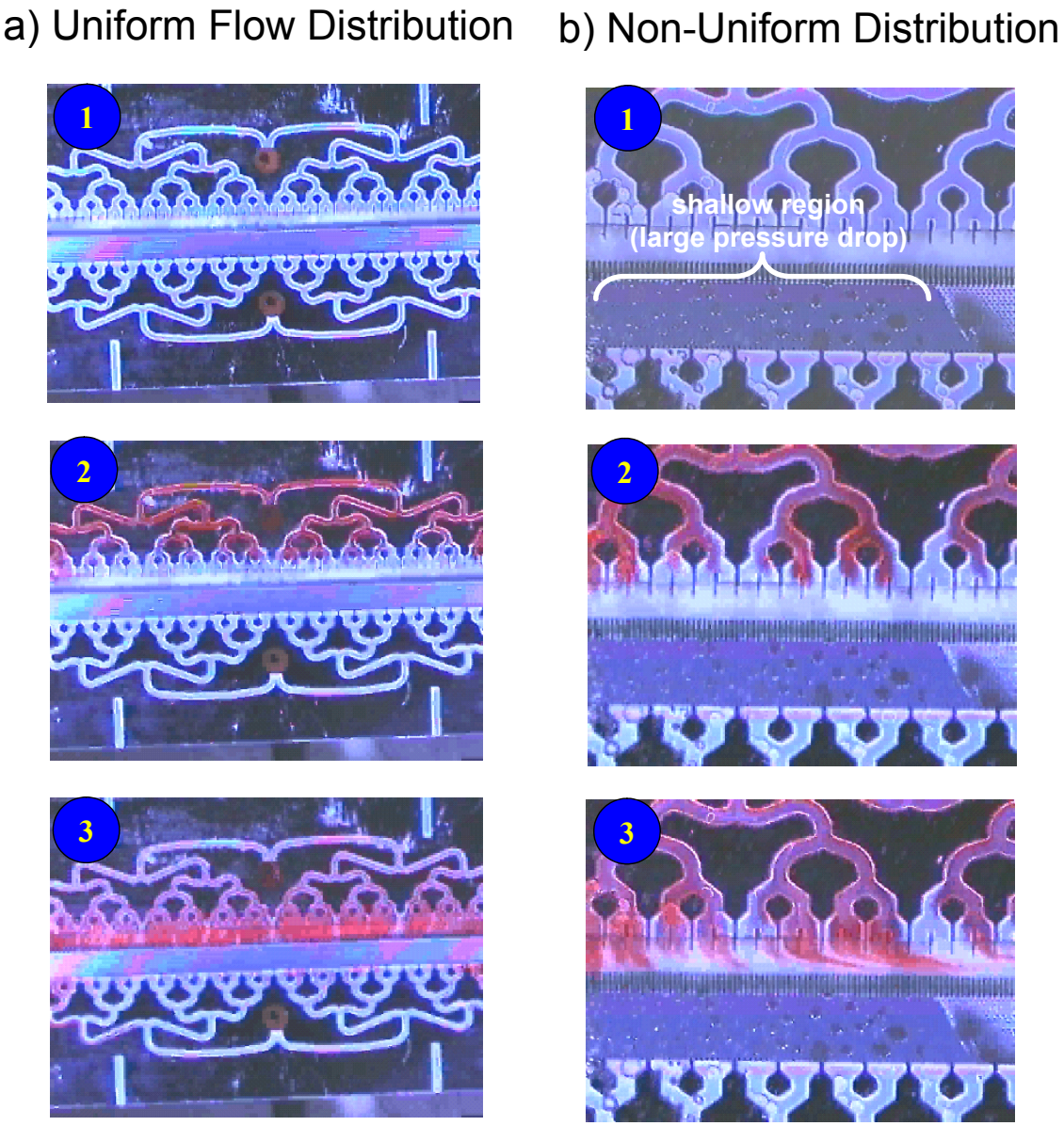


**Figure 4-9.** Flow of a 1 µL plug of phenol red in ethanol through two different microreactors. The total time span of the images is ~0.5 s. a) A typical microreactor with 20-25 µm deep pressure drop channels gives even flow distribution. b) In contrast, non-uniform flow distribution is seen in a reactor with a section of pressure drop channels etched only 5 µm deep (discolorations). The flow curves sharply away from this region of larger pressure drop towards regions of the reactor with deeper channels illustrating the strong influence the pressure drop channels have on flow in the microreactor.

### 4.4.1 Liquid and Multiphase Flow in the Cross-Flow Reactor

The cross-flow reactor was designed for gas phase chemistries. However, the geometry may be of interest for liquid phase systems, particularly biological applications where coated beads are commonly used. As was seen in the flow visualization experiments, the reactor works quite well for miscible fluids. However, surface tension effects become an issue for non-miscible or multi-phase flows. When a mixture of heptane and water is introduced into the system, the interface between the two liquids creates a meniscus that gets trapped at a bifurcation point and blocks a portion of the reactor from flow. This is seen even more clearly when a gas/liquid mixture is introduced through the inlet. In this case, bubbles of gas get trapped at either bifurcation points or in front of the catalyst retainers as is pictured in Figure 4-10.

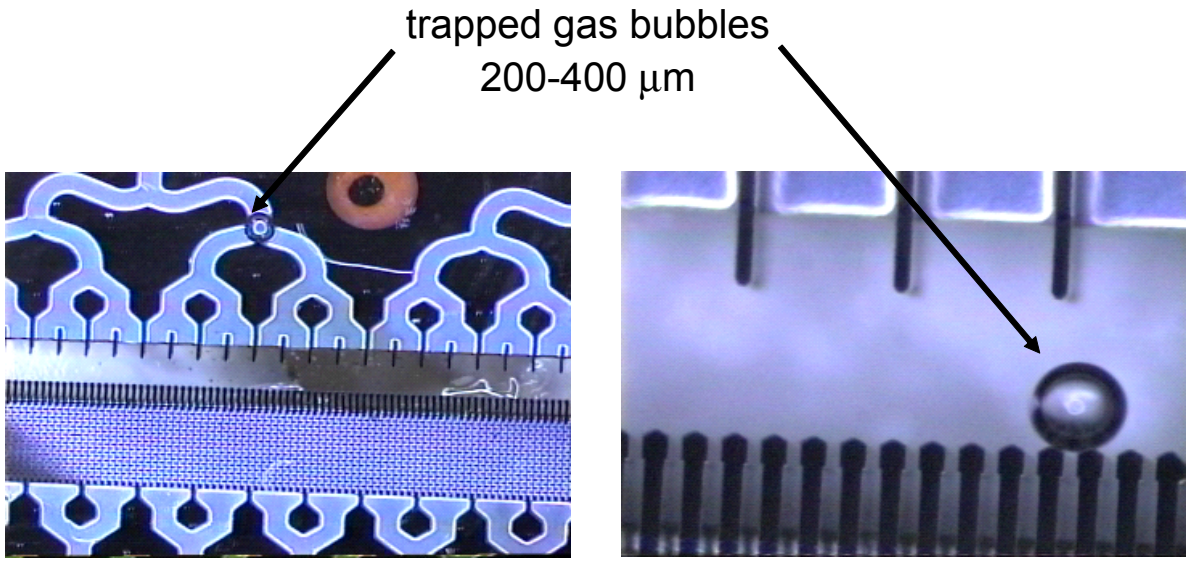


**Figure 4-10.** Air bubbles in water trapped in a bifurcation point or in front of the catalyst retainers.

Since the pressure drop through the reactor is quite low, it is hard to create enough force to dislodge the bubbles. A variety of techniques exist for coating microchannels to change their surface properties that could prevent the trapping of the bubbles. The dimensions of the bifurcation points can also be adjusted to promote the pass through of the bubbles. In conclusion, modification of the current geometry will be necessary for use with non-miscible or multi-phase chemistries.

## 4.5 Flow Distribution Across Reactor Depth- Modeling

The flow visualization experiments illustrate the distribution of flow across the width of the reactor. To understand the flow characteristics across the depth of the reactor, 2-D CFD calculations were performed using the reactor cross section shown in Fig. 3-5. 2-D modeling of gas flow in the reactor was performed using a commercial computational fluid dynamics software package (*CFD-ACE, CFD Research Corporation)* on a UNIX platform. The calculations were performed for the entire reactor cross section using air flow at an average velocity of 1 m/s at 373K for both an empty reactor and for a reactor with two layers of 50 μm "particles." The 2-D model is a reasonable approximation of the flow across the reactor cross-section as the width of the particle bed is approximately 60 times the length.

The velocity distribution through an empty reactor (Fig. 4-11) shows a laminar parabolic profile with non-symmetric distribution across the reactor depth (section A-B). This is expected due to the placement of the pressure drop channels at the top of the reactor. The parabolic flow distribution is not desirable for catalyst testing as it introduces a large variation in residence time across the reactor depth that can influence the ability to extract

accurate kinetics from the system. In particular, situations can arise where even though the total conversion is small enough to be considered differential, reactants flowing through areas with longer residence times can achieve very large conversions. In this case, the differential approximation would be invalid, and erroneous conclusions could be made if the differential approximation were applied during data analysis.

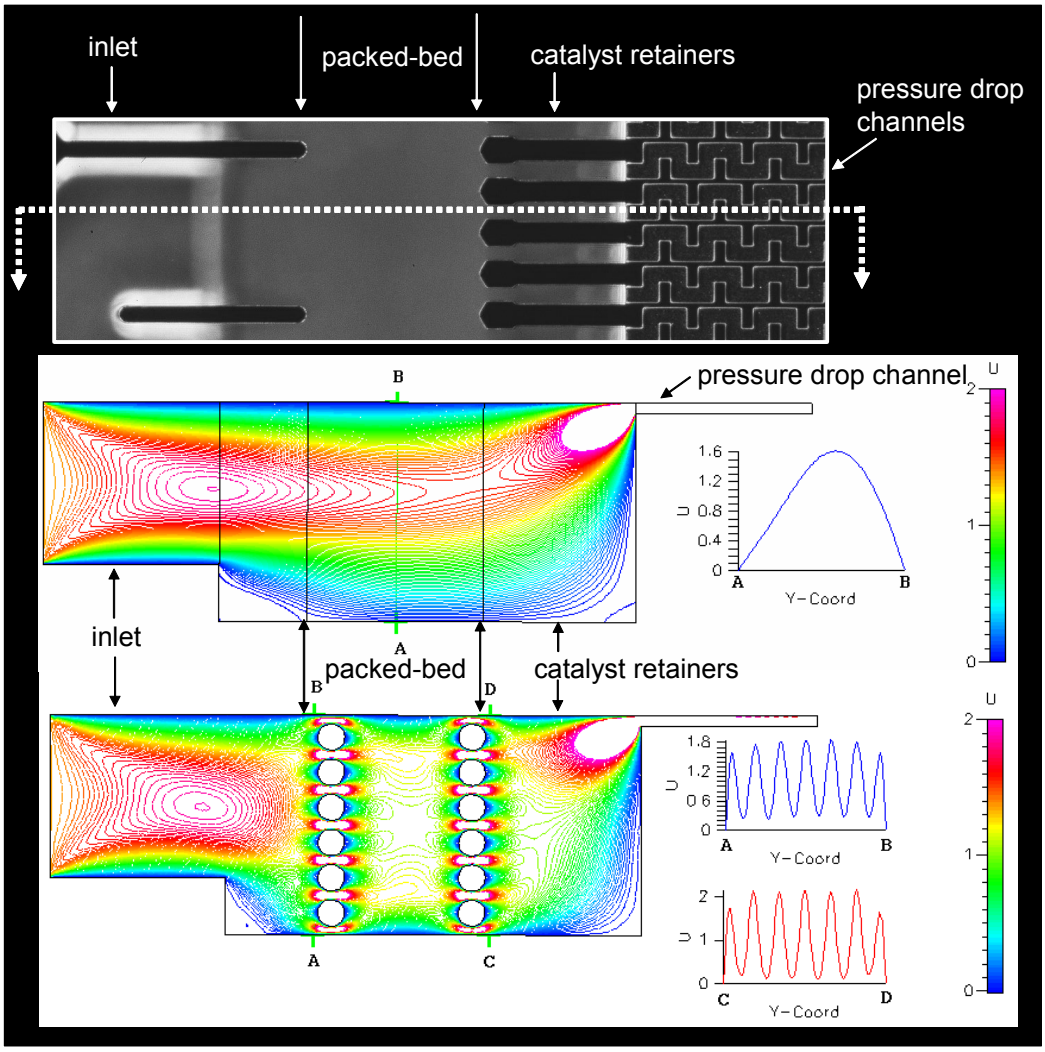


**Figure 4-11.** 2-D CFD model showing velocity profiles, U, (m/s) of a reactor cross-section with air at 1 m/s and 373K. (top) Top-view of microreactor section used in the model. The dashed line shows the cross section taken for the simulation and is the same as that shown in Figure 3-5. (middle) Flow through an empty reactor. (bottom) Flow through a reactor with 2 layers of 50 µm "particles" at the beginning and end of the packed-bed region. The velocity profile evens out after 2 layers (section C-D). The white region near the pressure drop channels are high velocity areas that are off the 0-2 m/s scale.

When the calculations are repeated for a case where the reactor has one layer of particles placed at the beginning and one at the end of the packed-bed, the flow profile changes considerably. The previously uneven velocity profile flattens out across the depth of the reactor (section C-D). The recirculation zones are considerably smaller (approximately 50-100 μm) than in the empty reactor and are away from the packed-bed region.

The simulation was redone using air flow at an average velocity of 1 m/s at 373K for a reactor filled with 8 layers of 2-D circular "particles" using a finite element calculation (*FEMLAB, Comsol, Inc.)*. The convective velocity field was calculated for the entire reactor cross-section and the velocity profile at a section in the center of the packed-bed is shown in Fig. 4-12. The parabolic velocity profile that was seen in the empty reactor is replaced by an even distribution of fluid across the reactor depth.

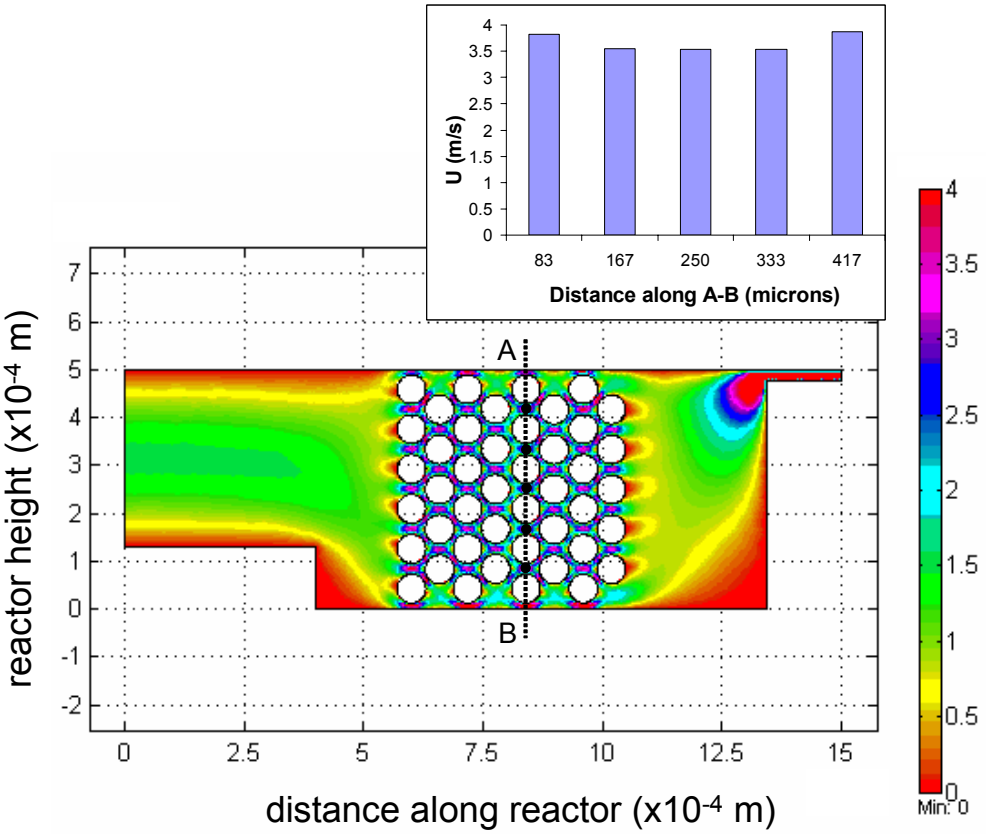


**Figure 4-12.** 2-D finite element model of the flow, U (m/s), through a reactor packed with 60 μm "particles" with air flow at 1 m/s and 373K. The particles serve to flatten the parabolic laminar profile that would occur in an empty reactor as seen in the velocity profile along section A-B. The velocities shown in the graph are the peak velocities in the space between the particles represented by the black dots.

The velocity profile for section A-B shows that the peak velocities between each particle (indicated by the black dots in Fig. 4-12) are slightly higher at the wall because of the higher porosity. This effect would be diminished with increasing particle loading as in a real 3D reactor. The peak velocities for the inner particles are quite flat. Further, the sizes of the recirculation zones created by the different channel depths are on the order of a single

particle diameter and are not directly inside the packed-bed region. If the flow is evenly distributed for this situation, it will be even more uniform in a 3-D randomly packed multiple particle bed.

### 4.5.1 Enhancing Effect of Diffusion

Since turbulent mixing is not present in laminar flow reactors, it is important to analyze the mixing properties of the microreactor. At the microreactor length scale, diffusion is the predominant form of lateral mass transport. An examination of the characteristic time of diffusion [6] should give insight to the relevance of the stagnant volumes seen in Figure 4-12. The characteristic diffusion time is given below in Equation 4-1,

$$\tau = \frac{L^2}{D} \tag{4-1}$$

where $L$ is the relevant length scale, $D$ is the diffusivity.

The characteristic diffusion time for a typical gas across 60 μm is calculated to be less than 0.02 ms while the residence time in the packed bed for the CFD and FEM simulations (typical of normal microreactor operation as seen in Chapter 5) is approximately 0.4 ms. At this length scale, diffusion is sufficiently fast to counter the trapping effects of any stagnant volume, preventing the flow profile from negatively effecting reactor operation. In the next chapter, more details on the effects of diffusion on cross-flow microreactor performance are

discussed, particularly in reducing gradients and expanding the window of operation for obtaining differential kinetics. In conclusion, the models and experiments indicate that a microreactor packed completely with spherical catalyst particles will have an even distribution of flow across the entire reactor width and depth with minimal effects from recirculation zones, rendering a desirable device for the characterization of catalytic reaction kinetics.

## 4.6 Summary

The cross-flow microreactor has been characterized through a combination of experiments and modeling to better understand the flow through the reactor and the functionality of the pressure drop channels. Pressure drop experiments confirmed the design of the pressure drop channels in creating a back pressure on the packed-bed. This back pressure diminishes the effect of variations in catalyst packing on the overall flow distribution in the microreactor, providing even flow across the wide packed-bed. Flow visualization experiments illustrated clearly the strong influence the pressure drop channels have on the flow in the microreactor. The pressure drop channels enable the cross-flow packed-bed reactor design and their proper fabrication is paramount in achieving a functioning device. This is why microfabrication is such an attractive technology for producing these types of devices, where a high level of reproducibility and uniformity can be achieved in the production of features on the sub-millimeter level. Finally, flow across the depth of the reactor was examined through modeling. The presence of particles strongly influences flow through the reactor, and serves to even out the velocity profile across the

channel depth. By providing even flow across the reactor width and depth and eliminating concerns of particle loading, the cross-flow reactor creates a desirable environment for catalyst testing. In the next chapter, kinetic studies are detailed using model chemistries and the reactor's ability for eliminating gradients and extracting accurate kinetics is further explored.

## Literature Cited


[1] M.W. Losey, M.A. Schmidt, K.F. Jensen, "Microfabricated Multiphase Packed-Bed Reactors: Characterization of Mass Transfer and Reactions," *Ind. Eng. Chem. Res.* **40** (2001) 2555-2562.

[2] M.W. Losey, "Novel Multiphase Chemical Reaction Systems Enabled by Microfabrication Technology," Thesis, M.I.T., Cambridge, MA, 2001, pp. 77-93.

[3] T.S. Harrison, "Packaging of the MIT Microengine," Thesis, Massachusetts Institute of Technology, Cambridge, 2000.

[4] H.S. Fogler, in: "Elements of Chemical Reaction Engineering," Prentice-Hall Inc., Upper Saddle River, NJ, 1999, pp. 738.

[5] R.B. Bird, W.E. Stewart, E.N. Lightfoot, in: "Transport Phenomena," Wiley, New York, 1960, pp. 200.

[6] W.M. Deen, in: "Analysis of Tranport Phenomena," Oxford University Press, New York, 1998, pp. 89.

# Chapter 5
# Kinetic Studies and Reactor Analysis

---

This chapter details kinetic studies using different model chemistry with the cross-flow microreactor. The performance of the reactor is analyzed with respect to obtaining accurate information such as activity, activation energy, and reaction order. Using these real reaction results, a detailed analysis is presented quantifying the reactor's ability to reduce unwanted gradients. Simulations are shown which expand on the effect of diffusion on reactor performance and the ability of the reactor to achieve differential operation. Finally, comparisons are made between the performance of the microreactor and macroscale reactors highlighting the advantages of using microfabricated chemical systems for catalyst testing.

## 5.1 CO Oxidation as a Model Chemistry

To validate the cross-flow microreactor as a tool for obtaining chemical kinetics, it is necessary to examine the performance of the reactor under real reaction conditions. One criterion for the selection of an appropriate model chemistry is that a moderately fast reaction such as an oxidation is desirable where larger, more practical flow rates can be used. Further, a system without side reactions and with easily detected reactants and products is important for initial reactor testing. CO oxidation was chosen because it is a well-studied reaction due to its importance in automotive catalytic converters and the observed kinetics are well understood, particularly in the "CO inhibiting regime" [1, 2].

$$CO + \frac{1}{2} O_2 \rightarrow CO_2 \qquad \Delta H = -283\, kJ/mol \tag{5-1}$$

A Langmuir-Hinshelwood mechanism is most often used to describe CO oxidation kinetics [3].

$$Rate = \frac{k \cdot C_{CO} \cdot C_{O_2}}{(1 + K \cdot C_{CO})^2} \tag{5-2}$$

For conditions where the $CO:O_2$ concentration ratio is greater than ~0.08, CO oxidation occurs in the CO inhibiting regime with CO dominating the surface coverage of the

catalyst due to its large sticking coefficient on metal catalyst surfaces [1, 4]. Due to this large sticking coefficient, the $K \cdot C_{CO}$ term in the denominator is large, reducing Eq. 5-2 to

$$Rate = \frac{k_1 \cdot C_{O_2}}{C_{CO}} \tag{5-3}$$

where $k_1 = k/K^2$ is the observable rate constant obtained from kinetic experiments. In this regime, the reaction rate is governed by the desorption rate of CO from the catalyst surface and therefore is approximately positive first order in $O_2$ concentration and approximately negative first order in CO concentration as described by Eq. 5-3. The microreactor experiments detailed later in this chapter were performed in the CO inhibiting regime. Oscillatory behavior corresponding to changes in the catalyst surface coverage has been reported at $P_{O2}$:$P_{CO}$ ratios higher than 25 for CO oxidation on Pt at atmospheric pressures [5]. This concentration ratio is approached at CO conversions of 98% or higher for the 1% CO, 1% $O_2$ feed used in the oxidation experiments described later in this chapter. Since only differential conversions of 10% or less were used for obtaining kinetic data, this oscillatory regime was avoided.

The reaction proceeds on a variety of supported metal catalysts such as Pd, Rh, and Pt supported on alumina catalysts and has been found to be structure insensitive at atmospheric pressures and near stoichiometric feeds [1, 6, 7], although Zafaris and Gorte [8] have reported some evidence of structure sensitivity for Pt. Structure insensitivity is important as it allows the comparison of the microreactor results directly to literature. The reaction also

proceeds measurably at temperatures compatible with the packaging scheme detailed in the previous chapter.

## 5.2 Experimental

The packaged microreactor is integrated into a catalyst testing station as shown in Figure 5-1. The reactor is placed in parallel to a bypass line and a pressure gauge is placed directly before the reactor inlet. A needle valve, placed directly after the reactor, acts as a manually tunable back pressure regulator. This is necessary because of the cross-flow reactor geometry. Since the pressure drop channels are placed after the packed-bed, the absolute pressure in the catalyst bed changes with flow rate. To ensure that data from a given experiment involving multiple flow rates are taken at the same pressure, the reactor pressure is held at the pressure corresponding to the largest flow rate by adjusting the needle valve. The down side is this sets a lower limit for pressure during experimentation as the pressure can never be lower than that produced by the largest flow rate. However, in typical kinetic experiments, it is more important to know that the catalyst bed is isobaric, as is the case with the cross-flow reactor.

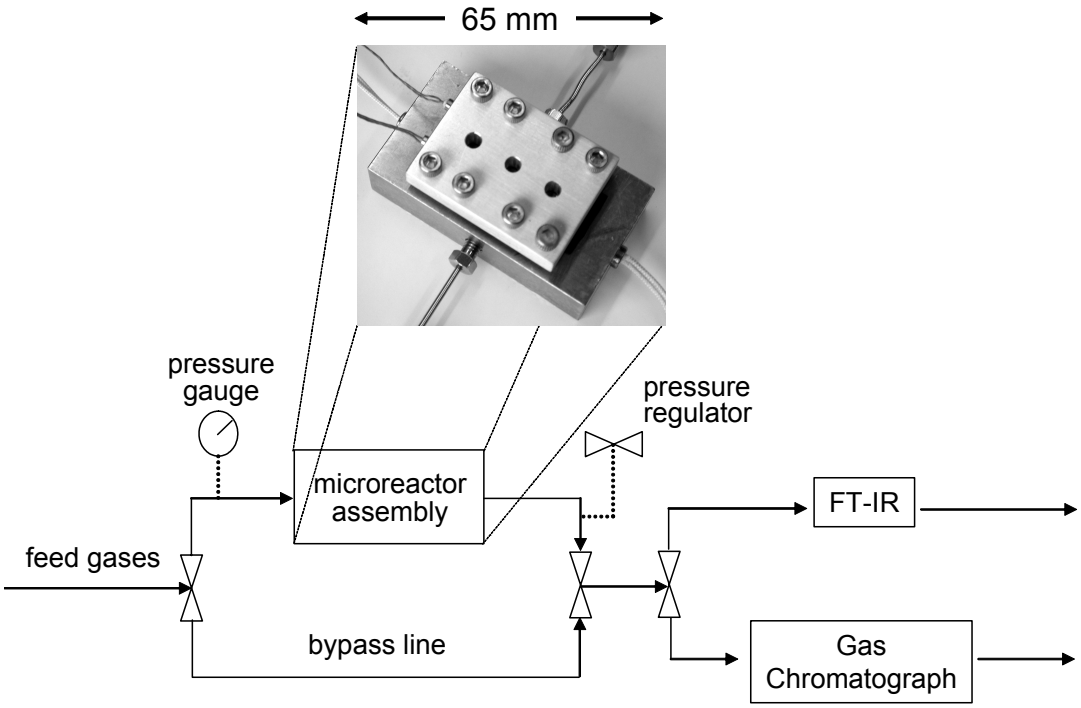


**Figure 5-1.** Catalyst testing setup: The reactor is compressed against a gasket with an aluminum top plate to form fluidic connections to a stainless-steel base that is integrated into a catalyst test station.

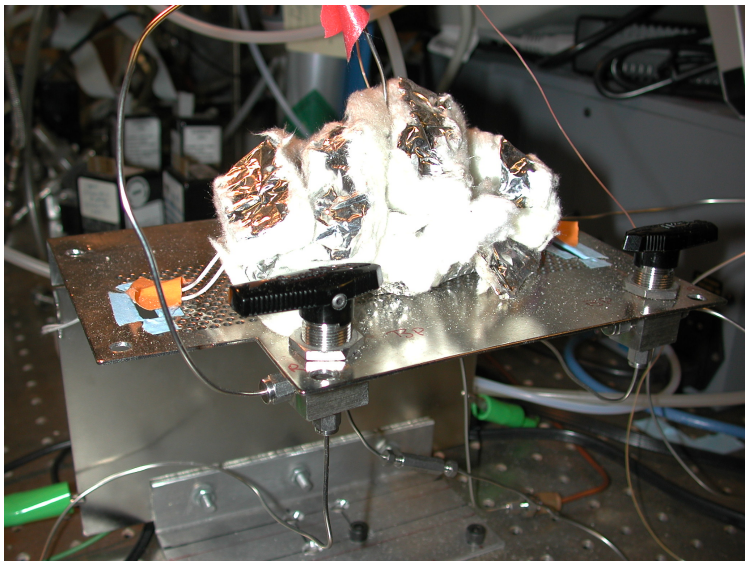

**Figure 5-2.** Photograph of the fully integrated catalyst testing unit. The packaged microreactor is covered with insulation to isolate the hot components.

Chemical detection was performed by either a micro gas chromatograph (μGC) with a thermal conductivity detector and a Mol Sieve 5Å column (*Agilent Technologies,* G2890A) or an FT-IR spectrometer (*Analect*) with a 100 $cm^3$ volume gas flow cell with sodium chloride windows (*Spectra-tech Inc.,* 1.5 mm thickness). The μGC was confirmed to be linear with concentration for both CO and $O_2$ at the concentrations used in the kinetic experiments described later in this chapter. Further, the μGC is unaffected by pressure or flow rate at the sample inlet as the internal sample injector is designed to equilibrate the pressure of the sample before injection into the column. However, the IR absorption response was non-linear with both flow rate (pressure) and concentration. Therefore, calibration curves were taken before the kinetic experiments to account for these variables during data analysis. The advantage of the IR is that it gives real-time feedback on the reaction, which is particularly useful at the lowest flow rates where significant lag time can exist.

The microreactor was loaded with approximately 3 mg of alumina supported metal catalyst (1 wt.% Rh, Pt- *Alpha Aesar,* 0.3 wt.% Pd- *Institut Français du Pétrole*) sieved between 53-71 μm and loaded with a vacuum in air. This corresponds roughly to 26,000 to 29,000 particles in the reactor channel. Available metal surface area for the rhodium and platinum catalysts was estimated using CO adsorption at 313.15K (*Micromeritics Instrument Co.)* and found to have dispersions of 2.9% and 23% respectively. The palladium catalyst was reported to have 35% metal dispersion by the supplier. The reactor was run vertically with downward flow in order to prevent fluidization of the particles.

### 5.2.1 Microscale vs. Macroscale Chemical Analysis

During the course of the experiments detailed in the next section, a variety of methods were employed for analysis of the reactants and products. A macroscale GC/mass spectrometer was initially used to analyze the reaction. The unit is rather large and bulky and significantly limits the flexibility that is gained by using microreactors. Further, difficulties arise in eliminating the volume of tubing required to connect the reactor to the large unit due to normal laboratory space constraints, resulting in a significant increase in lag time. Since the microreactor employs only a few milligrams of catalyst, the flow rates needed to sustain measurable reaction are quite small. At these small flow rates, a large lag time can eliminate most of the efficiency gained from using a microreactor. The use of the μGC significantly improved the data gathering process. Due to its small footprint, the unit is able to be placed in immediate proximity to the microreactor, and due to technological advancements achieved using microtechnology, the μGC is able to reduce a 15 minute analysis down to 90 seconds. The main conclusion that can be drawn from this experience is that for the development of future high-throughput catalyst testing platforms, the development of micro chemical detection will be imperative. As the paradigm shifts from running one microreactor as presented in this body of work to running multiple reactors, macroscale chemical detection will become a significant rate limiting step. In this high-throughput situation, smaller and faster chemical detection that can be directly integrated to the microreactor will be necessary.

## 5.3 CO Oxidation in the Cross-Flow Reactor

Before each experimental run, the catalyst was pretreated *in-situ* at 523 K for 1 hour with oxygen flow followed by 1 hour under hydrogen. A premixed tank of high purity 1%CO/1%$O_2$ in helium (*BOC Gases)* at flow rates between 20 and 600 sccm was used for the reactant feed. Helium was chosen over $N_2$ as the bath gas because He is the carrier gas in the μGC. Reaction order experiments were performed by blending the premixed feed with a second 1%CO or 1%$O_2$ in He mixture in the appropriate quantities. All experimental kinetics reported with the microreactor were performed in the differential regime for steady-state CO conversions of ~10% or less. Steady-state was typically obtained in under a minute. Temperatures up to 546K were used and the reactor assembly was heated without external cooling. The absolute pressure at the exit of the reactor was atmospheric. The pressure drop in the catalyst bed ranged between 0.002-0.15 atm depending on the flow rate. The catalyst bed was considered isobaric at these pressure drops. The pressure in the catalyst bed was adjusted between 1.0-2.5 atm and was held constant for a given set of data. The Reynolds number based on catalyst particle diameter ranged from 0.0051 to 0.153.

### 5.3.1 Kinetic Study

As expected, no temperature increase was detected upon switching flow from the bypass line to the reactor due to the ability of silicon to readily dissipate heat. The thermal mass of the stainless-steel packaging is also many orders of magnitude larger than the reactor and provides a significant heat-sink. Likewise, the energy provided by the cartridge heaters

to maintain the temperature of the reactor/packaging is significantly larger than the energy generated from the heat of reaction. This gives fine temperature control over the exothermic reaction.

Turnover frequency (TOF, molecules of product formed per catalyst site per second), apparent activation energy, and reaction orders for CO oxidation were determined experimentally. The use of TOF normalizes the differences in surface area between catalyst samples making it possible to compare experiments with different amounts of catalyst. Fig. 5-3 shows the experimental TOF for the 0.3 wt.% $Pd/Al_2O_3$ catalyst with 1%CO/1%$O_2$ reactant feed at 1.3 atm compared to previously published values by Rainer et al. [6] for 0.1 wt.% $Pd/Al_2O_3$. The original results by Rainer et al. were obtained for a 0.58% CO and 0.3% $O_2$ feed at atmospheric pressure. For proper comparison to our reaction conditions, their data shown in Fig. 5-3 were scaled appropriately to 1% using reaction orders of -0.78 for CO and +0.84 for $O_2$ as published. Both the TOF and the apparent activation energy (30.1 kcal/mol) agree well with the previously reported values. The error bars in all the plots in this chapter were calculated based on estimated equipment error including the flow controllers, mass balance (catalyst weight), and surface area measurement.

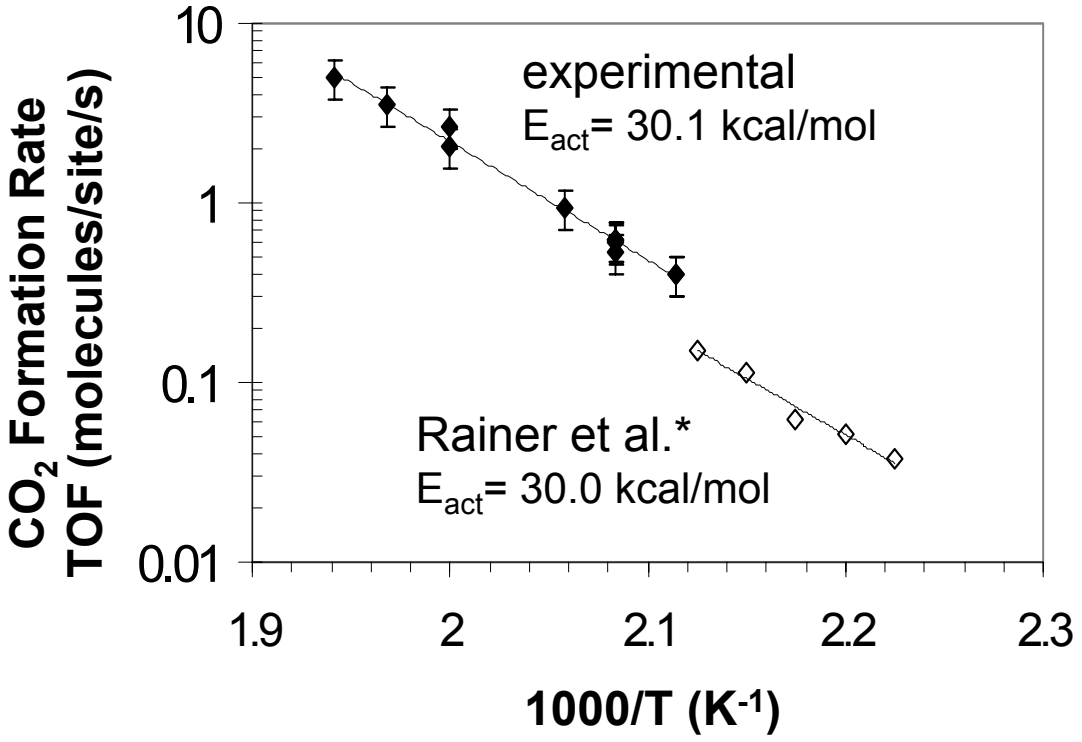


**Figure 5-3.** Experimental turnover frequency (TOF) for CO oxidation over 0.3 wt.% $Pd/Al_2O_3$ with 1%CO/1%$O_2$ feed. The results agree well with those of *Rainer et al. [6] taken for CO oxidation over 0.1 wt.% $Pd/Al_2O_3$. The data published by Rainer et al. was originally taken with a 0.58%CO/0.3%$O_2$ feed, and has been scaled to 1% in this figure using their published reaction orders.

Similar agreement with literature was also seen for the 1 wt.% $Pt/Al_2O_3$ and 1 wt.% $Rh/Al_2O_3$ catalysts. Figure 5-4, shown below, gives the TOF for the palladium, rhodium, and platinum catalysts with CO oxidation performed over the same temperature range. The results clearly show a unique activity (TOF) and activation energy (slope) for all three catalysts.

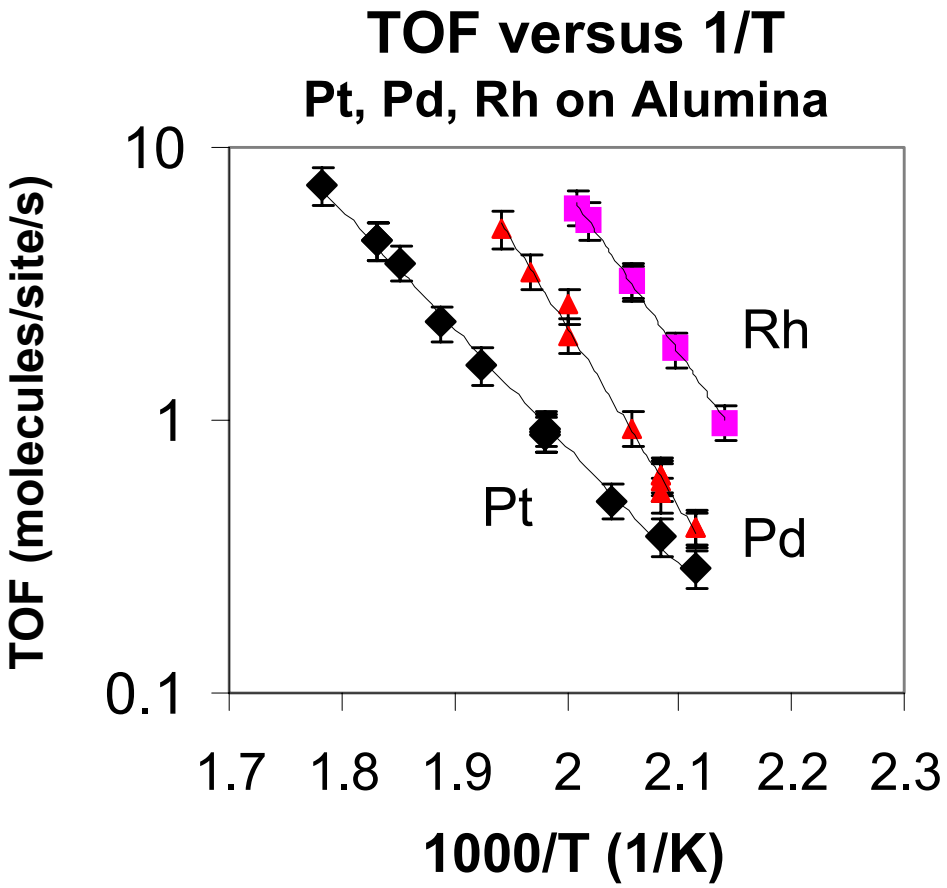


**Figure 5-4.** TOF vs. 1/T for CO oxidation over 1 wt.% $Pt/Al_2O_3$, 1 wt.% $Rh/Al_2O_3$, and 0.3% $Pd/Al_2O_3$ catalysts

Table 5-1 summarizes the activation energies obtained with the microreactor for the experiments shown above compared with previously published values [3, 6, 7, 9] determined under reaction conditions similar to the microreactor experiments.

**Table 5-1**

**Apparent activation energy for CO oxidation over different catalysts in the microreactor compared to literature values**

| Catalyst | Microreactor $E_{act}$ (kcal/mol) | Literature $E_{act}$ (kcal/mol) | Literature Reference |
|---|---|---|---|
| 0.3 wt.% $Pd/Al_2O_3$ | 30.1 | 30.0 | [6] |
| 1 wt.% $Pt/Al_2O_3$ | 20.0 | 21.6 | [3] |
| 1 wt.%$Rh/Al_2O_3$ | 27.6 | 24-31 | [7,9] |

The activation energies shown above agree well with literature values. Further, the relative activity of all three catalysts seen in Fig. 5-4, Rd > Pd > Pt, agrees with other high-throughput and single-crystalline surface experiments performed in literature [10-12]. This ability of the cross-flow microreactor to extract accurate kinetic information and clearly distinguish the performance of different catalyst samples for the same chemistry demonstrates its utility as a catalyst testing tool.

### 5.3.2 Mechanistic Study

During quantitative characterization involved with catalyst testing and during detailed research on new catalytic processes, more information is desired than just activity and activation energy. For example, it is important to understand the reaction mechanism to isolate the rate determining step. The cross-flow microreactor is designed to be a fully functional chemical reactor and not just a simple screening platform. Thus, the same types of information generated in a macroscale tube reactor are also obtainable in the microreactor.

To demonstrate the ability to study a reaction mechanism, the CO oxidation study was extended to examine reaction orders for both CO and $O_2$. Fig. 5-5 shows the dependence of TOF on both CO and $O_2$ partial pressures at 505 and 540 K with the 1 wt.% $Pt/Al_2O_3$ catalyst.

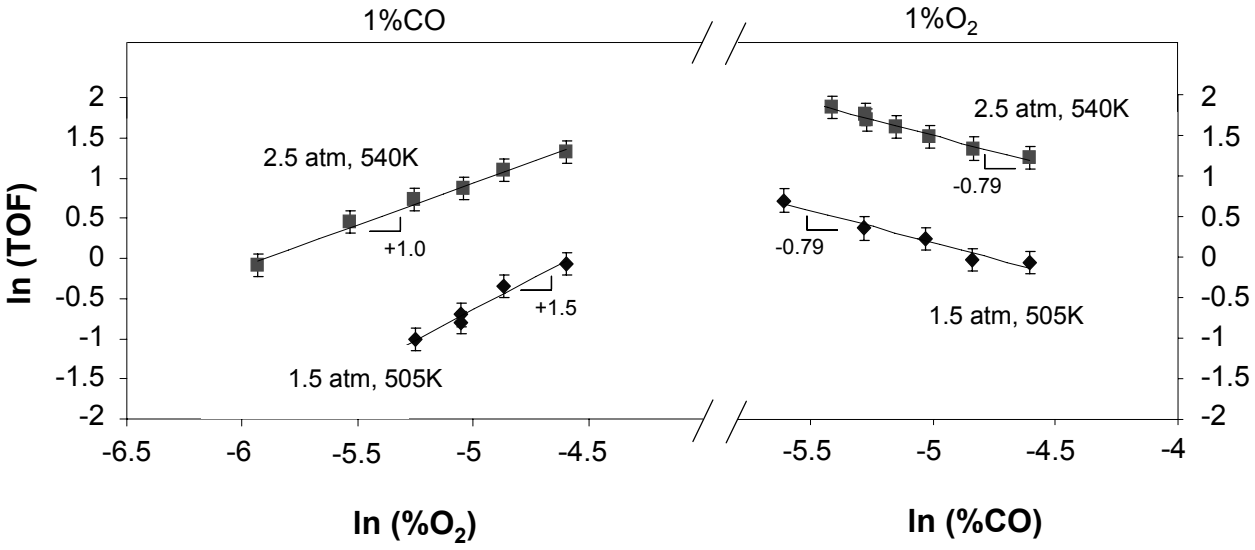


**Figure 5-5.** Reaction order for $O_2$ and CO at 505K and 540K for CO oxidation over 1 wt.% $Pt/Al_2O_3$ obtained at differential conversions. The negative order of CO and positive order of $O_2$ expected from proposed reaction mechanisms are clearly observed.

The experimental results shown above clearly show the positive dependence on $O_2$ and the negative dependence on CO predicted by proposed reaction mechanisms given in Eqs. 5-2 and 5-3. The experimental reaction orders of –0.78 for CO and +1.0 to +1.5 for $O_2$ also agree with the respective orders of $-0.6 \pm 0.3$ and $+1.3 \pm 0.3$ obtained by Zafaris and Gorte [8] at 650 K. The ability to obtain mechanistic information such as reaction order is important to fully characterize and understand a catalytic process, and is often the most

difficult type of information to obtain in high-throughput reactor systems. The consistency of the data with different catalysts and the ability to extract specific kinetic information such as reaction order illustrates the potential of the cross-flow microreactor as a robust tool for catalyst testing.

## 5.4 Selective Acetylene Hydrogenation- Kinetic Study

A second chemistry, the selective hydrogenation of acetylene (ethyne), was chosen for additional study. The particular reactions of interest are exothermic as given below and are important in the manufacture of polymer grade ethene. During the manufacture of high grade ethene, acetylene, which is present in low percentages (~1%) in the hydrocarbon mixtures obtained from cracking plants, must be removed from the complex gas mixture. The most widely used method for ethyne removal is via catalytic hydrogenation. However, this process must be selective as high losses from the hydrogenation of ethene otherwise make the process economically unviable. Palladium based catalysts have been shown to be able to perform these reactions economically [13].

$$C_2H_2 + H_2 \rightarrow C_2H_4 \qquad \Delta H_{298K} = -172\,kJ/mol \tag{5-4}$$

$$C_2H_4 + H_2 \rightarrow C_2H_6 \qquad \Delta H_{298K} = -137\,kJ/mol \tag{5-5}$$

Using the same experimental setup that was described for the CO oxidation experiments in Section 5.2, the hydrogenation was carried out in the cross-flow microreactor over 1.3 mg of the 0.3 wt.% Pd on alumina catalyst. A pre-mixed gaseous mixture of 1.8% $C_2H_2$, 3.06% $H_2$, and 9.5% $N_2$ in an ethylene bath gas was fed into the reactor at temperatures ranging between 27-110 $^oC$. The pressure was held constant at 2 atm and the flow rates were varied between 10 and 310 sccm giving particle Reynolds numbers ranging between 0.08 and 2.6. On-line analysis was performed by the μGC using a PLOT column (*Agilent Technologies,* PoraPlot U, 6M, 0.32mm). Steady-state conversions were held to less than 10% and the differential approximation was applied during data analysis. The figure below shows the results obtained for TOF (rate of ethyne consumption) and activation energy for these experiments.

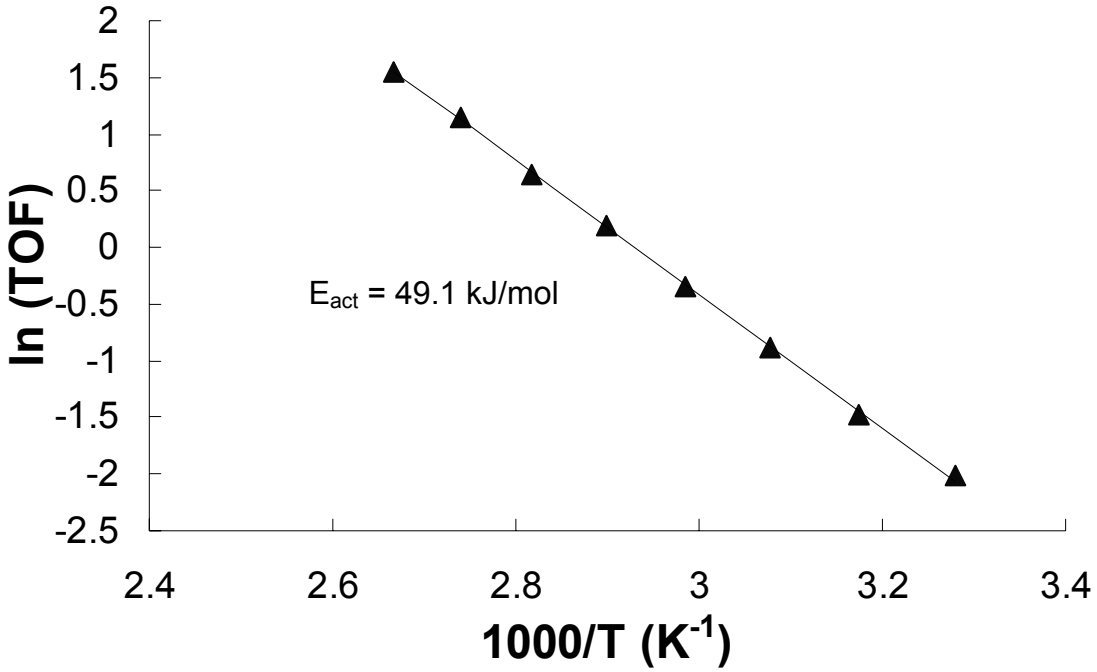


**Figure 5-6.** Selective acetylene hydrogenation on 0.3% (wt%) $Pd/Al_2O_3$

With an $R^2$ value (from linear regression) of 0.9996, the results show a strongly Arrhenius response. The activation energy of 49.1 kJ/mol matches excellently with the 50 ± 4 kJ/mol reported by Kho and Gva [14] under similar conditions. The good agreement with literature for acetylene hydrogenation demonstrates the ability of the microreactor to generate good kinetic data for chemistries more complex than CO oxidation. Further, the selectivity between the products, ethene and ethane indicated in the Reactions 5-4 and 5-5, were studied. Figure 5-7, given below, shows the results of these experiments. Selectivity is defined as the ratio of the production rate of the desired species (i.e., ethane or ethene) to the consumption rate of ethyne.

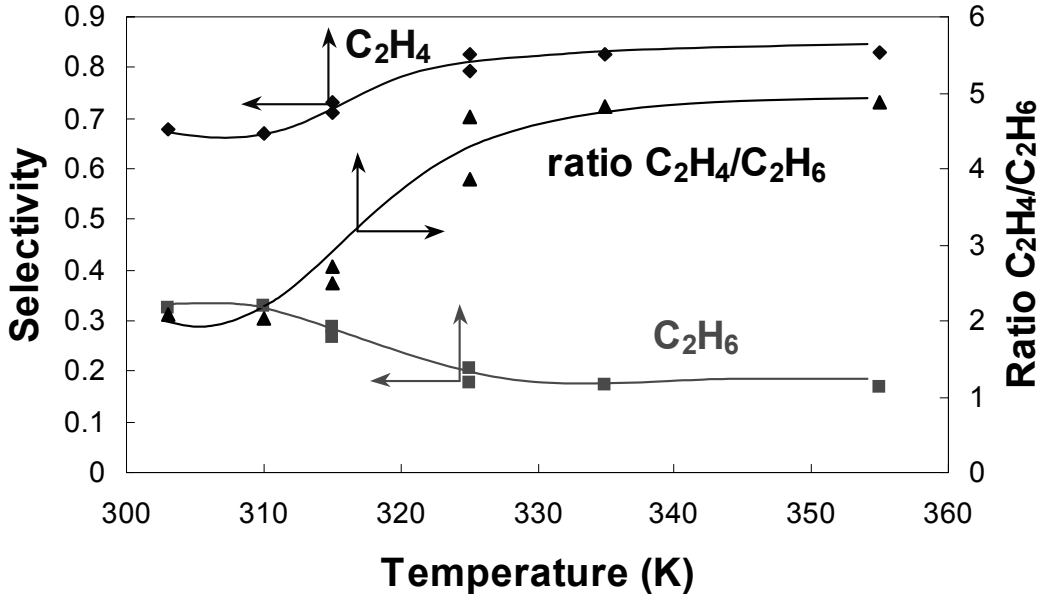


**Figure 5-7.** Selectivity study for selective acetylene hydrogenation on 0.3% (wt%) $Pd/Al_2O_3$ between ethene and ethane products. The ratio of ethene to ethane increases with increasing temperature consistent with published results. The arrows indicate the relevant Y-axis.

The selectivity trends indicate that ethene is increasingly favored over ethane at increasing temperatures, consistent with previously published results. This study with acetylene hydrogenation demonstrates the breadth of data achievable with the cross-flow microreactor, and indicates that the reactor is useful for chemistries significantly more complex than CO oxidation.

### 5.4.1 Deactivation Study

One important aspect during the quantitative catalyst testing phase is the detailed study of deactivation and poisoning. The cross-flow microreactor, unlike some other microscale systems for catalyst screening described in Chapter 1, utilizes catalyst particles for catalytic studies. Therefore, phenomena such as deactivation and catalyst poisoning that are seen in macroscale reactors should also be present with the cross-flow reactor. As a first step to demonstrate the cross-flow reactor as a viable tool for studying kinetics *and* deactivation, deactivation was briefly examined for acetylene hydrogenation.

Besides the main hydrogenation reactions, oligomerisation can also occur during acetylene hydrogenation yielding a complex mixture of $C_4^+$ compounds known as "green oil" that deactivate the catalyst as well as reduce selectivity [13]. Figure 5-8 shows the onset of this oligomerisation process in the cross-flow reactor at higher temperatures, resulting in a loss of activity.

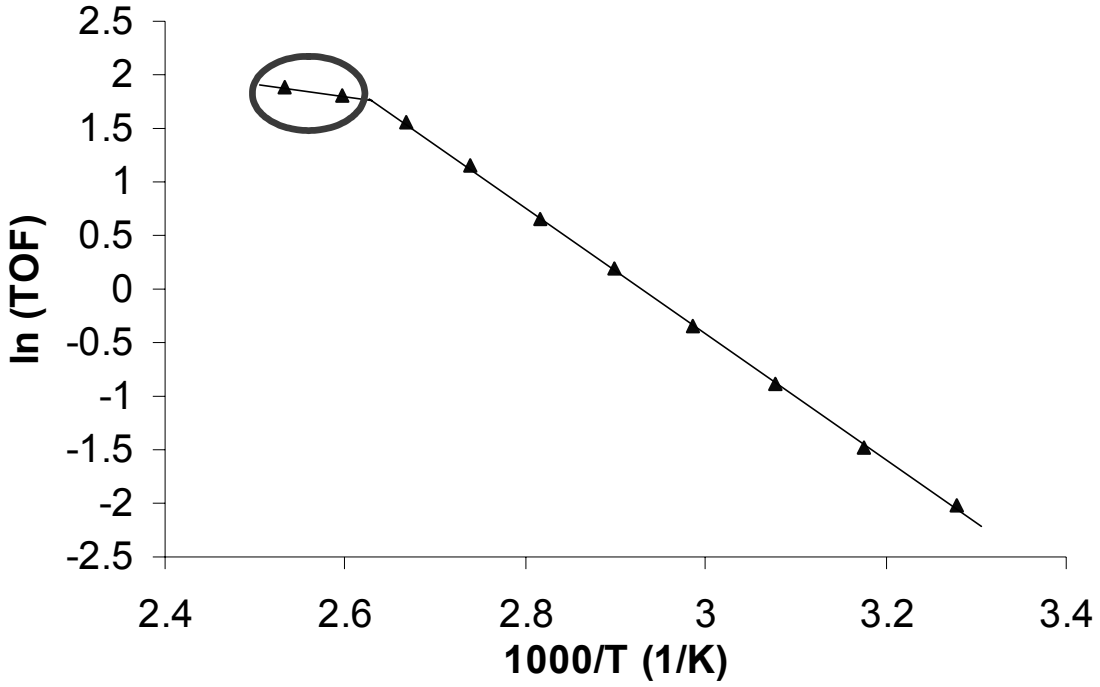


**Figure 5-8.** Acetylene hydrogenation over palladium on alumina catalyst. Onset of oligomerisation at higher temperatures that results in deactivation

This oligomerisation process is primarily time dependent, rather than temperature dependent, at the temperatures studied in Figure 5-8. The results appear to be temperature dependent simply because the experiment was begun at the low temperatures and ramped up. The onset of the oligomerisation coincided with the high temperature measurements. This apparent deactivation was studied further by examining the loss of reaction rate (measured as TOF) as a function of time at a fixed temperature. Figure 5-9 shows a deactivation curve gathered at 395 K.

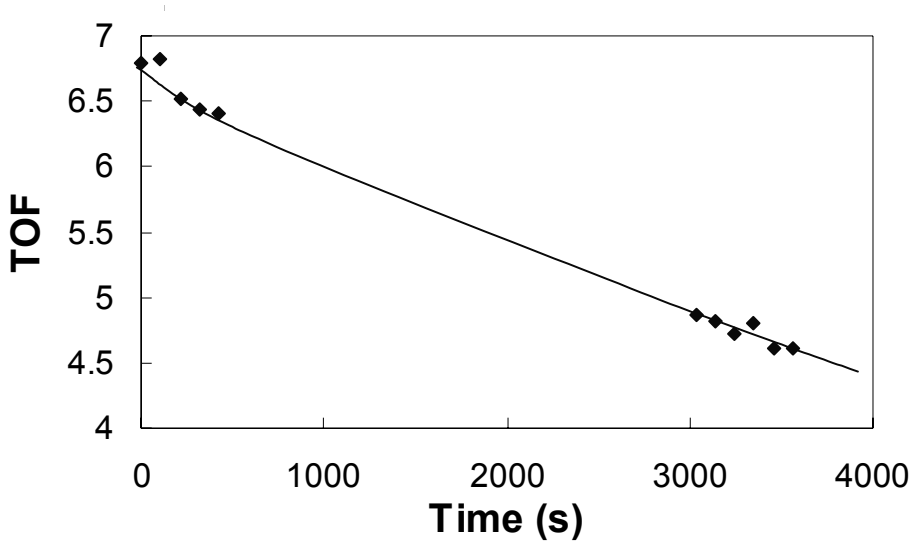


**Figure 5-9.** Deactivation curve at 395K of acetylene hydrogenation indicating the loss of reaction rate as a function of time.

It was confirmed that the deactivation was not a result of mass transfer limitations, but rather, the result of deposition of longer chain hydrocarbons because upon repeating the experiments at the lower temperatures without post-treatment of the catalyst, the catalyst was deactivated over the entire data range. Further, upon treating the catalyst for 1 hour under pure oxygen flow at 280$^{o}$C to remove all the carbonaceous compounds and then reducing under pure hydrogen for 1 hour at the same temperature, the activities seen in Figure 5-6 were returned. This reversibility implies that the oligomerisation side reactions were taking place as suggested in literature. This brief demonstration shows that the cross-flow reactor is a potential tool for the quantitative characterization of both kinetics and selectivity for a variety of reactions, as well as for deactivation studies. This is emphasized in the next section in which an analysis of heat and mass transport is detailed. As will be shown, the

cross-flow reactor decreases mass and thermal gradients in the reactor. Therefore, in the case just presented showing a decrease in activity, the researcher would have an easier time concluding that the drop in activity was due to deactivation and not a result of mass transfer limitations. By eliminating concerns about gradients, the cross-flow reactor brings more efficiency and certainty to experimental data analysis.

## 5.5 Examination of Transport Limitations Using CO Oxidation

It is desirable to quantitatively understand the advantages of the microreactor for reducing thermal and mass gradients during catalyst testing. This can be done by examining different transport phenomena in the reactor under real reaction conditions using representative criteria found in literature. The Weisz Modulus, $M_W$, given in Eq. 5-6, gives an indication of the internal diffusion limitations within a catalyst particle [15]. A small $M_W$ indicates that mass transport within the catalyst particle is fast enough to prevent gradients from forming implying that TOF is the same throughout the catalyst particle.

$$M_W = \frac{R_{rxn}\, r_p^{\,2}}{D_{eff} C_s} \tag{5-6}$$

$D_{eff}$, the effective diffusion coefficient, can be estimated from the porosity ($\varepsilon_p$) and tortuosity ($\tau$) of the catalyst particle as given below in Eq. 5-7.

$$D_{eff} = \frac{\varepsilon_p}{\tau} D_i \tag{5-7}$$

Using the fastest reaction rate observed (TOF~10), an estimated bed void fraction of 0.40, a typical particle void fraction of 0.5, and an estimated upper bound on particle tortuosity of 7.5, $M_W$ is approximately 0.01. The small Weisz modulus, even for the high estimate of tortuosity, indicates the catalyst particles are small enough to prevent concentration gradients from forming internally.

Anderson [16] proposed a criterion (Eq. 5-8) for assuring the observed reaction rate does not differ from the actual reaction rate within a catalyst particle by more than 5% due to intraparticle temperature gradients.

$$\frac{|\Delta H| R_{rxn} r_p^2 E_{act}}{k_p T_s (RT)} < 0.75 \tag{5-8}$$

The catalyst particles are considered isothermal as the left hand side of the inequality is ~0.01 using experimental data and an estimate of 0.1 W/(m·K) for the thermal conductivity of porous alumina. In both criteria above, mass and heat transport are inversely related to the square of particle size as the particle radius appears squared in both equations. The small particles used in the microreactor intrinsically help eliminate internal transport limitations. The advantages of using the microreactor over macroscale reactors with small particles lies in the ability to control reactor geometry and improve heat transfer as will be discussed in Section 5.7.

External transport effects are more difficult to estimate due to the lack of literature data for heat and mass transfer coefficients at low Peclet numbers. Correlations for the Sherwood and Nusselt numbers at low Peclet numbers are not well understood in the flow regimes seen in the microreactor and their applicability is unclear [17, 18]. The next chapter expands on this issue with a detailed discussion about the applicability of correlations found in literature developed with boundary layer theory and the validity of the analysis presented in the next paragraph for estimating external heat and mass transfer effects.

The reactor Peclet number, $Pe_r$, ranges between 0.1 and 1.0 for the oxidation experiments presented in the earlier sections. At these flow rates, diffusion plays a significant role in mixing and transport in the reactor and dominates over convection at the lower range of flow rates. In the limiting case of mass transfer, where Reynolds number approaches zero, diffusion is the only form of transport to the catalyst surface. An order of magnitude analysis of the transport around a catalyst particle can be made by examining the gradients needed to maintain the flux of molecules and energy corresponding to the reaction rates observed in the oxidation experiments. Since the kinetic data were taken differentially, the flux of reactants to each particle is approximately the same. By assuming a worst case scenario that the center of each particle is 2 particle diameters away from its closest neighbor (i.e., a "shell" with a radius of a particle diameter surrounds each particle as illustrated in Figure 5-10), a Fick's law analysis can be made to calculate the concentration gradient between the catalyst surface and the bulk fluid.

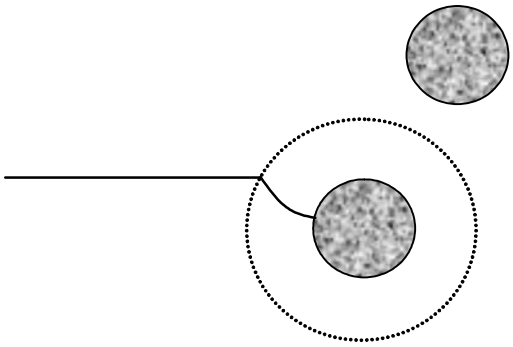

**Figure 5-10.** Illustration of hypothetical shell around a catalyst particle over which a Fick's law analysis can be made for external transport limitations.

The mass transport steady state continuity equation in spherical coordinates with constant density and diffusivity, with all convective velocity components equal to zero, and with the only variable being the radius ($r$) is given below [19].

$$0 = D_i\left(\frac{1}{r^2}\frac{\partial}{\partial r}\left(r^2\frac{\partial C_i}{\partial r}\right)\right) \tag{5-9}$$

The applicable boundary conditions are: 1) the flux of reactant into the catalyst particle is equal to the consumption of the reactant by the catalyst particle seen in the oxidation experiments (Eq. 5-10) and 2) the concentration at the shell surface is equal to the bulk concentration as given in Eq. 5-11 below.

$$BC1: -D_i \frac{\partial C_i}{\partial r} = R''_{rxn} \ at \ r = r_p \tag{5-10}$$

$$BC2: C_i = C_{bulk} \ at \ r = 2r_p \tag{5-11}$$

This gives the following expression for the concentration of species i at the surface of the catalyst, $C_{surface}$.

$$C_{surface} = C_{bulk} + \frac{R''_{rxn} r_p}{2D_i} \tag{5-12}$$

Using Equation 5-12, the concentration gradient across the shell is calculated to be approximately 0.015% of the bulk reactant concentration at the largest TOF observed in the oxidation reactions. For 1% CO at 1.3 atm total pressure, the concentration on the catalyst surface differs from the bulk by only $5 \times 10^{-5}$ mol/m$^3$ and is negligible compared to the bulk concentration of 0.3 mol/m$^3$. Furthermore, interstitial diffusion time from one particle to another (taken as 1 particle diameter) is on the same order as the residence time across a single particle, i.e. $Pe_{particle} \sim 1$. Therefore, mass transfer to the catalyst surface is not limiting and the reactant concentrations may be taken as the bulk during data analysis.

An analogous calculation to Fick's law for the thermal gradient necessary to completely remove the heat generated by reaction from the particle can be made. By employing the steady state continuity equation for heat transfer and applying analogous boundary conditions as given in Eqs. 5-10 and 5-11, an expression for the temperature profile across the shell can be written.

$$T_{surface} = T_{bulk} + \frac{Q'' r_p}{2k_b} \qquad (5\text{-}13)$$

For differential conversions as observed in the oxidation experiments, the heat generated by each particle (*Q"*) is approximately the same. The temperature at the catalyst surface calculated using Eq. 5-13 differs by only ~0.01 K from the surrounding fluid (taken 1 particle diameter away from the particle center), yielding no external temperature gradients. Again, heat transport across the particle length scale is sufficiently fast to prevent the formation of thermal gradients. Table 5-2 summarizes the calculations of transport properties in the microreactor given in this section.

**Table 5-2**

**Calculations of microreactor transport limitations for CO oxidation: Summary**

| **criterion** | | **estimation** | ***Not* transport limited if** |
|---|---|---|---|
| Internal | Mass ($M_W$) | 0.01 | <<< 1 |
| | Thermal (Anderson) | 0.01 | < 0.75 |
| External (diffusion only) | Mass | $\Delta C$= 0.015% | Close to 0 |
| | Thermal | $\Delta T$= 0.002% | Close to 0 |

The table shows that the small length scales obtainable in microfabricated reactors serve to avoid both internal and external gradients that would otherwise complicate kinetic analysis. Even though CO oxidation is a relatively simple chemistry, the reduction of

gradients indicated by the calculations in this section would still apply to more complicated systems, facilitating the extraction of useful information from the microreactor. This desirable characteristic stems primarily from the utilization of small particle sizes. The use of microfabrication technology enables the use of these small particles through controllable bed geometry and even flow distribution that would be difficult to achieve in macroscale reactors.

## 5.6 Expanded Window of Differential Operation

The small reactor dimensions and short bed length relative to the flow direction create different mixing characteristics on the reactor scale than that of a typical axial flow microreactor. In the axial flow micro packed-bed in Chapter 2, reactor Peclet numbers up to 360 were achieved for gas flow rates as low as 8 sccm. This allowed the plug-flow reactor (PFR) assumption to be valid during reactor analysis [20]. In contrast, the small cross-flow reactor Peclet numbers (0.1-1.0) seen in the oxidation experiments for flow rates as large as 600 sccm indicate that axial diffusion is extremely important and the reactor deviates significantly from plug-flow. The residence time across the cross-flow catalyst bed varied between 0.6 and 8.0 ms for the CO oxidation experiments. In comparison, the characteristic time of diffusion (Equation 4-1) across the 400 μm length of the packed-bed (assuming an empty reactor) is approximately 0.8 ms, and is within the same order as the bed residence time. Therefore, diffusion significantly effects the concentration profile along the microreactor, and hence, the reactor performance.

### 5.6.1 Reaction-Diffusion-Convection Finite Element Analysis

In order to better understand the effect of diffusion on the concentration profiles in the reactor, a 2-D reaction-diffusion-convection finite element model using the same cross-section shown in Figure 3-5 was examined for CO oxidation at various reactant conversions. The simulations were performed using a commercial finite element package (FEMLAB, *Comsol Inc.)* In order to simulate the effect of the bifurcated inlets, the inlet section in Figure 3-5 was extended upstream to include channels of appropriate length with decreasing cross-sectional area. This way, the increased convective velocity in each subsequent upstream bifurcation is captured and the extent that back diffusion effects the concentration of reactants before the packed-bed can be assessed. Both convective momentum (Navier-Stokes) and mass balances with reaction terms [21] were used in the calculations and the heterogeneous reaction was confined entirely to the surface of each catalyst particle as a flux boundary condition. Equation 5-3 was used to describe the kinetics in the simulations. As mentioned in Section 5.1, oscillatory behavior would seen at conversions approaching 98% or higher for the 1% CO, 1% $O_2$ feed used in the oxidation experiments. Therefore, flow rates for the simulations were chosen to give total conversions much lower than 98% to maintain the validity of using the mechanism represented by Eq. 5-3.

Figure 5-11a shows the calculated concentration profile for the reactor with approximately 2.75 mm of inlet channels extending up-stream of the packed-bed. Each cross-section reduction represents a point of bifurcation. The calculations were performed for CO oxidation at 540K with a feed velocity corresponding to 97 sccm and inlet CO and $O_2$ concentrations of 0.564 mol/$m^3$ (corresponding to 1% CO and 1% $O_2$ at 2.5 atm pressure as performed experimentally). The kinetic rate constant, $k_1$, was chosen to yield the same level

of conversion observed in microreactor experiments under the same reaction conditions. A conversion of 24% is seen for the model. Although the reaction only occurs in the catalyst bed, diffusion causes a drop in CO concentration over the entire 2.5 mm of inlet channels shown in the figure. Axial diffusion implies that the CO concentration decreases well before the beginning of the catalyst bed, showing that the reactor operates in a regime significantly deviating from a PFR. The behavior is similar to the classical dispersion models between a PFR and a continuous-stirred tank reactor (CSTR), with a small Pe lying closer to the CSTR limit [22]. A major difference between a classical CSTR and the highly dispersed state seen in Figure 5-11 is that a classical CSTR model assumes zero dispersion at the reactor inlet. That is, reactants are not free to diffuse out of the reactor through the inlet. This is a good assumption in macroscale reactors as the Pe in the inlet tubing is typically quite large. In the cross-flow reactor, there is no boundary limiting diffusion out of the packed-bed, leading to the depletion effects seen in Figure 5-11.

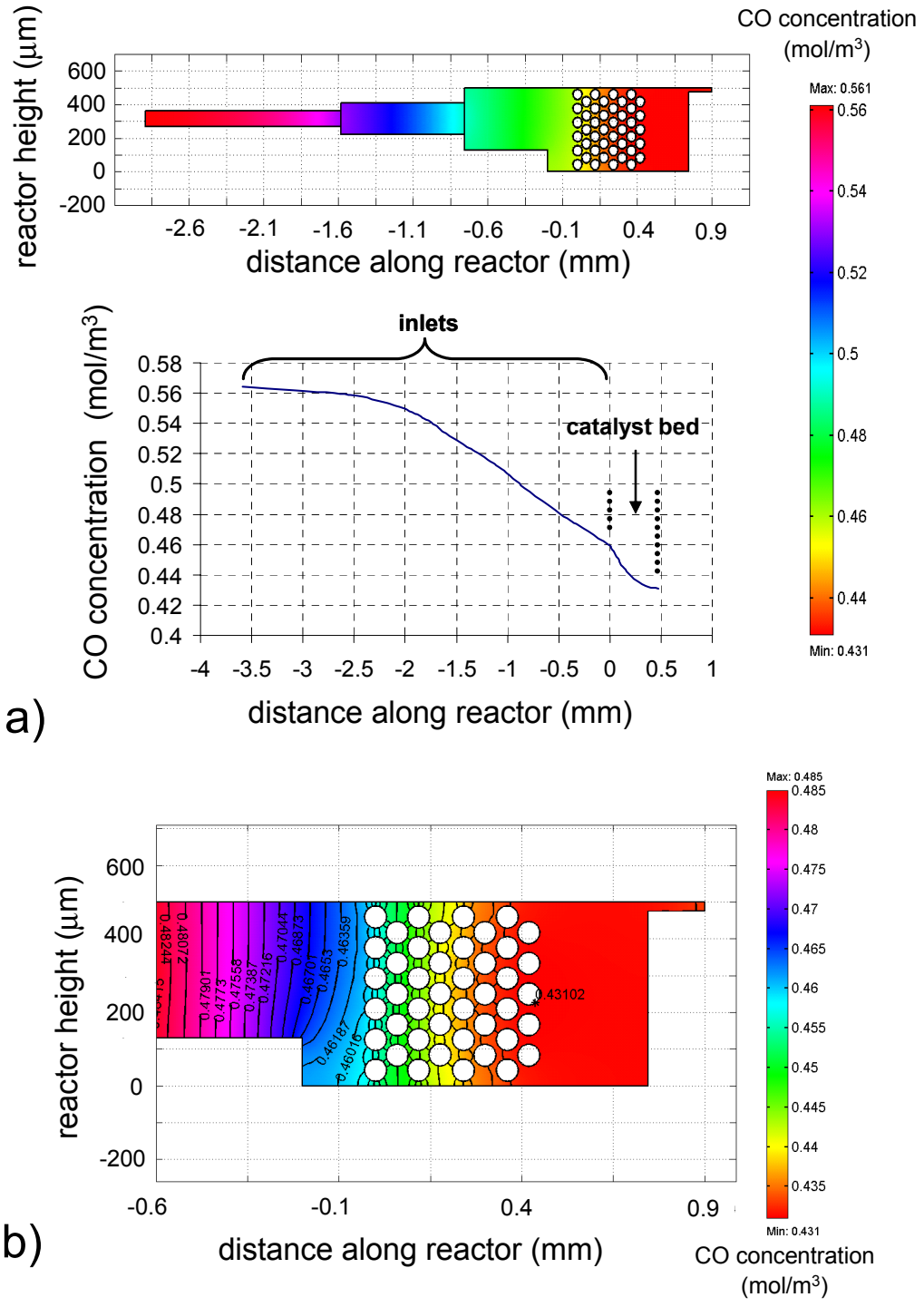


**Figure 5-11.** Finite element models of the CO concentration profile in the cross-flow microreactor for CO oxidation at 540K, 2.5 atm pressure, and an inlet concentration of CO of 0.564 mol/m$^3$. a) Profile along the reactor including 2.75 mm of upstream inlet channels. The decreasing cross-sectional areas indicate points of bifurcation and capture the corresponding increases in convective velocity. b) Close-up view of the CO concentration profile across the catalyst bed.

An added benefit of the bifurcated inlet design is seen as the increased upstream convective flow velocities lead to higher and higher Peclet numbers, and serve to impede back diffusion all the way to the inlet. With over 17.5 mm of inlet channels in the reactor, the 2.75 mm penetration depth seen in Figure 5-11 is small enough that all back diffusion is confined to the microreactor and will not affect system components upstream of the reactor. Figure 5-11b shows the catalyst region in more detail. The concentration at the beginning of the packed-bed of ~0.46 mol/$m^3$ corresponds to a conversion of ~18.4% even though no reaction occurs in the inlet channels. In fact, the concentration in the catalyst bed itself varies only by ~6%, indicating that even at large total conversions (24%, as in the present case), the bed still operates close to differentially. This behavior allows differential kinetic measurements to be obtained at what would have been large conversions in a traditional reactor and thus expands the utility of the cross-flow reactor for catalyst testing.

The calculations were repeated for various reaction rate constants while keeping a constant flow rate to simulate reactor performance at different levels of conversion. Table 5-3 summarizes these results.

**Table 5-3**

**Summary of convection-diffusion-reaction calculations at varying reaction rates**

T= 540 K, CO feed concentration= 0.564 mol/$m^3$, total feed rate= 97 sccm, feed= 1% CO/1%$O_2$ in He

| kinetic rate constant ($k_1$)* | CO conc. at front of catalyst bed (mol/$m^3$) | CO conc. at end of catalyst bed (mol/$m^3$) | total CO conversion in reactor | variation of CO across catalyst bed |
|---|---|---|---|---|
| $0.6k_1$ | 0.51 | 0.49 | 12 % | 3.9 % |
| $k_1$ | 0.46 | 0.43 | 24 % | 6.5 % |
| $1.3k_1$ | 0.42 | 0.38 | 34 % | 9.5 % |
| $1.6k_1$ | 0.36 | 0.31 | 45 % | 13.9 % |

*$k_1$ is based upon the level of conversion observed in the microreactor CO oxidation experiments at the same conditions

The calculations indicate that for conversions as high as 34%, the concentration across the catalyst varies by less than 10%, consistent with the interpretation that the reactor approximates a CSTR. With the given reactor conditions, differential kinetics (previously defined as conversions less than 10%) can be obtained even at these traditionally large conversions. If tighter limits on reactant conversion are desired to characterize differential operation (e.g., <2%), the microreactor behavior scales accordingly.

The cross-flow microreactor, due to diffusion effects, expands the window of operation for obtaining differential kinetics in catalytic processes. This means that when operating at traditional differential conversions, no part of the bed is operating in a regime extending beyond the conversions being measured adding confidence to the data analysis and the application of the differential approximation. Also, the expanded window of operation improves the efficiency for obtaining differential data as reactant conversions can extend much further into non-traditional conversion regimes without manipulating flow rates and pressure as is required in macroscale systems.

### 5.6.2 Examination of the CSTR Approximation

As described above, diffusion effects create a reactor behavior that approaches a CSTR. To assess the applicability of the CSTR approximation to the cross-flow microreactor, an analytical model was examined for CO oxidation and compared to experimental results. The model was developed for CO oxidation over $Pt/Al_2O_3$ catalyst at 505K, 2.5 atm pressure, with a 1%/1% $CO/O_2$ in He reactant feed. Using the basic CSTR design equation,

$$-r_i = F_{i_o} - F_i \tag{5-14}$$

a model for CO oxidation can be developed, where $-r_i$ is expressed in mol/s. The rate expression for the forward reaction was modeled after Equation 5-3, but was expressed in terms of partial pressures, and the experimentally determined reaction orders shown in Figure 5-5 were incorporated into the expression given below.

$$-r_i = k_{rxn} \frac{P_{O_2}^{1.5}}{P_{CO}^{0.79}} \tag{5-15}$$

Substituting the rate expression above into Equation 5-14, an expression for the total volumetric flow rate of premixed reactant feed into the reactor, $F_{total}$, can be obtained as a function of CO conversion ($\xi_{CO}$)

$$F_{total} = \frac{k_{rxn} P_T^{0.71} (\chi - 0.5\xi_{CO})^{1.5} 100^{0.29}}{\xi_{CO}(1-\xi_{CO})^{0.79}} \frac{60RT}{P} \qquad (5\text{-}16)$$

where the ideal gas law is used to reference the flow rate to sccm ($R$ is the universal gas constant, $T$ is 273.15K, and $P$ is 1 atm). Using a value for the reaction rate constant, $k_{rxn}$, obtained from experiments, the CSTR reactor model is shown below in Figure 5-12 compared to experimental reaction data for the conversion of CO at decreasing flow rates.

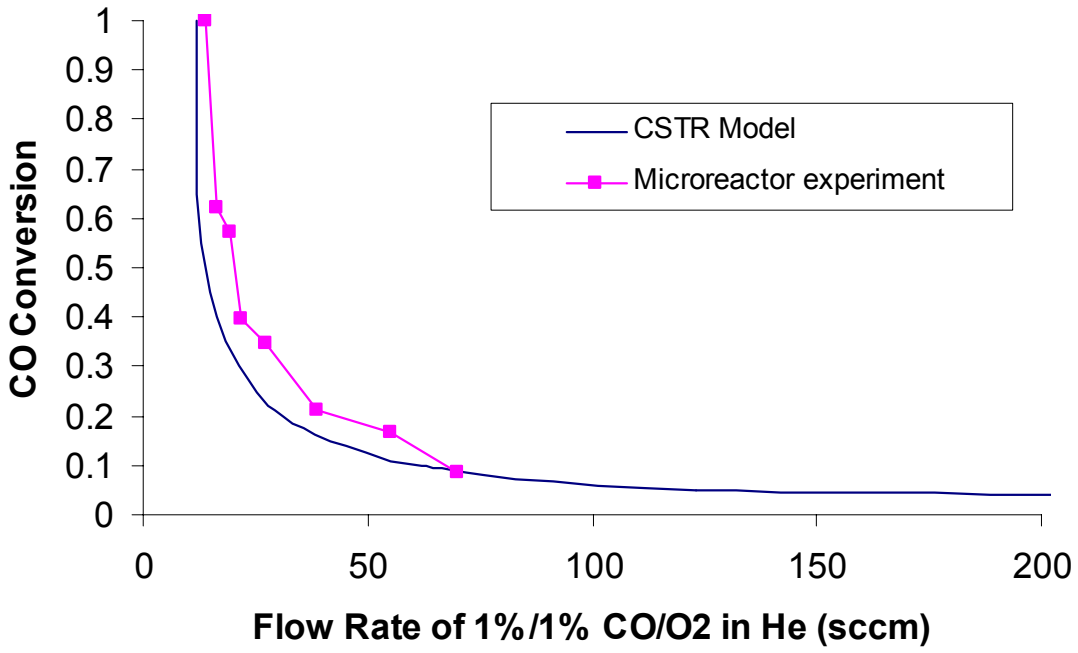


**Figure 5-12.** CSTR model compared to experimental data for CO oxidation over $Pt/Al_2O_3$ at 505K, 2.5 atm pressure, and 1%/1% $CO/O_2$ feed.

The experimental results agree quite well with the model, which contains no fit parameters, supporting the notion that the microreactor approximates a CSTR. The ignition-like behavior seen at the lowest flow rates is actually a kinetically induced instability. Because the reaction is negative order in the limiting reactant (CO), the overall reaction rate increases exponentially with increasing conversion. An instability is reached at a critical flow rate below which near total conversions are obtained in the reactor. This behavior is also seen in the experimental data, validating the use of the form of the rate expression in Equation 5-15.

The discrepancy between the CSTR model and the experimental data is a result of the finite non-zero Peclet number seen in the microreactor, indicating a small convective contribution to dispersion. A 1-D diffusion-convection-reaction PFR with dispersion model of the microreactor was assessed for CO oxidation using the rate expression given in Equation 5-2. The model was setup with Danckwerts boundary conditions at the inlet and outlet using the Newton-Raphson method for non-linear equations. An arc length technique was used to trace bifurcations. CO conversion versus flow rate was calculated using the model at various values for $K$ in the denominator of Equation 5-2. Typical values of $K$ found in literature vary from as low as 3 up to 1000. The figure below shows the results in the previous figure along with the calculated values for conversion at $K$ = 40 and 70 with the dispersion model.

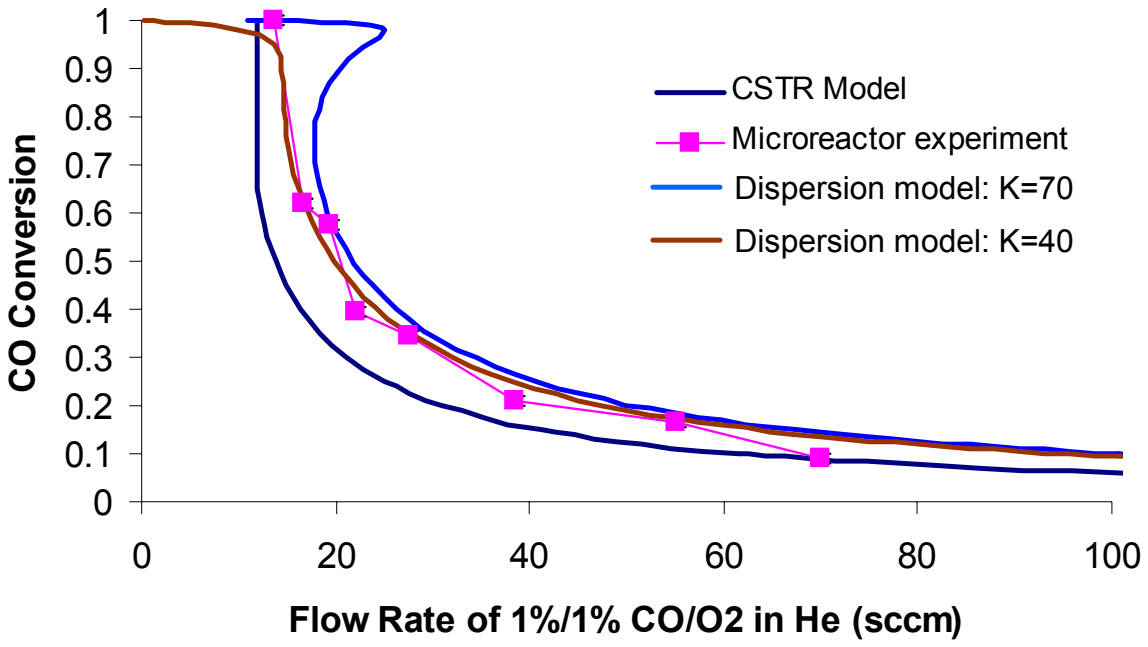


**Figure 5-13.** PFR with dispersion model compared to experimental data for CO oxidation over $Pt/Al_2O_3$ at 505K, 2.5 atm pressure, and 1%/1% $CO/O_2$ feed.

The dispersion model closely approximates the experimental data obtained in the microreactor. Unstable steady state points calculated by the model lie along the "S" curve indicating the predicted ignition and extinction points. Through the development of accurate models to describe the behavior of the cross-flow microreactor, a broad range of kinetic parameters can be extracted including equilibrium constants and adsorption energies using experimental data gathered during catalyst testing. Further, the CSTR approximation provides an excellent first order approximation of reactor behavior for reactor analysis at low conversions. The applicability of the CSTR model to conversions larger than the limit imposed by the differential approximation in macroscale reactors facilitates the extraction of kinetics from experimental data making catalytic research more efficient and accurate.

## 5.7 Comparison to Bench Scale Reactors

The cross-flow reactor displays several advantages that have been detailed throughout this chapter. With respect to macroscale tube reactors commonly used in catalyst testing, additional favorable characteristics of the microfabricated reactor are addressed in this section.

### 5.7.1 Thermal

Heat transfer into and out of the catalyst bed is enhanced in the cross-flow design over bench-scale shallow packed-beds due to geometric effects. First, the smaller reactor volume leads to a natural increase in surface area-to-volume ratio, which increases the ability to remove (or provide) heat. Second, the specific shape of the catalyst bed in the cross-flow reactor further enhances heat transfer. In the microreactor, heat transfer along the *shortest* bed dimensions (500 μm height and 400 μm length) is the primary mode of heat removal. In addition, most of the reactor wall area in contact with the particles lies along this primary mode of heat transfer. In contrast, in a bench-scale shallow packed-bed, radial heat transfer to the side-walls (the *largest* bed dimension) is the primary mode of thermal transport out of the packed-bed and only a small fraction of the reactor wall area in contact with the catalyst particles lies along this direction as illustrated below. The particle configuration in the microreactor is therefore beneficial for maintaining an isothermal catalyst bed.

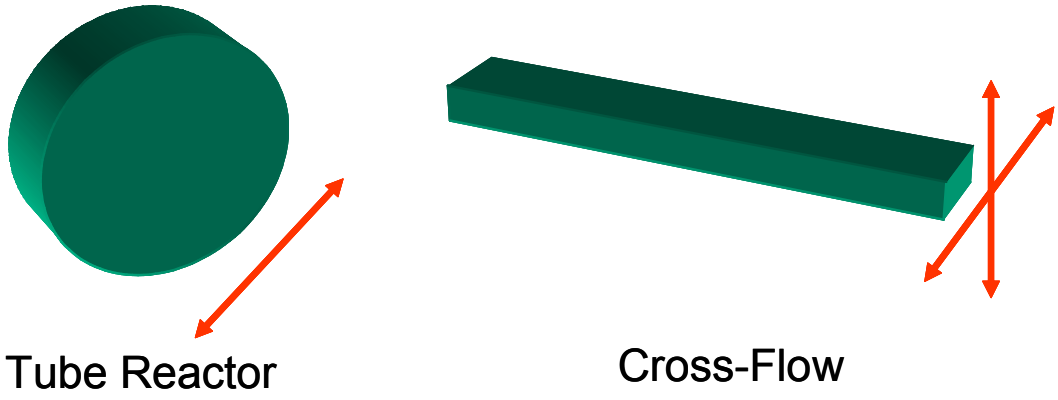


**Figure 5-14.** Illustration of the geometric effects of heat transfer for a macroscale tube reactor versus the cross-flow microreactor.

### 5.7.2 Low Pe Number Operation

As described in Section 5.6.1, operating the cross-flow reactor at low Peclet numbers leads to an expansion of the window of operation for differential kinetics due to the importance of axial diffusion. A conventional bench-scale shallow bed reactor, when packed with a few layers of particles of similar size as the microreactor, also has the capability of achieving the low Peclet numbers needed to expand the range of conversions for which the differential reactor assumption is applicable. However, these reactors have difficulty ensuring even distribution of reactants across the wide bed because variations in packing density (voids) and non-uniformities in the glass frit significantly impact the pressure drop through the reactor. These variations lead to channeling and bypassing of catalyst particles as fluids preferentially take paths of lower pressure drop. Further, the use of larger particles increases the reactor Peclet number and diminishes the beneficial effects of back diffusion in

the reactor. The integration of the microfabricated pressure drop channels and bifurcated inlets eliminates these concerns in the cross-flow microreactor. The small length scales achievable microreactor and the management of flow geometry and catalyst bed dimensions serve to controllably expand the window of operation for differential catalyst testing, adding flexibility and efficiency over many current catalyst testing platforms.

## 5.8 Summary

Kinetic studies with CO oxidation as a model chemistry have shown that the cross-flow microreactor is capable of providing accurate kinetic data with respect to activity, activation energy, and reaction mechanism. The latter is particularly important when studying an unknown chemistry or when conducting fundamental research. The experiments also demonstrated the ability to accurately distinguish between the performance of different catalysts for the same chemistry which is important for testing a large array of catalyst samples in a high-throughput fashion.

The use of a second chemistry, acetylene hydrogenation, showed the ability of the reactor to produce accurate kinetics for a chemistry more complex than CO oxidation. Furthermore, deactivation studies with this chemistry illustrated the potential for using the cross-flow microreactor to study phenomena such as deactivation or catalyst poisoning. This ability is further enhanced by the fact that the length scales seen in the microreactor help reduce the gradients that lead to phenomena such as mass transfer limitations. By eliminating these limitations, loss of catalytic activity can be confidently isolated as occurring from deactivation or poisoning instead of from transport effects.

The small reactor Peclet numbers inherent in the cross-flow reactor significantly change the flow properties of the reactor. Simulations demonstrate that the reactor performance is consistent with a small Pe number dispersion model approaching CSTR behavior (Pe $\rightarrow$ 0). The models suggest the cross-flow geometry enables differential operation across the catalyst bed at what is considered large total conversions in traditional plug flow reactors. This increased window of operation is advantageous for greater efficiency and robustness in catalyst testing and suggests the cross-flow geometry could serve as basis for the development of microfabricated packed-bed reactors that operate as CSTRs.

Since the cross-flow microreactor was designed to be a fully functional chemical reactor utilizing catalyst particles, the reduction of gradients, expanded window of operation, low pressure drop, and even flow distribution are advantages that broadly apply to chemical systems more complicated than CO oxidation, facilitating the extraction of useful information during catalyst studies.

## Notation

$\chi$ = ratio of $O_2$ to CO mol fractions in the reactor feed, dimensionless

$C_{bulk}$ = concentration of species in the bulk (measurable) phase, mol/m$^3$

$C_i$ = concentration of species *i*, mol/m$^3$

$C_s$ = concentration of limiting reactant at the catalyst surface, mol/m$^3$

$C_{surface}$ = calculated concentration of species *i* at the catalyst surface, mol/m$^3$

$D_{eff}$ = effective diffusivity of limiting reactant in the catalyst pores, m$^2$/s

$D_i$ = diffusivity of species *i* in the bath gas, $m^2/s$

$E_{act}/RT$ = Arrhenius group (activation energy, gas constant, temperature)

$F_{io}$ = flow rate in species *i* into the reactor, mol/s

$F_i$ = flow rate in species *i* out of the reactor, mol/s

$\Delta H$ = change in enthalpy of forward reaction, kJ/mol

$k_b$ = thermal conductivity of the bulk gas phase (bath gas), W/(m·K)

$k_p$ = catalyst thermal conductivity, W/(m·K)

$P_i$ = partial pressure of species *i* in the reactor, atm

$Pe_{particle}$ = Peclet number with respect to particle diameter, dimensionless

$Pe_r$ = Peclet number with respect to reactor length in flow direction

$P_T$ = total reactor pressure, atm

$Q''$ = reaction heat generated by catalyst particle as flux to the particle, $J/(m^2s)$

$R_{rxn}$ = effective reaction rate, $mol/(m^3 \cdot s)$

$R''_{rxn}$ = rate of reaction represented as a flux to the catalyst surface, $mol/(m^2s)$

$r$ = variable representing radius taken from the particle center, m

$-r_i$ = rate of consumption of species *i* in the reactor, mol/s

$r_p$ = catalyst particle radius, m

*sccm* = volumetric gas flow referenced to 273.15 K and 1 atm pressure, $cm^3/min$

$T_{bulk}$ = temperature of the bulk gas phase (measurable temperature), K

$T_s$ = catalyst surface temperature taken as the bulk fluid temperature, K

$T_{surface}$ = calculated temperature at the catalyst surface, K

## Literature Cited


[1] A.G. Sault and D.W. Goodman, "Model Studies of Surface Catalyzed Reactions," *Adv. Chem. Phys.* (1989) 153-210.

[2] J.D. Cox, D.D. Wagman, V.A. Medvedev, in: "CODATA Key Values for Thermodynamics," Hemisphere Publishing Corp., New York, 1984.

[3] R.H. Venderbosch, W. Prins, W.P.M. Van Swaaij, "Platinum catalyzed oxidation of carbon monoxide as a model reaction in mass transfer measurements," *Chem. Eng. Sci.* **53** (1998) 3355-3366.

[4] T. Ionnides, A.M. Efstathiou, Z.L. Zhang, X.E. Verykios, "CO Oxidation over Rh Dispersed on SiO2, Al2O3, and TiO2: Kinetic Study and Oscillatory Behavior," *J. Catal.* **156** (1995) 265-272.

[5] P.K. Tsai, M.G. Wu, M.B. Maple, "Oscillatory Oxidation of CO over Pt at Pressures from 10 to 760 Torr," *J. Catal.* **127** (1991) 512-523.

[6] D.R. Rainer, M. Koranne, S.M. Vesecky, D.W. Goodman, "CO + $O_2$ and CO + NO Reactions over Pd/$Al_2O_3$ Catalysts," *J. Phys. Chem. B.* **101** (1997) 10769-10774.

[7] S.H. Oh, G.B. Fisher, J.E. Carpenter, D.W. Goodman, "Comparative Kinetic Study of CO-$O_2$ and CO-NO Reactions over Single Crystals and Supported Rhodium Catalysts," *J. Catal.* **100** (1986) 360-376.

[8] G.S. Zafiris and R.J. Gorte, "CO Oxidation on Pt/$\alpha$-$Al_2O_3$ (0001): Evidence for Structure Sensitivity," *J. Catal.* **140** (1993) 418-423.

[9] S.H. Oh and C.C. Eickel, "Influence of Metal Particle Size and Support on the Catalytic Properties of Supported Rhodium: CO-$O_2$ and CO-NO Reactions," *J. Catal.* **128** (1991) 526-536.

[10] P. Cong, R.D. Doolen, Q. Fan, D.M. Giaquinta, S. Guan, E.W. McFarland, D.M. Poojary, K. Self, H.W. Turner, W.H. Weinberg, "High-Throughput Synthesis and Screening of Combinatorial Heterogeneous Catalyst Libraries," *Angew. Chem. Int. Ed.* **38** (1999) 483-488.

[11] K.C. Taylor, *Ing. Eng. Chem. Prod. Res. Dev.* **15** (1976) 264-268.

[12] J.A. Rodriguez and D.W. Goodman, *Surf. Sci. Rep.* **14** (1991) 1-107.

[13] A.N.R. Bos, E.S. Bootsma, F. Foeth, H.W.J. Sleyster, K.R. Westerterp, "A kinetic study of the hydrogenation of ethyne and ethene on a commercial $Pd/Al_2O_3$ catalyst," *Chem. Eng. and Processing.* **32** (1993) 53-63.

[14] L.Z. Gva and K.E. Kho, "Kinetics of Acetylene Hydrogenation on Palladium Deposited on Alumina," *Kinet. Catal.* **73** (1988) 331-335.

[15] O. Levenspiel, in: "Chemical Reaction Engineering," John Wiley & Sons, New York, 1999, pp. 388-391.

[16] J.B. Anderson, "A criterion for isothermal behaviour of a catalyst pellet," *Chem. Eng. Sci.* **18** (1963) 147.

[17] G. Rexwinkel, A.B.M. Heesink, W.P.M. Van Swaaij, "Mass transfer in packed-beds at low Peclet numbers- wrong experiments or wrong interpretations?," *Chem. Eng. Sci.* **52** (1997) 3995-4003.

[18] D. Kunii and M. Suzuki, "Particle-to-Fluid Heat and Mass Transfer in Packed Beds of Fine Particles," *Int. J. Heat Mass Transfer.* **10** (1967) 845.

[19] R.B. Bird, W.E. Stewart, E.N. Lightfoot, in: "Transport Phenomena," Wiley, New York, 1960, pp. 559.

[20] S.K. Ajmera, M.W. Losey, K.F. Jensen, M.A. Schmidt, "Microfabricated Packed-bed Reactor for Phosgene Synthesis," *AIChE J.* **47** (2001) 1639-1647.

[21] R.B. Bird, W.E. Stewart, E.N. Lightfoot, in: "Transport Phenomena," Wiley, New York, 1960, pp. 200.

[22] H.S. Fogler, in: "Elements of Chemical Reaction Engineering," Prentice-Hall Inc., Upper Saddle River, NJ, 1999, pp. 877.

# Chapter 6
# Analysis of Correlations for Particle-to-Fluid Mass Transport in Packed-beds

---

This chapter explores the use of correlations for particle-to-fluid mass transport in packed-beds. It has been found that a controversy exists over the use various correlations in literature, and that there is a broad discrepancy in how these different correlations predict the operation of the microreactor. This chapter opens with an overview of current literature on this apparent controversy. Using experimental data and modeling, it will be shown that the cross-flow microreactor suppresses mass transfer gradients. This is in agreement with current theories on mass transfer in packed-beds, justifying the use of the Fick's law flux analysis in the previous chapter.

## 6.1 Review of Correlations

The rate of mass and heat transport between the external fluid and a particle in a packed-bed is generally predicted with the use of generalized correlations that relate the Sherwood (Sh) or Nusselt (Nu) number to parameters such as Reynolds and Peclet numbers. Both Reynolds and Peclet numbers are directly related to the fluid velocity through the packed-bed, and therefore a large Reynolds number generally implies a large Peclet number. A significant amount of research has focused on mass transfer in packed-beds at Peclet numbers above 200. Correlations for Sh at these Peclet numbers are typically modified versions of the well-known Ranz-Marshall equation originally derived for a single sphere in an infinite medium,

$$Sh = \alpha + \beta \,\mathrm{Re}^{\gamma}\, Sc^{\delta} \tag{6-1}$$

where $\alpha$ is 2.0 giving a minimum limiting value for mass transfer at low flow rates due to diffusion effects. Correlations of this type, such as those proposed by Wakao and Funazkri [1], have been shown to be relatively accurate at high Peclet numbers where most industrial scale reactors operate and have proven useful in reactor design and analysis.

In contrast, less attention has been given to low Peclet number packed-bed correlations and controversy exists in literature regarding whether the Sherwood number (and Nusselt number) approaches a lower limiting value as Reynolds number goes to zero (as suggested by Equation 6-1) or continues to decrease approaching zero [2, 3]. A significant

amount of data exists suggesting that the Nusselt and Sherwood numbers decrease continuously with decreasing Reynolds number and do not approach a limiting value. The figure below shows a summary of a variety of experiments on the Nusselt number at low Reynolds numbers as compiled by Wakao et al. [4]. Similar data has also been published for Sherwood number.

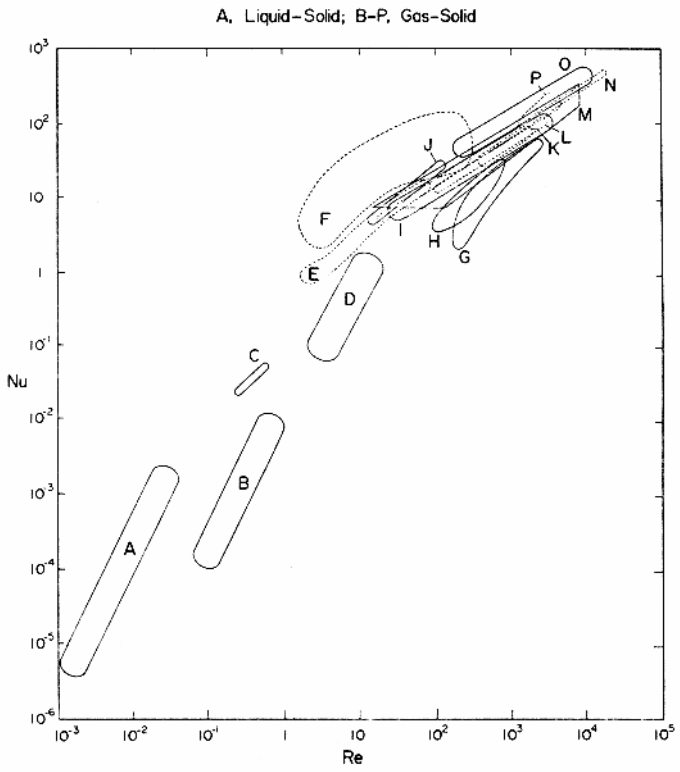


**Figure 6-1.** Heat transfer data as a function of Reynolds Numbers as compiled by Wakao et al. [4]. These experiments indicate no limiting value for transport at low Reynolds numbers.

These experiments indicate no clear limiting value for transport at low Reynolds numbers. Satterfield [5] suggests that data [6, 7] obtained at $0.1 < Re_p < 10$ (typical microreactor gas phase Reynolds numbers are near 0.1) may be approximately represented by:

$$Sh \approx Nu \approx 0.07\,\mathrm{Re}_p \qquad (6\text{-}2)$$

Even theoretical studies are contradictory. Pfeffer and Happel [8] demonstrated a limiting value greater than 10 for creeping flow around a packed-bed with a void fraction of around 0.4. Kunii and Suzuki [6] represented a packed-bed by an array of channels and showed that the Sherwood number is directly proportional to Reynolds number with no limiting value. In perhaps what is considered a defining work on this matter, Sørensen and Stewart [9] obtained numerical solutions for the Navier-Stokes and conservation equations for a cubic array of spherical particles and demonstrated that if axial dispersion in a fixed bed is neglected, Sherwood number becomes directly proportional to Reynolds number. Taking account axial mixing in the analysis, however, produced a limiting Sherwood number of 4. Wakao et al. [1, 4] have also suggested that some correlations for Sherwood and Nusselt numbers are erroneous due to the improper neglect of axial dispersion during data analysis. Kehinde et al. [2] have found experimental evidence of a limiting value for Sherwood number of 2 for flow around non porous particles.

Many Sherwood numbers that are reported in literature were calculated assuming plug flow behavior of fluid through the packed-bed, thereby neglecting the effects of axial dispersion [3]. As discussed in the previous chapter, axial dispersion can have a tremendous effect on mass transport in a system at low Peclet numbers where the local driving force for mass transfer can vary significantly from models that only account for an averaged "mixing-cup" driving force. The omission of flow channeling effects is also commonly cited as another reason for the large discrepancies seen in literature. Martin [10] was able to match experimental results on heat transfer using a model of a packed-bed that took into account

variations in void fraction, and hence, non-uniform fluid velocity (channeling). He found that wall channeling results in the over-estimation of the average driving force in the bed, and thus leads to an apparent drop in Nusselt number. An analogous argument can also be made for the impact of wall channeling on Sherwood number. Rexwinkel et al. [3] has recently expanded on Martin's model by taking into account both channeling effects and axial dispersion. They have shown that for undiluted beds, their model leads to an improvement in the agreement between historical data and theory. However, significant discrepancies still remain for understanding transport in diluted beds, and therefore, a comprehensive understanding of low Peclet number mass and heat transfer still remains elusive. It is thought that perhaps issues such as the internal porosity of the particles and entrance and end effects in the packed-bed are effecting the interpretation of experimental results. In short, current belief is that diffusion, which is not dependent on flow, should provide an intrinsic lower limit to the mass transfer potential in a packed-bed. That is, at zero flow, diffusion still provides mass transfer in the system, naturally leading to a limiting value for Sherwood number that is significantly higher than that predicted by some data and correlations such as Eq. 6-2. However, current correlations do not well represent the complete nature of mass transfer in packed-beds. Therefore, care must be taken when choosing appropriate correlations for Sherwood number in microfabricated packed-beds which almost always operate in a low Peclet/Reynolds number regime.

## 6.2 Application of Correlations to the Cross-Flow Reactor

Of interest is how these correlations compare to the measured performance in micro packed-beds. This is of particular interest for the cross-flow reactor as axial dispersion has been shown to significantly influence mass transfer in the reactor. Furthermore, since the use of correlations during data analysis greatly simplifies reactor design and interpretation of experimental results, it is of interest to the microreaction community to assess the usefulness of these correlations to microfabricated reactors.

Mears [11] proposed a criterion to assess the impact of interphase mass transport in packed-bed reactors. This criterion was derived to determine quantitatively whether or not deviations in concentration between the bulk fluid and the surface of the catalyst particle effect the rate of reaction by less than 5%. It is often assumed in chemical engineering practice that variations of less than 5% can be neglected during reactor analysis. The criteria given by Mears for mass transfer is

$$\frac{R_{rxn} r_p}{C_{bulk} k} \leq \frac{0.15}{n} \tag{6-3}$$

where $k$ is the fluid-particle mass transfer coefficient and $n$ is the reaction order. The mass transfer coefficient can be calculated from the Sherwood number as follows:

$$k = \frac{Sh\, D_i}{d_p} \tag{6-4}$$

The difficulty is in accurately estimating the Sherwood number as discussed in the previous section. In the case of this analysis, two extremes will be calculated; a lower limit for Sherwood number as predicted by Equation 6-2, and an upper bound using a Sherwood number of 2 as derived from the classical sphere in an infinite medium problem.

Using CO oxidation as a model, and picking an experimental point at 546K and 280.5 sccm flow of 1%CO/1%$O_2$ over the platinum on alumina catalyst at 1.75 atm, a mass transfer analysis can be conducted. The TOF at this temperature was experimentally determined to be 4.54 molecules per site per second, which is approximately 55.1 moles/s/$m^3$ catalyst. The particle Reynolds number is approximately 0.1 and the Peclet number with respect to particle diameter is 0.14. At these conditions, the Sherwood number is approximately 0.0073 according to Equation 6-2, significantly below the value of 2 given by traditional single particle analysis. The table below summarizes the calculations for Mears' criterion given in Eq. 6-3 for interphase mass transfer limitations at these two extremes using experimental data obtained for CO oxidation. The reaction order has been assumed to be unity.

**Table 6-1**

**Mears' Criterion for Mass Transfer Limitations at Various Sherwood Numbers**

| **Particle-to-Fluid Sherwood Number** | | **Estimation** | ***Not* transport limited if** |
|---|---|---|---|
| Interphase | Sh = 0.0073 | 0.20 | <0.15 |
| Mass Transfer | Sh = 2.0 | 0.0009 | < 0.15 |

The calculations using Mears' criterion indicate that mass transfer limitations are important for the low estimate of Sherwood number, but are completely negligible at the larger estimate for Sherwood number. However, even for the lower estimate, significant mass transfer limitations do not exist as the estimation is very close in magnitude to the 5% criteria given by the inequality in Eq. 6-3 and is roughly within the error of the experimentally determined parameters. This is an inherent attribute of micro packed-beds with small particle sizes as significant mass transfer limitations are not predicted to exist even for a Sherwood number as small as 0.0073 and a relatively fast reaction such as CO oxidation.

For the cross-flow microreactor operating differentially, using Eq. 6-2 as an estimate of Sherwood number will always result in roughly the same result for Mears' criterion for a given reaction at any reaction condition. This is because, in a differential reactor, the conversion is kept at a constant low value. For example, if temperature is increased resulting in an increase in reaction rate, flow rate would also be proportionately increased to yield similar conversions. Since Eq. 6-2 predicts that Sherwood number is proportional to flow rate, the mass transfer coefficient in the packed-bed would increase proportionately to the reaction rate, keeping Mears' criterion roughly constant.

The calculation shows that a Sherwood number of 2 indicates negligible effects from mass transfer. The same conclusion would also be seen with a variety of Sherwood numbers of similar order. Therefore, in this chapter, a Sherwood number of 2 will be used to represent the variety of correlations in literature that predict a finite non-zero minimum value for Sherwood number. In order to further examine the impact of mass transfer on the CO oxidation experiments, the next section examines some experimental data and modeling

together to show that mass transfer limitations are not significant in the reactor and that the upper limit of Sherwood number is a realistic approximation.

## 6.3 Mass Transfer Analysis with CO oxidation

It is believed that the low estimate of Sherwood number used in Mears' criterion calculated in the previous section significantly underestimates the true value of the Sherwood number in the packed-bed, and in fact, mass transfer limitations do not exist in the microreactor. However, it is important to confirm experimentally the absence of mass transfer limitations. In Chapter 5, reaction kinetics were presented for CO oxidation that agreed well with literature, giving initial evidence to the absence of mass transfer limitations as much smaller activation energies would have been observed. Other data also can be used to assess mass transfer in the microreactor. The following subsections examine these experimental and modeling results.

### 6.3.1 Reaction Order

As discussed in Section 5.1, CO oxidation in the CO inhibited regime leads to the rate expression for $CO_2$ formation given below,

$$Rate = \frac{k_1 \cdot C_{O_2}}{C_{CO}} \tag{5-3}$$

where $k_1$ is the apparent Arrhenius reaction rate constant and not a mass transfer coefficient. In this regime, CO is negative order. However, if the reaction were to operate under significant external mass transfer limitations, the apparent rate of reaction would become dependent on the flux of limiting reagent (CO) to the catalyst surface, and the rate of reaction in terms of flux could be approximated using a mass transfer coefficient, $k_m$, as given below.

$$Rate = k_m \left( C_{CO_{bulk}} - C_{CO_{surface}} \right) \tag{6-5}$$

In this case, the reaction would become positive order in CO under mass transfer dominated reaction conditions. The change from negative to positive order due to mass transfer limitations has been observed by Venderbosch et al. [12] for CO oxidation with similar particle sizes as that used in the microreactor, but at temperatures hundreds of degrees higher than the cross-flow reactor oxidation experiments. As was shown in Section 5.3.2, the order for CO was clearly negative at both 505K and 540K, demonstrating the fact that the oxidation experiments carried out in the microreactor were not strongly controlled by external mass transfer effects.

### 6.3.2 Flow Rate Dependence

Another method to examine mass transfer in the microreactor is to examine the Reynolds number dependence on reaction rate. The expression given in Equation 6-2 implies that the Sherwood number linearly depends on Reynolds number. In a mass transfer limited regime, this would imply that the mass transfer coefficient, $k_m$, given in Equation 6-6 would

vary linearly with flow rate, and therefore, the observed reaction rate should vary similarly. By examining CO oxidation over the platinum on alumina catalyst at varying flow rates, the impact of flow rate on reaction rate, and hence mass transfer, can be seen. The table below shows data taken at various temperatures, flow rates, and concentrations.

**Table 6-2**

**The Impact of Flow Rate on Reaction Rate for CO oxidation over $Pt/Al_2O_3$**

| Temperature | $\%CO/\%O_2$ in He | Flow Rate (sccm) | Apparent TOF |
|---|---|---|---|
| 505 K | 0.997/1.01 | 70.1 | $0.89 \pm 0.06$ |
| | 0.997/1.01 | 140 | $0.94 \pm 0.07$ |
| 505 K | 1.00/0.639 | 75.3 | $0.50 \pm 0.04$ |
| | 1.00/0.639 | 111 | $0.45 \pm 0.03$ |
| 546 K | 0.997/1.01 | 281 | $4.6 \pm 0.32$ |
| | 0.997/1.01 | 581 | $4.2 \pm 0.29$ |

It can be seen from the table above that although the flow rates were approximately doubled for each case, the reaction rate is relatively constant (to within experimental error). According to the correlations suggested by Equation 6-2, in a strongly mass transfer limited regime, the apparent TOF should have approximately doubled, implying again that severe mass transfer limitations are absent.

### 6.3.3 Reaction-Diffusion-Convection FEM Analysis in a 2-D Bed

A better understanding of mass transfer in the cross-flow reactor can be seen by revisiting the FEM analysis performed in Section 5.6.1 on the impact of axial diffusion on the concentration profiles in the reactor. The simulation also captures the specific flow and concentration profiles around each active catalyst particle that can help assess the presence or absence of mass transfer limitations in the reactor. The figure below shows a zoom-in around four catalyst particles in the middle of the packed-bed shown in Figure 5-11 for CO oxidation at 540 K and 2.5 atm pressure.

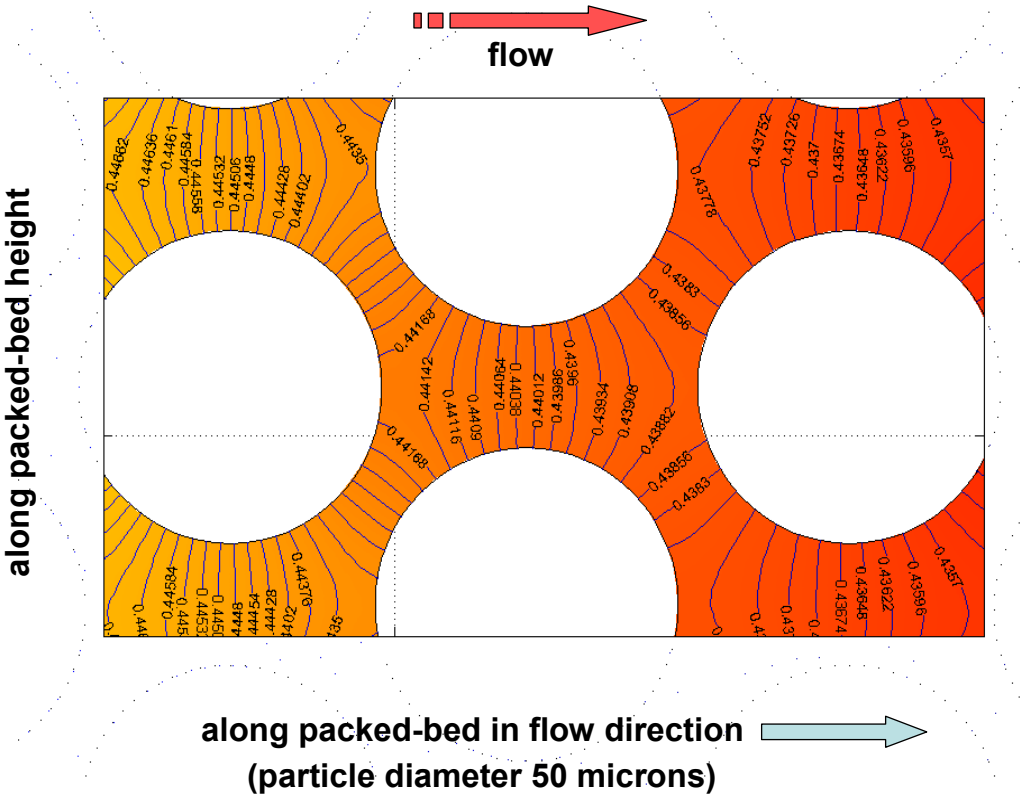


**Figure 6-2.** 2-D FEM of CO oxidation at 540 K and 2.5 atm of pressure as performed in Figure 5-11. Close up of 4 particles in the center of the bed. The contour lines represent CO concentration in mol/m$^3$.

In this simulation, as with the results in Figure 5-11, a total CO conversion of ~24% is seen through the entire reactor. Upon examining the contour lines of constant CO concentration in the figure above, mass transfer limitations seem to be absent. The contour lines project radially outward from the surface of each particle indicating negligible local mass transfer limitations around each particle. As expected at the low Re, there is no evidence of a boundary layer around each particle as would be seen at high Re. This eliminates the need for a separate simulation for mass transfer across a boundary layer and indicates that the contour lines seen in the figure indeed extend to the surface of each particle.

The calculation shown in Table 6-1 using the Sherwood number correlations represented by Equation 6-2 (no lower limit for Sherwood number) suggests that mass transfer limitations are large enough to affect the reaction rate on the order of 5%. Examining the reaction mechanism, this suggests a variation of CO concentration from the bulk to the particle surface of about 5-6% (depending on the reaction order assumed for CO). A 5% variation in the simulation shown above translates to a variation in CO concentration of ~0.022 mol/$m^3$, which would indicate that while the bulk concentration is ~0.44 mol/$m^3$, the concentration on the particle surface is ~0.418 mol/$m^3$. As can be seen from the simulation, the true variation from the center of two particles to the particle surface is at least 2 orders of magnitude smaller than the 5% criterion. This 2-D simulation implies that at the length scales seen in the microreactor, diffusive mass transport is fast enough to completely eliminate mass transfer concerns, supporting the correlations that assume a lower limit of Sherwood number around 2.

### 6.3.4 Reaction-Diffusion-Convection FEM Analysis in Interstitial Channels

To get a better quantitative handle on mass transfer at the low flow rates seen in the microreactor, a different FEM analysis of the cross-flow packed-bed reactor was performed incorporating the CO oxidation reaction as well as both convection and diffusion effects. The purpose of this model is to assess the relative importance of mass transfer limitations by building a realistic model of the flow through the packed-bed. The model breaks down the packed-bed into a bundle of small diameter channels. These channels represent the interstitial channels between particles that are the means by which flow through any packed-bed actually occurs. The pressure drop channels in the cross-flow reactor minimize channeling effects, which are detrimental to apparent mass transfer in packed-beds, across the width of the reactor (largest bed dimension). This also increases the validity of assuming in this model that each interstitial channel has the same flow rate. By using a complete diffusion-convection model for flow and mass transfer in these small channels, mass transfer coefficients and other approximations are not necessary. The model was performed using 2-D axisymmetry in cylindrical coordinates using the commercial software package FEMLAB to represent the 3-D nature of the interstitial channels.

Using a void fraction of 0.4 and an estimation of a interstitial channel diameter of 20 μm, it is estimated that approximately 16261 channels exist in the packed-bed. The channels are assumed to be 400 μm long. In reality, the channels would travel along a tortuous path and could combine and split with other channels. However, the mass transfer effects with respect to diffusion from the center of the channel to the catalytic side-wall should be similar to the straight channel case. The surface area of the 16261 channels is approximately $4 \times 10^{-4}$ $m^2$ and compares quite well with the estimated particle surface area of $3.11 \times 10^{-4}$ $m^2$

calculated from an assumption that all catalyst particles are a uniform 62 µm in diameter. This indicates that the model is a reasonable order of magnitude approximation of the mass transfer effects in the interstitial channels. The simulation was performed using experimental reaction conditions for CO oxidation over $Pt/Al_2O_3$ at 546 K, 1.75 atm pressure, and initial CO and $O_2$ concentrations of 0.391 $mol/m^3$ (1%). The reaction was confined entirely to the wall boundary (catalyst surface) as a flux boundary condition and was expressed using the rate expression given in Equation 5-2. A low flow rate of 40 sccm was chosen in order to achieve larger conversions and give a worst case scenario for mass transfer as suggested by Equation 6-2. The flow was divided evenly across the entire bundle of channels. The figure below shows the simulation results of a single channel.

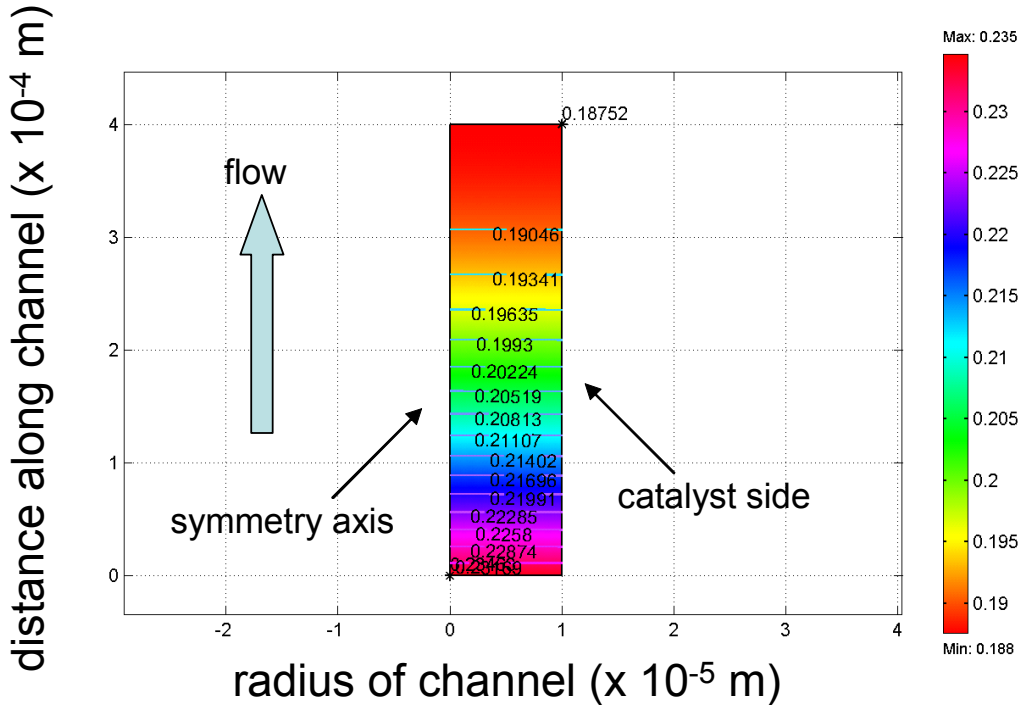


**Figure 6-3.** FEM simulation of CO oxidation at 546 K through a 20 µm interstitial channel. The flat concentration profiles of CO at conversions as high as 50% indicate no mass transfer limitations.

Since the flow profile through the channel is laminar, diffusive mixing is the only form of radial (lateral) mass transfer. The flat CO concentration profiles along the reactor length for conversions as high as 50% indicate that mass transfer limitations are minimal for this model. As in the previous section, the variation of concentration from the center of the channel to the active sidewall in the simulation is at least two orders of magnitude smaller than the variation suggested by Equation 6-2. This indicates that Equation 6-2 under-estimates the Sherwood number in the reactor and supports the current idea that diffusion must create a lower bound for mass transport and hence, Sherwood number, in packed-beds.

### 6.3.5 Fick's Law flux analysis

The simulation results in the previous section indicate that mass transfer in the packed-bed microreactor is fast enough to avoid mass transfer limitations, agreeing with correlations that suggest finite minimum Sherwood numbers. This brings credibility to using a Sherwood number of 2 in the calculations presented in Section 6.2. A more specific way to capture the nature of mass transfer in the packed-bed would be to examine the concentration profile around each spherical particle. Although a full 3-D simulation of a packed-bed would be ideal, it would prove to be computationally difficult. Instead, the simple Fick's law flux analysis presented in Section 5.5 of the previous chapter is a reasonable approximation and is justifiable given the results presented in this chapter. By examining the concentration gradient around an individual catalyst particle due solely to diffusion as was done in Section 5.5, a finite lower limit on Sherwood number (as opposed to a Sherwood number approaching zero) was implicitly assumed. As found using the Mears criterion with a

Sherwood number of 2, the analytical flux analysis in Section 5.5 also predicts a negligible effect from mass transfer effects.

## 6.4 Summary

A controversy exists over the application of various correlations for the particle-to-fluid Sherwood number in packed-beds at low Reynolds and/or Peclet numbers. Even though the lowest approximations for Sherwood number, which suggest that Sherwood number approaches zero at low flow rates, indicate that the microreactor is not significantly mass transfer limited, they still indicate that mass transfer limitations are not negligible. Diffusion, which is not flow dependent, will always provide mass transfer in the system. As reflected by correlations that are becoming increasingly accepted in literature, this inherent mass transfer should yield a finite lower limit for Sherwood number closer to the value of 2 derived for the classical "sphere in an infinite medium" problem. These correlations indicate that mass transfer limitations are negligible for most reactions and flow rates in the cross-flow microreactor, altogether eliminating concerns over external mass transfer. An examination of CO oxidation data such as reaction order and flow rate dependence gives clear evidence that severe mass transfer limitations do not exist in the cross-flow microreactor. To assess the impact of diffusion on mass transfer in the packed-bed, a finite element model was examined that approximated the packed-bed as a bundle of individual interstitial flow channels. The model suggests that even at conversions as high as 50%, mass transfer limitations do not exist in these small flow channels, lending support to current theories that diffusion indeed gives a lower limit to Sherwood number and that the

correlations that suggest Sherwood number approaches zero at small flow rates must have misinterpreted experimental data. The acceptance of diffusion as creating a finite lower boundary for mass transfer gives credence to the Fick's law flux analysis performed in Section 5.5 to assess the impact of external mass transfer limitations in the CO oxidation experiments. The material explored in this chapter strongly suggests that care must be taken when choosing appropriate correlations for micro packed-beds and microreactors in general. Unlike high Reynolds number correlations which have been extensively tested and improved upon, low Reynolds number correlations which are most relevant to microreactors are strikingly lacking in experimental validation.

## Notation

$\beta$ = constant

$\delta$ = constant

$\gamma$ = constant

$C_{bulk}$ = concentration of species in the bulk (measurable) phase, mol/m$^3$

$C_{CO_{bulk}}$ = concentration of CO in the bulk (measurable) phase, mol/m$^3$

$C_{CO_{surface}}$ = concentration of CO on a catalyst particle surface, mol/m$^3$

$C_i$ = concentration of species $i$, mol/m$^3$

$d_p$ = catalyst particle diameter, m

$D_i$ = diffusivity of species $i$ in the bath gas, m$^2$/s

$r_p$ = catalyst particle radius, m

$R_{rxn}$ = effective reaction rate, mol/($m^3$·s)

$Re$ = Reynolds number, dimensionless

$Re_p$ = Reynolds number based on particle diameter, dimensionless

$Sc$ = Schmidt number, = Reynolds number * Peclet number, dimensionless

*sccm* = volumetric gas flow referenced to 273.15 K and 1 atm pressure, $cm^3$/min

*TOF* = turnover frequency, a measure of reaction rate, molecules/active site/s

## Literature Cited


[1] N. Wakao and T. Funazkri, "Effect of fluid dispersion coefficients on particle-to-fluid mass transfer coefficients in packed beds," *Chem. Eng. Sci.* **33** (1978) 1375.

[2] A.J. Kehinde, R.R. Hudgins, P.L. Silveston, "Measurement of Mass Transfer in Packed Beds at Low Reynolds Numbers by Imperfect Pulse Chromatography," *J. Chem. Eng. Japan.* **16** (1983) 483.

[3] G. Rexwinkel, A.B.M. Heesink, W.P.M. Van Swaaij, "Mass transfer in packed-beds at low Peclet numbers- wrong experiments or wrong interpretations?," *Chem. Eng. Sci.* **52** (1997) 3995-4003.

[4] N. Wakao, S. Kaguei, T. Funazkri, "Effect of Fluid Dispersion Coefficients on Particle-to-Fluid Heat Transfer Coefficients in Packed Beds, Correlation of Nusselt Numbers," *chem. Eng. Sci.* **34** (1979) 325-336.

[5] C.N. Satterfield, in: "Heterogeneous Catalysis in Industrial Practice- Second Edition," Krieger Publishing Company, Malabar, Florida, 1996, pp. 516-518.

[6] D. Kunii and M. Suzuki, "Particle-to-Fluid Heat and Mass Transfer in Packed Beds of Fine Particles," *Int. J. Heat Mass Transfer.* **10** (1967) 845.

[7] N. Wakao and S. Tanisho, "Chromatographic measurements of particle-gas mass transfer coefficients at low Reynolds numbers in packed beds," *Chemical Engineering Science.* **29** (1974) 1991.

[8] R. Pfeffer and J. Happel, *AIChE J.* **10** (1964) 605.

[9] J.P. Sørensen and M.E. Stewart, "Computation of forced convection in slow flow through ducts and packed beds-III" Heat and mass transfer in a simple cubic array of spheres," *Chem. Eng. Sci.* **29** (1974) 827-832.

[10] H. Martin, "Low Peclet Number Particle-to-Fluid Heat and Mass Transfer in Packed Beds," *Chem. Eng. Sci.* **33** (1978) 913-919.

[11] D.E. Mears, *Ind. Eng. Chem. Process Des. Dev.* **10** (1971) 541.

[12] R.H. Venderbosch, W. Prins, W.P.M. Van Swaaij, "Platinum catalyzed oxidation of carbon monoxide as a model reaction in mass transfer measurements," *Chem. Eng. Sci.* **53** (1998) 3355-3366.

# Chapter 7
# Membrane Microreactors: Integrating Heterogeneous Catalysts

---

With this chapter, we depart from previous chapters concerning packed-beds and take a glance at heterogeneous catalysis in membrane based microreactors. For membrane reactors, integrating heterogeneous catalysts is difficult because loading the reactor channel with catalyst particles proves impractical. This chapter explores various techniques for using standard wet deposition techniques to deposit catalysts onto the reactor membrane to increase catalyst surface area. Also, the ability to manipulate the thermal properties of the membrane microreactor is discussed. By modifying the thickness and material of the membrane, the microreactor is shown to display an increased window of operation that results in the ability to extract low temperature kinetic information previously inaccessible in both microreactors and macroscale reactors.

## 7.1 Catalyst Integration in Membrane Microreactors

The MIT gas phase microreactor, shown in Fig. 7-1, consists of a 500 μm wide channel etched in silicon capped by a thin membrane structure. The membrane is typically silicon nitride or silicon and is on the order of a few microns or less in thickness. Patterned temperature sensors, heaters, and flow sensors are integrated into the design on the topside of the membrane. On the underside of the membrane, catalyst is coated or deposited. The reactor is then sealed to a metal plate with fluidic through-holes for testing. The fabrication and testing of a prototype microreactor with platinum thin film catalyst for partial oxidation reactions has been previously described [1, 2]. Safe ignition of several highly explosive mixtures in the flammable regime has been demonstrated in this microreactor .

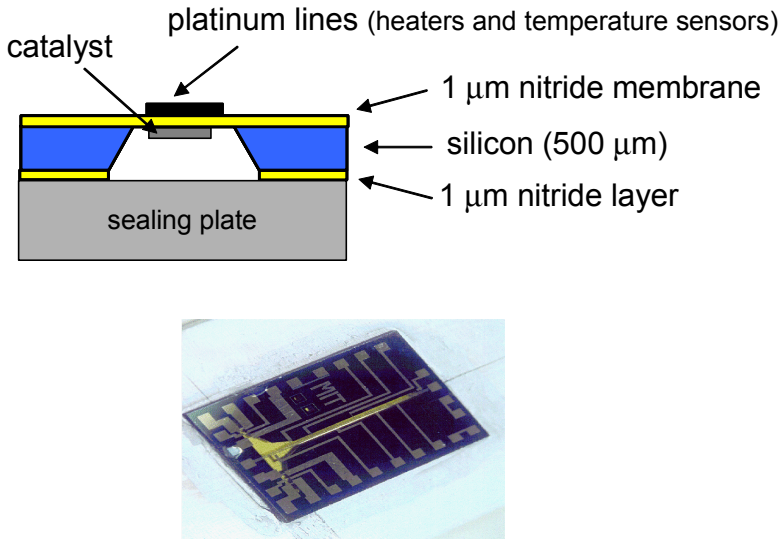


**Figure 7-1.** The MIT gas phase membrane microreactor (Srinivasan [2]). Photograph, Felice Frankel (MIT).

Catalyst deposition in this microreactor presents a unique set of challenges due to the membrane structure. The membrane is reasonably fragile and the heating elements are localized on the membrane surface. Therefore, filling the reactor channel with catalyst particles would be impractical as only the small portion of catalyst in direct contact with the membrane would be heated, leaving most of the catalyst unused. Initially, catalysts were deposited in the microreactor using physical vapor deposition (PVD) during the fabrication process. Noble metal catalysts were evaporated onto the underside of the membrane using an electron beam evaporator in a uniform coat, or in areas defined by a shadow mask. This approach to catalyst deposition has the advantages of control over deposition area and utilization of standard microfabrication technology. However, only a very limited number of catalysts can be deposited using PVD and these catalyst films are smooth, resulting in low surface areas. To increase throughput in the microreactor, it is essential in increase the catalyst surface area.

### 7.1.1 Wet Deposition- Drop Method on Nitride Membranes

To increase the number of catalysts that can be integrated into the microreactor and increase catalyst surface area, standard wet deposition techniques for metal catalysts have been adapted to the constraints imposed by the microreactor design. A common wet catalyst deposition technique, impregnation, involves exposing a catalyst support to an aqueous or organic solution of a metal salt [3]. As the solvent evaporates, the original solid phase catalyst precursor is finely dispersed onto the support. The precursor is then further treated through reduction and calcination to yield a high surface area metal catalyst. Platinum is

deposited by reducing hexachloroplatinic acid ($H_2PtCl_6$) deposited on the membrane. There are many recipes for using hexachloroplatinic acid to yield platinum. The recipe chosen for integration with the microreactor was adapted from Jackson et al. [4] and is as follows:

- Fill entire channel with 0.60% (wt.% Pt) aqueous hexachloroplatinic acid using a micropipette
- Dry under $N_2$ stream at 353K
- Reduce:
    1. 30 minutes under 10%/90% $H_2/N_2$ flow at room temperature
    2. Heat to 573K under same $H_2/N_2$ flow for 3 hours
    3. Cool to room temperature under same flow
    4. Purge with helium for 30 minutes at room temperature to remove hydrogen

The drying and reduction procedures are performed in a tube furnace. This procedure can be repeated to add multiple coats as desired. It has been found that reducing in pure hydrogen yields the same results. The figures below show pictures of the microreactor channel after three coats of platinum on a silicon nitride membrane.

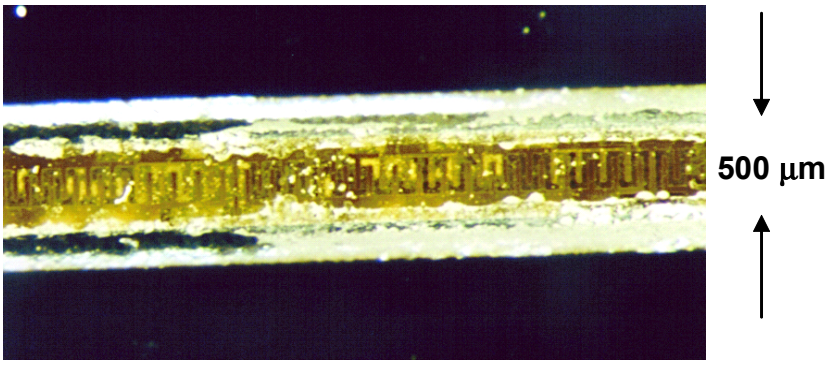


**Figure 7-2.** Photograph of a microreactor channel after three full coating sequences. Note that most of the catalyst deposition lies in the corners near the side-walls.

The membrane acts as a catalyst support for thin film metal adhesion. However, simple wetting of the microreactor channel with the metal salt solution does not yield satisfactory results. As shown in Figure 7-2 and illustrated below, the catalyst solution does not wet the silicon nitride membrane as well as it wets the silicon sidewalls due to surface tension effects. These effects cause the catalyst to coat the channel corners, resulting in very limited catalyst deposition in the desired area (center) of the membrane. Since the heaters and temperature sensors lie along the channel center, it is important to improve membrane coverage to better utilize the catalyst.

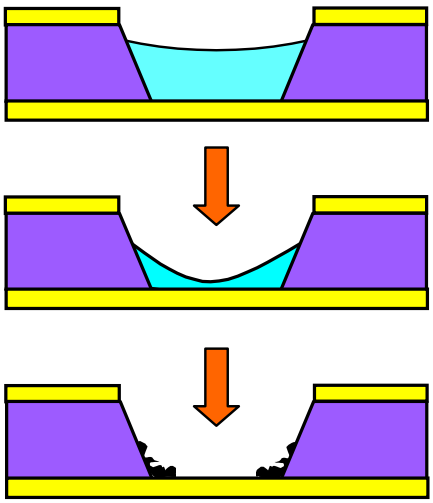

**Figure 7-3.** Catalyst deposition in the microreactor using a metal salt solution: surface tension causes selective deposition in corners.

In order to counter these surface effects, a few drops of surfactant, namely a polyethoxylated alcohol ($C_9EO_{11}OH$), were mixed with the precursor solution. This surfactant was chosen because it pyrolizes easily in the presence of oxygen and can be completely removed before

running a reaction. The addition of surfactant to the solution slightly improves the deposition process. However, majority of the catalyst still continues to deposit near the junction of the membrane and the channel wall as can be seen in Figure 7-4.

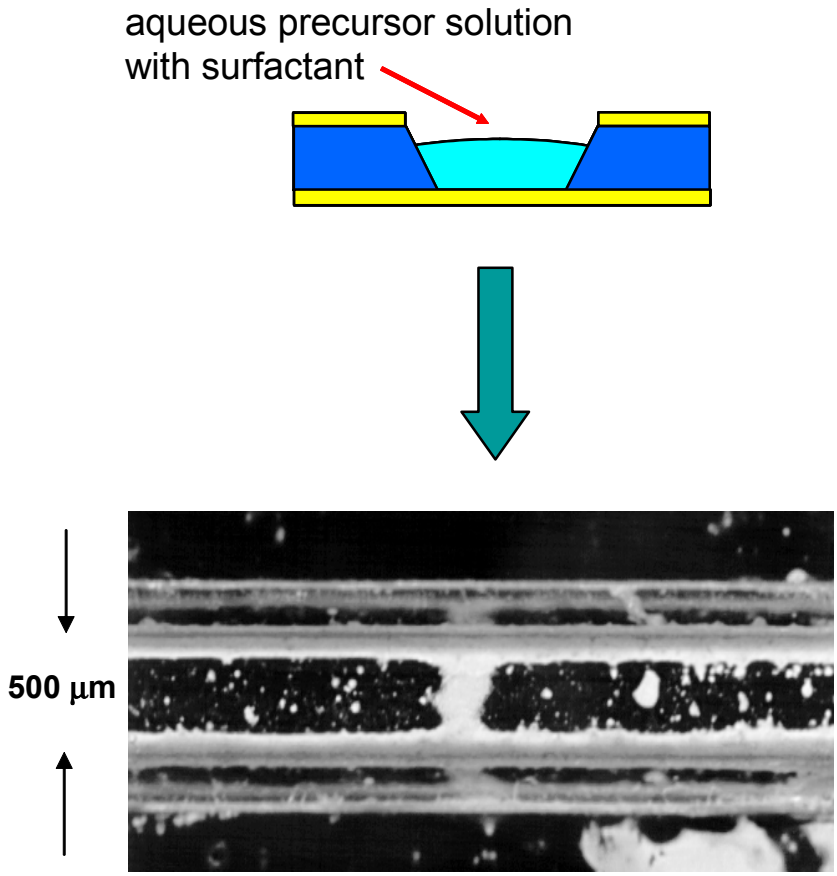


**Figure 7-4.** Platinum deposited using a metal salt solution with added surfactant. The addition of surfactant shows improvement in coverage over the membrane center.

Two wet deposited platinum catalyst reactors with surfactant in the precursor solution were successfully run with the ammonia oxidation reaction. Ignition was very simple and easy, and the reaction was reproducible. Further, both reactors ignited upon initial heating without

any catalyst pretreatment indicating that the surfactant was sufficiently removed during reduction. The added surface area that is intrinsic to wet deposition methods gives greater catalyst activity than e-beam evaporated thin films. The small amount of catalyst seen in the figure above is active enough to sustain a reaction. In addition to platinum, silver, palladium, iridium, and rhodium have been successfully deposited from silver nitrate, palladium acetate, iridium chloride, and rhodium chloride on nitride membranes.

### 7.1.2 Wet Deposition- Drop Method on Silicon Membranes

Silver was also deposited using the wet deposition technique described in the previous section on reactors with all silicon membranes fabricated from silicon-on-insulator (SOI) wafers. Similar results as for the nitride membranes were seen for an aqueous precursor solution with most of the catalyst deposition occurring in the channel corners. However, when the aqueous precursor solution was mixed with a few drops of surfactant, the SOI reactors gave excellent coverage of the heating zone as shown below. This shows how modification of surface properties can strongly affect the deposition of catalyst in microchannels.

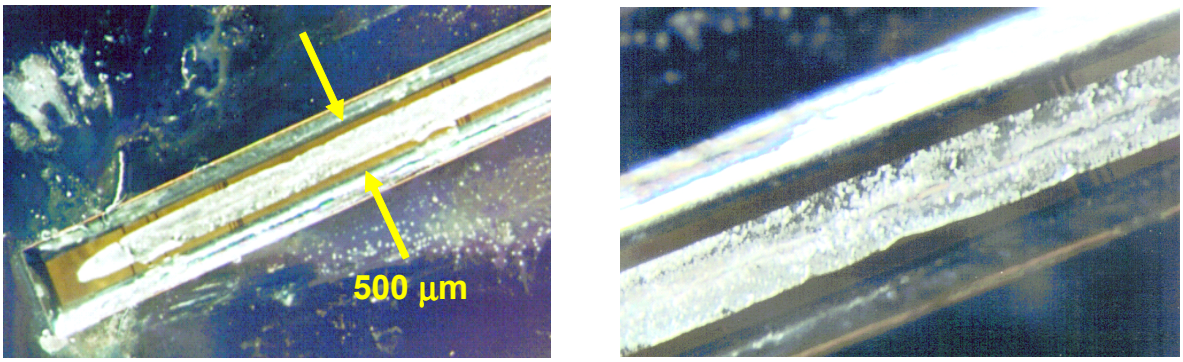


**Figure 7-5.** Deposition of silver with surfactant onto a silicon membrane. The catalyst deposits evenly and uniformly in the center of the reactor channel.

### 7.1.3 Membrane Resiliency

The resiliency of the thin membrane during processing is an important issue. It was found that when using hygroscopic precursors such as platinic acid, it is necessary to perform the reduction procedure immediately after drying, avoiding any exposure to moisture during the entire process. This is because the membrane ruptures if the dried precursor is exposed to air between the drying and reducing steps. During drying, the hygroscopic precursor changes crystal structure to eliminate water. If exposed to moisture after this state, the readsorption of water causes a structural change that stresses the membrane causing catastrophic failure within a few seconds. Therefore, multiple catalyst coats can only be applied after going through the entire deposition sequence completely, including reduction.

## 7.2 Aerosol Catalyst Deposition

To overcome the negative effects of surface tension and achieve a more uniform high surface area coat regardless of membrane type, a method for deposition of high surface area catalysts using aerosols of metal salt solutions has been developed. The aerosol is applied to the reactor membrane, which is heated during the deposition process. As long as the aerosol drops do not coalesce to form a meniscus across the channel, the solution evaporates and deposits the catalyst precursor at the point of droplet impact. The concept of using an atomizer to generate a fine mist of solution lead to the use of an airbrush with a 0.1mm dispersion tip (*Paasche,* AUXSRS-000) to spray the precursor solution into the channel as illustrated below.

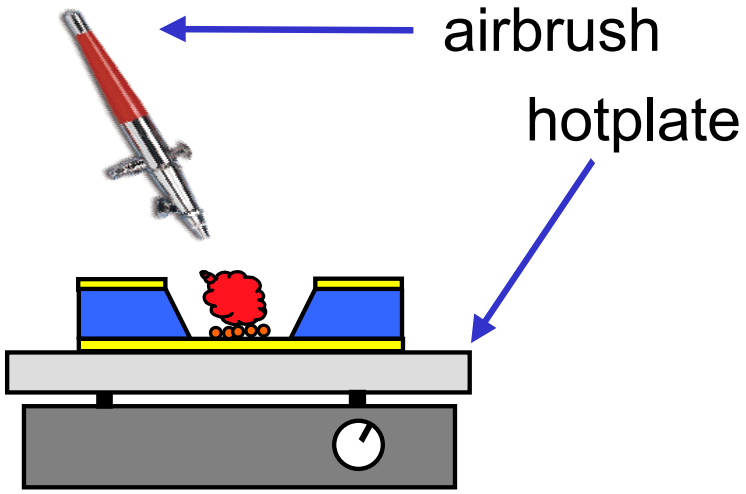


**Figure 7-6.** Illustration of the aerosol technique of catalyst deposition. An airbrush is used to generate a fine mist of precursor solution that deposits into the channel.

The hotplate is heated to above 100 $^{o}$C to evaporate the solvent immediately upon impact. The fine mist that is deposited in the channel lands in individual droplets smaller than the 0.1mm tip. Adjacent droplets do not interact with each other or the channel side-walls, preventing coalescence. Pure nitrogen is used to aspirate the precursor solution in the airbrush. Spraying time and aspiration pressure can be varied to adjust the amount of catalyst deposited. Over depositing leads to some coalescence that results in clumping, decreasing metal dispersion on the membrane. After spray deposition, the standard reduction procedure is followed. Using this technique, issues regarding surface tension and side-wall affinity are eliminated, and a more homogeneous layer of catalyst can be deposited. As shown in Fig. 7-7, this approach is very effective in depositing high surface area catalyst in the central region of a nitride membrane. Similar to the PVD approach, a shadow mask can be used to control the area of catalyst deposition. Using the aerosol approach, platinum, silver, rhodium, and iridium catalysts have been successfully deposited.

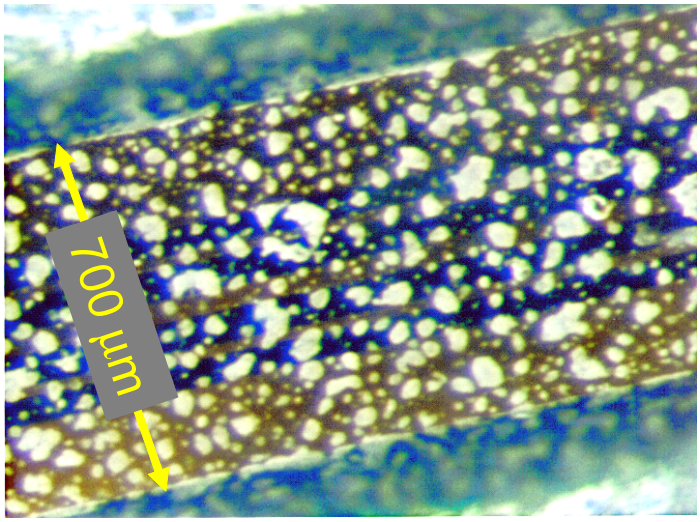


**Figure 7-7.** Airbrushed platinum on 1 µm nitride membrane

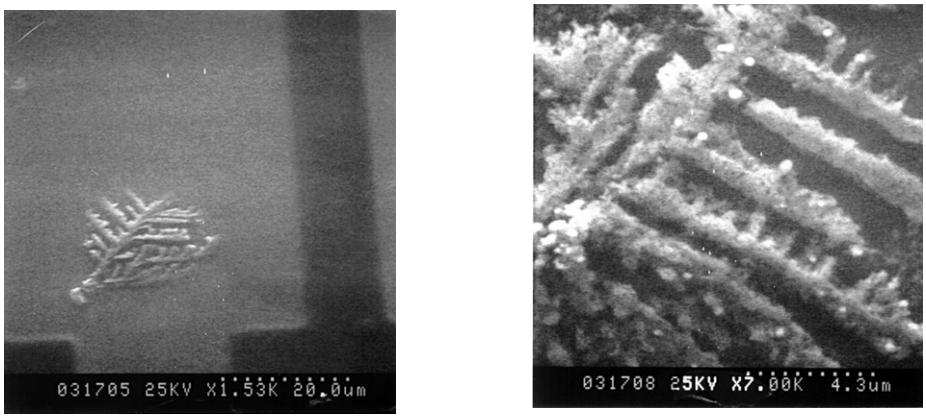


**Figure 7-8.** SEMs of a single airbrushed platinum particle on a nitride membrane at different magnifications. The particle has a large surface area.

### 7.2.1 Poisoning of Catalyst

One problem that occurred during airbrush deposition was the aerosol deposited catalyst initially proved inactive even though the coverage and morphology looked ideal to sustain a reaction. XPS analysis of a platinum deposited membrane reactor showed lead (Pb) contaminating the surface of the catalyst at levels reaching up to 15%. After some research with the airbrush and component manufacturers, it was found that lead solders are commonly used in airbrush manufacturing processes. Therefore, it is important to obtain specially manufactured airbrushes for catalyst deposition with all stainless-steel and Teflon components, fittings, and seals to avoid catalyst poisoning and assure chemical compatibility.

## 7.3 Measuring Catalyst Surface Area

Determining the active surface area of wet deposited catalyst in the membrane reactor continues to be a challenge. Due to the small amount of catalyst in the reactor (i.e. 0.1 micron thick e-beam Pt), some basic surface area characterization techniques are eliminated. Assuming a completely flat and smooth thin film catalyst surface, a minimum surface area of platinum in the membrane microreactor is estimated at $2.5 \times 10^{-6}$ $m^2$ per reactor. BET techniques usually need around 0.05 to 10 $m^2$ for accurate determination [5]. Gravimetric methods can record mass changes as low as $10^{-8}$ g, but typically detect changes around $10^{-6}$ g, corresponding to ~1 $m^2$ of absorbed nitrogen [6]. Dynamic GC methods are typically sensitive to surface areas of 2 $m^2$ [6]. Even if the wet deposited catalyst has surface areas 10,000 times larger than the thin film catalysts, it would be difficult to accurately measure surface area using any of the above methods.

Chemisorption may be a viable technique to measure surface area, particularly on metals, with the limiting factor being the detection scheme. CO or hydrogen are good choices for adsorbing species on noble metal catalysts. Unfortunately, chemisorption is not as accurate for non-metal catalysts, and may limit the use of this technique. Pulsed chromatographic chemisorption has been shown for characterizing the surface area of catalyst micro packed-bed reactors with surface areas of ~0.02 $m^2$ of platinum [7]. In theory, this method can be extended to the low surface areas in the membrane reactor. Finally, titration is an option for catalyst screening experiments, as each catalyst can be standardized against others by measuring the amount of water evolved from passing oxygen over a catalyst saturated with absorbed hydrogen. This could be taken a step further by running a continuous standard reaction over each catalyst such as hydrogen oxidation. The relative

performances of the reaction coupled with known characteristics of the reaction over the various catalysts would give an insight into the relative surface areas, allowing a comparison to be made between catalysts for combinatorial screening. However, surface area measurement in the membrane microreactors remains a difficult challenge.

## 7.4 Integrating Catalyst Supports

In general, silicon nitride and silicon are not commonly used support materials for heterogeneous catalysts. Ultimately, if membrane reactors are going to be useful for catalyst testing, it will be necessary to integrate more commonly used supports such as alumina into the reactor fabrication or catalyst deposition processes. Silica is a common support material. Thermally oxidizing the silicon membrane during fabrication is a means to obtain a silica-like membrane. $TiO_2$ membranes can be obtained via a solid state reaction between titanium, silicon-oxide, and silicon [8]. The procedure involves depositing a thin film of titanium onto a thin silicon oxide on bulk silicon stack. Upon heating at temperatures above 800 $^oC$ in oxygen, a solid state reaction occurs involving titanium atoms substituting for silicon atoms in the silicon oxide. This creates a $TiO_2$/TiSi/Si structure. This procedure was followed for a thermally oxidized silicon membrane reactor with approximately 100 nm of oxide with 300 nm of e-beam PVD titanium. After being exposed to oxygen in a tube furnace at 800 $^oC$ for 1 hour, the reflective titanium film turned a hazy blue color. This procedure provides a method to obtain thin films of catalyst support material. There are also a variety of sol-gel, coating, and deposition techniques available to obtain alumina thin films that can be integrated with the membrane reactors. Janicke et al. [9] has also reported an atmospheric

CVD process utilizing aluminum isopropoxide ($Al[(CH_3)_2CHO]_3$ as an alumina precursor to deposit thin films of alumina in microchannels.

## 7.5 Enabling Improved Catalyst Temperature Control

The unique design of the gas phase membrane microreactor results in novel chemical reactor behavior, presenting new opportunities for obtaining chemical information. As described previously, the catalytic membrane based design results in thermal isolation of the catalyst region from the neighboring silicon walls [2]. The thermal isolation combined with low membrane thermal mass result in an unusually fast reactor thermal time constant of about 10 ms [1].

One potential area of application for these microreactors is for safely carrying out fast, highly exothermic reactions enabled by the integration of heterogeneous catalysts. Oxidation and partial oxidation reactions of hydrogen, ammonia, carbon monoxide, methane, ethane, and ethylene have been successfully carried out in the flammable regime [2]. The ability to control the catalyst temperature, and therefore the selectivity, of partial oxidation reactions is the key factor determining reactor performance. One advantage of microfabrication technology is the ability to control catalyst temperature for partial oxidation reactions through small design and fabrication modifications to the microreactor platform that significantly change the thermal properties of the reactor.

### 7.5.1 Thermal Properties of the Membrane Reactor

The thickness and thermal conductivity of the catalytic membrane, along with the heater design, determine the catalyst temperature profile. The illustration below shows the heat fluxes during microreactor operation. During an exothermic reaction, heat is supplied to the membrane by both the heaters and the reaction. The primary heat loss mechanism has been shown through simulations to be via conduction in the membrane from the reaction zone to the cold silicon reactor walls [10]. Therefore, by varying the thickness and thermal conductivity of the membrane, the ability of the reactor to dissipate the heat of the reaction can be controlled.

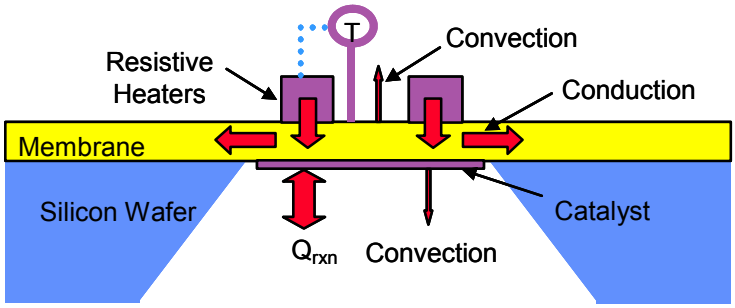


**Figure 7-9.** Heat streams in the membrane microreactor

### 7.5.2 Expanded Window of Operation- Ammonia Oxidation

In the prototype microreactor with a silicon-rich silicon nitride ($SiN_x$) membrane (1 μm thick), fast, exothermic oxidation reactions exhibit typical ignition/extinction behavior. That is, when the heat of the reaction exceeds the ability of the membrane to dissipate it, the temperature increases rapidly to a new steady state. These reactors can be operated autothermally under many conditions, that is, no power needs to be supplied following ignition. The heat generated by the reaction is enough to sustain the reactor at a constant elevated temperature. This type of operation is non-ideal from the standpoint of catalyst temperature control, since the reactor cannot be operated at intermediate temperatures between the ignition point and the upper steady state.

By switching the membrane to a material with a larger thermal conductivity, more heat can be extracted from the reaction zone. Likewise, a thicker membrane increases the cross-sectional area for heat transport and thus facilitates heat transfer out of the channel center. It has been previously shown that if the reactor membrane is made out of 2.6 μm silicon (30 times larger thermal conductivity than silicon nitride [11]), the ability of the reactor membrane to dissipate heat increases by an order of magnitude [1]. Therefore, the increased ability of the silicon membrane microreactors to dissipate heat can have a dramatic effect on reactor performance. In Fig. 7-10 ignition/extinction curves are shown for ammonia oxidation over aerosol deposited platinum in three different types of membrane reactors: a 1 μm silicon rich nitride membrane, a 1.5 μm silicon, and a 2.6 μm silicon membrane. The reaction was run with 20% ammonia in pure oxygen with no diluent at a total flow rate of 50 sccm. The power indicated in the graph is the power output by the heater and the temperature indicates the measured temperature of the reaction zone.

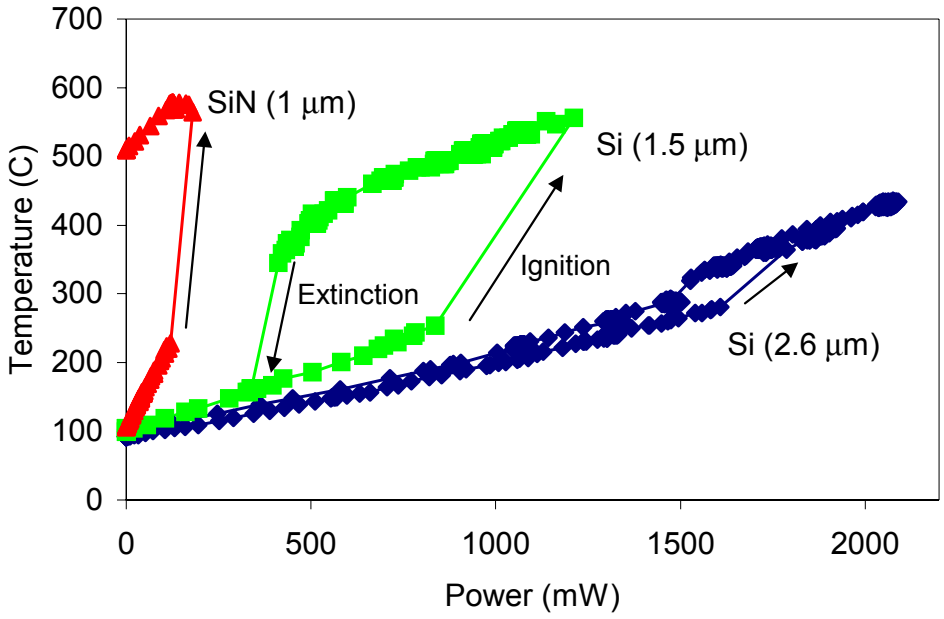


**Figure 7-10.** Ignition/extinction curves for ammonia oxidation (20% ammonia in $O_2$ at 50 sccm) over platinum in different membrane based microreactors.

The silicon rich $SiN_x$ membrane exhibits ignition, followed by autothermal operation. In contrast, the silicon membrane reactors exhibit ignition/extinction behavior for identical reaction conditions. The thicker silicon membrane reactor (2.6 µm) ignites at higher temperatures and reaches lower steady state temperatures than the 1.5 µm silicon membrane reactor. Increasing the ability of the membrane to dissipate heat expands the microreactor thermal operating range for highly exothermic reactions. This allows stable operation at previously inaccessible temperatures in the nitride membrane reactors (as well as macroscale reactors), expanding the window of operation for partial oxidation reactions.

The ability to control the reactor temperature over a broader temperature range due to improved heat dissipation enables greater control over selectivity. In Fig. 7-11, the $NO/N_2$ selectivity for ammonia oxidation is shown for the three reactors in Fig. 7-10.

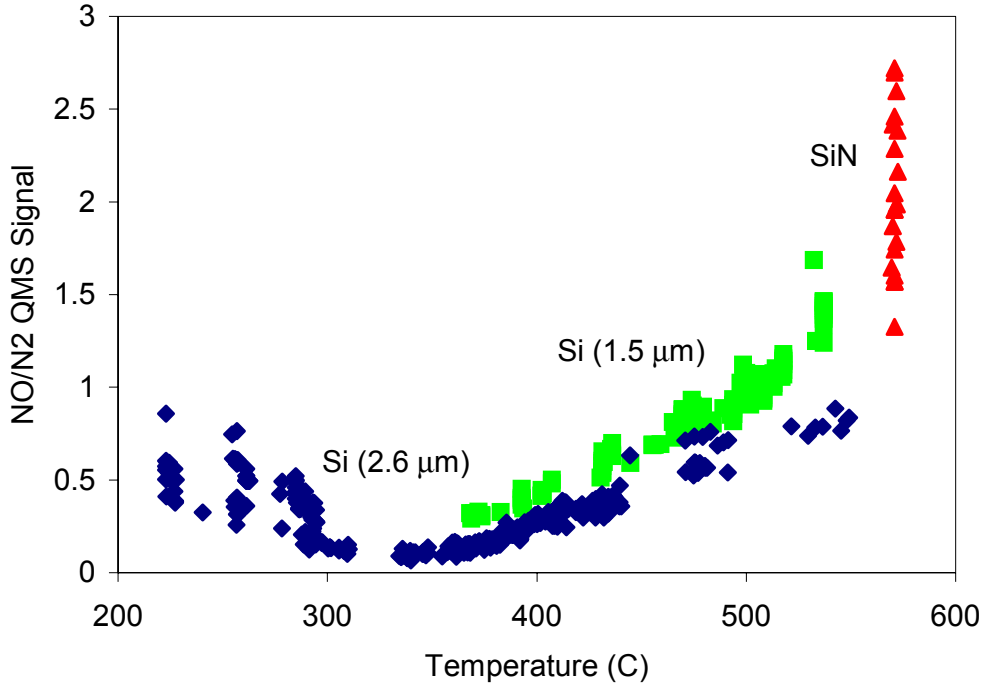


**Figure 7-11.** Dependence of NO/N2 selectivity for ammonia oxidation (20% ammonia in $O_2$ at 50 sccm) on reactor membrane characteristics for the three reactors shown in the previous figure.

The $SiN_x$ membrane reactor operated autothermally at temperatures of about 550 ºC; lower operating temperatures could not be accessed. The $NO/N_2$ selectivity has been shown to increase with temperature in this temperature range [12]. Therefore, the SiN reactor has a relatively high selectivity to NO, consistent with previously reported results. In contrast, the silicon membrane reactors are capable of carrying out the ammonia oxidation at much lower

temperatures, resulting in lower NO selectivities. The thicker silicon membrane reactor expands the thermal operating window enough to apparently access a previously unseen kinetic operating region, where NO selectivity begins increasing with decreasing temperature. This shows the ability of membrane microreactors to operate in previously inaccessible operating regimes and provide new chemical information.

Typical platinum wire experimental reactors exhibit steady state reaction temperatures no lower than 650 ºC for comparable $NH_3/O_2$ ratios, but with air, rather than pure oxygen, fed into the reactor [12]. The nitrogen in the air stream acts as a diluent and a heat sink, lowering the minimum reactor operating temperature. In contrast, the microreactors use pure oxygen feeds and are still capable of carrying out the oxidation reaction at temperatures of 300 ºC or lower. The NO selectivity decreases at lower operating temperatures. The lower NO selectivity could be a desirable feature in the catalytic removal of small amounts of ammonia from farm exhausts. For most partial oxidation reactions it is desirable to avoid high operating temperatures, which lead to complete oxidation products. Therefore, microreactors expand the range of operating conditions and selectivity for oxidation reactions, allow for increased control over operating conditions, and provide a new means to study highly exothermic reactions at low temperatures. In addition, the ability to control the temperature over an expanded range is useful for kinetic studies, which are used to determine rate laws for design of large-scale equipment. Increasing the temperature range over which the rate law is determined increases its accuracy and applicability.

## 7.6 Summary

This chapter detailed work on integrating heterogeneous noble metal catalysts into the membrane microreactor developed at MIT. To increase the surface area of the catalysts over thin film PVD metals, standard wet deposition techniques were adapted to the microreactor. Due to the small channel width, surface tension effects proved to be significant leading to the development of an aerosol based catalyst deposition technique. The aerosol technique allows catalyst layers to be integrated with the thin membrane in a reproducible manner regardless of membrane material and surface tension properties. Using this technique, platinum, palladium, iridium, and rhodium have been deposited. The increased surface area enabled the study of utilizing different membrane materials and thicknesses to control the thermal properties of the microreactor. It was shown that by increasing the thermal transport capabilities of the membrane, an increased window of operation at low temperatures for highly exothermic reactions is achievable. Selectivity studies in this newly accessible regime showed an inversion in $NO/N_2$ selectivity not previously observed in literature. The ability to obtain information such as selectivity in new operating regimes further demonstrates the ability of utilizing microreaction technology to build chemical reactors that improve the way researchers understand chemistry.

## Literature Cited


[1] A.J. Franz, D. Quiram, R. Srinivasan, I.-M. Hsing, S.L. Firebaugh, K.F. Jensen, M.A. Schmidt, "New Operating Regimes and Applications Feasible with Microreactors," in: Process Miniaturization: 2nd International Conference on Microreaction Technology-Topical Conference Preprints, New Orleans, LA, 1998, pp. 33.

[2] R. Srinivasan, I.-M. Hsing, P.E. Berger, K.F. Jensen, S.L. Firebaugh, M.A. Schmidt, M.P. Harold, J.J. Lerou, J.F. Ryley, "Micromachined Reactors for Catalytic Partial Oxidation Reactions," *AICHE JOURNAL.* **43** (1997) 3059.

[3] C.N. Satterfield, in: "Heterogeneous Catalysis in Industrial Practice, Second Edition," Krieger Publishing Company, Malabar, Florida, 1996, pp. Chapter 4.

[4] S.D. Jackson, J. Willis, G.D. McLellan, G. Webb, M.B.T. Keegan, R.B. Moyles, S. Simpson, P.B. Wells, R. Whyman, "Supported Metal Catalysts: Preparation, Characterization, and Function," *Journal of Catalysis.* **139** (1993) 191-206.

[5] C.N. Satterfield, in: "Heterogeneous Catalysis in Industrial Practice," Krieger Publishing Company, Malabar, Florida, 1996, pp. 137.

[6] J.M. Thomas and T.W. J., in: "Principles and Practice of Heterogeneous Catalysis," VCH, 1997, pp. 257-318.

[7] M.W. Losey, "Novel Multiphase Chemical Reaction Systems Enabled by Microfabrication Technology," Thesis, M.I.T., Cambridge, MA, 2001, pp. 184-189.

[8] K. Yokota, T. Yamada, F. Miyashita, K. Hirai, H. Takano, M. Kumagai, "Preparation of titanium-oxide films by solid-state reactions of titanium/silicon-oxide/silicon structures," *Thin Solid Films.* **334** (1998) 109-112.

[9] M.T. Janicke, H. Kestenbaum, U. Hagendorf, F. Schuth, M. Fichtner, K. Schubert, "The Controlled Oxidation of Hydrogen from an Explosive Mixture of Gases Using a Microstructured Reactor/Heat Exchanger and Pt/Al2O3 Catalyst," *Journal of Catalysis.* **191** (2000) 292-293.

[10] I.-M. Hsing, "Simulation Strategies for Microfabrication Chemical Systems," Thesis, Massachusetts Institute of Technology, Cambridge, MA, 1998.

[11] P. Eriksson, J.Y. Andersson, G. Stemme, "Thermal Characterization of Surface-Micromachined Silicon Nitride Membranes for Thermal Infrared Detectors," *J. Microelectromechanical Sys.* **6** (1997) 55.

[12] T. Pignet and L.D. Schmidt, "Selectivity of Ammonia Oxidation on Pt," *Chem. Eng. Sci.* **29** (1974) 1123-1131.

# Chapter 8
# Final Discussion

This chapter summarizes this study on microfabricated chemical systems for improved catalyst testing with a brief review of the accomplishments and general conclusions derived from this work. The chapter closes with a discussion of potential limitations of micro packed-beds and expands on a few points for further study.

As microreaction engineering has progressed over the last ~10 years, new applications beyond chemical production are being increasingly explored. This thesis focuses on exploring the advantages and capabilities of microreactors for heterogeneous catalyst testing; specifically, the development of gradientless reactors for kinetic studies of gas phase processes using catalyst particles. By employing catalyst particles instead of thin-films or coatings, current industrial catalysts and preparation methods for a wide range of applications can be tested, and relevant kinetic parameters can be determined quantitatively. To this end, the cross-flow packed-bed microreactor detailed in Chapters 3-5 provides a clear demonstration of the increased capabilities of properly designed micro packed-bed reactors for improved kinetic studies.

Standard axial flow (tube packed with catalyst particles), used in packed-beds of all sizes, scales unfavorably at the microreactor length scale. Due to the significant increase in pressure drop with the reduction of particle size, large flow rates and differential operation become impractical and kinetic analysis can become convoluted, particularly for gas phase chemistries. However, the advantages of micro packed-beds were demonstrated by the ability to control thermal and mass transfer effects during the production of phosgene in an axial flow microreactor. The concern over reducing pressure drop while maintaining the transport advantages of employing micro packed-beds directly led to the development of the cross-flow microreactor. The cross-flow design yields an isobaric catalyst bed that utilizes practical quantities of catalyst and flow rates. Coupled with the inherent heat and mass transfer advantages at the sub-millimeter length scale, the cross-flow microreactor has been proven through a variety of kinetic experiments and reactor simulations to be an advantageous design for catalyst testing.

## 8.1 Principal Accomplishments and Conclusions

Accomplishments and general conclusions from this study into using microreaction technology for improved kinetic studies are detailed in this section.

### 8.1.1 Axial flow packed-bed microreactor for kinetics extraction

Using the production of phosgene over activated carbon as a model chemistry, standard plug flow reactor and pressure drop models were used to extract kinetic parameters that agreed well with literature demonstrating the use of standard chemical reactor analysis to analyze micro packed-beds. Although shown to be a less desirable geometry for kinetics extraction due to the inherently large pressure drop, the axial flow packed-bed configuration is the first demonstration of obtaining useful heterogeneous gas phase kinetic information from a microfabricated packed-bed reactor.

### 8.1.2 Protective coating for increased chemical compatibility

The use of a thin silicon dioxide coating to protect the silicon reactor from etching from chlorine shows the ability to microfabricate chemically robust reactors. The use of protective coatings, which can be deposited during fabrication or later in the laboratory, expands the ability to use silicon as the base substrate for microfabrication. Silicon is desirable due to the large wealth of fabrication knowledge and techniques developed from the integrated circuit and MEMS industries. The ability to use silicon based reactors for a robust set of chemistries opens the door to future growth of commercial microreactors as

silicon microfabrication naturally lends itself to low cost/ high volume manufacturing with excellent reproducibility.

### 8.1.3 Novel differential reactor geometry with even flow distribution

Silicon micromachining technology enabled the design and fabrication of the cross-flow packed-bed reactor that would have been difficult to achieve on the macroscale. This reactor design employs a novel flow geometry to achieve a low pressure drop, while still benefiting from the advantages of utilizing micro packed-beds to achieve near gradientless operation. The ability to fabricate a variety of precise features at different channel depths provides a passive means to achieve even flow distribution via shallow pressure drop channels. Combined experiments and modeling confirm the even distribution of flow across the wide catalyst bed with a pressure drop ~1600 times smaller than typical microfabricated packed-bed configurations. Through novel geometries enabled by silicon technology, micro packed-bed reactors can be used for catalyst testing with minimal effects from pressure gradients and uneven flow.

### 8.1.4 Catalyst testing in the cross-flow microreactor

Quantitative kinetic information for a variety of chemistries and catalysts has been obtained using the cross-flow microreactor including TOF, apparent activation energy, reaction order, selectivity, and deactivation. The consistency of these parameters with

previously reported values demonstrates the potential of microfabricated cross-flow reactors as laboratory tools for heterogeneous catalyst testing. Unlike previous "micro" catalyst screening platforms, this microreactor was intentionally designed for quantitative catalyst testing. The ability to obtain accurate, detailed, and relevant kinetic parameters in a near gradientless setting opens to door for improved fundamental studies of catalytic processes using catalyst particles.

### 8.1.5 Quantitative Analysis of transport in micro packed-beds

A quantitative analysis of transport effects in the cross-flow microreactor using CO oxidation as a model chemistry indicates that the small catalyst particle size and reactor geometry eliminate mass and thermal gradients both internal and external to the catalyst particles. The small reactor length scale also increases the surface area-to-volume ratio of the reaction channel allowing a larger percentage of catalyst particles in the packed-bed to be in contact with the reactor sidewalls. This reduces temperature gradients across the reactor. Furthermore, the cross-flow reactor geometry provides one more axis for heat transfer over typical shallow circular packed-beds, increasing the ability to add or remove heat from the reaction area. By reducing thermal, mass, and pressure gradients and ensuring even flow distribution over the catalyst bed, employing micro packed-bed reactors in appropriate geometric configurations provides an advantageous platform for the determination of kinetic parameters.

### 8.1.6 Advantage of low Peclet number operation

Reactor simulations demonstrate that reactor performance is consistent with a small Pe number dispersion model approaching CSTR behavior (Pe $\rightarrow$ 0). The models suggest that due to diffusion effects, the cross-flow geometry enables differential operation across the catalyst bed at what would be large total conversions in traditional plug flow reactors. As in a CSTR where an external mixer or stirrer provides near infinite dispersion, diffusion in the cross-flow reactor provides the large dispersive effect. This increased window of operation due to diffusion is advantageous for greater efficiency and flexibility in data gathering and suggests the cross-flow geometry could serve as basis for the development of microfabricated packed-bed reactors that operate as CSTRs.

### 8.1.7 Caution on applicability of correlations to microreactors

Quantitative analysis of transport effects in the cross-flow reactor led to an examination of commonly used correlations for mass transfer coefficients in packed-beds at low Reynolds and/or Peclet numbers. Most chemical engineering correlations are well tested only in Reynolds number regimes higher than those used in microreactors. It has been found that many of these correlations severely under-predict the apparent mass transfer rates in the microreactor, possibly due to erroneous interpretation of experimental data or neglect of flow phenomena such as channeling or axial dispersion. Although current development in literature is beginning to incorporate these previously neglected phenomena, a comprehensive understanding of low Reynolds and Peclet number flow through packed-beds

is still lacking. Thus, such macroscale correlations should be applied to microfabricated systems with caution. Significant care must be taken to understand the assumptions and factors that go into the development of macroscale correlations to assess their applicability to microsystems. This is often difficult as assumptions that are commonly applied to macroscale systems may not apply to microchannels or novel geometries enabled by microfabrication. Unfortunately, these assumptions are not always clearly delineated in literature.

### 8.1.8 Alternate geometries for kinetic studies

Membrane microreactors with thin film catalysts were examined as another means to obtain kinetic information. Using an aerosol based wet catalyst deposition technique, a variety of high surface area noble metal catalysts were deposited. The increased surface area enabled a study utilizing different membrane materials and thicknesses to finely control the thermal properties of the microreactor. It was shown that by increasing the thermal transport capabilities of the membrane, a highly exothermic partial oxidation reaction could be run at previously unachievable low temperatures. Selectivity studies in this newly accessible regime showed an inversion in selectivity not observed in literature. The ability to obtain information such as selectivity in new operating regimes further demonstrates the potential of microreaction technology for providing a variety of geometries that improve the way researchers understand chemistry.

## 8.2 Current Limitations: Non-homogeneous catalyst particles

The cross-flow microreactor, and micro packed-beds in general, are excellent tools for determining intrinsic kinetic information from a catalytic process due to the suppression of gradients that would ordinarily convolute data. The suppression of mass transfer gradients naturally lends itself to the testing of catalyst particles with active sites homogeneously dispersed throughout the particle. However, in industrial reactors, non-homogeneously dispersed active sites are sometimes used such as the "eggshell-deposit" illustrated below.

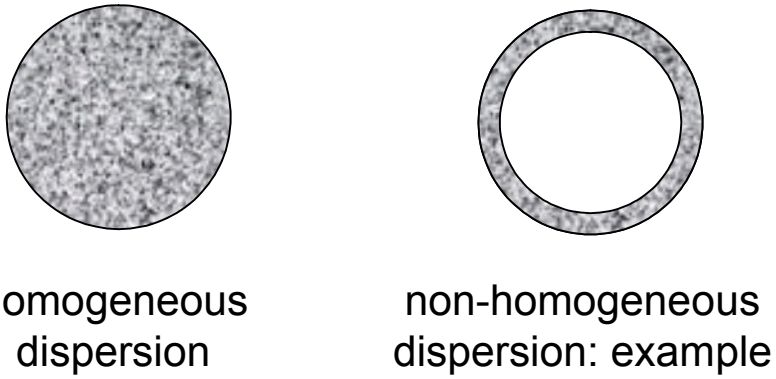


**Figure 8-1.** Illustration of homogeneous and non-homogeneous dispersion of active sites in a catalyst particle.

These types of catalysts take advantage of mass transfer limitations on the macroscale to promote the selectivity of one product over another or to conserve expensive catalysts such as noble metals in mass transfer limited catalytic converters. Other types of depositions that leave an outer shell of inert support material on the catalyst particle are used if high

molecular weight compounds that would poison the active sites tend to only deposit at the particle surface [1].

In the case of testing catalysts with non-homogeneous dispersion, simply crushing the large catalyst particles to sizes useful for the microreactor would lead to an uneven distribution of active sites in the reactor, with some areas containing mostly inert support material and others completely filled with active sites. Even if microscale catalyst particles could be manufactured with appropriate catalyst dispersions, the microreactor, due to enhanced mass transfer capabilities, would not well represent the industrial reactor. This is because the use of particles with non-homogenous dispersion in industrial reactors is usually a result of unavoidable mass transfer limitations. In both these cases, the microreactor would be able to give accurate intrinsic information on the reaction kinetics, but would not be able to directly predict the performance of the industrial catalytic reactor. The translation of data from the microscale to the industrial reactor would require the use of detailed models to couple the intrinsic kinetics to the transport processes in the reactor and inside the large catalyst particles. Although this is becoming computationally feasible with advances in the capabilities of modern computing, this methodology of "intelligent" catalyst design is not currently utilized by many commercial entities. Currently, catalysts are tested in pilot scale reactors with little knowledge of fundamental kinetic and thermodynamic processes, and catalysts are often tested in whatever geometry is available from the supplier. With the advent of modern computing and microfabricated chemical reactors, the current paradigm may shift towards a bottom-up approach to catalyst design, where fundamental catalytic information obtained in a microreactor will be used to design optimal industrial catalysts with tailor-made catalyst particle shapes, sizes, and dispersions.

## 8.3 Recommendations for further development

In order to achieve a robust and useful catalyst testing platform, a variety of areas exist for continuing the development of microchemical system technology. These points of further study are highlighted below.

### 8.3.1 Packaging

Some initial work is presented in this thesis on high temperature and pressure packaging (See Appendix B). However, a rapidly manufacturable high temperature/pressure packaging scheme still needs to be successfully demonstrated in order for the microfabricated cross-flow reactor to truly become a broadly applicable tool. Even with the new packaging scheme using brazed tubing, the reactor is limited to 25 atm and approximately 500 $^{o}$C. Although covering a broad range of catalytic processes, there are many that run at higher temperatures and pressures. It is often for these processes where kinetics are least understood, and where microreactors could make the largest impact. The development of a manufacturable and robust packaging scheme will be necessary for the broad application of microreaction technology.

### 8.3.2 Correlation development

The development of applicable correlations for transport in microchannels will be of increasing interest to the general field of microreaction technology. In specific, understanding the geometric effects of flows in micro packed-beds will help determine the

applicability of currently used correlations for heat and mass transport and pressure gradients. Of particular interest would be the development of a general correlation for microreactors that maps out the entire region of parameter space as a function of flow rate, concentration, and reaction rate to determine whether mass transfer and/or heat transfer are negligible. Other correlations based on a better understanding of flows in micro packed-beds to determine Nusselt and Sherwood numbers would aid in the design of future microreactors and the interpretation of data obtained from catalytic processes in microfabricated packed-beds.

### 8.3.3 Parallelization

In order for high-throughput catalyst testing to become a reality, a significant effort is necessary to develop large scale parallel operation. This includes the integration of control systems, flow manifolds, and sensors onto a single platform that can accommodate a large number of cross-flow reactors in a small form factor. Initial work towards this end has been done at MIT with collaboration with The DuPont Company for the parallel operation of 2 reactor chips with 2 membrane reactors on each chip [2]. Quiram et al. have shown that microreactors can be integrated onto a fluidic circuit board and directly integrated with other system components such as valves, controllers, and electronics on a common PCI chassis in much the way different components of a desktop computer such as the video card and sound card are plugged into slots on the motherboard. Further areas to achieve large scale parallelization involve the integration of chemical detection at the micro-level. This can be done either by the direct fabrication of a chemical sensor into each reactor chip, or perhaps

more practical, the microfabrication of sensors such as micro-gas chromatographs on separate chips that are integrated into the catalyst test station.

Needless to say, much work is left to be done to obtain a fully automated and robust high-throughput catalyst testing platform. However, the cross-flow microreactor, which provides near gradientless operation for kinetics extraction, is an important step towards the goal of achieving superior rapid catalyst testing enabled by microfabrication technology.

## Literature Cited

[1] C.N. Satterfield, in: "Heterogeneous Catalysis in Industrial Practice- Second Edition," Krieger Publishing Company, Malabar, Florida, 1996, pp. 328.

[2] D.J. Quiram, J.F. Ryley, J.W. Ashmead, R.D. Bryson, D.J. Kraus, P.L. Mills, R.E. Mitchell, M.D. Wetzel, M.A. Schmidt, K.F. Jensen, "Device Level Integration to Form a Parallel Microfluidic Reactor System," in: Micro Total Analysis Systems 2001, Monetery, CA USA, 2001, pp. 661-663.

# Appendix A

# Microreactor Fabrication Details

This appendix covers in detail the complete fabrication procedure for the cross-flow microreactor presented in Chapters 3, 4, and 5. The fabrication of the cross-flow microreactor was performed entirely at the clean room facilities of the Microsystems Technology Laboratories at MIT. Most of the fabrication was performed inside the Technology Research Laboratory (TRL) portion of the lab which is a class 100 clean room. The oxidation steps were performed in the Integrated Circuits Laboratory (ICL) which is a class 10 facility. In the next sections, an explanation of the fabrication procedure, along with appropriate photolithography masks, are given.

## A.1 Overview of the Fabrication Procedure

The reactor features are etched using anisotropic deep reactive ion etching (DRIE) with a time-multiplexed inductively coupled plasma etcher (*Surface Technology Systems*). This etch will be referred to as "STS" throughout this Appendix. The main fabrication issue in the cross-flow reactor is to achieve 3 different channel depths. The packed-bed region and inlet/outlet ports are 500 μm deep, the bifurcated channels are 370 μm deep, while the pressure drop channels are only 20-25 μm deep. These different depths require both front (top) and back-side (bottom) etches as well as a nested oxide mask on the front-side. The back-side etch was performed roughly a quarter way through the wafer to define all features that will be eventually etched all the way through. Then on the top side, oxide is patterned with all the reactor features. This is the nested mask. On top of the patterned oxide, thick photoresist is patterned with all the reactor features except the shallow pressure drop channels. In this way, when the first top side etch is performed, the pressure drop channels are left masked. Once the resist is stripped, the nested oxide mask is exposed defining the pressure drop channels.

The patterning on both sides of the wafer requires the use of front and back-side alignment to the photolithography masks. This was achieved using an IR microscope on the older exposure tools or using front and back-side optics on the newer exposure tools. All processing was done with single crystal silicon wafers 100 mm diameter ("4-inch") and 500 μm thick. The fabrication process involves three photolithography masks for reactor features and one more for alignment marks, all used with contact lithography (1x). The masks were standard 5 inch quartz substrates with chrome features with a 9-15% reflectivity and were obtained from *Photronics Inc*.

The capping wafers were standard Pyrex 7740 wafers (*Corning)*. One of the capping wafers was pre-drilled with through holes before bonding to the silicon reactor. The drilling was done in one of two ways. 1) The *DuPont Company* mechanically drilled 2 mm holes through the wafer using a diamond tipped drill, or, 2) The holes were ultrasonically drilled by *Bullen Ultrasonics, Inc.* The ultrasonic drilling is cleaner and more precise with no apparent microcracks forming around each hole, but is more expensive. The mechanically drilled holes are rough, imprecise, and slightly non-uniform and microcracks are apparent around each hole. However, for fluidic through-holes, the mechanically drilled holes are fine.

For convenience, the overview of the fabrication procedure given in Chapter 3 is repeated here. The next section will breakdown this procedure into individual fabrication steps with details on processing.

In the first fabrication step, 0.5-1.5 μm of oxide is thermally grown (or PECVD deposited and thermally annealed) on both sides of the starting wafer (Fig. A-1a). The oxide protects the bonding surfaces during processing from physical damage such as scratches or unwanted deposits from the STS. On the front-side, the oxide also serves as a nested mask for etching the pressure drop channels. In order to prevent wafer bow, it is important if using deposited oxide to maintain the same thickness of oxide on both sides of the wafer. Both thermal and annealed deposited oxide work equally well in this procedure. Next, the entire reactor geometry is patterned into the oxide on the front-side of the wafer. This mask includes the inlet/outlet ports, flow channels, packed-bed region, pressure drop channels, and thermocouple wells. On the back-side, the features to be etched through the wafer (packed-bed region and inlet/outlet ports) are patterned (Fig. A-1b). The back-side features are then etched with DRIE ~150 μm deep (Fig. A-1c). Using a photoresist (AZ P4620, *Clariant*)

spin-coated 10 μm thick, the entire reactor geometry except the pressure drop channels is aligned to the oxide and patterned on the wafer front-side (Fig. A-1d). A second DRIE is performed approximately 350 μm deep (Fig. A-1e). This step opens up the features etched on the back-side and creates the flow channels. Removal of the photoresist reveals the previously patterned oxide layer. A timed etch is performed to etch all the features ~20-25 μm, creating the pressure drop channels (Fig. A-1f). During this final etch process, the wafer is rotated approximately 5 times. This is to ensure that the overall etch depth across the wafer is as uniform as possible. Typically, a variation of 1 μm is seen across an entire wafer, with sub-micron variation seen across any individual reactor. The oxide layer is thick enough to serve as a resist against the shallow etch as the silicon to oxide etch rate in the STS is at least 50:1. The flow channels and thermocouple wells end up ~370 μm deep. In the final step, the oxide is stripped and the channels are capped on the top and bottom with Pyrex wafers (*Corning* 7740) by anodic bonding (Fig. A-1g). Mechanically drilled holes (2 mm) in the bottom Pyrex wafer are aligned to the inlet/outlet ports during the bonding process. The final bonded wafer stack is diced to obtain eight individual reactor chips (15 mm × 40 mm × 1.5 mm).

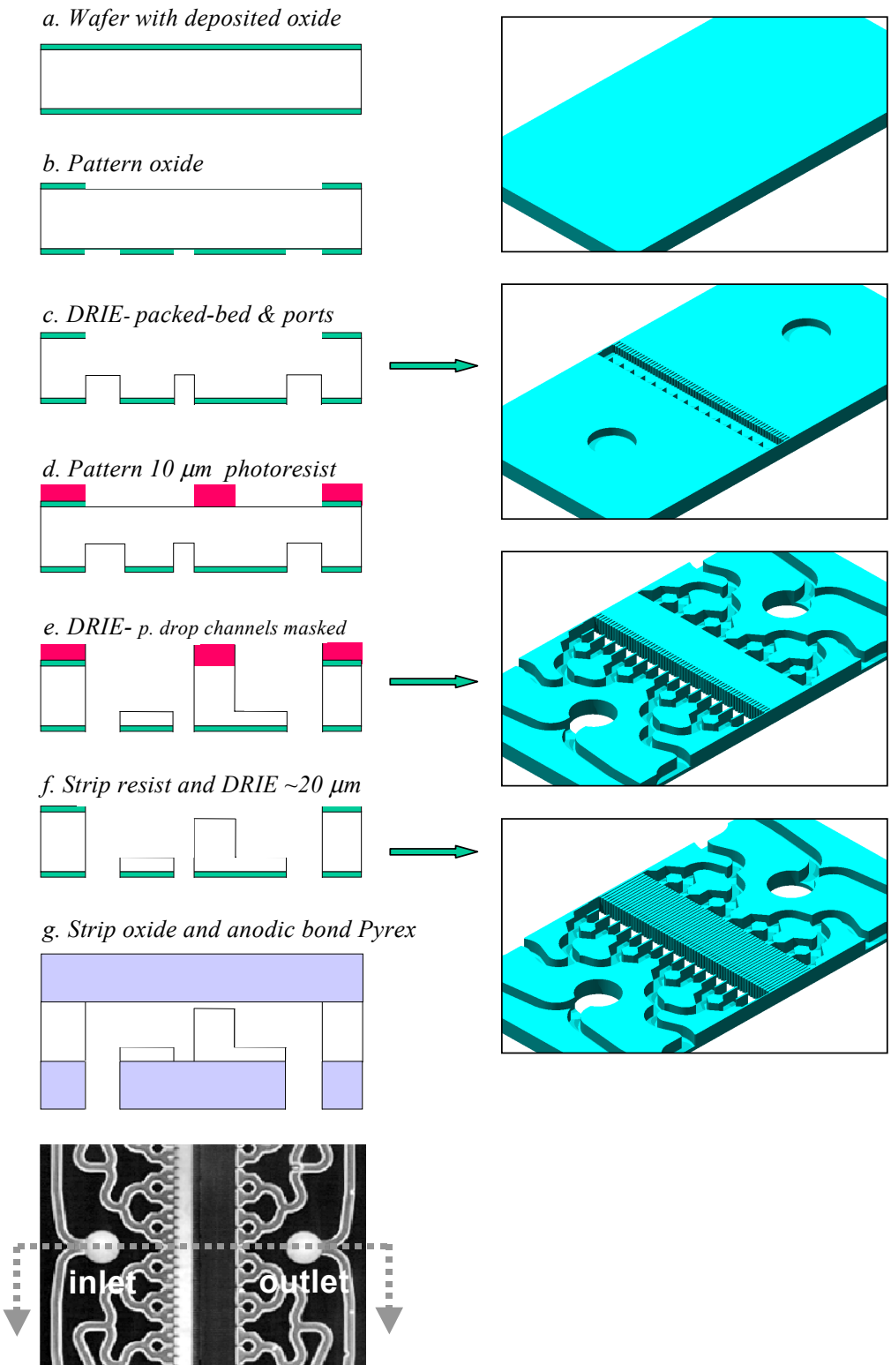


**Figure A-1.** The cross-flow microreactor fabrication sequence. The photograph at the bottom is a top view of the cross section represented by the illustrations.

## A.2 Detailed Fabrication Process Flow- Reactor Wafer

The next pages show a detailed process flow for the fabrication of the cross-flow microreactor complete with machine name, recipe, facility, and chemicals used. Each step of the process flow is numbered sequentially. After the process flow, any details about the specific process steps such as alternate fabrication procedures or difficulties will be given. The following section details the photolithography mask designs.

| Procedure | Process # | Facility | Process Description | machine | café name | Chemical | Recipe | Comments | Status |
|---|---|---|---|---|---|---|---|---|---|
| **Reactor Wafer: DSP 500 micron silicon wafer** | | | | | | | | | |
| **Clean** | 1 | TRL | piranha | acid-hood | acid-hood | sulfuric acid and H2O2 | STD | Clean wafers at process start | Brown |
| **Photolithography 1** | 2 | TRL | HMDS | YES vapor Prime Oven | HMDS | HMDS | STD | 150 deg., 25 minutes | Green |
| | 3 | TRL | Spin on 1 um resist (top) | Solitec Coater 5110 | coater | OCG 825-20CS | STD | 1um, positive resit | Green |
| | 4 | TRL | Soft-bake | Blue DDC-146C | pre-bake | | STD | 90 deg, 30 min, immediately follow | Green |
| | 5 | TRL | Exposure | Karl Suss Aligner | ksaligner-2 | | STD | Mask 0, use masking jig, 45 sec. | Green |
| | 6 | TRL | Develop | photo-wet left | photo-wet-l | OCG 934 1:1 | STD | 1 minute in developer | Green |
| | 7 | TRL | Inspect | fluoroscope | | | | look for good exposure | Green |
| | 8 | TRL | Spin on 1 um resist (bottom) | Solitec Coater 5110 | coater | OCG 825-20CS | STD | protect backside from AME scratches | Green |
| | 9 | TRL | Soft-bake | Blue DDC-146C | pre-bake | | Short | 90 deg, 5 minutes | Green |
| | 10 | TRL | Spin on 1 um resist (bottom) | Solitec Coater 5110 | coater | OCG 825-20CS | STD | protect backside from AME scratches | Green |
| | 11 | TRL | Post-bake | Blue DDC-146C | post-bake | | STD | 120 deg, 30 min, immediately follow | Green |
| | 12 | TRL | Bag up wafers | | | | | Transfer to ICL | Green |
| **AME Etch Mask 0** | 13 | ICL | pre-clean | pre-clean station | pre-clean | DI:HF 50:1 | STD | Green, 15 sec HF dip | Green |
| | 14 | ICL | Etch alignment marks | AME Prec 5000 | AME5000 | | STD | Etch 1 micron deep, polysi etch 145 s at 70 A/s | Green |
| **Deposit Oxide** | 15 | ICL | Remove resist | wet station | pre-metal | piranha | STD | Strip resist in blue beaker, 10 min | Blue |
| | 16 | ICL | Pre-metal clean | wet station | pre-metal | piranha/HF dip | STD | 10-min piranha in green + 15 sec in HF | Green |
| | 17 | ICL | Transfer to Clean box | | | | | Transfer to Clean ICL box | Green |
| | 18 | ICL | deposit oxide on bottom | Novellus Concept 1 | concept1 | | STD | deposit 5000A oxide on bottom, 5000aox | Green |
| | 19 | ICL | deposit oxide on top | Novellus Concept 1 | concept1 | | STD | deposit 5000A oxide on top, 5000aox | Green |
| | 20 | ICL | densify oxide | Tube B6 | tubeB6 | Nitrogen | G-190, 1h | 1100 deg, 1 hour, Nitrogen | Green |
| | 21 | ICL | Bag up wafers | | | | | Transfer to TRL in TRL box | Green |
| **Photolithography 2** | 22 | TRL | Piranha clean | acid-hood | acid-hood | piranha | STD | 10 minutes | Green |
| | 23 | TRL | HMDS | YES vapor Prime Oven | HMDS | HMDS | STD | 150 deg., 25 minutes | Green |
| | 24 | TRL | Spin 10 um resist (top) | Solitec Coater 5110 | coater | AZ P4620 | STD | 10 um positive thick resist | Green |
| | 25 | TRL | Pre-bake | Blue DDC-146C | pre-bake | | STD | 90 degree, 1 hr | Green |
| | 26 | TRL | Exposure | Karl Suss Aligner | ksaligner-2 | | STD | Mask "Pressure Drop", 500s, top-side, use jig | Green |
| | 27 | TRL | Develop | photo-wet left | photo-wet-l | AZ 440 | STD | 4-5 minutes at least | Green |
| | 28 | TRL | Inspect | fluoroscope | | | | look for good exposure | Green |
| | 29 | TRL | Spin 10 um resist (bottom) | Solitec Coater 5110 | coater | AZ P4620 | STD | 10 um thick positive resist, use Ravi's jig | Green |
| | 30 | TRL | Post-bake | Blue DDC-146C | post-bake | | STD | 90 deg, 30 min immediately follow | Green |
| **BOE Dip** | 31 | TRL | BOE Dip | acid-hood | acid-hood | HF 7:1 | STD | 5.5 minutes, 5000A at 1000A/min | Green |
| | 32 | TRL | Inspect | fluoroscope | | | | | |
| **Photolithography 3** | 33 | TRL | Remove resist | acid-hood | acid-hood | piranha | STD | Strip resist, 15 min | Green |
| | 34 | TRL | HMDS | YES vapor Prime Oven | HMDS | HMDS | STD | 150 deg., 25 minutes | Green |
| | 35 | TRL | Spin 10 um resist (bottom) | Solitec Coater 5110 | coater | AZ P4620 | STD | 10 um, positive thick resist | Green |
| | 36 | TRL | Pre-bake | Blue DDC-146C | pre-bake | | STD | 90 deg, I hr, immediately follow | Green |
| | 37 | TRL | Exposure | Karl Suss Aligner | ksaligner-2 | | STD | Mask "reactor bottom", backside align,500s, jig | Green |
| | 38 | TRL | Develop | photo-wet left | photo-wet-l | AZ 440 | STD | 4-5 minutes at least | Green |
| | 39 | TRL | Inspect | fluoroscope | | | | look for good exposure | Green |
| | 40 | TRL | Spin 10 um resist (top) | Solitec Coater 5110 | coater | AZ P4620 | STD | 10 um thick, positive resist | Green |
| | 41 | TRL | Post-bake | Blue DDC-146C | post-bake | | STD | 90 deg, 30 min, immediately follow | Green |
| **BOE Dip** | 42 | TRL | BOE Dip | acid-hood | acid-hood | HF 7:1 | STD | 5.5 minutes, 5000A at 1000A/min | Green |
| | 43 | TRL | Inspect | fluoroscope | | | | | |

| | | | | | | | | |
|---|---|---|---|---|---|---|---|---|
| **Handle Wafer** | 44 TRL | Spin 1 um resist (quartz) | Solitec Coater 5110 | coater | OCG 825-20CS | | 1 um, outer 1 cm of quartz wafer | Green |
| | 45 TRL | Wipe out resist | | | Q-tip, acetone | | wipe out pie-shapes with Q-tip | Green |
| | 46 TRL | Contact wafers to top | | | | | | Green |
| | 47 TRL | pre-bake | | pre-bake | | STD | 90 deg, 30 minutes | Green |
| **STS Etch** | 48 TRL | Etch reactor bottom | STS2 etcher | sts2 | | MIT 37A | timed etch, remove at around 200 um | Green |
| | 49 TRL | remove handle wafer | photo-wet left | photo-wet-l | acetone | STD | let sit over night | Green |
| | 50 TRL | Remove resist | acid-hood | acid-hood | piranha | STD | 15 minutes | Green |
| **Photolithography 4** | 51 TRL | Clean wafers | acid-hood | acid-hood | piranha | STD | 10 min | |
| | 52 TRL | HMDS | YES vapor Prime Oven | HMDS | HMDS | STD | 150 deg., 25 minutes | Green |
| | 53 TRL | Spin 10 um resist top | Solitec Coater 5110 | coater | AZ P4620 | STD | 10 um thick, positive resist | Green |
| | 54 TRL | Pre-bake | | pre-bake | | STD | 90 deg, 1 h | Green |
| | 55 TRL | Exposure | Karl Suss Aligner | ksaligner-2 | | STD | Mask "Reactor Top", 500s, use jig | Green |
| | 56 TRL | Develop | photo-wet left | photo-wet-l | AZ 440 | STD | 4-5 minutes at least | Green |
| | 57 TRL | Inspect | fluoroscope | | | | look for good exposure | Green |
| | 58 TRL | Post-bake | Blue DDC-146C | post-bake | | STD | 90 deg, 30 min, immediately follow | Green |
| **Handle Wafer** | 59 TRL | Spin 1 um resist (quartz) | Solitec Coater 5110 | coater | OCG 825-20CS | | 1 um, outer 1 cm of quartz wafer | Green |
| | 60 TRL | Wipe out resist | | | Q-tip, acetone | | wipe out pie-shapes with Q-tip | Green |
| | 61 TRL | Contact wafers to bottom | | | | | | Green |
| | 62 TRL | pre-bake | | pre-bake | | STD | 90 deg, 30 minutes | Green |
| **STS Etch** | 63 TRL | Etch reactor top | STS2 etcher | sts2 | | MIT 37A | timed etch, etch ~350 um | Green |
| | 64 TRL | remove handle wafer | photo-wet left | photo-wet-l | acetone | STD | let sit over night | Green |
| | 65 TRL | Remove resist | acid-hood | acid-hood | piranha | STD | 15 minutes | Green |
| **Handle Wafer** | 66 TRL | Spin 1 um resist (quartz) | Solitec Coater 5110 | coater | OCG 825-20CS | | 1 um, outer 1 cm of quartz wafer | Green |
| | 67 TRL | Wipe out resist | | | Q-tip, acetone | | wipe out pie-shapes with Q-tip | Green |
| | 68 TRL | Contact wafers to bottom | | | | | | Green |
| | 69 TRL | pre-bake | | pre-bake | | STD | 90 deg, 30 minutes | Green |
| **STS Etch** | 70 TRL | Etch pressure drop (top) | STS2 etcher | sts2 | | MIT 28 A | 20 um, rotate every 4 um to improve uniformity | Green |
| | 71 TRL | remove handle wafer | photo-wet left | photo-wet-l | acetone | STD | let sit over night | Green |
| | 72 TRL | Remove resist | acid-hood | acid-hood | piranha | STD | 10 minutes | Green |
| **BOE Dip** | 73 TRL | BOE Dip | acid-hood | acid-hood | HF 7:1 | STD | 5.5 minutes, 5000A at 1000A/min | Green |
| | 74 TRL | Inspect | fluoroscope | | | | | |

### A.2.1 Process Flow Details

- **Photolithography 1**: Steps 2-12

This purpose of this photolithography sequence is to create alignment marks on the silicon wafer that will be used to align all future masks to each other. The alignment mark mask used is a standard mask used in MTL known as "Mask 0." This mask contains two alignment marks spaced 72 mm apart. Care must be taken when choosing the appropriate Mask 0 in the clean room as older masks are still used that look very similar but have alignment features only 70 mm apart. The figures below show an overview of the placement of the alignment marks on a wafer and a zoom in of the features on a single alignment mark. The critical dimension of the center cross is 3 μm.

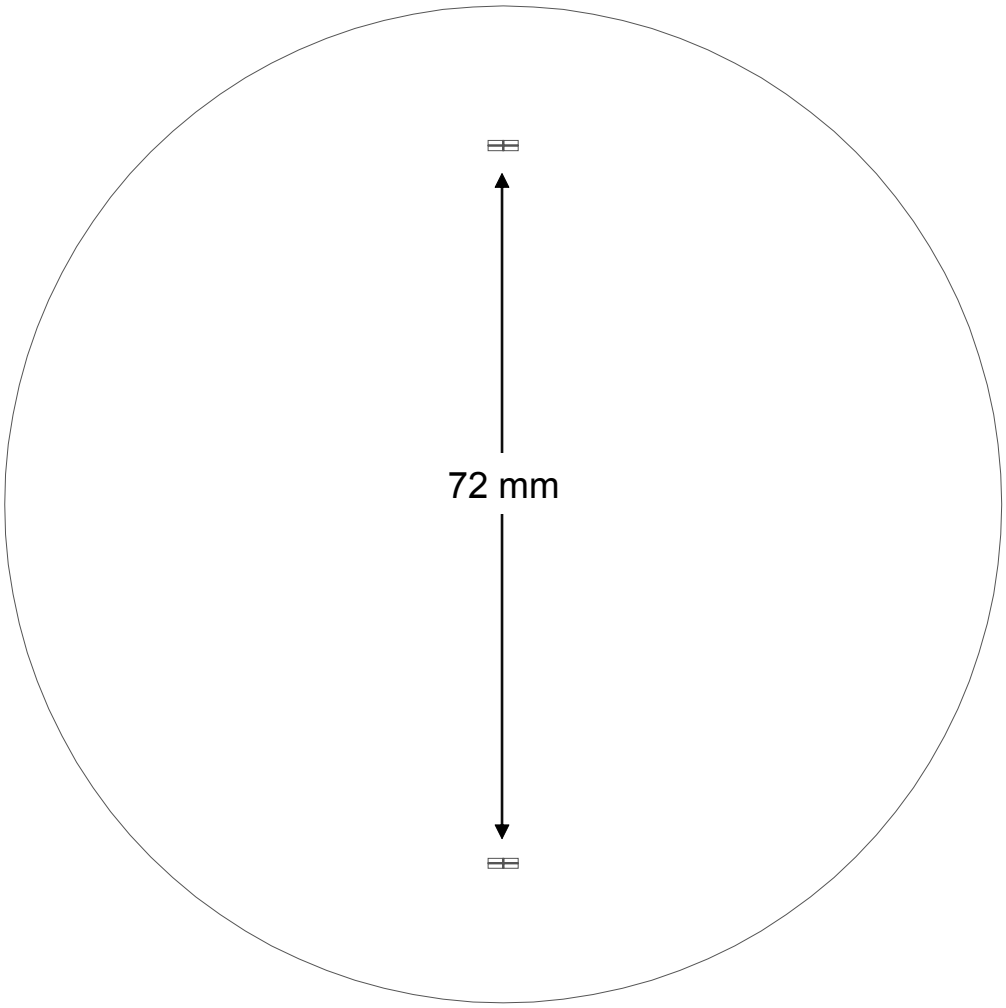


**Figure A-2.** Placement of alignment marks with respect to a 100mm diameter wafer.

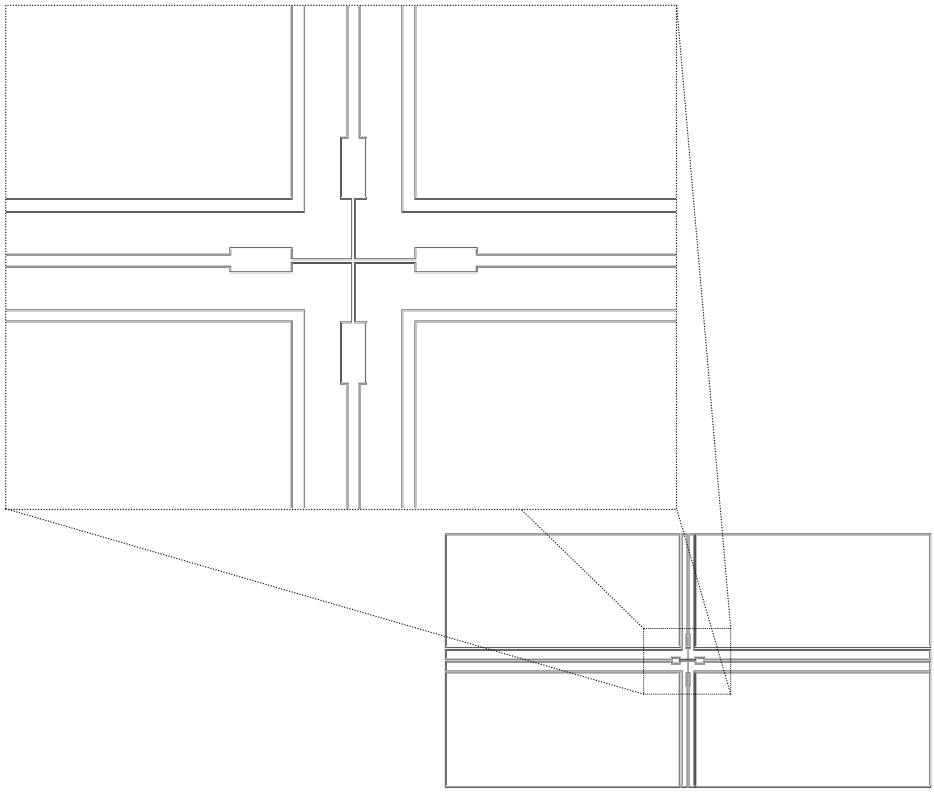

**Figure A-3.** Zoom-in of an alignment mark. The critical dimension (line thickness) of the center cross is 3 μm.

After the alignment marks are developed, it is necessary to coat 1 μm thick resist on the backside before the post-bake. This back-side coating is needed to protect the wafer from scratches during the etch of the alignment marks. The AME machine used for this etch is notorious for scratching the back-side of wafers. However, it is generally good practice to protect all bonding surfaces during wafer processing.

- **AME Etch Mask 0**: Steps 13-14

The alignment marks are etched only about 0.5 μm deep or less. This is shallow enough that spin coating subsequent resist will not be affected. This step can also be done in the STS etchers. A new STS recipe exists called "alignment" which etches excellent shallow alignment marks. Both methods have been used with equal success.

- **Deposit Oxide:** Steps 15-21

The oxide is necessary for two reasons: 1) The oxide serves as a protection layer for the two bonding surfaces. 2) On the top-side, the oxide serves as a nested mask for patterning the pressure drop channels.

It is very important that exactly the same thickness of oxide is deposited on both sides of the wafer. Because oxide on silicon is compressively stressed, a variation in oxide thicknesses will lead to excessive wafer bow that can prevent good wafer bonding. It is advisable to use a thermally grown oxide of desired thickness rather than a PECVD oxide followed by a densification as is shown in the process flow for simplicity. However, both routes work equally well.

- **Photolithography 2:** Steps 22-30

The purpose of this step is to pattern the entire reactor into the top-side oxide with "Mask Pressure Drop." This mask contains all reactor features, and will be the nested oxide mask used to pattern the pressure drop channels. After developing the pattern, it is necessary to coat the backside with 10 μm thick photoresist to prevent the entire back-side oxide from

being etched away in the subsequent BOE dip. It is also necessary at this point to dab photoresist over the alignment marks on the silicon wafer with a fab-tip in order to prevent any removal of the oxide in this area during BOE.

- **Photolithography 3:** Steps 33-41

This photolithography step patterns the bottom-side of the silicon wafer with "Mask Reactor Bottom." This mask contains all patterns that are to be etched through the wafer (500 μm deep regions). As with the previous lithography step, it is necessary after developing to coat the opposite side with thick photoresist to protect the patterned oxide from being removed. Again, dabs of resist over the alignment mark regions are necessary. During exposure, a backside alignment is necessary. This was originally done using IR alignment, with an alignment accuracy of approximately 5 microns. Using the newer EV1 exposure tool with integrated front and backside optics, much tighter alignments can be achieved.

- **Photolithography 4:** Steps 51-58

This final photolithography step patterns the top-side of the wafer using "Mask Reactor Top." This mask patterns everything except the pressure drop channels.

- **STS Etch 2:** Steps 63-65

This step etches the top-side of the wafer approximately 350 μm deep, blowing out the through-etched regions and etching the bifurcated channels. The process flow indicates that the acid-hood was used to remove the resist, and then the wafer was remounted to a handle wafer for the final STS etch. However, a more efficient method exists. This alternate

process performs an in-situ ash of the photoresist in the STS etcher allowing Steps 63-65 and Steps 70-72 to be combined into one continuous sequence. Once Step 63 is done, the STS recipe "O2 Clean" is used for 20 minutes to remove all resist from the top-side. Then Step 70 is performed to etch the pressure drop channels.

- **STS Etch 3:** Steps 70-72

For the shallow etch of the pressure drop channels, recipe "MIT 28A" on STS2 works the best. In order to ensure better uniformity across the wafer, the wafer is rotated by approximately $72^{o}$ ($1/5^{th}$ of a rotation) after every 4 μm of etching.

### A.2.2. Fabrication Issue- Teflon Side Walls

The use of a nested oxide mask to pattern the pressure drop channels creates an artifact during the DRIE process. The STS uses a fluorinated carbon compound as a passivation layer during the etch process that is relatively inert and is sputtered onto the sidewalls of the channels. This thin Teflon-like layer left behind by the primary 370 μm etch is not etched during the secondary shallow etch, leaving a thin wall of inert material at the end of the pressure drop channels as is shown below.

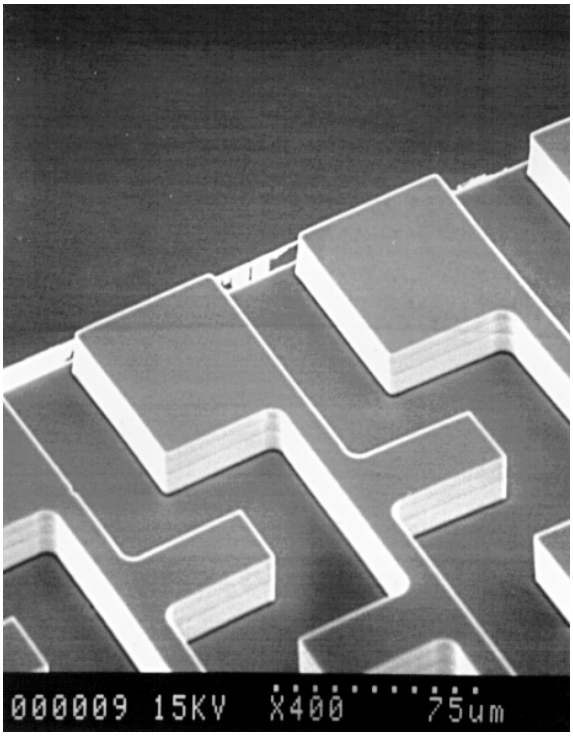


**Figure A-4.** Teflon side walls remaining after nested oxide etch.

These Teflon side walls can be problematic for shallow etches <10 μm as they can be quite thick and difficult to remove. For the more common deeper etches of 20-25 μm, they are quite thin and easily removed in a Piranha clean. However, the easiest solution to remove these walls is to perform a 2-3 second pure $SF_6$ isotropic plasma etch in the STS etcher after all anisotropic etching is complete. The isotropic etch removes a little silicon and thus undercuts the side walls, allowing them to fall away. Care must be taken to avoid generation of particles within the STS chamber. This procedure can be performed in the STS right after the shallow etch step.

### A.2.3. Uniformity of etching

During the design stage of the cross-flow microreactor, the commonly used etch recipe for DRIE on the STS machines was MIT 69A. This recipe gave the etch profiles seen in Figure 3-6 and repeated here for convenience.

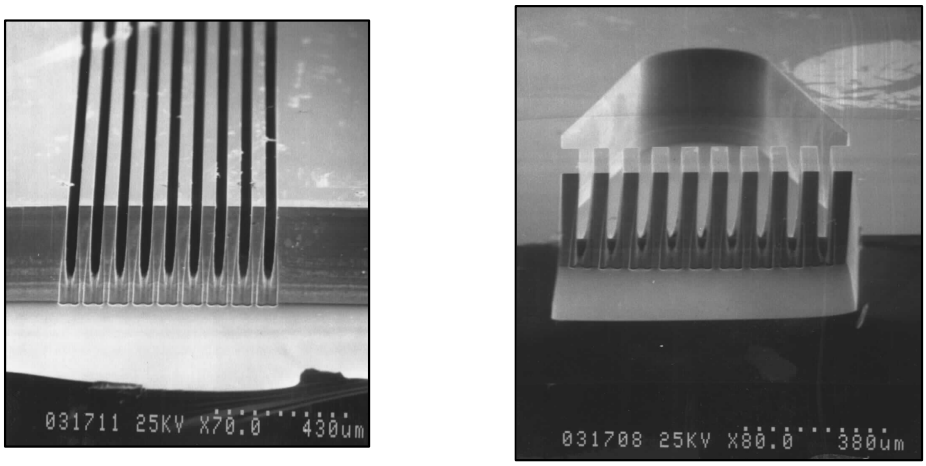


**Figure A-5.** Uneven etching due to transport limitations in high aspect ratio structures.

The STS etches wider regions faster than narrow and confined ones, particularly for high aspect ratio structures. This is presumably due to transport limitations impeding the flux of reactive ions to the bottom surface as the aspect ratio of the etch increases. Due to this performance, the reactor was designed with the packed-bed region through-etched in order to avoid any stagnation volume and assure even flow across the packed-bed as described in Section 3.3. Since that time, an alternate recipe developed at MIT called "MIT 37A" gives a more uniform etch. Shown below are SEMs taken for a test reactor etched with "MIT 37A" where the packed-bed region is etched approximately 300 μm deep.

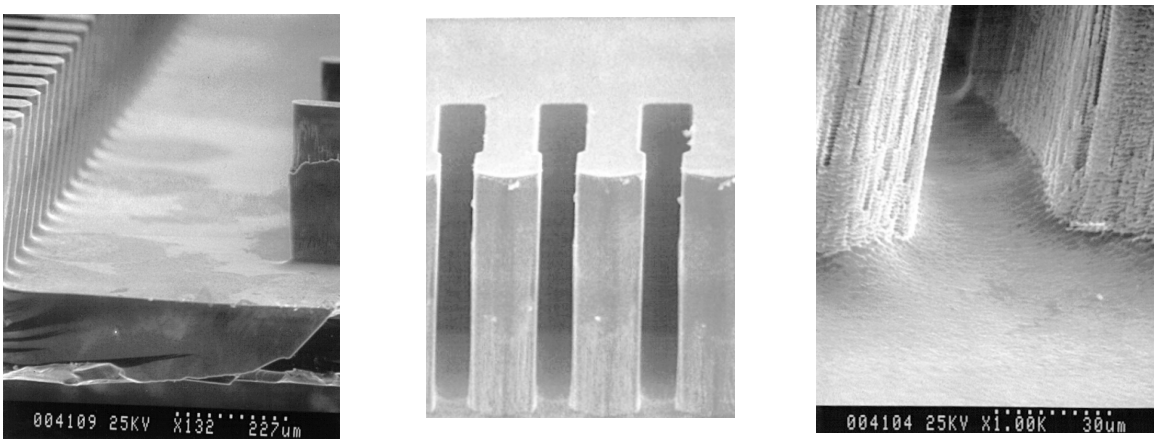


**Figure A-6.** Uniformity of etching using STS2 recipe "MIT 37A"

The etch is significantly more uniform than the reactor shown in Figure A-4. The spaces between the catalyst retainers are almost as deep as the wide, open packed-bed region. The difference between the depth of the wide channel and the spaces between the catalyst retainers is about 10 μm, or about $1/6^{th}$ of a particle diameter, effectively eliminating any bypassing of the catalyst. Although this recipe is significantly more uniform than previous recipes for etches within narrow spaces, the depth of the channels across a wafer typically varies by at least 20-30 microns. Therefore, it is still a good idea to perform the through-etch to guarantee a constant and reproducible packed-bed volume reactor to reactor.

### A.2.4. Photolithography Masks

The photolithography masks are shown on the next pages. All masks were dark field masks used with positive photoresist.

The vertical 100 μm channel that runs along the left side of Mask "Pressure Drop" and Mask "Reactor Top" was designed for alignment to the optics of the diesaw. However, it was found that the wafer weakened significantly with such a long channel etched across it and frequent fractures along the channel line occurred. Therefore, in future processing with these masks, a photoresist dab is required to cover up this channel before etching.

The 8 holes that are seen on the sides of each reactor in all three masks were intended to be contact holes for electrical connections to heaters and temperature sensors that were to be designed in future iterations. However, they were never used and are currently artifacts on the reactor chip. They can be covered up with photoresist dabs before etching to prevent their fabrication into silicon, but it is not necessary.

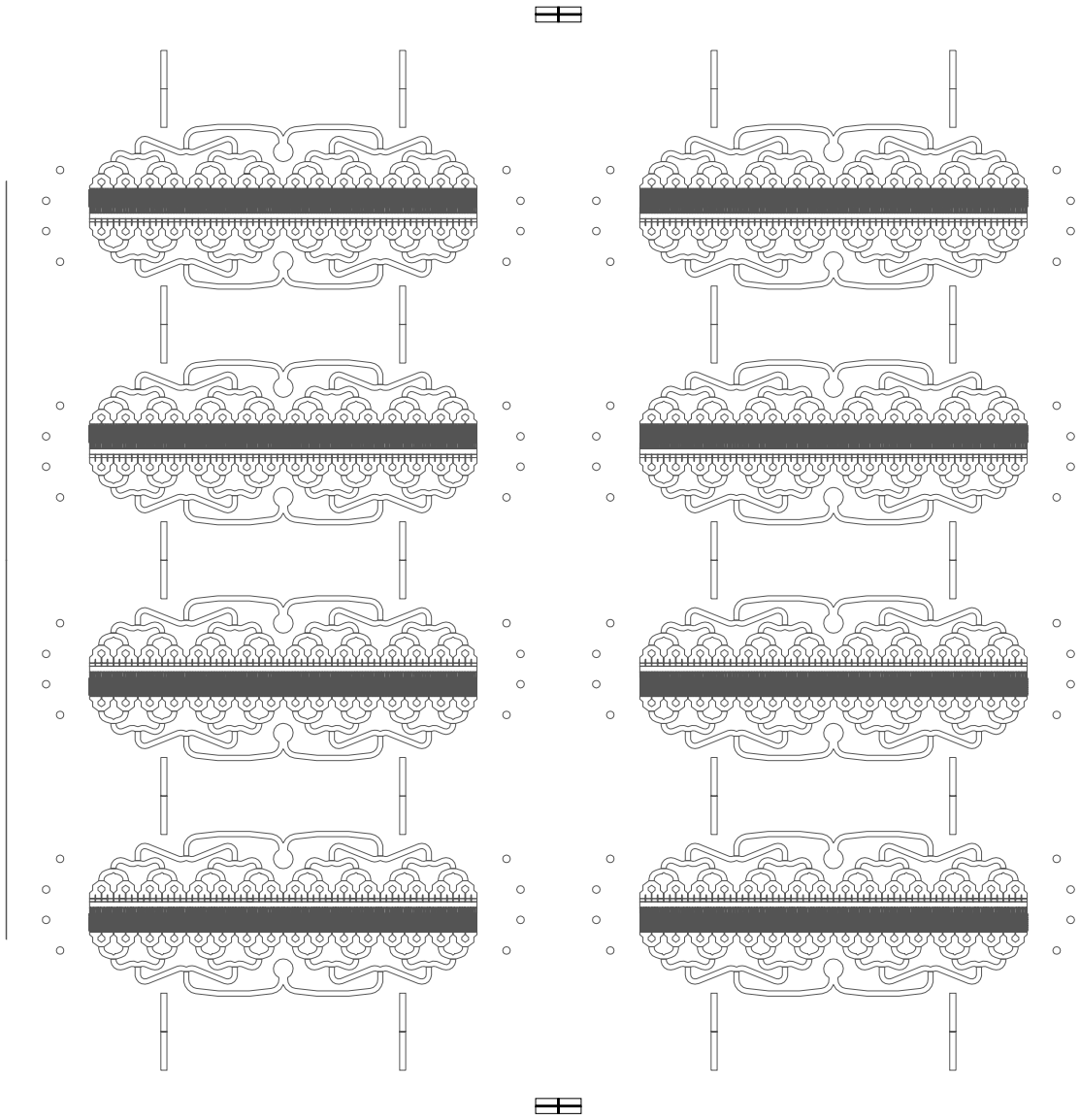

**Figure A-7.** Mask “Pressure Drop”

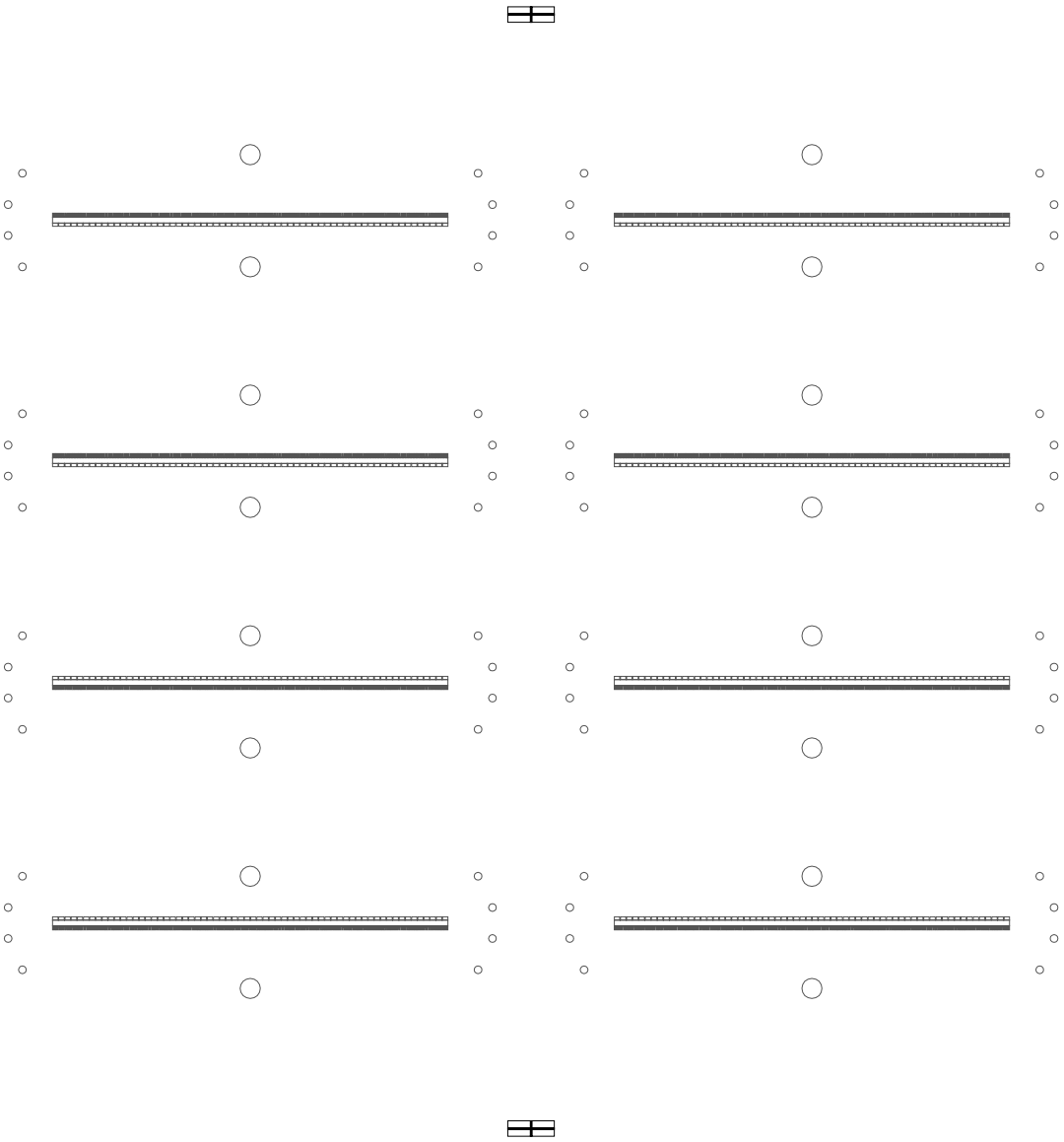

**Figure A-8.** Mask “Reactor Bottom”

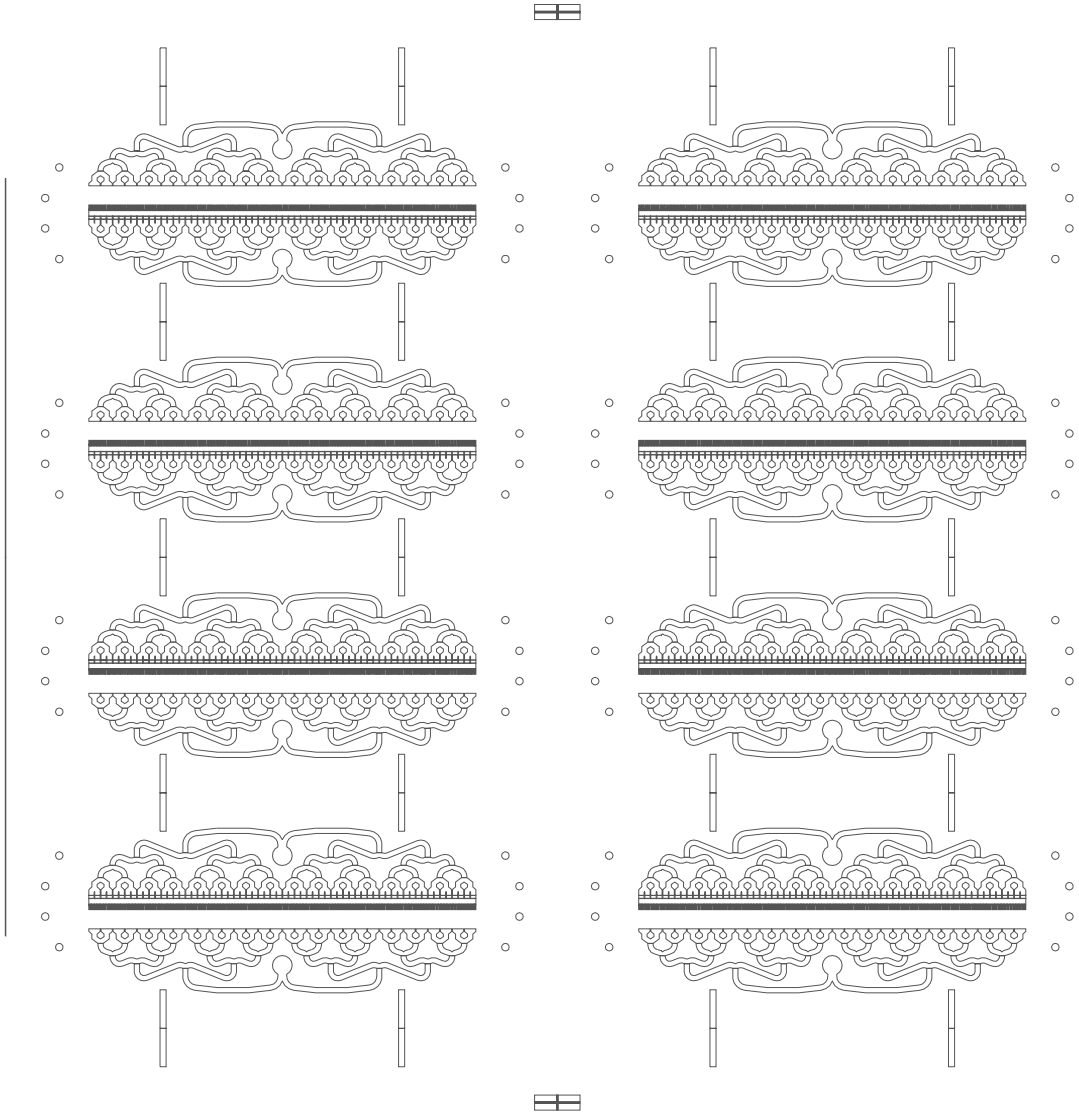

**Figure A-9.** Mask “Reactor Top”

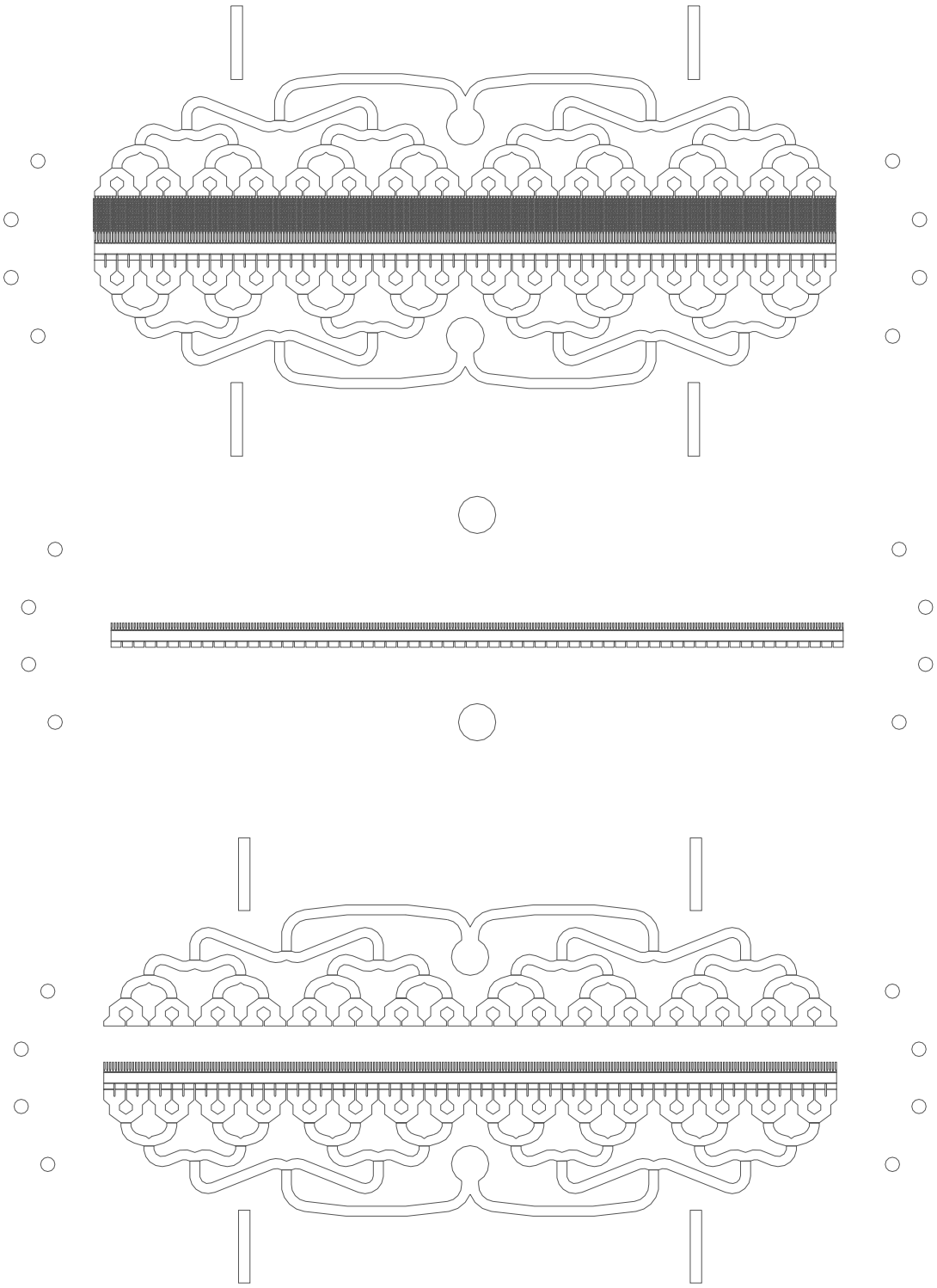

**Figure A-10.** Close-up views of a single reactor on Masks “Pressure Drop,” “Reactor Bottom,” and “Reactor Top” in order from top to bottom.

## A.3. Detailed Fabrication: Wafer Bonding and Diesaw

Once the reactor wafer is fabricated, the wafer must be capped on the top and bottom with Pyrex wafers using an anodic bond. The bottom Pyrex wafer, bonded first, consists of 16 fluidic through-holes for the inlets and outlets of the 8 reactors. The top wafer, bonded second, is a flat featureless Pyrex capping wafer. Although the anodic bonding procedure is quite standard and robust, one issue exists regarding performing two anodic bonds to the same silicon wafer. Anodic bonding requires electrical contact via electrodes to both the silicon and Pyrex bonding wafers. This electrical contact is essential for forming the electrical depletion layer necessary for a good bond. However, once the first Pyrex wafer has been bonded, electrical contact to the silicon wafer becomes blocked by the bonded Pyrex, preventing the anodic bond of the second wafer.

To work around this problem, an extra through-hole was drilled through the center of the bottom Pyrex wafer. This through-hole provides an opening through which electrical contact can be made to the underside of the silicon wafer for the second bond. To make this contact, a small metal spring was used that expands to make contact to both the electrode and the silicon wafer as shown in the figure below.

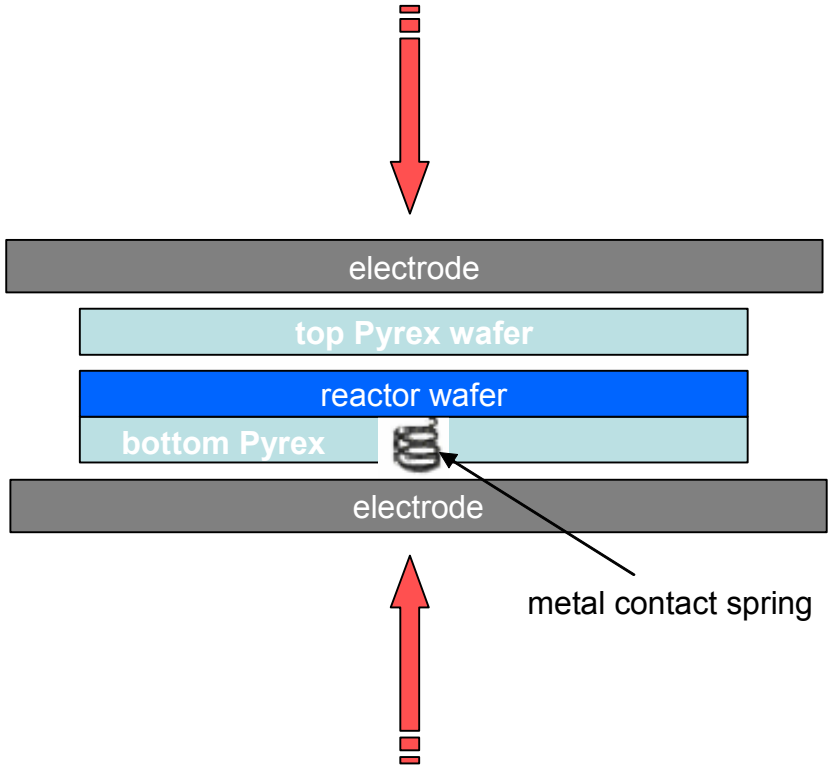


**Figure A-11.** Setup using a metal contact spring to make electrical contact to the reactor wafer during the second anodic bonding step.

The requirements for this metal spring are that it must survive the conditions of the anodic bond; specifically, 800 Volts at 500 $^{o}$C. The spring's diameter must also be less than the thickness of the silicon wafer. If the spring bulges out of the hole once it is compressed due to its thickness, the wafer stack will crack. Further, the spring should be cut short enough that the number of turns of the coil times the spring diameter must also be less than the silicon wafer thickness, preventing stressing and subsequent cracking of the wafer stack. The MIT machine shop has a variety of spring materials that meet these criteria. The spring

is most easily loaded into the setup using the Electronic Visions contact aligner, even though the actual bond requires no alignment. The process flow and hole layout are given below.

| Procedure | Process # | Facility | Process Description | machine | café name | Chemical | Recipe | Comments | Status |
|---|---|---|---|---|---|---|---|---|---|
| **Bonding Device** | | | | | | | | | |
| **Clean** | 1 | TRL | Piranha Si and Pyrex through-hole wafer | acid-hood | acid-hood | piranha | STD | Clean wafers before bonding, 10 minutes | Red |
| **Anodic Bond** | 2 | TRL | Bond reactor wafer to through-hole wafer | Electronic visions | Evalignerbonder | | STD | Align by hand, recipe 500 C, 800V, 5 minutes | Red |
| **Clean** | 3 | TRL | Piranha wafer stack and pyrex | acid-hood | acid-hood | piranha | STD | 10 minutes | Red |
| **Anodic Bond** | 4 | TRL | anodic bond pyrex to stack | Electronic visions | Evalignerbonder | | STD | **USE spring**, recipe 500 C, 800V, 5 minutes | Red |
| **Die Saw** | | | | | | | | | |
| **Die Saw** | 5 | ICL | dice reactors | Disco DAD-2H/6T | diesaw | use black blade | STD | 36400 um horiz x 3 cuts, 15540 um vert x 5 cuts | Dirty |

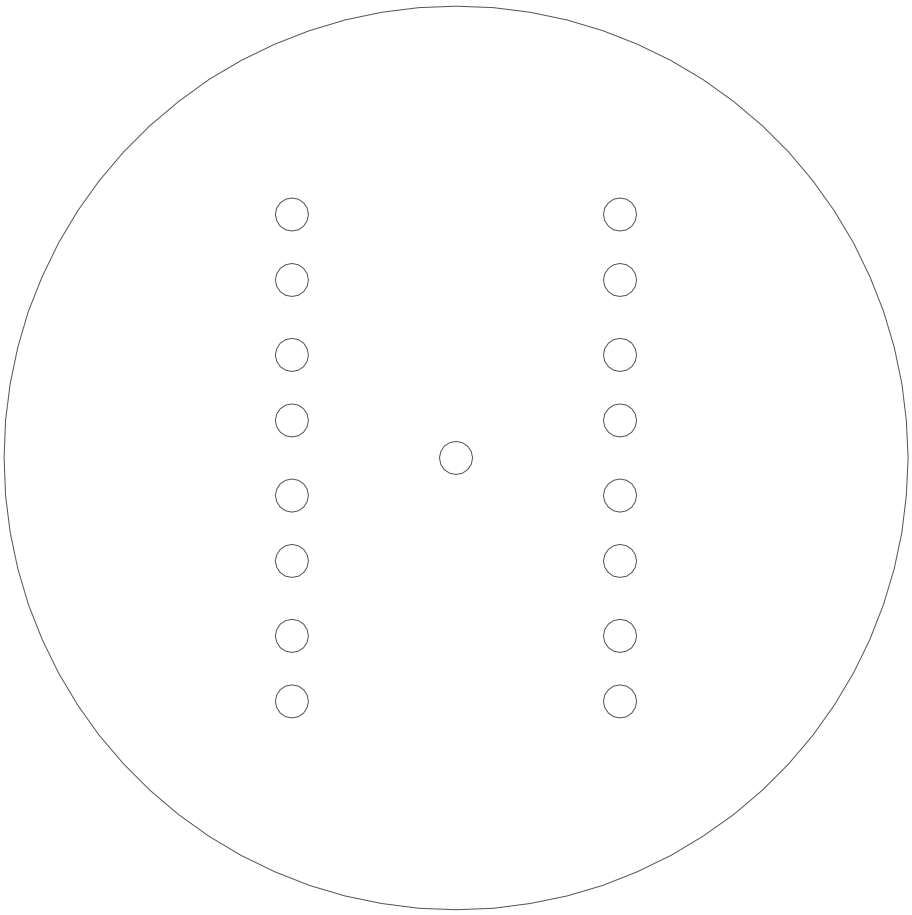

**Figure A-12.** Layout of the 2 mm through-holes in the bottom Pyrex wafer. The two vertical columns of through-holes are inlet and outlet ports for the reactors. The center hole is for the metal contact spring for the second anodic bond. This wafer is bonded to the reactor wafer first.

# Appendix B

# Packaging: Direct Brazing of Tubing to the Microreactor

This appendix summarizes the progress to date on the development of a new packaging scheme for microreactors; specifically, the brazing of Pyrex or Kovar tubing directly to the anodic bonded Pyrex capping wafer of a microreactor. The brazing procedure is covered as well as a discussion of initial tests and difficulties.

In Section 4.1.2, an alternate packaging scheme to the compression seal methodology used throughout this thesis was presented. This alternate scheme involves the direct sealing of tubing to the Pyrex microreactor capping wafer in order to obtain a higher temperature and pressure fluidic seal. The compression packaging scheme has an upper limit of approximately 10 atm pressure and 280-300 $^{o}$C, limiting the versatility of the microreactor for catalyst testing. Brazing tubing directly to the reactor allows the reactor to be isolated from the large thermal mass of the metal base, enabling the use of integrated microfabricated heaters for reactor heating and temperature control. Further, power requirements to maintain the microreactor at elevated temperatures would be reduced dramatically. Although not important for catalyst testing, the reduction in operating costs due to the reduced heat load would be a significant advantage when applying a microchemical platform for chemical production. Finally, difficulties involved with disassembling the compression seal reactor packaging can be avoided.

## B.1 Brazing Scheme

The concept of forming fluidic connects using tubing directly brazed to a microfabricated device has been previously demonstrated for the direct connection of Kovar tubing to silicon fluidic ports by Harrison [1] for the packaging of the MIT microengine. Harrison brazed preformed glass frits that were thermally matched to the Kovar tubing and silicon chip to create a hermetic seal directly at the surface of the wafer. This concept was extended to microreactors with the development of a similar technique to braze tubing directly to the Pyrex capping wafer in the cross-flow microreactor. Unfortunately, the same

materials used by Harrison cannot be used for the microreactor as the temperatures employed during the braze to silicon is hundreds of degrees higher than the upper stability limit (for short times) of Pyrex of approximately 600-700$^{o}$C. Therefore, new materials and recipes were employed for this process.

The brazing scheme utilizes a grass frit material that has been preformed into an annulus as illustrated below.

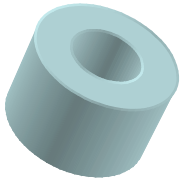

**Figure B-1.** Illustration of a glass frit perform annulus.

The bead material is chosen to have a thermal coefficient of expansion as close as possible to Pyrex as well as a softening temperature that is close to the annealing temperature of Pyrex. The tube to be bonded is inserted into the center hole, and the bead is compressed under a weight at temperatures near the bead's softening point. Pyrex is internally mobile at these temperatures, creating active bond interfaces between the Pyrex wafer, the tube, and the bead. Upon cooling, a bond forms at these interfaces that creates the hermetic seal. Shown below are photographs of microreactor test pieces with 2.0 mm O.D. Pyrex and Kovar tubes directly brazed to the Pyrex capping wafer. It has been found that Pyrex 7740 tubes give better reproducibility and higher yields than Kovar, but Kovar tubing is rated to higher pressures than the Pyrex tubing. Pyrex tubing is rated by the manufacturer to approximately 25 atm of pressure.

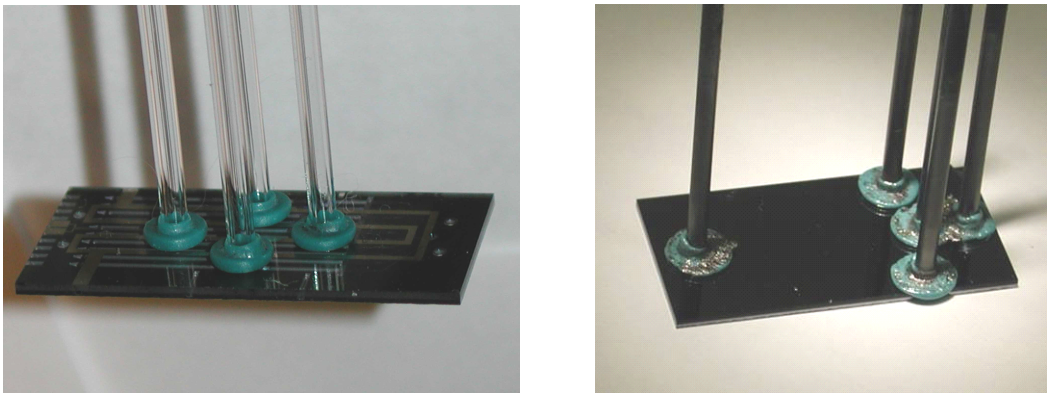

**Figure B-2.** Photograph of test pieces with Pyrex (left) and Kovar (right) tubes brazed to the Pyrex capping wafer.

The interfaces between the bonding surfaces are shown in the cross-section photograph below.

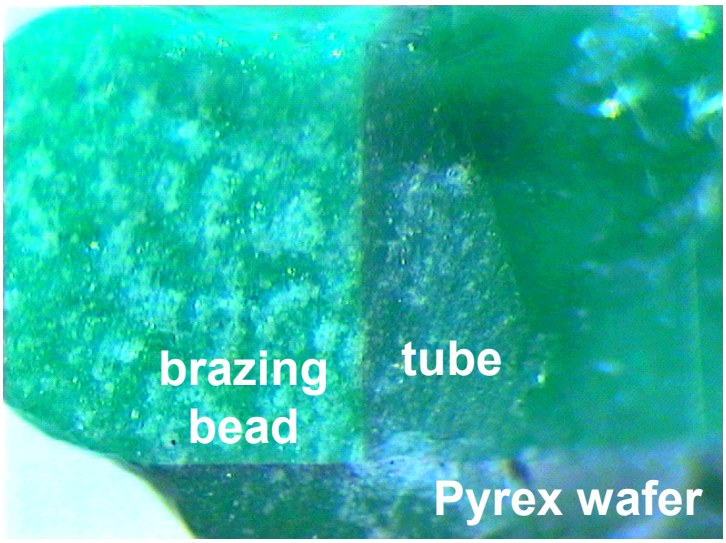


**Figure B-3.** Photograph of the cross-section of a bond with a Pyrex tube. The bonding interfaces are clearly seen.

The bond cross-section indicates clear and seamless interfaces between bonding surfaces creating the fluidic seal. The cross-section also indicates that the bead does not wet the Pyrex wafer surface (from contact angle), indicating a potential area for improvement of the brazing process. Improved wetability between the Pyrex surfaces and the bead would improve the quality of the bond. Although surface treatments were used to improve surface activation as will be discussed in following sections, wetability can be improved by changing the atmosphere under which the bond occurs. Currently, a nitrogen rich air atmosphere is used for brazing. Harrison [1] has reported that wet nitrogen and propane/air atmospheres improved the wetability of glass bonds to silicon.

With Pyrex tubing, bonds have been tested at nitrogen pressures up to 25 atm at 450-500$^{o}$C. The upper pressure limit is controlled by manufacturer ratings on the Pyrex tubing and not by the bond quality. Room temperature tests with brazed Kovar tubing have been performed successfully at pressures up to 50 atm.

### B.1.1 Failure Modes- Using a stabilizer plate

Any moment applied at the end of a tube provides significant stress at the bond. The primary modes of failure are either the breakage of the tube (particularly for Pyrex tubing) or the shearing of the Pyrex. When the latter occurs, the Pyrex layer underneath the bond actually breaks away, leaving the bond interface completely intact as shown below.

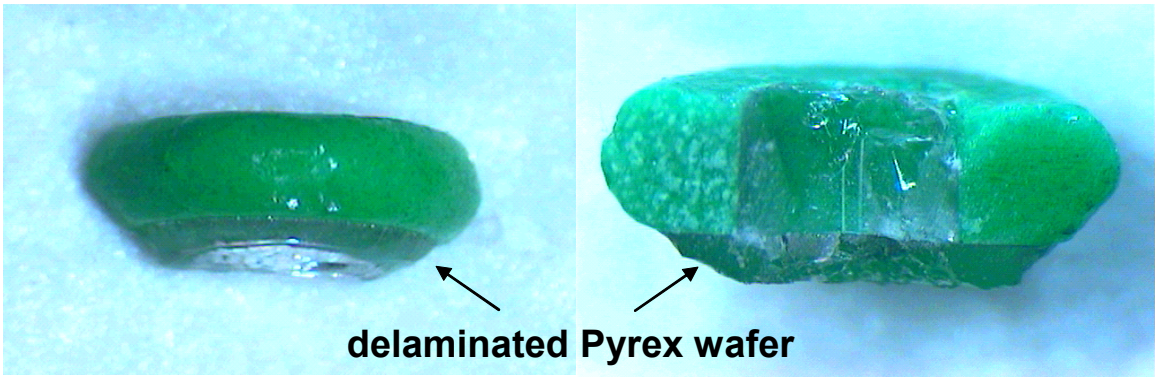


**Figure B-4.** Photographs of a cross section of the delamination of the Pyrex wafer underneath the bonding interface. The bond interface remains intact attesting to the strength of the bond.

The cross-sections above show that the Pyrex wafer underneath has completely given away and delaminated, while the bead/Pyrex interface remains intact. These failure modes attest to the integrity of the bond. The most common failure when using Pyrex tubing is breakage of the tubing right above the bond, while with the stronger Kovar tubing, the most common failure is delamination of the Pyrex as shown in the above figure.

To add strength to the package, particularly for the Pyrex tubing, a thin metal plate is epoxied to every tube as shown below, preventing moments at the tube ends from being transferred to the bond. The stabilizer plate also spreads out any torque on the reactor to all the tubes, strengthening the entire reactor package. Once the stabilizer plate is epoxied, the package is quite robust to impacts and moments.

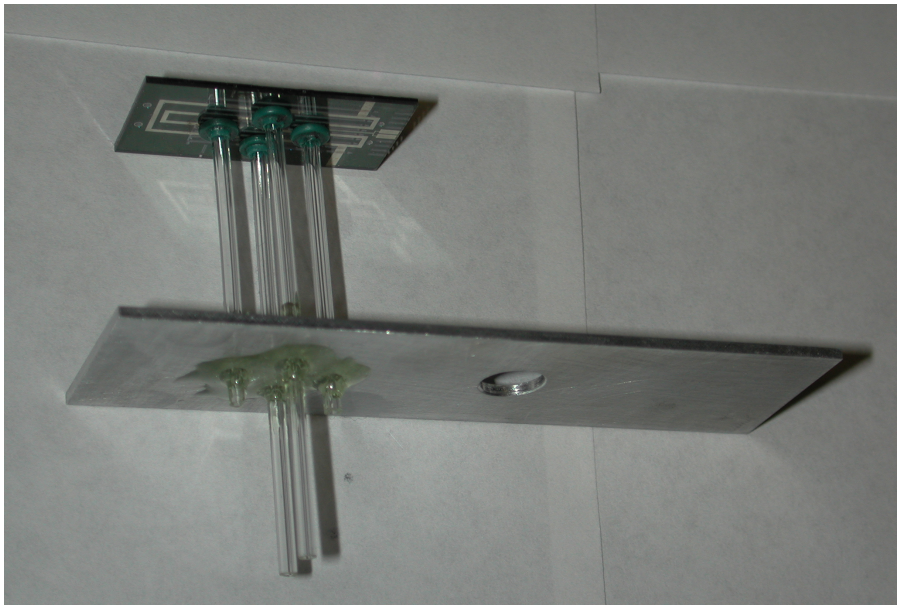

**Figure B-5.** Photograph of the stabilizer plate glued with epoxy to a microreactor with brazed Pyrex tubes.

The plate is glued with epoxy at least 1.5 inches from the chip using a standard quick setting epoxy (5 minute epoxy, *DEVCON)*. The choice of epoxy and distance is very important for the ability of the packaging to survive high temperatures. When the chip is heated, the tubes provide a pathway to conduct heat away from the chip. Therefore, if the plate is fixed too close to the chip, the epoxy would quickly burn or degrade as it reaches its upper temperature limit of approximately 100$^{o}$C. Section B.3 shows some thermal profile results for brazed tubes at elevated temperatures. If a high temperature ceramic adhesive is used instead of epoxy, the Pyrex tubing cracks at high temperatures. This is due to the thermal expansion of the Pyrex tubing as heat is transferred down the tube. Ceramic adhesives are too rigid to allow this expansion. It was found that '5 minute epoxy' when cured remains soft enough to allow repeated expansion and contraction from thermal cycling

while still providing the necessary strength to absorb moments without transferring stress to the bond.

### B.1.2 Fluidic Seal to the Brazed Tubes

Once the stabilizer plate is fixed to the tubing, fluidic connections need to be made to the tube ends. A variety of methodologies were tested including HPLC fittings and graphite ferrules. It was found that the most efficient and effective technique to make fluidic connections to the package is through o-rings sealed to a machined metal base as shown in the photograph below.

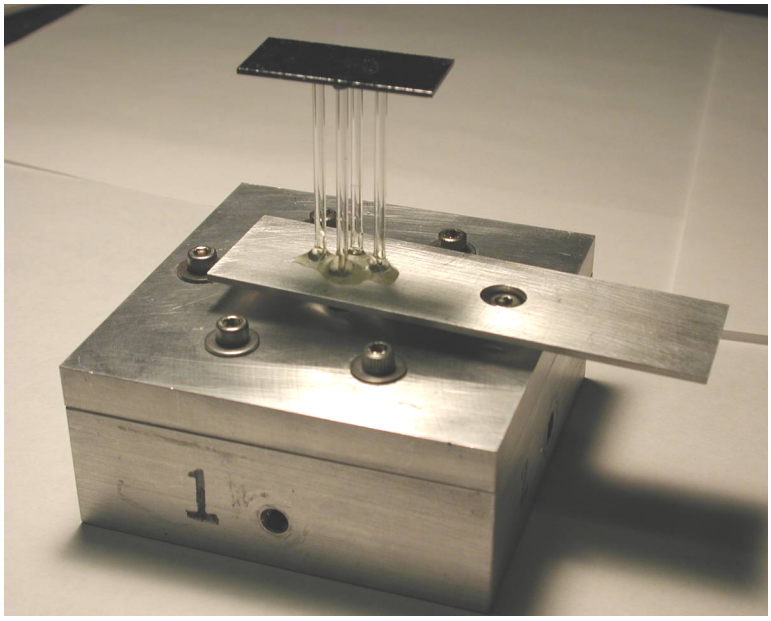


**Figure B-6.** Photograph of the fully packaged microreactor. Fluidic connections are made to direct brazed tubing via o-rings sealed to a stainless steel base.

These seals are reversible, allowing multiple packaged reactors to be tested on the same platform while maintaining the integrity of both the metal base/o-rings and the reactor/tube package. In this way, the reactor can also be reused.

The design of the metal base and compression plate/o-ring groove is not trivial for this type of seal. This seal requires o-rings to seal in two different directions, vertically between the metal base and a compression plate, and radially between the o-ring and the tube. Traditional o-ring grooves are intended to only seal in one direction. Therefore, a modified crush seal was used to obtain the bi-directional seal. This seal is illustrated below.

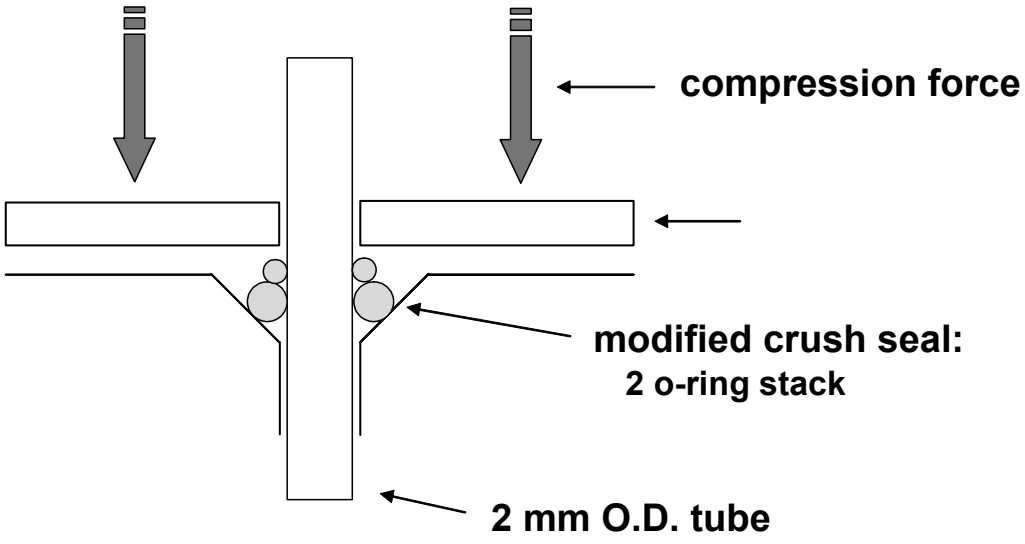


**Figure B-7.** Illustration of the modified crush seal technique used to create a bi-directional o-ring seal

In traditional crush type seals, the o-ring is squeezed beyond it's recovery limit, making the o-ring one time use only. The use of two o-rings is not standard but was found to prevent the squeezing of the o-rings beyond their limits, rendering them both reusable for

multiple seals. Further, the use of two o-rings was found to create a more reproducible seal as the face to face seal between the o-rings leads to a natural bi-directional squeezing due to the round shape of the top o-ring squeezing into the bottom o-ring. This leads to an excellent seal with 100% reproducibility. The hardness of the o-rings was chosen carefully after consultation with the manufacturer to ensure a bi-directional seal and prevent the breakage of the Pyrex tube (as described in the next paragraph). This seal works equally well with both Pyrex and Kovar tubing.

The choice of hole diameter is also a very important issue. The Pyrex tubes do not stay perfectly straight during the brazing process. Since the Pyrex is heated up to temperatures that ensure active bond interfaces, the Pyrex tubes bend slightly. Therefore, the tubes do not stay on center after the braze. Typically, o-ring seals self-center upon compression, which would lead to significant stress on the tubes. The hole diameters were made large enough to ensure that the off-center tubes could be inserted into the metal base while still being small enough that the o-rings could make a reproducible seal. The use of 2 o-rings helps in this matter as well. The specifications on all machined components, the o-rings, and the stabilizer plate are given in Section B.5.

## B.2 Test Results

### B.2.1 Thermal Profile of a Pyrex Tube

A test was performed to determine the thermal profile of a brazed Pyrex tube with a chip heated to ~500 $^{o}$C. A single tube test piece was fabricated. A type K thermocouple was used to determine the temperature of the surface of the 2 mm tube as a function of distance along the tube.

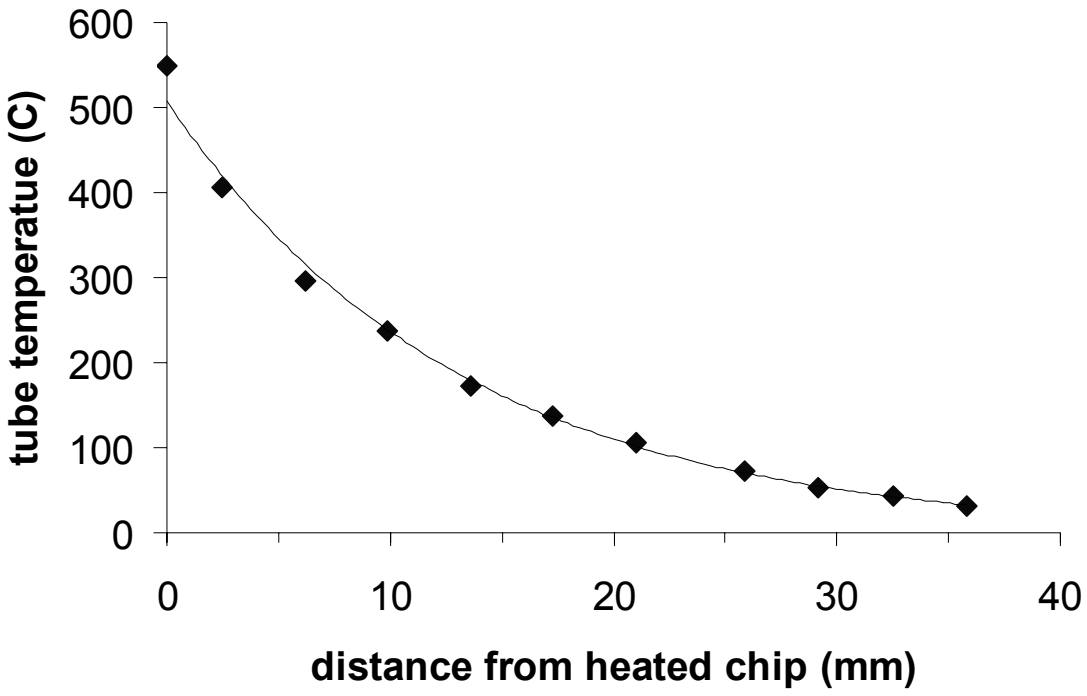


**Figure B-8.** Thermal profile along a brazed 2 mm Pyrex tube with a heated chip.

The thermal profile confirms that the stabilizer plate should be placed approximately 1.5 inches (38.1 mm) away from the chip to ensure that even at the highest operating temperatures, the epoxy stays cold.

### B.2.2. Power Required for Heating

The brazed tubing adds additional conduits for heat transfer out of a heated reactor chip, increasing the power required to maintain a given temperature. Heating studies were performed using a cross-flow microreactor test piece in the two different orientations shown below. Although the reactor has only 2 fluidic inlet/outlet ports, 4 brazed tubes were used to increase stability during the brazing process. With 2 tubes, the compression weight used to provide pressure during the bond would tip over causing poor bonding. With 4 tubes, an even pressure is able to be applied.

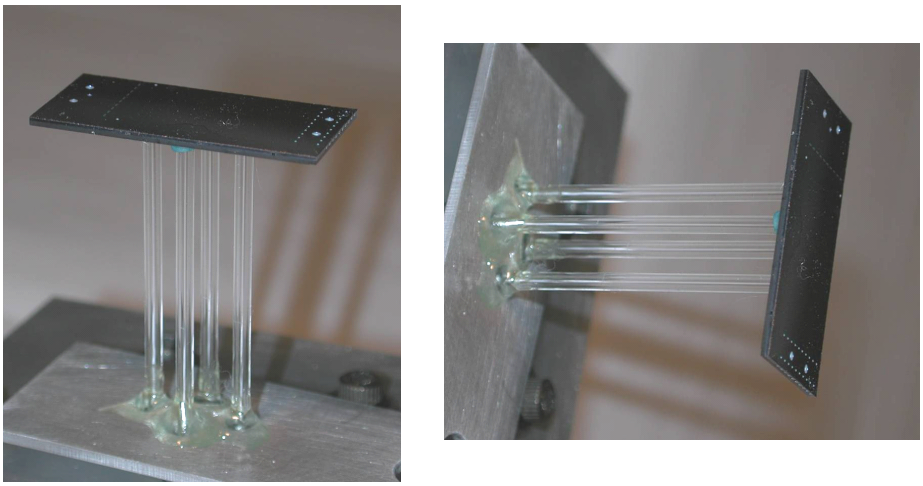

reactor horizontal

reactor vertical

**Figure B-9.** Orientations used for heating tests.

Using these orientations, the reactor was pressurized to 312 psi (22.2 atm) and heated using on-chip thin-film platinum heaters. The figure below shows the power required to heat up the cross-flow microreactor with integrated heaters.

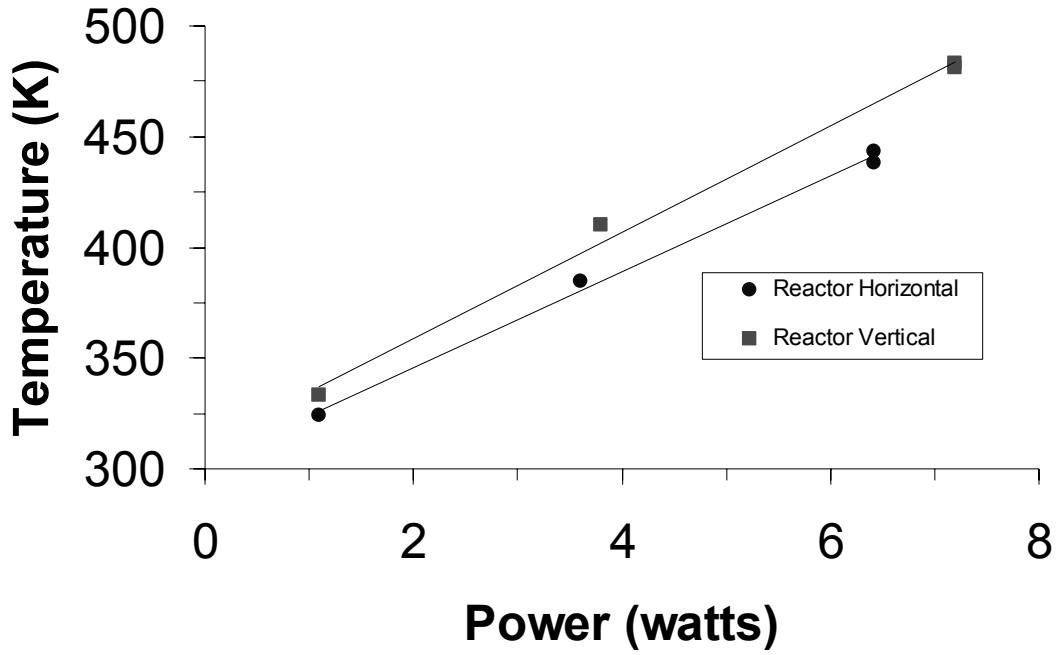


**Figure B-10.** Temperature versus power for the cross-flow microreactor heated with an integrated thin-film platinum heater for two reactor orientations. The reactor was pressurized to 22.2 atm with 4 brazed Pyrex tubes.

### B.2.3. Heating and Cooling Time

One advantage of microreactors is that the small thermal mass of the chips allows for relatively fast heating and cooling, speeding up set-point changes and experimentation. However, with the compression seal packaging used throughout this thesis, the thermal mass of the system was dictated by the thermal properties of the metal base and compression plate, preventing rapid set-point changes as well as requiring significant heater power to maintain

elevated temperatures. The brazed tubing packaging scheme should reduce the heat load needed to heat the reactor. Heating and cooling tests were performed on a cross-flow reactor with 4 brazed 2 mm Pyrex tubes for the two orientations. For the horizontal reactor, the integrated heaters were set at a constant power of 6.4 W at time zero and allowed to reach steady state. Once at steady state, the power was shut off and the cooling rate was measured. For the vertical reactor, a power set-point of 7.2 W was used. The curves show that about 150 seconds are needed to heat or cool the reactor about 200 $^{o}$C.

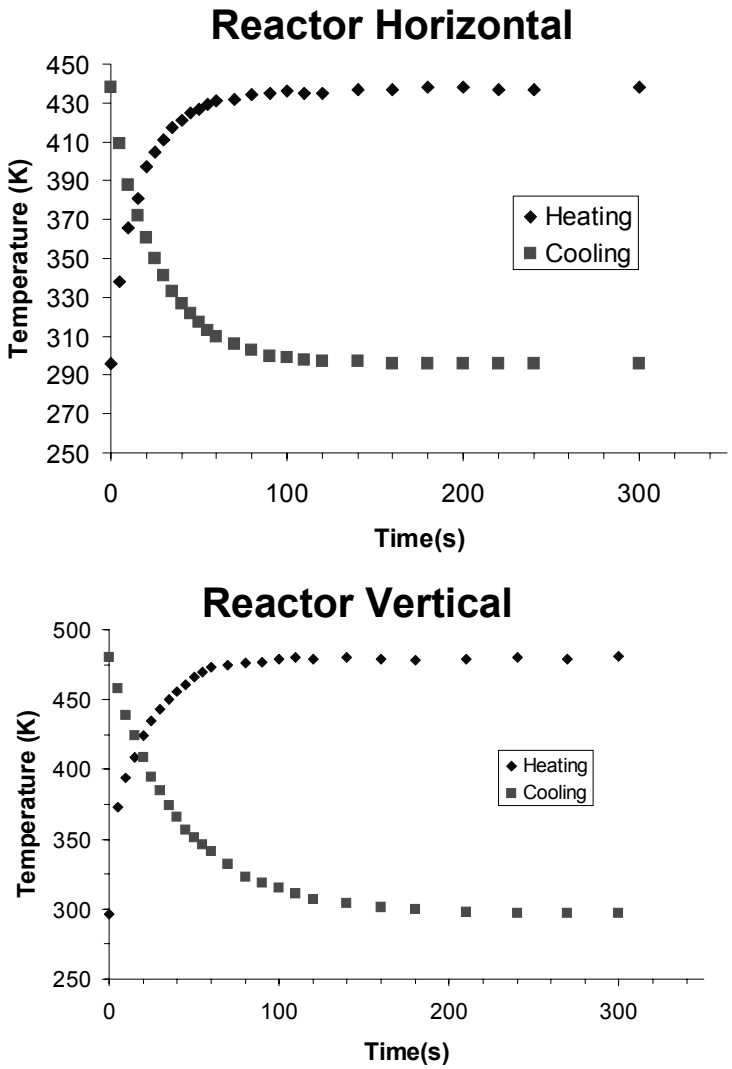


**Figure B-11.** Heating and cooling curves for the cross-flow microreactor with integrated heaters and 4 brazed Pyrex tubes

## B.3. Current Limitations

The application of direct brazed packaging is currently limited by the ability of the bonds to survive a large number of thermal cycles. This is due to the overall packaging scheme employed with the o-ring seals and Pyrex tubing. A single tube bonded to a reactor can withstand a multitude of thermal cycles from room temperature to 500 $^{o}$C. In fact, failures have not been seen with a single tube bond. However, when multiple tubes are bonded to the same chip, after a few thermal cycles, failures begin appearing in the form of leaks in the bonding bead. This is presumably due to the lateral thermal expansion of the silicon chip at high temperatures. The Pyrex tubes are rigidly held in place at both ends by the brazing bond and by the o-ring seals. However, a differential thermal expansion exists because the silicon laterally expands when heated, but the o-ring seals remain at room temperature. This puts significant stress on the tube/bond as the tubes are being pulled apart at one end, leading to eventual failure of the packaging. For the successful implementation of this packaging scheme, either a different method to making fluidic connections to the tubes is needed that can accommodate the expansion of the silicon chip or flexible tubing materials need to be explored. With flexible tubing, the tube would be able to absorb the stress by changing shape instead of focusing the stress at the bond. As of now, temperatures up to 150-200 $^{o}$C remain the upper operating limit for thermal cycling with this packaging scheme.

## B.4. Detailed Brazing Procedure and Specifications

### B.4.1. Specifications

**Glass beads**: Vendor: Electro-Glass Products
ATTN: Pat Brady
724-423-5000 (USA phone number)
Material SCC-7
Color: Natural
Shape: Annulus, 1 hole
Dimensions: O.D.= 0.185 – 0.2 in.
I.D. = 0.080-0.084 in
Height=0.096 in.
Properties: Working Temp: 690 $^{o}$C
Expansion: $32x10^{-7}$
Cost: Roughly US $500 for 500 beads

**Pyrex Tubes:** Pyrex brand Glass Tubes (7740)
Vendor: Corning (1-800-492-1110 USA phone number)
Catalog Number: 234440
Size: O.D. 2 mm
Wall Thickness: 0.5 mm
I.D..: 1 mm
Length for brazing: 2.5 inches (63.5 mm)
Cost: Approximately 5 cents (US) per brazed tube.
Thermal Expansion: $32.5x10^{-7}$ cm/cm/$^{o}$C
Upper working Temp: 490$^{o}$C
Maximum pressure: 370-500 psi (25.3 – 34 atm) at 25$^{o}$C

**Kovar Tubes:** Glass Sealing Alloy Tube
Iron 54% Nicket 29% Cobalt 17%
Vendor: Goodfellow (England)
O.D.: 2 mm
I.D. 0.9 mm
Catalog Number: FE047301
Cost: Expensive

**Straightening Needles:** single-use B-D brand Needles
Material: stainless steel
Vendor: Becton Dickinson and Company
Model number: 21g2 Precision Glide Needle
Remove plastic and adhesive and then insert into tube

**Grafoil:** Grafoil GTB
0.010" Thick
Item #: 2400240002GTB
Vendor: Sealing Devices, Inc. (Lancaster, NY)

**Cleaning Chemicals:** Standard Acetone, Ethanol, and DI water

**$O_2$ plasma sterilizer:** Harrick Plasma Cleaner/Sterilizer
Model #: PDG-32G

**Brazing Oven:** Thermolyne 48000 Furnace

**Epoxy:** 5 minute epoxy, DEVCON corp.

**Drawings of Machined Parts:** See Section B.5

### B.4.2. Procedure

The brazing procedure involves a careful cleaning step and then assembly into a machined setup for alignment. The beads and the tubing come from their respective manufacturers with some variation in their inner and outer diameters respectively. Therefore, the first step involves selecting beads and tubing together that have at most a 0.05 mm difference between the inner diameter of the bead and the outer diameter of the tubing. The tubes are cut approximately 2.5 in. using a standard capillary scorer used for cutting glass capillaries. The reactor, tubes, and beads are then rigorously cleaned using an acetone, ethanol, DI water rinse and dried in an standard convection oven at 80 $^{o}$C for 10-15 minutes. Following the drying procedure, all the pieces including the reactor are placed into an air plasma sterilizer at high power for 10 minutes. The air plasma serves to remove all residual organics from the bonding surfaces. Following this plasma clean, care must be taken when handing the pieces and only Teflon tweezers must be used from this point onwards. As a

general rule, powder free nitrile gloves must be used during the entire brazing process. After the plasma clean, the pieces are assembled into the brazing setup.

The brazing setup is comprised of a stainless steel platform upon which the reactor is placed bonding side up. The tubing and beads are assembled and a stainless steel compression plate is placed on top. The holes of the compression plate are 33 mm in diameter and the plate weighs ~130 g. A thin layer of porous laminated graphite (grafoil) with punched through-holes is placed between the compression plate and the brazing beads. The grafoil prevents the compression plate and the beads from bonding together, enabling the reuse of the plate for subsequent bonds. It is important to use a thin layer of grafoil as provided in the specifications as thicker layers tend to prevent even transfer of compression force to the beads, resulting in uneven bead compression. To keep the Pyrex tubing from bending during the brazing process, it is necessary to place a straightening needle inside each tube. The stainless steel needle does not bend at the brazing temperatures. The needles are easily removed after the braze and can be reused about 3-4 times before they must be replaced due to oxidation of the surface. An illustration of the brazing setup is given below. It is necessary to place compression stops on the sides of the reactor to control the final thickness of the brazing bead after heating. Stops 1 mm thicker than the reactor chip have been used. These stops are usually just stacks of old or broken microreactor chips and have worked quite well.

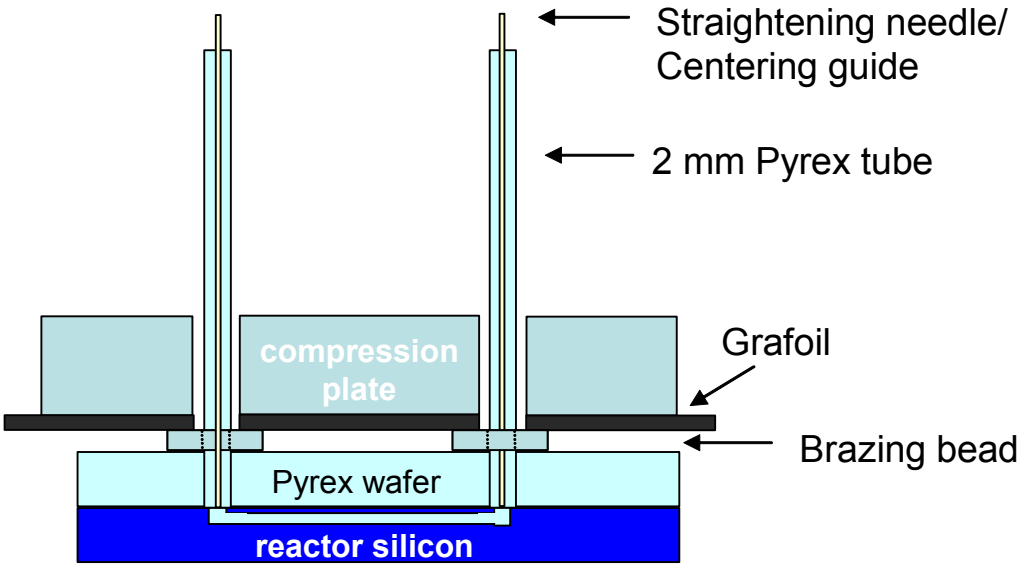


**Figure B-12.** Illustration of the brazing setup

The tubes cannot stand perfectly vertical on their own. Further, even though the straightening needles prevent bending of the tubing, the tubing is still free to fall from perpendicular. Therefore, a centering guide must be placed above the apparatus that holds either the tubing or the needles fixed in place 90$^{o}$ to the reactor chip. A variety of techniques can be used to achieve this. We have used a 1.5 inch thick centering block with 2.4 mm through-holes for the tubes that is elevated by rods. This centering block keeps the tubes straight and centered. However, disassembly is difficult as the tubes must be carefully slid out of the block evenly so as not to break the tubing. In the future, a design where a thin metal plate supported above the reactor by rods (stilts) that centers the needles would make both assembly and disassembly much easier.

The assembly is placed inside a furnace with a nitrogen purge. However, the atmosphere during the braze, although nitrogen rich, still contains some air as the furnace does not seal to the environment particularly well. The recipe used is as follows:

Step to 300 $^{o}$C
Hold for 1 hour (to equilibrate the atmosphere)
Step to 630 $^{o}$C (or 670 $^{o}$C- see next section)
Hold for 1 hour
Step to room temperature- slow cool (takes about 5 hours)

Once the reactor is disassembled from the setup, the stabilizer plate is epoxied and cured at 80 $^{o}$C for 30 minutes. This curing time provides the right mixture of strength and softness to survive the thermal cycling of the reactor chip. Once the stabilizer plate is glued, the package is surprisingly strong.

### B.4.3. Thermal Stability of Pyrex During Brazing

One issue arises about the thermal stability of Pyrex at the elevated temperatures during the brazing procedure. Pyrex is known to undergo a phase transformation at temperatures around 700 $^{0}$C and higher [2]. The phase transformation is a devitrification process where the bulk Pyrex transforms to cristobalite. Cristobalite has a lower density than bulk Pyrex borosilicate and therefore expands inside the Pyrex wafer. The expanding phase tends to initially form at energetically favorable areas such as channel corners, where it bulges into the reaction channel and changes the channel dimensions. This can be seen in the

photographs below of a cross-flow microreactor with and without this phase transformation occurring.

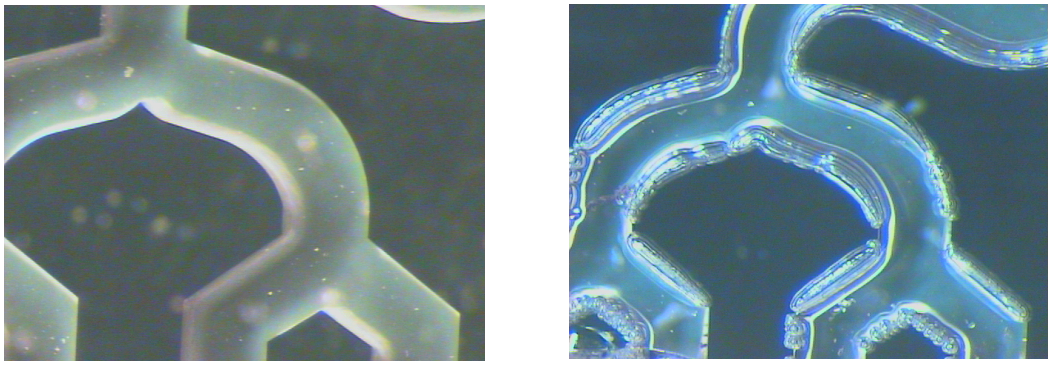


**Figure B-13.** Photographs of the cross-flow microreactor with normal channels and with channels where the cristobalite phase transformation has occurred The less dense phase primarily forms at channel corners.

This phase transformation does not occur for 1 hour at 630 $^{o}$C. However, better bonds are yielded at 670 $^{o}$C as the glass bead is closer to its working temperature. The phase transformation inconsistently occurs at the higher temperature, with some reactors holding up fine and others showing results like that in the above figure. The complete nature of this discrepancy has not been yet isolated. However, it is currently theorized that the top electrode used during anodic bonding plays a role. It has been noticed that for wafers where a graphite top electrode was used during the anodic bond yields reactors that undergo the phase transformation while wafers with a metal top electrode do not. This still requires more testing.

## B.5. Other Specifications

**O-rings:** Vendor: Parker Seals
Small o-ring size: 2-003
Large o-ring size: 2-004
Material: Proprietary fluoropolymer- V0763
Hardness: 60 Durometer

**Drawings of the machined parts:** Found on the next pages.

ALL DIM IN MILLIMETERS UNLESS NOTED

~~MODIFY EXISTING BRASS~~
(big St. steel block)
~~add 4 new holes of same size~~

CENTERING BLOCK FOR BRAZING
1.5 INCH THICK, STAINLESS-STEEL

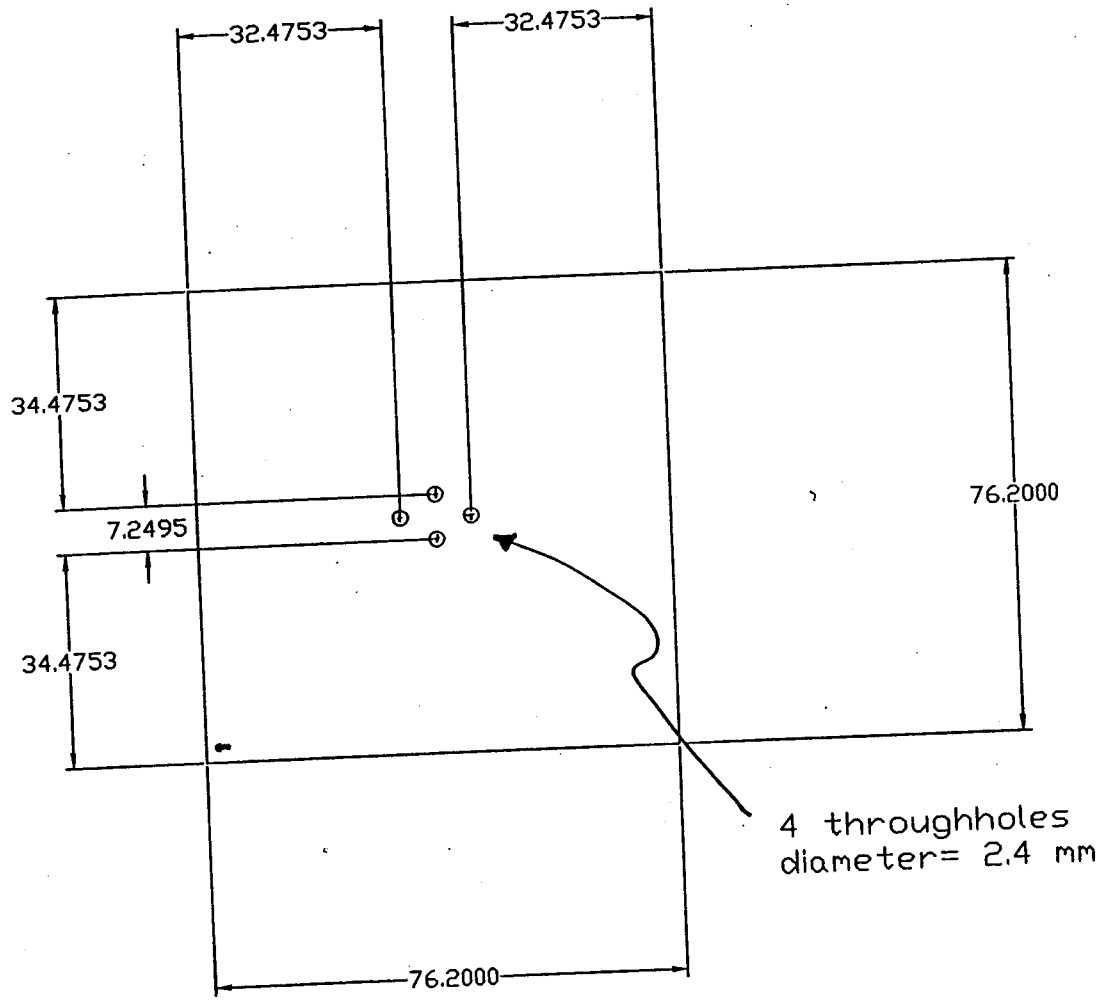

COMPRESSION PLATE: FOR BRAZING
QTY: 1
Stainless Steel
0.5 Inches Thick

ALL DIMENSIONS IN millimeters
except where noted

4 throughholes
diameter= 3.3 mm

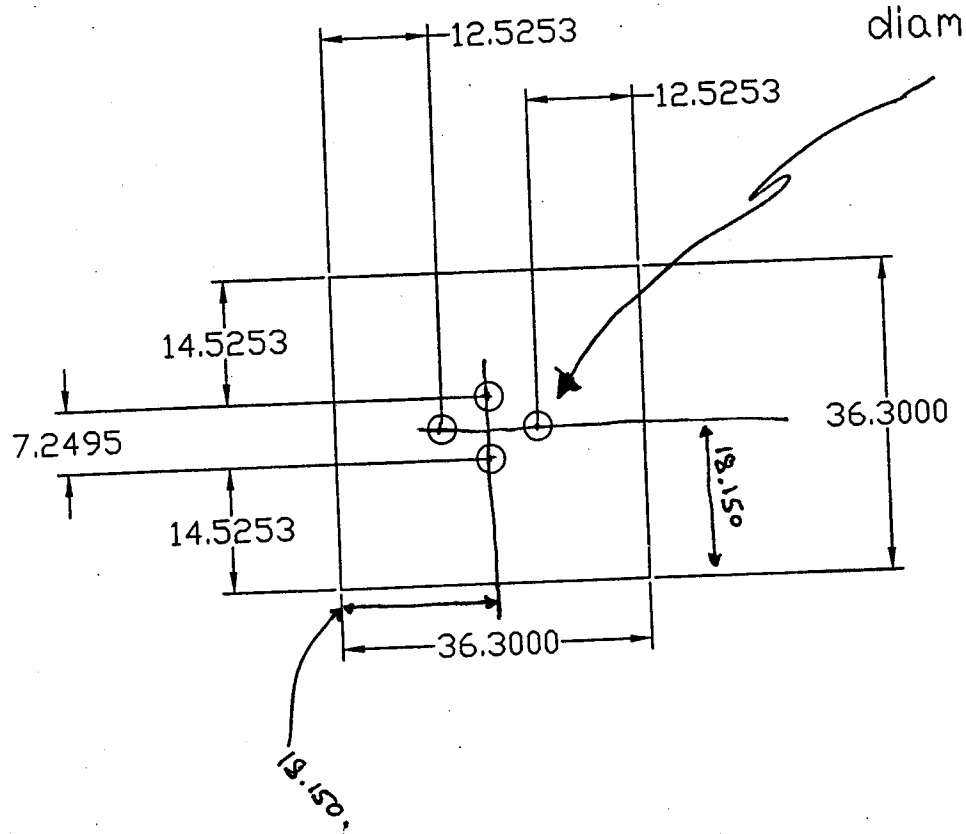

.UNITS, AS MARKED

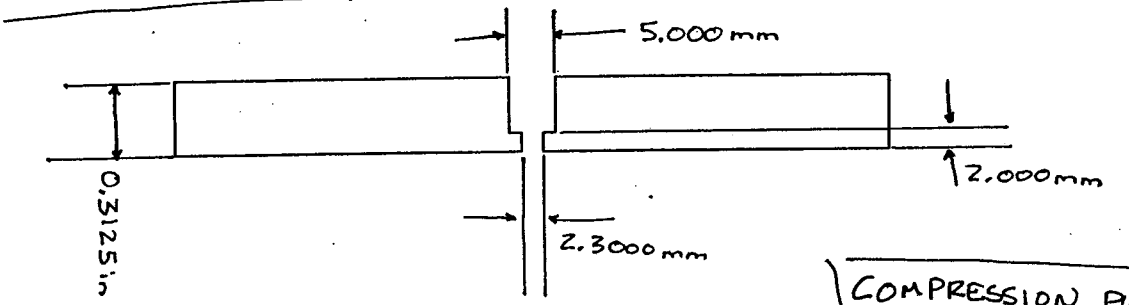


COMPRESSION PLATE FOR FLUIDIC PACKAGING - ALUMINUM

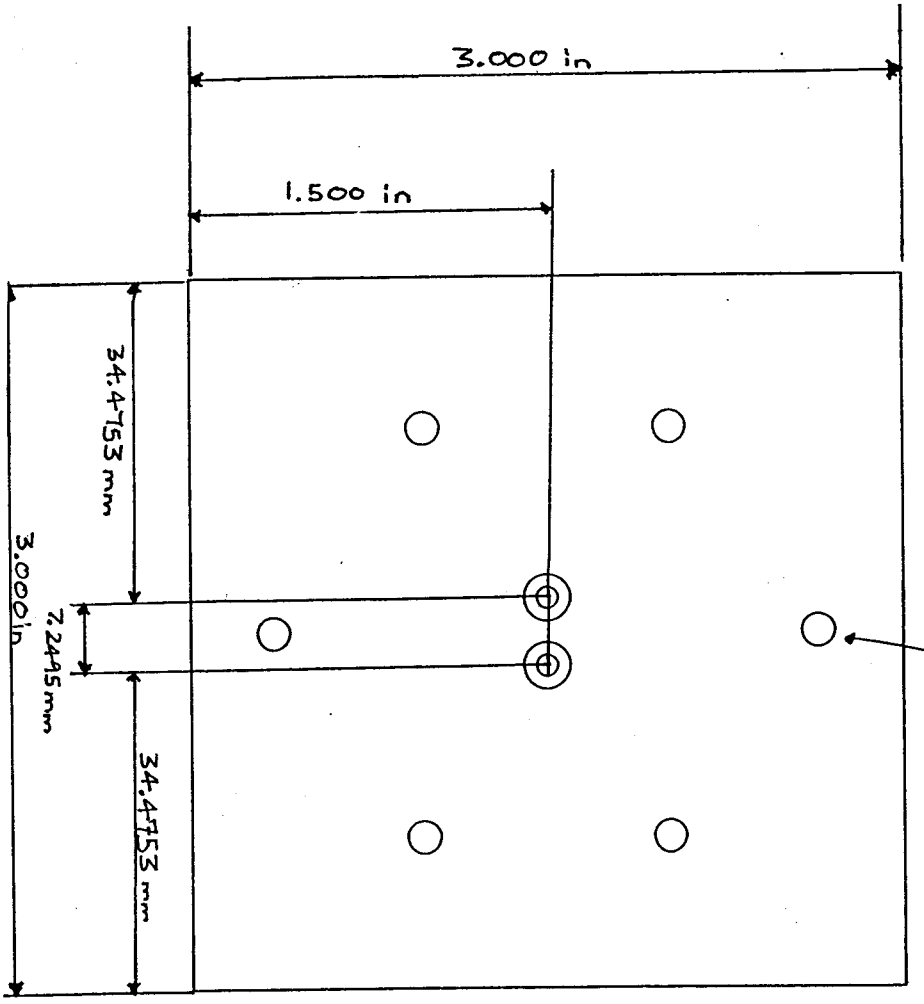


DIA: 3.500mm through-holes X 6

See PAGE A-1 for hole placement

PAGE A-1
Hole Placement.

UNITS, AS MARKED

PAGE A-1
HOLE PLACEMENT

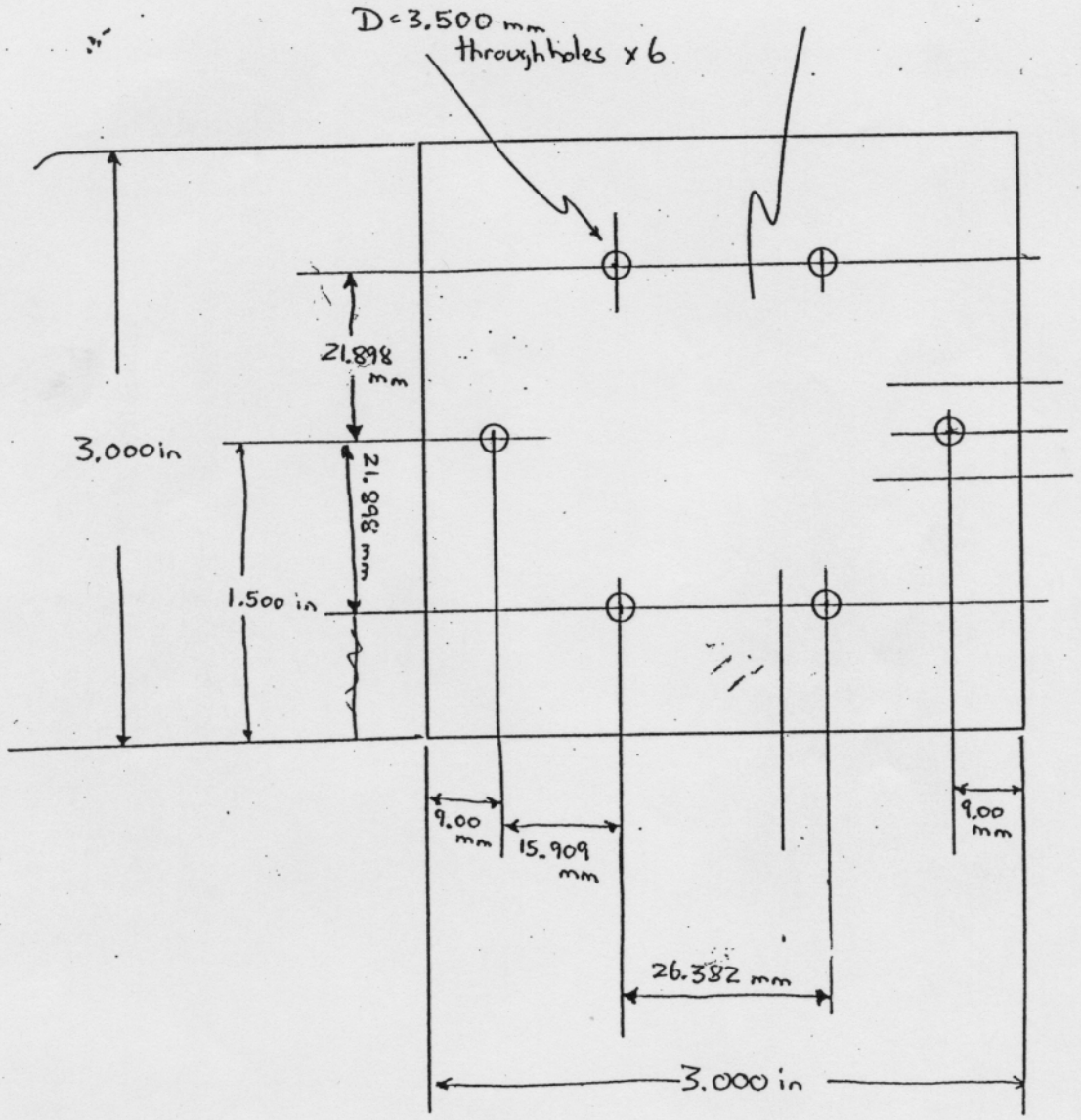

QTY 1.
UNITS, as marked

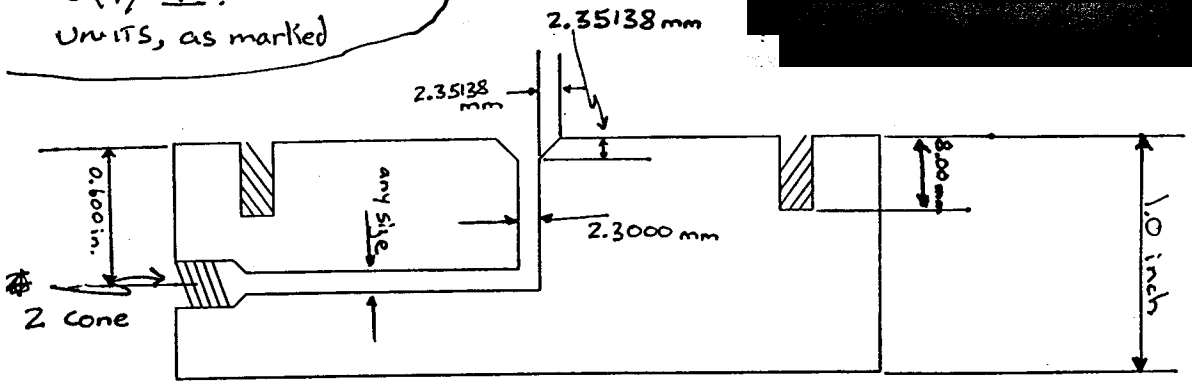


METAL BASE FOR O-RING SEAL

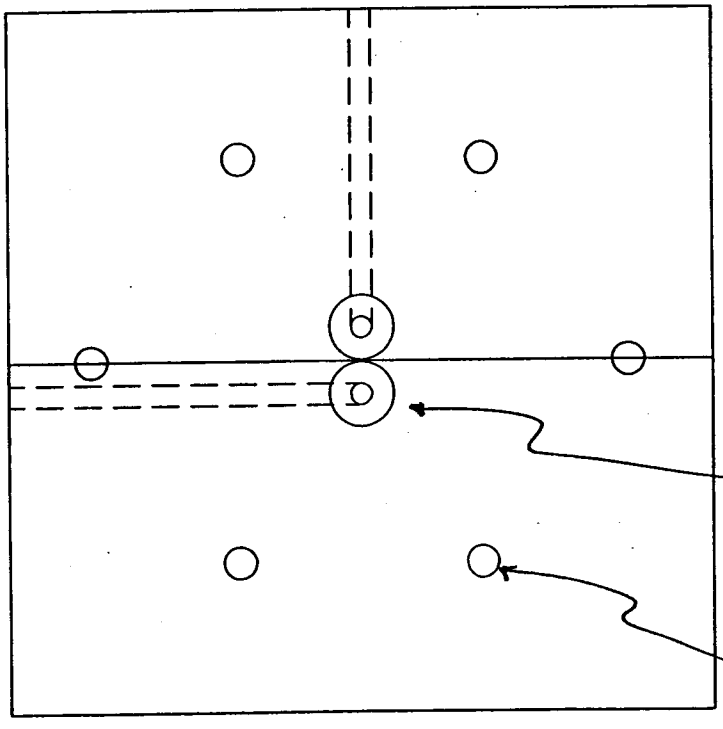

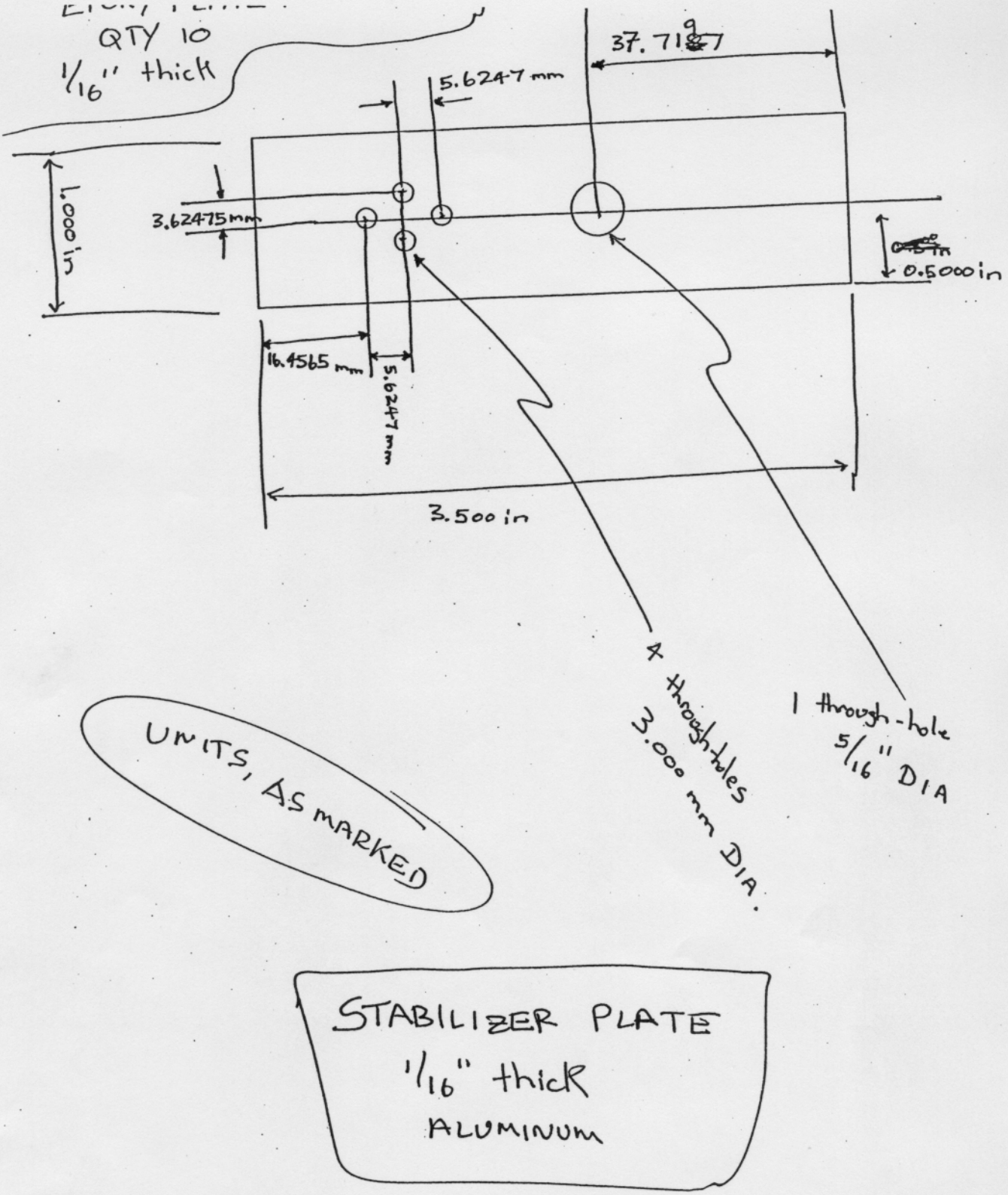


STABILIZER PLATE
1/16" thick
ALUMINUM

## Literature Cited

[1] T.S. Harrison, "Packaging of the MIT Microengine," Thesis, Massachusetts Institute of Technology, Cambridge, 2000.

[2] J.-H. Jean and Y.-C. Fang, "Devitrification kinetics and mechanism of Pyrex borosilicate glass," *J. Mater. Res.* **16** (2001) 1752.